High performance numerical simulation of coupled processes for CO2 storage in saline aquifers

Nicolas Pillardou

THÈSE

Pour l'obtention du grade de

DOCTEUR DE L'UNIVERSITÉ DE PAU ET DES PAYS DE L'ADOUR

DOMAINE DE RECHERCHE : Mathématiques Appliquées [1]

Présentée par

Nicolas Pillardou

High performance numerical simulation of coupled processes for CO_2 storage in saline aquifers

Simulation numérique haute performance de processus couplés pour le stockage du CO_2 dans les aquifères salins

Soutenance prévue le 27/09/2023

JURY

Carole ROSIER	Professeure, Université du Littoral-Côte-d'Opale	Rapporteure
Denis VOSKOV	Professeur, TU Delft and Stanford University	Rapporteur
Sylvie GRANET	Docteur - Ingénieur de Recherche, EDF	Examinatrice
Guillaume GALLIERO	Professeur, UPPA	Examinateur
Sylvain THIBEAU	Docteur - Ingénieur de Recherche, TotalEnergies - CSTJF	Examinateur
Brahim AMAZIANE	Maître de Conférences HDR, UPPA	Examinateur
Etienne AHUSBORDE	Chargé de Recherche CNRS HDR, UPPA	Directeur
Fabrizio CROCCOLO	Professeur, UPPA	Co-directeur

[1] Thèse préparée au sein du Laboratoire de Mathématiques et de leurs Applications de Pau (LMAP) et Laboratoire des Fluides Complexes et leurs Réservoirs (LFCR) dans l'École Doctorale des Sciences Exactes et leurs Applications de l'UPPA.

Abstract

Numerical simulations of coupled processes in porous media are used in many energy and environmental applications. This work is concentrated on the application of CO_2 storage in saline aquifers, a strategy for reducing CO_2 emissions that is at the center of today's environmental debates. This type of application is described by coupled Thermal, Hydraulic, Mechanical, and Chemical (THMC) processes that interact with each other. The thesis focuses on nonisothermal multiphase flow coupled with reactive transport (THC) and geomechanical effects on the isothermal multiphase flow (HM). A literature review is proposed in Chapter 1 to investigate the global issue of CO_2 storage and the numerical methods used to solve the highly coupled THMC processes.

The first part is dedicated to Thermal-Hydro-Chemical coupling. The mathematical problem for THC is exposed in Chapter 2, governed by a highly nonlinear system of partial differential equations (nonisothermal multiphase flow), coupled with algebraic and/or ordinary differential equations (geochemistry). Two different types of resolution approaches are investigated: the sequential and the fully implicit approaches, which are described in Chapter 3. A cell-centered finite volume scheme, two-point or multi-point flux approximation (TPFA/MPFA), is adopted for spatial discretisation, depending on the mesh complexity. An implicit Euler or second-order backward differentiation formula (BDF2) is used for the time discretisation. The sequential and fully implicit numerical algorithms are implemented in the *DuMu*^{X} simulation platform. The accuracy, efficiency, and scalability of the developed models and solvers are thoroughly validated through comparisons with other studies in 1D, 2D, and 3D test cases using High-Performance Computing.

The second part is dedicated to the study of Hydro-Mechanical coupling. In Chapter 4, the poroelastic problem is presented. It is composed of mass conservation laws (governing an isothermal compositional two-phase flow) coupled with a momentum conservation law supplemented by constitutive relations (modeling the geomechanics). A two-way coupling between the two latter problems is performed by effective quantities (pressure, density) as well as porosity and permeability depending on the displacement. The spatial discretisation is carried out by combining a cell-centered finite volume scheme for the flow with a vertex-centered Control Volume Finite Element Method (Box scheme) for the geomechanics. A fully implicit numerical scheme is implemented in *DuMu*^{X}. In Chapter 5, several validations of the numerical HM coupling scheme are provided through the multi-dimensional consolidation processes, known for their analytical solutions. CO_2 storage scenarios in 2D layered geological formations are also investigated and validated by comparisons with recent studies, including computations performed with the industrial simulator CMG-GEM.

Some conclusions are given in Chapter 6, which allow us to identify several perspectives that could improve the numerical framework in terms of accuracy and computational time, but also to investigate realistic scenarios with more complex coupling (THMC).

Résumé

Les simulations numériques des processus couplés en milieux poreux sont utilisées dans de nombreuses applications énergétiques et environnementales. Ce travail se concentre sur l'application du stockage du dioxyde de carbone dans les aquifères salins, un processus visant à réduire les émissions de gaz à effet de serre, au cœur des débats environnementaux actuels. Ce type d'application est décrit par des processus couplés Thermiques, Hydrauliques, Mécaniques et Chimiques (THMC) qui interagissent ensemble. La thèse se concentre sur l'étude d'écoulements réactifs multiphasiques non-isothermes (THC) et aux effets géomécaniques sur un écoulement multiphasique isotherme (HM). Un état de l'art est proposé dans le Chapter 1 pour étudier le sujet du stockage du CO_2, mais aussi pour avoir un aperçu des différentes méthodes numériques pour le couplage THMC.

La première partie est consacrée au couplage Thermo-Hydro-Chimique. Le modèle mathématique pour le THC, exposé dans le Chapter 2, est gouverné par un système, fortement non-linéaire, d'équations aux dérivées partielles (écoulement multiphasique non-isotherme), couplé à des équations différentielles algébriques et/ou ordinaires (modélisant la géochimie). Deux approches de résolution différentes sont étudiées : les approches séquentielles et entièrement implicites, détaillées dans le Chapter 3. Un schéma numérique volume-finis centrés sur les cellules est adopté pour la discrétisation spatiale, avec une approximation de flux à deux points ou multi-points (TPFA/MPFA), dépendant de la complexité du maillage. Un schéma d'Euler implicite ou de second ordre Backward Differentiation Formula (BDF2) sont utilisés pour la discrétisation temporelle. Les algorithmes des méthodes séquentielle et implicite sont implémentés sur la plateforme de simulation *DuMu*^{X}. La précision, l'efficacité et la scalabilité des modèles et des solveurs développés sont évaluées par comparaison avec des études 1D, 2D et 3D, grâce à du Calcul Haute Performance.

La deuxième partie est consacrée à l'étude du couplage Hydro-Mécanique. Dans le Chapter 4, le modèle poroélastique linéaire est détaillé. Il se compose de lois de conservations de la masse (régissant un écoulement diphasique compositionnel isotherme) et de la loi de conservation du moment complétée par des relations constitutives (modélisant la géomécanique). Un couplage bi-directionnel entre les deux problèmes est effectué à l'aide de variables effectives (pression, densité) mais aussi grâce aux porosité et perméabilité qui dépendent du déplacement. La discrétisation spatiale est réalisée en combinant un schéma de type volumes-finis centrés sur les cellules pour l'écoulement, avec une méthode centrée sur les sommets de type "Control Volume Finite Element Method" (schéma Box) pour la géomécanique. Dans le Chapter 5, le schéma numérique est validé au travers des processus de consolidation multidimensionnels, connus pour leurs solutions analytiques. Des scénarios de stockage du CO_2 sont également étudiés et validés par des comparaisons avec des études récentes et des calculs réalisés sur le simulateur industriel CMG-GEM.

Des conclusions sont présentées dans le Chapter 6, permettant d'identifier plusieurs perspectives pouvant améliorer le cadre numérique en termes de précision et de temps de calcul, dans le but d'investiguer des scénarios réalistes avec des couplages complexes de types THMC.

Acknowledgements

This thesis has been a challenging project carried out under the framework of the E2S-UPPA Hub Newpores and Industrial Chair CO_2ES supported by the Investissements d'Avenir French programme managed by ANR (ANR16IDEX0002). We acknowledge financial support from E2S-UPPA, TotalEnergies, BRGM, and CNES. During the last three years at the Université de Pau et des Pays de l'Adour, I have met many people on the campus, at various seminars and meetings or conferences. They are all involved in this work in their own way and I would like to address them with some words to thank them.

First, I would like to thank Etienne Ahusborde and Fabrizio Croccolo, my supervisors, who hired me and trusted me to carry out this research project. I would note the kindness they showed me, their constant availability, and their expertise on many subjects which were very helpful. I would particularly like to thank Brahim Amaziane and Mustapha El Ossmani for all the support, and advice, as well as the instructive talks and debates we had during these three years. I also thank Michel Kern for agreeing to be a member of the CSI and for evaluating my work each year. This doctoral work would not have been possible without them.

I would like to express my sincere gratitude to the members of the jury. First I would like to thank Carole Rosier, and Denis Voskov for agreeing to report on my thesis. Their scientific expertise is a reference, and I am very grateful that they are associated with this work, for the pertinent comments you provided to improve this document. I would also like to gratefully thank Guillaume Galliero for agreeing to chair the jury and Sylvie Granet for her presence on the jury. I'm honoured to be able to count on both of them. Finally, I would like to thank Sylvain Thibeau for his interesting comments and his industrial perspective, which allowed me to focus on important physical aspects.

I thank the *DuMu*^{X} developer team as well as the user community for all the support and discussions we had to give solutions to our problems. Thanks to Computer Modelling Group Ltd for providing licenses and support.

To all the people I met Pau, with whom I shared my time, particularly the members of the CO_2ES Chair, the Methode Numerique et Fluides complexes group, the LMAP and LFCR laboratories. A big thanks to the other PhD students, Salah, Adrien, Puneeth, Sarah, Rodrigo, Manos, Giulio, Aimene, Rong, Joyce, Ibtissem, Magdalena, and those I forget. The daily moments, meals, drinks, outdoor activities, and crazy football matches we had together made me cheerful.

Finally, I want to have a word for my closest friends, my girlfriend, my family, and my parents who always supported me during the moments we shared and pushed me to do my best. This thesis work would not have been possible without any of you.

Résumé long

Le stockage géologique du dioxyde de carbone (CO_2) est largement reconnu comme l'une des stratégies les plus prometteuses pour réduire les conséquences des gaz à effet de serre, qui sont les principaux responsables du réchauffement climatique. Différents types de formations géologiques sont couramment utilisés pour ce stockage, en particulier les réservoirs de gaz et de pétrole déplétés, les veines de charbon et les aquifères salins. Ces formations géologiques agissent comme un réservoir naturel, retenant le CO_2 et le maintenant séquestré à des profondeurs importantes. Durant ce processus de stockage, divers mécanismes de piégage sont combinés, agissant chacun à des échelles de temps différentes variant d'années à des millénaires. En effet, la dissolution du CO_2 gazeux ou supercritique dans l'eau se produit seulement au bout de dizaines d'années alors que la formation de minéraux carbonés peut nécessiter plusieurs milliers d'années. Ainsi, l'évaluation de la fiabilité et et la durabilité du stockage géologique nécessite l'utilisation de simulations numériques pour obtenir des prédictions puisque les expérimentations sont impossibles sur des échelles de temps aussi longues. Le Chapter 1 donne l'aspect contextuel de ce travail qui s'inscrit dans un but environnemental. Un état de l'art est également proposé dans ce chapitre afin d'étudier et de comprendre ce procédé complexe qui implique des couplages entre les processus thermiques, hydrauliques, mécaniques et chimiques (THMC). Au coeur de ces couplages, les processus hydrauliques concernent le mouvement des fluides, en particulier l'injection du CO_2 sous la forme gazeuse ou supercritique et la migration des fluides dans la formation géologique. Ainsi, il est essentiel de comprendre les phénomènes d'écoulement multiphasique, les interactions fluide-roche et les échanges de masse entre les phases. La prise en compte des effets thermiques complexifie les équations d'état, qui dépendent alors de la température et de la pression. Le couplage chimique concerne les réactions chimiques qui surviennent entre le CO_2, les fluides et les minéraux présents dans la formation géologique. Ces réactions peuvent avoir une incidence sur la stabilité chimique des minéraux, l'alcalinité des liquides et la capacité de stockage à long terme du CO_2puisque que les phénomènes de précipitation et dissolution peuvent modifier la porosité et donc la perméabilité de la formation géologique. L'étude des réactions chimiques permet de prévoir l'évolution à long terme du système et d'en assurer la pérennité. Enfin, la prise en compte des effets mécaniques permet d'étudier les changements de contraintes et de déformations induits par l'injection du CO_2. Lorsque ce dernier est injecté, la formation géologique subit une surpression pouvant générer des effets mécaniques tels que la fracturation, la déformation de la roche et la modification de la perméabilité. La compréhension de ces processus est cruciale pour évaluer l'intégrité de la formation et la sécurité du stockage. Ces differents sujets ont été largement étudié avec de nombreuses contributions dans les dernières années. Ce travail se concentre principalement sur deux axes, à savoir les méthodes de couplage Thermo-Hydro-Chimique (THC) et Hydro-Mécanique (HM).

Dans le Chapter 2, le modèle mathématique pour le couplage THC est donné. La séquestration du CO_2 dans un aquifère salin conduit à l'étude d'un écoulement nonisotherme diphasique (eau-gaz) couplé avec la géochimie (étude des réac-

tions). Les équations régissant ce modèle sont obtenues en écrivant les équations de conservation de la masse, une loi de conservation de l'énergie, la loi de Darcy généralisée et diverses équations de fermeture. Le couplage avec la chimie intervient par l'intermédiaire des taux de réactions, qui peuvent être soit des fonctions (non-linéaires) données des concentrations, dans le cas de réactions cinétiques, soit inconnus pour des réactions à l'équilibre. Dans ce dernier cas, chaque réaction donne lieu à une loi d'action de masse, soit une relation algébrique liant les concentrations des espèces concernées. D'un point de vue mathématique, cela nécessite donc de résoudre un large système d'équations aux dérivées partielles fortement non linéaires couplées à des équations différentielles algébriques. Pour finir, les diverses équations d'état utilisées dans le cadre de ce travail sont explicitées.

Le Chapter 3 présente le cadre numérique dans le but d'effectuer des simulations numériques sur des scénarios de stockage de CO_2. Deux stratégies de résolution différentes ont été étendues au couplage THC, à savoir une approche totalement implicite et une approche séquentielle. Précisément, l'approche couplée totalement implicite résout le système comme un système monolithique global unique à chaque itération dans le temps, ce qui entraîne des non-linéarités plus importantes. L'approche séquentielle, quant à elle, consiste à découpler le système en deux sous-problèmes distincts, à savoir un écoulement compositionnel non-isotherme multiphasique et un problème de transport réactif. La résolution de ces deux sous-problème est effectuée séquentiellement, au moyen de communications de variables nécessaires. Les deux stratégies ont été implémentées dans la plateforme de simulation *DuMu*^{X}. Cette plateforme open source propose une gamme de fonctionnalités, notamment la gestion de la géométrie et du maillage, les discrétisations spatiale et temporelle, les solveurs et méthodes numériques, le calcul haute performance, etc... Elle bénéficie également d'une implémentation modulable rendant le développement des deux stratégies décrites ci-dessus possibles. Pour cela, les approches totalement implicite et séquentielle, ont été discrétisées en utilisant un schéma volumes-finis, centré sur les cellules. Précisément, une approximation des flux à deux points (TPFA) ou une approximation de flux à plusieurs points (MPFA) est utilisée selon la complexité du maillage. Des simulations 1D, 2D et 3D ont été réalisées pour valider et illustrer la capacité du modèle à simuler des scénarios de stockage de CO_2. La prise en compte des effets de température entraîne une augmentation de la dissolution du CO_2 et de la calcite, respectivement dans les régions proches du puits et de la zone du panache de CO_2 , ce qui améliore à la fois l'injectivité du puits et le piégeage par dissolution. Les cas 2D et 3D sont étendus au couplage THC et les résultats obtenus sont en accord avec la littérature concernant l'évolution de l'écoulement. Des comparaisons entre les deux stratégies de résolution implicite et séquentielle ont été réalisées, mettant en évidence le fait que l'approche entièrement implicite est conservative. L'approche séquentielle introduit une erreur de découpage qui dégrade la précision du schéma malgré un gain de temps de calcul. Afin d'évaluer le comportement du modèle numérique sur plusieurs centaines de processeurs, des calculs haute performance ont été réalisées et les scalabilités fortes et faibles ont été analysées. De plus, le dernier cas a été modifié pour examiner le comportement à long terme de la minéralisation, ce qui n'était pas envisageable avec la formulation initiale du problème. Les résultats obtenus concernant la précipitation et la dissolution d'espèces minérales sont cohérents avec la littérature,

montrant une efficacité croissante de la minéralisation sur de longues échelles de temps (de 100 à plusieurs milliers d'années). Une partie de ce chapitre a donné lieu à la publication d'un article en révision pour publication dans le journal *Computational Geosciences*.

Dans le Chapter 4, le modèle mathématique pour le couplage HM est introduit. Il est gouverné par des lois de conservations de la masse décrivant l'écoulement isotherme compositionnel diphasique, couplé à une loi de conservation du moment décrivant l'équilibre géomécanique. Des relations constitutives sont également introduites, caractérisant le tenseur de contraintes effectives et totales en utilisant les lois de poroélasticité linéaire issues de la littérature. Le couplage entre ces deux sous-problèmes est réalisé au moyen de variables effectives. D'une part le problème géomécanique requiert les pressions et densités effectives pour calculer un équilibre géomécanique. D'autre part, des variations de porosité et perméabilité sont prises en compte, dépendant des déplacements géomécaniques et affectant l'écoulement. Par conséquent, un système fortement non linéaire d'équations aux dérivées partielles couplées est formulé pour les processus couplés Hydro-Mécaniques. La discrétisation du modèle est également donnée en détail. Un schéma volumes-finis, centré sur les cellules est utilisé pour la discrétisation de l'écoulement diphasique compositionnel en utilisant des schémas TPFA ou MPFA selon la complexité du maillage. Pour la discrétisation du problème poroélastique, une méthode méthode d'éléments finis avec volume de contrôle (CVFEM) est utilisée. Précisément une méthode "bOX", centrée sur les sommets est mise en place, en utilisant des fonctions de base linéaires par morceaux pour approcher les variables et gradients à l'intérieur du maillage.

Finalement, le Chapter 5 traite les stratégies de résolution, l'implémentation et la validation du couplage HM sur trois cas tests. Une approche totalement implicite est utilisée comme stratégie de résolution, signifiant que les deux sous-problèmes couplés sont résolus simultanément sous la forme d'un seul système fortement non-linéaire. L'implémentation de ce modèle est également réalisée dans $DuMu^X$. La validation du schéma numérique a été effectuée grâce à des problèmes multi-dimensionnels de consolidation, en confrontant les résultats à des solutions analytiques issues de la littérature. Par la suite, trois différents cas d'étude 2D ont été traités afin d'étudier le comportement du modèle numérique en matière de séquestration de CO_2. Plus précisément, le premier cas s'est concentré sur la validation grâce à une comparaison avec une version précédente de $DuMu^X$ qui utilisait une formulation du problème mécanique différente. Une extension au couplage Hydro-Mécanique a été réalisée dans le deuxième cas, où le maillage du domaine est constitué de cellules non K-orthogonales, nécessitant l'utilisation du schéma MPFA. Dans le troisième cas, les calculs ont également été effectués avec le simulateur industriel GEM afin de comparer précisément les deux différents simulateurs. De légères différences ont été observées, pouvant résulter des différentes stratégies de résolution utilisées dans chacun des simulateurs.

Des conclusions et plusieurs perspectives envisageables concernant les deux parties de ce travail sont formulées dans le Chapter 6. Pour le couplage THC, le temps de calcul pour la méthode totalement implicite doit être améliorer. Une meilleure stratégie pour une gestion dynamique du pas de temps ou bien l'utilisation d'estimateurs d'erreurs afin de mieux gérer les tolérances de convergence (linéaire

et non linéaiure) pourraient être envisagées. De plus, l'utilisation de schéma numériques non-linéaires pourrait apporter une plus grande précision aux résultats de simulation. D'autre part, concernant la partie Hydro-Mécanique, du fait de large temps de calcul, des simulations 3D n'ont pas pu être réalisées dans ce travail. Pour cela, des stratégies d'améliorations dans cette optique sont proposées comme par exemple la mise en place d'un schéma séquentiel ou l'utilisations de solveurs itératifs. De plus, la température pourraient également être ajouté au couplage afin d'étudier les effets thermique sur le scénario d'injection de CO_2. Le point culminant de ce projet réside dans le couplage complet des processus THMC, ce travail s'inscrit donc comme une contribution dans la continuité de ce qui a été effectué auparavant dans [106].

Contents

1 General Introduction **1**

1.1 General context . . . 2

1.1.1 CO_2 emissions and global warming . . . 2

1.1.2 Mitigation Strategy . . . 2

1.1.3 Carbon Capture and Storage . . . 3

1.1.4 Trapping Mechanisms . . . 4

1.1.5 Existing Projects . . . 7

1.2 Reservoir modelling for CO_2 storage in saline aquifers . . . 7

1.2.1 Hydraulic processes for CO_2 storage . . . 9

1.2.2 Hydro-Chemical processes for CO_2 storage . . . 12

1.2.3 Thermal-Hydro-Chemical processes for CO_2 storage . . . 14

1.2.4 Mechanical coupling in the process of CO_2 storage . . . 15

1.2.4.1 Coupling management applied to CO_2 storage . . . 16

1.2.4.2 Hydro-mechanical coupling . . . 17

1.2.4.3 Thermal-hydro-mechanical coupling . . . 19

1.2.5 Thermal-Hydro-Mechanical-Chemical coupling for CO_2 storage 20

1.3 Contribution of the thesis . . . 21

1.3.1 Objectives of the thesis . . . 21

1.3.2 Structure of the manuscript . . . 22

2 Thermal-Hydro-Chemical coupled model for geological CO_2 storage **25**

2.1 Introduction . . . 26

2.2 Fundamental terms . . . 26

2.2.1 State variables . . . 26

2.2.2 Fluid properties . . . 28

2.2.3 Porous media properties . . . 29

2.3 Geochemical model . . . 32

2.3.1 Chemical model . . . 33
2.3.2 Equilibrium reactions . . . 35
2.3.3 Kinetic reactions . . . 36
2.4 Two-phase flow model . . . 36
2.5 Temperature processes . . . 38
2.6 Global Thermo-Hydro-Chemical model . . . 38
2.7 Closure relations . . . 39
2.8 Constitutive relations . . . 40
2.8.1 CO_2 fluid properties . . . 40
2.8.2 Brine fluid properties . . . 41
2.9 Conclusion . . . 43

3 Numerical simulation of Thermal-Hydro-Chemical processes for CO_2 storage 45
3.1 Introduction . . . 46
3.2 Resolution methods . . . 46
3.2.1 Sequential approach . . . 46
3.2.2 Global implicit approach . . . 49
3.3 Numerical schemes . . . 50
3.3.1 Time discretisation . . . 50
3.3.2 Fully coupled fully implicit finite volume scheme . . . 51
3.4 Implementation . . . 53
3.4.1 $DuMu^X$ numerical simulation platform . . . 53
3.5 Numerical simulations of CO_2 storage scenarios . . . 54
3.5.1 Test case 1: 1D radial problem . . . 55
3.5.1.1 Problem configuration . . . 55
3.5.1.2 Numerical results . . . 57
3.5.2 Test case 2: 2D layered problem . . . 61
3.5.2.1 Problem configuration . . . 61
3.5.2.2 Numerical results . . . 64
3.5.3 Test case 3: 3D heterogeneous problem . . . 67
3.5.3.1 Problem configuration . . . 67
3.5.3.2 Numerical results . . . 70
3.5.3.3 Sequential and implicit comparisons . . . 73
3.5.3.4 High Performance Computing . . . 79
3.5.3.5 Long-term evolution of CO_2 . . . 84
3.6 Conclusion . . . 87

4 Hydro-Mechanical processes coupled model for CO_2 storage 89
4.1 Introduction . . . 90
4.2 Fundamental terms in geomechanics . . . 90
4.3 Mathematical model for Hydro-Mechanical coupling . . . 93
4.3.1 Momentum balance equation . . . 93
4.3.2 Constitutive relations and constraints . . . 94
4.3.3 Mass balance equation . . . 95
4.3.4 Closure relations . . . 96
4.4 Numerical scheme for Hydro-Mechanical coupling . . . 97
4.5 Conclusion . . . 101

5 Numerical simulation of Hydro-Mechanical processes 103
5.1 Introduction . . . 104
5.2 Resolution strategies . . . 104
5.2.1 Fully coupled approach . . . 104
5.2.2 Sequential methods . . . 105
5.2.3 Two-step procedure for solution strategy . . . 106
5.2.4 Implementation . . . 106
5.3 Numerical simulations . . . 106
5.3.1 Consolidation problems . . . 107
5.3.1.1 One-dimensional consolidation . . . 107
5.3.1.2 Two-dimensional consolidation . . . 109
5.3.1.3 Three-dimensional consolidation . . . 112
5.3.2 Hydro-Mechanical simulations for CO_2 storage . . . 115
5.3.2.1 Test 1: 2D domain involving a heterogeneous band . 116
5.3.2.2 Test 2: 2D layered problem . . . 123
5.3.2.3 Test 3: Comparison with reservoir simulator . . . 128
5.4 Conclusion . . . 135

6 Conclusion and perspectives 137
6.1 Conclusion . . . 137
6.2 Perspectives . . . 139

Bibliography 143

List of Figures

1.1 Annual global carbon emissions per region since 1800 from the Global Carbon Project dataset [164] . . . 3

1.2 Process for the capture of carbon dioxide from a power plant emission [52] . . . 4

1.3 Diagrams of the four trapping mechanisms involved in geological CO_2 storage from [74] and illustration of the temporal evolution of storage security as a function of the trapping contribution from [139] on the right of the figure. . . . 5

1.4 Cross couplings between THMC coupling from [198]. . . . 8

2.1 Phase diagram for CO_2 as a function of pressure and temperature. The critical point is at a pressure of 73.8 bar and a temperature of 304.25 K. . . . 27

2.2 Capillary pressure evolution as a function of liquid saturation for the two empirical models of Brooks-Corey and Van-Genuchten. . . . 31

2.3 Liquid and gas relative permeability evolution as a function of liquid saturation for the two empirical models of Brooks-Corey and Van-Genuchten. . . . 32

2.4 Variations of CO_2 density (a) and CO_2 viscosity (b) as a function of pressure and temperature. . . . 40

2.5 Variations of CO_2 enthalpy (a) and CO_2 solubility (b) as a function of pressure and temperature. . . . 41

2.6 Variations of brine density (a) and viscosity (b) as a function of pressure and temperature. . . . 42

2.7 Variations of brine enthalpy (a) and gas solubility (b) as a function of pressure and temperature. . . . 42

3.1 Coupling algorithm between compositional nonisothermal two-phase flow and reactive transport modules. . . . 47

3.2 Admissible grids for using Two-Point Flux Approximation method in a cell-centered FV scheme. . . . 52

3.3 Schematic diagram of the 1D test case proposed in [229]. . . . 55

3.4 Mesh convergence for the saturation of the gaseous phase (a) and $CO_{2(l)}$ concentration (b) at 10 years. 57
3.5 Mesh convergence for the pressure of the gaseous phase (a) and temperature profile (b) at 10 years. 58
3.6 Mesh convergence for the pH (a) and concentration of calcite (b) profiles at 10 years. 58
3.7 L^2-relative error for $CO_{2(l)}$ concentration, gas saturation, gas pressure, calcite, and temperature as a function of cell size. 59
3.8 Evolution in time of concentration of liquid CO_2 and saturation of the gaseous phase for isothermal and nonisothermal cases. 59
3.9 Evolution in time of gaseous phase pressure and temperature for isothermal and nonisothermal cases. 60
3.10 Evolution in time of pH and concentration of calcite for isothermal and nonisothermal cases. 60
3.11 Schematic diagram of the 2D test case proposed in [179]. 61
3.12 Evolution of gaseous saturation and CO_2 liquid molar fraction at 1, 2 and 4 years from top to bottom. 65
3.13 Evolution of liquid overpressure and temperature at 1, 2, and 4 years from top to bottom. 65
3.14 Evolution of pH and calcite at 1, 2, and 4 years from top to bottom. 66
3.15 Evolution of anorthite and kaolinite at 1, 2, and 4 years from top to bottom. 66
3.16 Evolution of mineral quantities as a function of time. 67
3.17 Geophysical configuration of the aquifer for the 3D Benchmark [54]. 68
3.18 Evolution of gaseous saturation over time. 70
3.19 Evolution of CO_2 liquid molar fraction over time. 71
3.20 Evolution of gaseous pressure over time. 71
3.21 Evolution of temperature over time. 72
3.22 Evolution of pH over time. 72
3.23 Evolution of calcite concentration over time. 73
3.24 Evolution of CO_2 quantities as a function of time. (a) total injected mass of CO_2, (b) mass of CO_2 in gas phase, (c) mass of CO_2 dissolved in liquid phase, (d) mass of CO_2 in mineral phase. 73
3.25 Simulation results obtained by GEOS at $t = 50$ years. 74
3.26 Comparison of gaseous saturation profile for the sequential and implicit approaches at 50 years. 74
3.27 Comparison of liquid CO_2 molar fraction profile for the sequential and implicit approaches at 50 years. 74
3.28 Comparison of pH profile for the sequential and implicit approaches at 50 years. 75

3.29 Comparison of calcite dissolution profile for the sequential and implicit approaches at 50 years. 75

3.30 Comparison of the evolution of CO_2 quantities as a function of time between fully implicit and sequential approaches. 76

3.31 Comparison between the implicit and sequential approaches: (a) CPU time evolution as a function of time for the different stages of the computation, (b) time step, (c) number of Newton iterations per time step, (d) total number of linear iterations per time step. . . 77

3.32 Temperature profiles for both isothermal (left) and nonisothermal (right) problems. 79

3.33 Temperature difference between isothermal and nonisothermal profiles at 50 years. 80

3.34 Evolution of CO_2 dissolved in the liquid phase for the isothermal and nonisothermal case with several temperature injections. 80

3.35 CPU time evolution for the two different mesh sizes 82

3.36 Evolution of quantities with respect to the number of processors: (a) Speedup, (b) strong scaling efficiency, (c) global CPU time, (d) average CPU Time per iteration, (e) detailed CPU time for the mesh composed of 876096 elements, (f) detailed CPU time for the mesh composed of 3504384 elements. 83

3.37 Weak scalability (a) and weak efficiency (b) for fully implicit and sequential approaches. 84

3.38 Load imbalance (a) for different meshes and mesh partitioning (b) for 16 processors with 219024 elements. 85

3.39 Modifications of configuration for long-term CO_2 storage benchmark. 85

3.40 Evolution of several quantities of interest at 300 years. 87

3.41 Long-term evolution of CO_2 quantities in the aquifer. 88

4.1 Continuum mechanics sign convention for stress 92

4.2 Schematic of the discretisation of a control volume with the Box method. 99

5.1 Algorithms of fully coupled, one-way, and two-way coupling approaches to solve Hydro-Mechanical problems. 105

5.2 Table data and schematic configuration for the 1D consolidation problem. 108

5.3 Representation of the pressure evolution at several times for Terzaghi's consolidation problem. 109

5.4 Evolution of the pressure as a function of the vertical position in the beam for several times. 109

5.5 Configuration of the 2D consolidation problem (taken from [113]). . 110

5.6 Representation of the pressure evolution at several times for Mandel's consolidation problem. . . . 112

5.7 Evolution of the liquid pressure for the 2D consolidation as a function of time. . . . 112

5.8 Evolution of horizontal and vertical displacements as a function of time. . . . 113

5.9 Configuration of Cryer's consolidation problem [94]. . . . 113

5.10 Evolution of the liquid pressure in the domain as a function of time. 114

5.11 Comparison of the evolution of the pressure for different values of the Poisson coefficient as a function of time. . . . 116

5.12 Configuration for the "fracture" test case (a) and the mesh used (b) (taken from [31]). . . . 117

5.13 Gaseous saturation and overpressure profiles obtained with $DuMu^X$ (a) and from [31] (b) for the case without "fracture" at the final time. 119

5.14 Gaseous saturation and overpressure profiles obtained with $DuMu^X$ (a) and from [31] (b) for the case with a "fracture" at the final time. 119

5.15 Horizontal and vertical, displacements and stresses results obtained with $DuMu^X$ (a) and from [31] (b) for the case without "fracture" at the final time. . . . 121

5.16 Horizontal and vertical, displacements and stresses results obtained with $DuMu^X$ (a) and from [31] (b) for the case with a "fracture" at the final time. . . . 122

5.17 Relative deviation in percentage of the pressure (a) and porosity (b) with respect to initial values. . . . 123

5.18 Configuration and mesh used to simulate the test case from [179]. . . 124

5.19 Results for several quantities at 2315 days of injection. . . . 125

5.20 Evolution of CO_2 quantities in different phases . . . 126

5.21 Differences for CO_2 liquid and gas quantities for several salinity values. 127

5.22 Results for the MPFA (a-c) and TPFA (b-d) approaches for gas saturation (left) and CO_2 liquid molar fraction (right) at the final time. 127

5.23 Difference between MPFA and TPFA schemes for gas saturation and liquid pressure at the final time. . . . 128

5.24 Configuration for the test cases developed in [201]. . . . 129

5.25 Saturation results on the left from $DuMu^X$ (a) and GEM on the right (b). Results are shown for three different times, 397 days (a1-b1), 5 years (a2-b2), and 8 years (a3-b3). . . . 131

5.26 Pressure results on the left from $DuMu^X$ (a) and GEM on the right (b). Results are shown for three different times, 397 days (a1-b1), 5 years (a2-b2), and 8 years (a3-b3). . . . 132

5.27 Vertical displacement results on the left from $DuMu^X$ (a) and GEM on the right (b). Results are shown for three different times, 397 days (a1-b1), 5 years (a2-b2), and 8 years (a3-b3). 133

5.28 Comparison of the CO_2 quantities evolution for both simulators $DuMu^X$ and GEM, with respect to the simulation time. 134

5.29 Comparison of the vertical displacement between $DuMu^X$ and GEM at several times. 134

List of Tables

1.1 Chemical reactions associated with the CO_2 dissolution [36]. 10

2.1 Parameters for plotting capillary pressure and relative permeability. 32
2.2 Example of a chemical system. 34
2.3 Summary table of the different equations of state used in our model approach, adapted from [36]. 43

3.1 Simulation data of the 1D test case proposed in [229]. 56
3.2 Chemical reactions involved in 1D test case developed in [229]. . . . 56
3.3 Initial conditions for primary species. 56
3.4 Data for the extension to THC coupled processes of the 2D test case proposed in [179]. 62
3.5 Simulation data of the 2D test case proposed in [179]. 62
3.6 Chemical reactions involved in the 2D layered test case from [78]. . . 63
3.7 Chemical information about mineral species involved in kinetics reactions. 63
3.8 Initial conditions for primary species. 63
3.9 Simulation data for the 3D heterogeneous test case from [54]. 68
3.10 Chemical reactions involved in the 3D heterogeneous test case from [78]. 69
3.11 Chemical information about mineral species involved in kinetics reactions. 69
3.12 Initial conditions for primary species. 70
3.13 Relative difference in L^2-norm between several quantities computed by the fully implicit and sequential approaches on 54756 cells at 50 years. 75
3.14 Numerical performances. CPU: elapsed time, TS: number of time steps, NI: average number of nonlinear iterations per time step, LI / NI: average number of linear iterations per Newton iteration 79

5.1 Data for the 2D consolidation problem. 111

5.2 Data for Cryer's problem. 114
5.3 Mechanical data for case modelling from [31]. 118
5.4 Fluid data for case modelling from [31]. 118
5.5 Fluid constitutive laws for the flow part of problem [179]. 124
5.6 Mechanical properties for the different layers from [179]. 125
5.7 Computational time for the two different approaches for flow description. 128
5.8 Thickness and number of cells that constitute each layer of the domain. 129
5.9 Constitutive laws for the different layers for the problem extracted from [201]. 130
5.10 Data for the fluid part of the problem from [201]. 130
5.11 Computational time comparison between GEM and $DuMu^X$. 135

Chapter 1

General Introduction

Contents

1.1 General context 2
1.1.1 CO_2 emissions and global warming 2
1.1.2 Mitigation Strategy 2
1.1.3 Carbon Capture and Storage 3
1.1.4 Trapping Mechanisms 4
1.1.5 Existing Projects 7
1.2 Reservoir modelling for CO_2 storage in saline aquifers . 7
1.2.1 Hydraulic processes for CO_2 storage 9
1.2.2 Hydro-Chemical processes for CO_2 storage 12
1.2.3 Thermal-Hydro-Chemical processes for CO_2 storage . . . 14
1.2.4 Mechanical coupling in the process of CO_2 storage 15
1.2.5 Thermal-Hydro-Mechanical-Chemical coupling for CO_2 storage 20
1.3 Contribution of the thesis 21
1.3.1 Objectives of the thesis 21
1.3.2 Structure of the manuscript 22

1.1 General context

This section provides a literature review of the general information on CO_2 gas emissions that are causing global warming in the world. Carbon Capture and Storage (CCS) processes appear to be a promising technology to reduce these emissions that are polluting the planet we live on. Some explanations of the CO_2 storage process are given by explaining the four main mechanisms that trap the CO_2 underground. Finally, a discussion of existing pilots, projects, and storage sites is given to illustrate this process, which is experiencing a real upsurge.

1.1.1 CO_2 emissions and global warming

Over the last few centuries, human activity has increased significantly in most areas due to many technological advances. Since the Industrial Revolution, the world has become completely dependent on the use of fossil fuels. Fossil fuels are burned to produce a significant amount of energy. Almost 86 % of the world's primary energy use is based on the combustion of fossil fuels [159]. Fossil fuels with a high carbon content include oil, coal, and natural gas. They are all continuously formed by natural processes. They are generally classified as non-renewable resources because they take millions of years to form and known viable reserves are depleted much faster than new ones are created [143].

The problem with the massive use of fossil fuels is that their combustion releases large quantities of gases, in particular the greenhouse gas carbon dioxide (CO_2), which is specifically an anthropogenic emission. The production of CO_2 is estimated to be around 35 billion tonnes (gigatonnes) per year [194] (see Figure 1.1). Most of the CO_2 is released into the atmosphere, causing real damage to the environment. The accumulation of CO_2 in the atmosphere is thought to have a direct effect on the Earth's climate. In fact, CO_2 is classified as a greenhouse gas that increases radiative forcing and contributes to global warming. Climate change has many effects, including rising sea levels due to melting permafrost, rising ocean temperatures, and ocean acidification. It also has a significant impact on ecosystems, with many species threatened with displacement or worse, extinction. As a result, there is a global movement towards the production of low-carbon renewable energy to help reduce global greenhouse gas emissions.

1.1.2 Mitigation Strategy

Although global warming is of concern to a growing number of people who are aware of the critical situation, the rate of increase is expected to continue due to dependence on fossil fuels. By 2095, if nothing is done to improve the situation, the amount of CO_2 emitted into the atmosphere will be almost three times that of [139]. Industries have based their production on the use of carbon combustion. As a result, the transition to avoiding carbon combustion may be difficult, both technically and financially. Nevertheless, governments have decided to take action against global

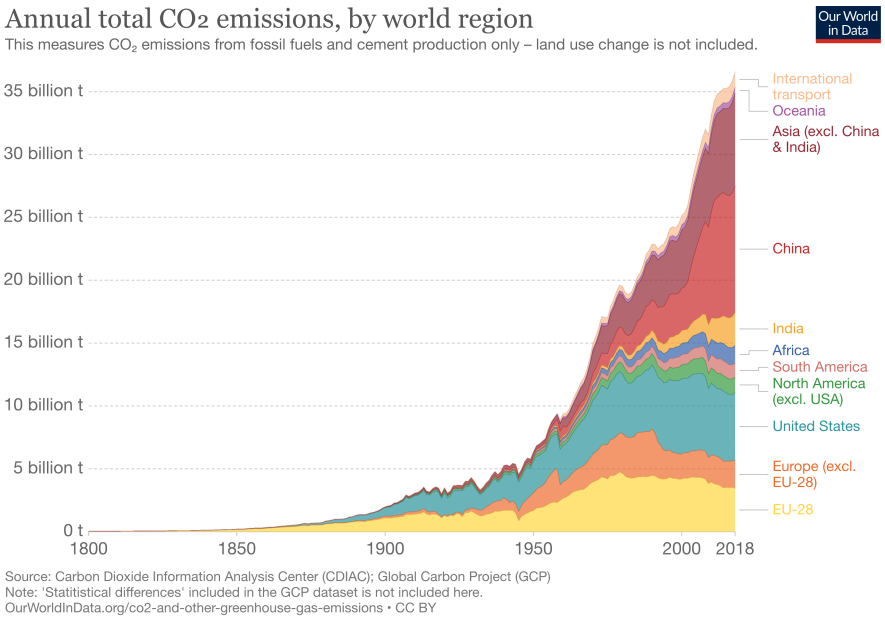

Figure 1.1: Annual global carbon emissions per region since 1800 from the Global Carbon Project dataset [164]

warming. 195 countries have come together to form a group of experts called the Intergovernmental Panel on Climate Change (IPCC). Its aim is to reduce carbon emissions by producing reports that highlight the critical situation and encourage governments to take action. Another organisation, the International Energy Agency (IEA), works on mitigation and is famous for publishing its annual report. Indeed, this agency provides the world with a medium-term outlook for the oil, gas, coal, and more recently, renewable energy and energy efficiency markets. IEA's Energy Technology Perspectives suggest strategies for regions of the world to keep the long-term global temperature increase below 2 °C [107, 112]. More recently, the IEA's position is much more committed, calling for a halt to investment in fossil fuel projects from 2021 [108]. Both the IEA and the IPCC have highlighted the critical role that *Carbon Capture and Storage (CCS)* will have to play to meet the goal of reducing global emissions in the future.

1.1.3 Carbon Capture and Storage

Carbon Capture and Storage is one of the most promising technologies for reducing anthropogenic CO_2 emissions into the atmosphere [152]. The process of this technology consists in capturing CO_2 at the source preventing it from being released into the atmosphere. Capturing CO_2 involves separating CO_2 from some other gases. The process of dealing with impurities can be very expensive for companies in technical, energy, and financial terms. Once the impurities have been removed, the CO_2 is compressed and piped to a suitable storage site, where it is injected and stored permanently (see Figure 1.2). Therefore, the added short-term benefit of CCS as a CO_2 mitigation option is that it allows the continued use of fossil fuels

while other renewable and alternative energy sources are developed [52].

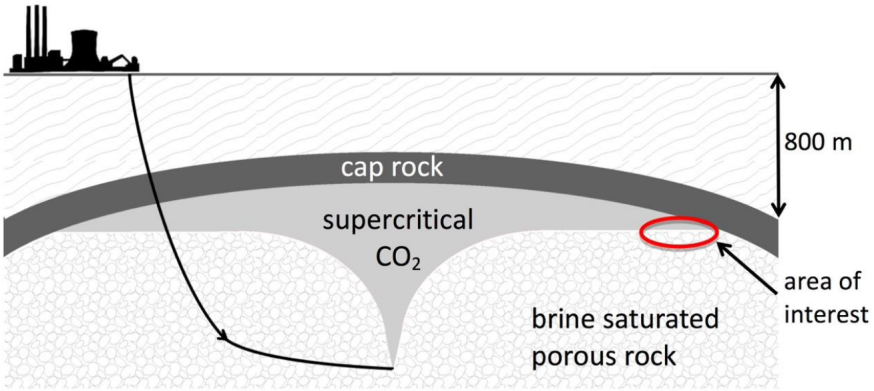

Figure 1.2: Process for the capture of carbon dioxide from a power plant emission [52]

Storage sites tend to be geological formations such as deep saline aquifers, coal beds, depleted oil and gas reservoirs, which are widely available and provide large storage capacity. Each type of reservoir represents a good option for storing carbon dioxide, but the best option appears to be saline aquifers, which offer the greatest storage capacity and are more widespread than other options [139]. In contrast to saline aquifers, which are not yet fully explored, depleted gas or oil fields are better explored through the Enhanced Oil/Gas Recovery (EOR/EGR) process. In these processes, CO_2 is injected to react with the oil and reduce its density, thereby increasing the recovery of oil at the top of the wellbore. It is usually injected when an oil reservoir begins to slow production because the oil is too viscous to flow properly.

The other storage option in coal beds consists of replacing the methane trapped in the porous structure with CO_2. Saline aquifers, like coal seams, have a sandstone or limestone pore structure, but they also have an impermeable cap that prevents CO_2 from migrating to the surface and back into the atmosphere (see Figure 1.2). These aquifers are generally found at greater depths than drinking water aquifers (depths greater than 800 m). They cannot be used as drinking water because of the high salinity of the water, known as brine. Not all aquifers are suitable for storage, they must meet certain characteristics such as storage size (between 1000 and 10 billion tonnes CO_2), depth, and a certain range of permeability and porosity [34]. Under all these conditions, an aquifer can be conceived as a potential site suitable for storing CO_2 for centuries or millennia through various trapping mechanisms.

1.1.4 Trapping Mechanisms

Carbon dioxide is one of the most abundant gases in the atmosphere and actively participates in the carbon cycle of the planet [18]. In fact, it can be found in four phase states: liquid, solid, gas, and supercritical fluid. A supercritical fluid is a fluid with physical properties close to those of a liquid and a gas. This state is achieved by applying pressure and temperature to the fluid. For supercritical CO_2, the pressure

and temperature must exceed 73.8 bar and 31.1 °C respectively. These conditions are geologically met in an underground formation at a depth greater than 800 m. The practical interest of injecting CO_2 in its supercritical form is that it retains some of its gas-like properties such as the ability to occupy the entire available volume, but it is also liquid-like with a high density and therefore it occupies less volume underground in this form [52]. Indeed, under standard atmospheric conditions CO_2 has a density of around 1.87 kg.m^{-3}, whereas under supercritical conditions [152] it varies from 600 to 750 kg.m^{-3}, creating a significant difference with the density of the resident brine. This difference in density means that the injected CO_2 displaces the surrounding fluid and will migrate out of the injection well and up towards the caprock due to buoyancy [152]. This process is usually referred to as the hydrological effect and a plume CO_2 has the form of a dense supercritical phase. To understand how CO_2 is trapped in the geological formation, it is necessary to understand some phenomena resulting from the trapping mechanisms.

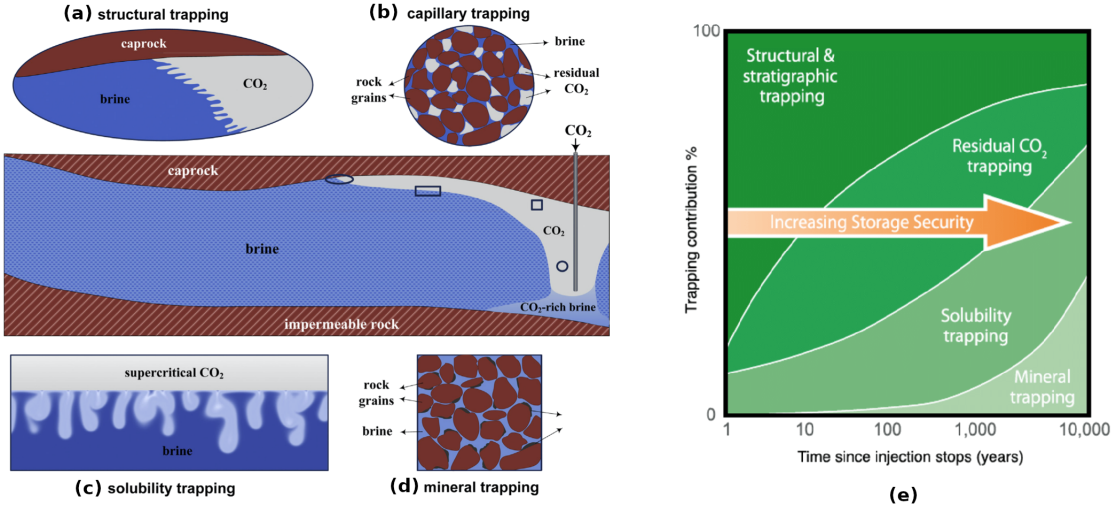

Figure 1.3: Diagrams of the four trapping mechanisms involved in geological CO_2 storage from [74] and illustration of the temporal evolution of storage security as a function of the trapping contribution from [139] on the right of the figure.

Structural Trapping

Structural or stratigraphic trapping is the first mechanism to occur during the time frame (see Figure 1.3 (a)). After being injected through a well, the buoyant CO_2 rises until it reaches an impermeable barrier. Then, in response to the injection pressure, the CO_2 plume spreads beneath the caprock as a gravity flow. Thus, the structural trapping method refers to the physical confinement of the supercritical CO_2 phase under an impermeable barrier of very low permeability. It is therefore entirely dependent on the local geology of the rock (often shale or clay). Such structural traps are often found in sedimentary basins and are occupied by saline water, oil, and gas. They result from variations in rock types caused by changes in the way the sediments were deposited, or changes in the structure of the subsurface

due to tectonic and other processes. Some faults can disrupt structural trapping by weakening the caprock. In fact, faults in the caprock can form in two different ways. On the one hand, as CO_2 is generally injected in its supercritical form, the injection can cause a significant pressure build-up that can damage the geological formation and thus induce some fractures and faults. On the other hand, as a result of seismic events that create fractures, the CO_2 trapped under the caprock can leak and penetrate into an overlying layer. If this happens, the CO_2 could contaminate drinking water aquifers or even return to the atmosphere. For this reason, aquifers need to be monitored to limit the risks during the period when CO_2 is retained by structural trapping (see Figure 1.3 (e)).

Residual Trapping

Residual or capillary trapping is the next level of trapping methods. It has a significant effect between tens and thousands of years (see Figure 1.3 (e)). The trapping of CO_2 by capillary forces in the pore space of rocks is a key process for optimising the capacity and ensuring the integrity of CO_2 sequestration. When CO_2 is injected through a well, it displaces the resident brine. Over time, as the aquifer brine is reabsorbed into the pore space by the migrating CO_2 plume, small isolated bubbles of CO_2 are trapped by capillary forces, hence the name: capillary or residual trapping (see Figure 1.3 (b)). Some engineering strategies to maximise capillary trapping have suggested the use of injection schemes that maximise sweep or improve imbibition [121].

Solubility Trapping

The third stage is called solubility or dissolution trapping and is one of the most important traps. Even if CO_2 is weakly soluble in brine, slow dissolution occurs at the interface between the CO_2 and the resident brine due to the very low viscosity of the supercritical CO_2. Chemical reactions lead to a small increase in the density of the CO_2-saturated brine from 0.1 to 1 %, making it heavier than the surrounding brine. The instability is driven by buoyancy, which contributes to the generation of small CO_2 plumes that migrate downwards in the form of fingers (see Figure 1.3 (c)) [74] [152]. The flow induced by the instability creates a constant contact between the upper layer of CO_2 and the fresh brine, which significantly increases the dissolution rate of CO_2. This phenomenon, called convective dissolution or convective mixing, has been studied by many authors interested in finding a way to improve finger formation. The dissolution process is very useful for good safety because the CO_2 starts to sink instead of rising. This reduces the risk of leakage as it becomes more important over time (see Figure 1.3 (e)).

Mineral Trapping

The final trapping mechanism is known as mineral or chemical trapping. It occurs when the CO_2 reacts chemically with the minerals of the formation to form or precipitate carbonate components, thereby immobilising the CO_2 as depicted in Figure 1.3 (d). Dissolution of CO_2 in brine can also alter the mineralogy of the aquifer by changing the pH of the solution and the concentration of ions [74]. The

precipitation of carbonate minerals can also reduce the permeability of the aquifer, but these precipitation phenomena only occur in a region far from the well [23]. The rate of formation of stable precipitates is higher than the rate of mineral dissolution, therefore mineral trapping is considered to be the most perennial trapping method [52]. Despite the great certainty of this process, it occurs only a hundred or a thousand years after the cessation of injection. Over thousands of years, the mineralisation process can eliminate more than 90 % of the injected [23]. Therefore, this process ensures long-term environmental safety.

All of these capture methods guarantee a way to capture CO_2 and allow it to be consumed by chemical reactions to keep it trapped in another form in the geological formation. As shown in Figure 1.3 (e), these phenomena provide increasing storage security over time, so each of them is crucial. They are also current topics for researchers, who are actively trying to find out how these trapping methods can be improved to make a greater contribution.

1.1.5 Existing Projects

As CCS seems to be one of the most promising ways to reduce CO_2 emissions into the atmosphere, this topic has received a lot of attention from many authors during the last five decades, according to the importance of climate change. Alongside these studies, large-scale storage experiments began in the 1970s in the United States of America with the aim of extracting oil from the ground (EOR) [130]. The first truly large-scale commercial carbon storage project in the world took place in Norway in 1996. This project called *Sleipner*, is an offshore storage site in the sands of the *Utsira* formation, located about 900 m below the bottom of the North Sea. It has allowed the storage of more than 20 million tonnes of CO_2 cumulatively since the start of injection. Besides, many real projects have been created in the world, one can mention some pilots or demonstration plants with for example the *Lacq* pilot in Rousse [65, 200], but also larger projects such as the Quest project in Alberta, the In Salah project [167], the Longship project including Northern Lights consortium in Norway, the Acorn project in UK, and in the longer term (2030), the Pycasso project (Pyrenean Carbon Abolition through Sustainable Sequestration Operations) in which many industrial companies are involved including some laboratories such as UPPA, BRGM, and IFPEN. According to a report published by the Global CCS Institute in 2022, 61 new plants have been added to the pipeline, bringing the number of CCS projects to 30 in operation, 11 under construction, and 153 in development [4]. This recent increase therefore reflects the popularity of carbon storage in recent years, which is unlikely to diminish as a result of the IPCC and IEA recommendations [107, 139].

1.2 Reservoir modelling for CO_2 storage in saline aquifers

Carbon storage is a new area of research due to the worrying problem of global warming. In fact, the main technological advances have been made in the last 40

to 50 years. As a result of the continuous progress in research, scientists have been able to develop some physical models that allow a better understanding of the phenomena taking place in the world. Computer technology has also made important advances in the last twenty years, providing new tools such as supercomputers to run large-scale model simulations with greater precision. The long-term evolution of the carbon storage problem can be described by many models, each with its own specificities, depending on the focus chosen. Figure 1.4 details all the possible interactions between processes that occur during CO_2 injection.

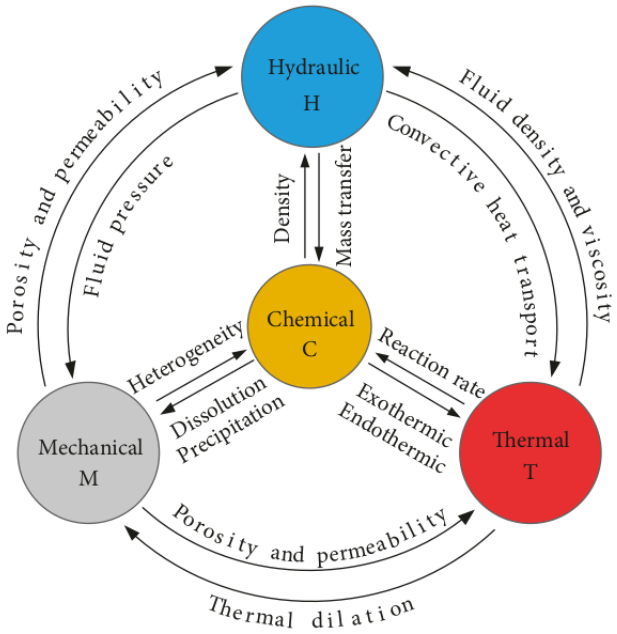

Figure 1.4: Cross couplings between THMC coupling from [198].

According to [198], these processes are coupled pairwise as a series of doublets:

- Hydraulic processes (H) are coupled to thermal processes with convective heat transport and fluid properties that vary with temperature.
- Mechanical processes (M) are coupled with hydraulic (H) and thermal (T) processes through variations in porosity and permeability due to poroelastic effects and thermal dilatation/expansion.
- Chemical processes (C) are coupled with mechanical processes (M) through dissolution and precipitation, which affect porosity and permeability, leading to heterogeneity. They are also coupled with thermal processes due to temperature-dependent reaction rates, and with hydraulic processes due to density variations and mass transfer.

Together, these processes form a complex coupling of physical phenomena known as Thermal-Hydro-Chemical-Mechanical coupling (THMC). A non-exhaustive literature review of mathematical models used to model multiphase flow in porous media is given here. The coupling with chemical, mechanical, and temperature processes

is then reviewed to characterise the global description of CO_2 storage in porous media.

1.2.1 Hydraulic processes for CO_2 storage

In general terms, hydraulic processes (H) are involved in the movement, distribution, and management of a liquid or gaseous phase state. Hydraulic processes are important to understand in fields such as engineering, geology and environmental science, as they can have a significant impact on the natural world. Depending on the approach taken, different characterisations of the flow may be encountered. In particular, phase descriptions are the key element in the modelling approach. The following sections detail how single and multiphase flow have been used in the literature to perform CO_2 storage modelling and simulations. In the case of multiphase flow, a distinction is made between miscible and immiscible fluids.

Single phase flow model

In order to use single-phase flow, researchers make some simplifications to focus just on one phenomenon: the migration of the dissolved CO_2 in the liquid phase. It also provides approximate results compared to a more complicated simulation of coupled systems with more phases, which is closer to reality. Single-phase flow models require less specialised technical knowledge, so more people are able to use them and understand the results [151]. Mathematically, single-phase flow models are described by a set of partial differential equations (PDEs) where mass conservation for each species involved is modelled by a diffusion-convection equation. These models are currently used to focus on specific phenomena that occur throughout the storage process. For example, in [82], a single-phase flow model is used to study the impact of flow in fractured porous media. Four benchmark test cases were developed to see the effect of fracture networks on flow. In [151], a study is performed to investigate the pressure effect far away from the well and the injection point in a geological formation. It appears that three regions are created during a CO_2 injection, the first one which is the closest to the well, becomes completely saturated with CO_2 and is called the "drying" region. Farther away is a two-phase region where brine and CO_2 coexist. Finally, the farthest region is made up entirely of brine, because CO_2 cannot flow up to this part of the geological formation. Of these three regions, the third is only taken into account in the assessment of pressure increases. The conclusions given in [151] depict that comparisons between a compositional flow and a single-phase flow provide reasonable results if the study position is far enough away from the injection well. In addition, most studies using a single-phase flow model neglect the effects of the high compressibility of the CO_2. Therefore, in [162], a comparative study was carried out to compare the effect of faults between a single-phase and two-phase flow. Such a study confirms that the use of a two-phase flow does not lead to underestimated results.

Two phase and multiphase flow models

In general, CO_2 storage problems are governed by multiphase multicomponent flow coupled with reactive transport in order to model the rock–fluid interactions

in groundwater movement [150, 152, 156, 178]. Multiphase flow is the dominant process describing the movement of the injected CO_2 phase in a brine formation. The parameters influencing the movement of CO_2 are the pressure gradient due to injection and the buoyancy due to the lower density of CO_2 compared to the resident brine. When the injection of CO_2 occurs, it is found that the void space is occupied by two coexisting fluids, the resident brine, and the injected CO_2, both separated by a sharp interface [152]. This sharp interface allows the immiscible fluids to remain separated, considered as two different phases. The only way to cross the sharp interface is by the chemical reaction of dissolution between the two species. In fact, a carbonation phenomenon takes place between CO_2 and H_2O, resulting from the dissolution of CO_2 in brine, thus creating a new species called carbonic acid (see Table 1.1). The dissolution reaction only occurs between two fluids that are partially miscible.

CO_2 dissolution	$CO_{2(g)} \rightleftharpoons CO_{2(aq)}$	(1)
Carbonic Acid formation	$CO_{2(aq)} + H_2O \rightleftharpoons H_2CO_{3(aq)}$	(2)
Carbonic Acid dissociation	$H_2CO_{3(aq)} \rightleftharpoons HCO_3^- + H^+$	(3)
Bicarbonate dissociation	$HCO_3^- \rightleftharpoons CO_3^{2-} + H^+$	(4)

Table 1.1: Chemical reactions associated with the CO_2 dissolution [36].

From a mathematical point of view, the consideration of the two phases complicates the problem by introducing new nonlinearities in the system. The mass conservation law has to be exposed for each phase by considering a wetting and a non-wetting phase. There is a pressure jump between the two phases, so a capillary pressure is introduced. Following the same idea, a relative permeability and an equation of state (EOS) characterising the properties of the fluids or their mixture must be taken into account. The relative permeability represents the inhibition of the mobility of one phase by the presence of the other, meaning that the two fluids interfere with each other [51, 152]. Two-phase flow can be described in two parts, the first referring to the flow of two immiscible fluids in a geological formation and the second referring to miscible flow that can form a mixture.

Two-phase immiscible flow As explained earlier, a two-phase flow model is based on a coupled system of equations. These equations describe the evolution of pressure and saturation of each phase, i.e. each fluid. In this part, the resident brine and the injected CO_2 represent two immiscible fluids, which means that there is no dissolution between immiscible fluids. Typically, two-phase flow models are used to predict phenomena such as the movement of the injected CO_2 plume, the pressure build-up during injection, or the development of a leakage path. The modelling of CO_2 storage in saline aquifers can be carried out using either analytical

or numerical models. For example, in [157], a simplified analytic or semi-analytic model is proposed to capture the dynamics of plume migration, pressure evolution, average regional pressure buildup, and impacts on injectivity around a well. Comparisons with a numerical model have validated the analytical approach. On the same idea, in [209], a semi-analytical solution is presented to study the evolution of CO_2 plumes. The buoyancy and compressibility of CO_2 have been taken into account by assuming that the CO_2 density can vary linearly with pressure since the pressure remains almost constant during the injection phase. However, analytical models require some assumptions to be simple. They cannot account for heterogeneities in aquifer properties and model geometry. In addition, geochemical reactions that occur in CO_2 aquifers cannot be reliably captured by analytical models due to their complexity. This is why numerical models are preferred for complex problems. In [27], the numerical approach of two-phase immiscible flow has been extensively investigated by giving all the background ideas necessary to properly model the CO_2 storage problem. As explained in the previous part (Section 1.2.1), the effects on faults induced by stress with a single phase and a two-phase flow model are examined in [162]. In fact, the pressure build-up in the single-phase model is lower than that obtained in the two-phase model. Therefore, the single-phase model can underestimate some results, justifying the use of the two-phase flow model to obtain better predictions and to be more consistent with reality.

Two-phase miscible flow Contrary to what was developed in the previous paragraph, the fact that the two fluids are partially miscible causes the dissolution of CO_2 in the resident brine. This phenomenon of dissolution allows us to consider the system as composed of two components (brine and CO_2), both present in each phase (supercritical or gas phase and liquid phase). As in the case of immiscible two-phase flow, the equations describing the evolution of the pressure and saturation of each phase remain in the same form. The only thing that may change is the presence of a second member in the mass conservation equations, resulting from the interphase change term. In [149], the author proposes a new approach using permanent primary variables such as the nonwetting phase and the capillary pressure. This approach allows to use a unique set of primary variables that can be used for the single-phase as well as the two-phase case. In [153], the interest is on mixed modelling of the problem in a heterogeneous porous medium. For this reason, the numerical approach separates the different study zones with respect to the distance of the injection well. In the vicinity of the well, the system contains supercritical CO_2 and resident brine. Due to the presence of a large amount of CO_2, the dissolution process has a significant effect, which is the reason why the two fluids have to be considered miscible. Further away from the injection point, the amount of dissolved CO_2 is negligible, so the fluids can be considered immiscible. However, in [153] some assumptions are made such as incompressibility of fluid and rock matrix, neglect of capillary pressure, isothermal, no gravity, and no external sink or sources. Both fine and coarse scale simulations are perturbed by the heterogeneity of the domain. In [168], a discontinuous Galerkin method is performed to investigate the resolution of a two-phase flow model, including interphase transfers. The latter seems to show stability and robustness in many cases involving homogeneity and heterogeneity in one dimension. Finally, a multi-participant benchmark has

been published in [54]. Three different cases are presented to illustrate CO_2 storage issues. The first relates to a leaky scenario where the leakage rate is estimated as a function of the injection rate. The second one examines a quantification of the amount of CH_4 recovered in an enhanced oil recovery scenario where CO_2 and CH_4 are stored in a depleted gas reservoir. The last one concerns a CO_2 injection in a heterogeneous geological reservoir in order to estimate the amount of CO_2 stored. All these cases provide good opportunities for comparative studies. The miscibility of CO_2 in brine also opens the way to the study of convective dissolution which is an essential trapping mechanism. In particular, in [73], the author compared the dissolution process using single-phase or two-phase flow models. It has also been investigated in [132] and extended in 2D and 3D in [131] accounting for thermal effects. The latter consideration of temperature enhances the mass flux resulting from convective dissolution while it postpones the onset time of convection. These phenomena are also observed at field-scale simulations with heterogeneities in [131].

1.2.2 Hydro-Chemical processes for CO_2 storage

Recently, the scientific community has made great efforts to adapt models for reactive multiphase flow in subsurface geological formations. In such systems, geochemical modelling is key to establishing an accurate description of the states of the fluids present in the aquifer [9]. Indeed, the full problem of CO_2 geological storage does not only involve CO_2 dissolution between the supercritical/gas phase and the liquid phase. Geochemical interactions associated with CO_2 storage may induce some risk to caprock integrity through geochemical effects. These interactions can occur in two different ways. One is contact between ions and molecules already dissolved in the medium, leading to aqueous reactions, and the other is contact between ions and the rock matrix, leading to mineral reactions. It depends on the type of rock or species present in the brine, but generally, there is some precipitation or dissolution of minerals such as calcite, anorthite, kaolinite, dolomite, quartz, or others. It is also possible to use this coupling model to study problems such as salt deposition at the level of the injection well. These problems are often encountered when CO_2 is injected into saline aquifers, where a drying effect is created, leading to the deposition of salt from the brine present in the sandstone pore network. This crystalline salt can then cause a reduction in pore volume, restricting the space available for more CO_2 to flow through and affecting injectivity performance [60]. Aqueous reactions are relatively fast and reach equilibrium instantaneously, so they can be represented by equilibrium reactions modeled by mass action laws. Conversely, mineral reactions are relatively slow, so kinetic models are needed to describe the reaction rates and the time taken to reach equilibrium [123, 197]. Each kinetic reaction leads to an ordinary differential equation. Mathematically, the mass conservation laws for each chemical species involved in the flow, are coupled to chemical interactions through reaction rates. Reactive multiphase flows are governed by a system of partial differential equations (describing a multiphase compositional flow) coupled with algebraic or ordinary differential equations related to chemical reactions. This section provides a non-exhaustive overview of the codes used to solve multiphase reactive flows and also presents the resolution methods commonly used to solve hydro-chemical coupling processes.

Reactive multiphase flow for CO_2 storage

Recently, multiphase flow coupled with geochemical reactions has been the subject of numerous studies. Indeed, in [195], the author claims that "one of the most significant achievements in reactive transport analysis in recent years has been the application to multiphase systems". When CO_2 dissolves in brine, the geochemical conditions change and the pH drops significantly. This disturbs the initial equilibrium between the brine and the rock minerals and may induce some precipitation or dissolution processes.

Several codes with multiphase flow capabilities are described in [227] and [196]. Without being exhaustive, we can mention IPARS [214], PFLOTRAN [96], NUFT [98], TOUGHREACT [220], HYTEC [204, 185], MIN3P [137, 181], HYDROGEOCHEM [222], OpenGeoSys [120], AD-GPRS [78, 79], CORE^{2D} V4 [177], PROOST [86], DARTS [2] or GEM [3]. Other recent works dealing with reactive transport for two-phase or multiphase flow are presented in [16, 42, 118].

Resolution methods

Modeling reactive multiphase flow leads to a highly nonlinear coupled system of degenerate partial differential equations to algebraic or ordinary differential equations requiring special numerical treatment. Among the codes above-mentioned, one finds the usual two approaches for solving this system: the Sequential Approach (SA) and the Global Implicit Approach (GIA). The first approaches to be developed were the sequential ones, with the Sequential Non-Iterative Approach (SNIA) and the Sequential Iterative Approach (SIA) [221]. Both sequential methods involve a decoupling between the transport and the chemistry problems. Generally, the transport equations are computed first, followed by the chemical equilibrium calculation. This provides more modularity for the solution, is less expensive in terms of computational cost, and an external chemical solver can be coupled to solve the chemistry problem. These methods were widely used in the 1990s. Unfortunately, non-iterative methods have a major drawback. The decoupling introduces a splitting error which can affect the accuracy of results. One way to overcome this problem consists in using an iterative loop until a convergence criterion is reached (SIA). Several studies have focused specifically on the efficient solution of chemical equilibria, in particular in [19], where a new strategy for solving thermodynamic equilibria is proposed thanks to iterative acceleration algorithms. One can also mention [45, 133], where rigorous algorithms for chemical equilibrium calculations are proposed and compared in terms of efficiency for large chemical systems.

In contrast, implicit methods are difficult to implement due to the complexity of solving the fully implicit system. Despite the difficulty, large time steps can be used to solve the problem, which is an important advantage. Two recent surveys [184] for multiphase flow and [48] for single-phase flows outline the advantages and disadvantages of SA and GIA. For single-phase flows, discussions concerning the use of GIA and SIA are also addressed in [46] to perform the MoMaS benchmark [47]. This benchmark allowed an inter-code comparison by solving several test cases with

increasing complexity. Several participants used SA and GIA to perform the different test cases. Concerning SA, an SNIA, and an SIA are used in [44] and [122] respectively. The other contributions deal with GIA. In [138], the authors use the Direct Substitution Approach (DSA) which consists in substituting the chemical equations in the transport equations. Some studies showing the efficiency of this method are given in [77]. A technique called Global Differential Algebraic Equation (GDAE) is implemented in [67]. It consists in solving implicitly all the transport and chemical equations in a single system by coupling them with chemistry written as algebraic differential equations (DAE). In [21], a new global method is introduced that consists in eliminating the chemical equations locally and solving the transport equations with a source term coming from the reactions. Another efficient technique for reducing the scheme of the reactive transport problem with a global approach is presented in [101]. It consists of reducing the nonlinear system by a linear transformation of the equations and variables. This has the effect of reducing the nonlinearity of the system by eliminating unknown equilibrium reaction rates and thus reducing the sparsity pattern of the Jacobian matrix. The various MoMaS benchmarks have shown that sequential approaches can be as accurate as global approaches, provided they are implemented carefully. However, global approaches are now more efficient than originally thought.

1.2.3 Thermal-Hydro-Chemical processes for CO_2 storage

Temperature can play an influential role in the storage of hydrocarbons. In fact, it mainly affects the equations of state that characterise the fluids (salinity of the brine, densities, and viscosities), but also the rates of chemical reactions [13]. Several authors have attempted to identify and quantify the effects of temperature during CO_2 injection. Thermal coupling adds further complexity to the problem. Mathematically, energy conservation is applied to the whole system, which creates more nonlinearities leading to more difficult calculations. Generally, the CO_2 is injected under supercritical conditions, which means that the temperature and pressure of the gas are above the critical point of 31.1 °C and 7.38 MPa. Consequently, the CO_2 is injected colder than the temperature of the aquifers, which can vary between 50 and 100 °C. In [210], a comprehensive review is proposed to summarise all the thermal effects that could occur in the CO_2 storage process. According to [210], the solubility of CO_2 and carbonate rocks is higher at lower temperatures. Consequently, the process of dissolution will be more important in the cold region due to cold injection. We can mention first some articles focusing only on thermo-hydro processes [230, 231]. In [212], a numerical framework for thermal multiphase flow with mineral precipitation in CO_2-brine system has been developed and implemented in the coupled simulators AD-GPRS/GFLASH [6]. Several cases dealing with salt precipitation, mineral precipitation, and convective dissolution have been investigated to demonstrate the ability of the numerical model to capture such processes. In [37], a monitoring approach is carried out in the geological formation through the way of temperature signals. The literature also includes some studies where flow is coupled with chemical interactions to model thermo-hydro-chemical processes. In [22], the thermal impact of injected CO_2 on the chemical reactivity is focused and in particular, the Joule-Thomson effect which

may play a significant role in the temperature effects. In [36], the authors confirm that the Joule-Thomson effect cools the CO_2 region near the injection point. In fact, it is a thermodynamic process that can be related to the isenthalpic expansion of a real gas. When CO_2 is injected into a well, the CO_2 front is subject to a cooling effect. It represents a pressure drop due to the expansion of a real gas from high to low pressure at constant enthalpy. Because of higher ionic strength (higher than 0.5–0.7), the Pitzer formalism is preferred to the Debye-Hückel model in [22]. Two test cases were introduced to investigate the effect of temperature on reactivity, one with a low injection rate and a temperature similar to the aquifer, and the other with a high injection rate and a low temperature. Observations have revealed four regions with different effects. The first region is affected by the desiccation effect, where the gas completely dries out the near-well region and the Joule-Thomson effect is present. Then, in the second region (20-50 m), the effect is still present and a larger temperature decrease is observed. Further away, the other two regions are not affected by the Joule-Thomson effect, so the temperature increases gradually and obviously more in the third region. Globally, the Joule-Thomson effect causes a small temperature change of about 2 °C, which makes little difference to geological aquifers. These effects may be more important where there is a large difference between the injection temperature and the aquifer temperature, and in deep formations where the temperature and pressure are close to the supercritical state. In [203], the effects of temperature injection on the global behaviour of CO_2 injection into a calcite or dolomite rock formation are investigated. Several test cases with different injection and aquifer temperatures are considered. Groundwater flow of brine is imposed in the domain to see the effects of hydraulic head gradients. Calcite or dolomite dissolution and precipitation are observed over 50 years, as well as the Joule-Thompson effect and exothermic CO_2 dissolution. Their conclusions are that temperature appears to have little effect on the storage process, except in the vicinity of the injection well. We can also cite non-exhaustively other contributions where the authors consider thermal-hydro-chemical processes [124, 165, 215, 217]. The results of most of these studies show us that, unlike chemical processes, temperature does not significantly affect the trapping quantities. In fact, the differences between isothermal and nonisothermal models are small for values quantifying the CO_2 plume, but the pressure build-up is really affected. Therefore, nonisothermal models are necessary to accurately assess the phenomena around the injection well during the injection period.

1.2.4 Mechanical coupling in the process of CO_2 storage

Many studies have been carried out over the last twenty years to investigate the effects of fluid injection on the host rock. When CO_2 is injected into a fully saturated brine formation, the pressure of the fluid increases. In addition, the injected CO_2 is generally not in thermal equilibrium with the aquifer, so the overpressure and temperature difference can change the effective stresses and induce deformations in the rock [152], which could compromise the mechanical stability of the caprock. Most geomechanical aspects are observed close to the injection well because this region is subject to large variations in pressure and temperature [172]. However, these changes can also generate vertical expansion, which can lead to sur-

face uplift, causing fault reactivation, seismicity, or worse, leakage. Some numerical models have been developed to analyse the behaviour of geological formation in advance. This section first gives an overview of the numerical management of coupling with mechanical processes and then reviews hydro-mechanical and thermal-hydro-mechanical processes in CO_2 storage scenarios.

1.2.4.1 Coupling management applied to CO_2 storage

The numerical simulation of coupled hydraulic and geomechanical (HM) or thermal-hydraulic and geomechanical (THM) processes requires the choice of an appropriate coupling scheme. Partially and fully coupled schemes are the most commonly used, as discussed in [129] and [115]. Another coupling method, called pseudo-coupling, which is used less frequently, deals with empirical correlations. Porosity is calculated from an empirical model implemented directly in the reservoir simulator, avoiding the use of a geomechanical module. Despite the low computational time, the results are roughly estimated and therefore the geomechanics are not rigorously taken into account.

Partial coupling

In general, in partially coupled schemes, the stress and flow equations are solved separately and sequentially, while information is exchanged between the two sub-problems or potentially two different simulators. Nevertheless, different levels of coupling can be achieved from the partially coupled methodology. In particular, explicit or loose coupling refers to the fact that the geomechanical problem is solved singularly after a certain time step of the flow problem. Furthermore, the feedback to the fluid flow is neglected (one-way coupling). As this type of coupling has no mechanical effects on the reservoir simulation, mechanical results are only focused on the analysis of stress and strain localisation for well equipment damage or environmental problems, as performed in [201]. This coupling allows interesting physical effects and is relatively easy to implement to couple codes specifically dedicated to solve multiphase flow or geomechanics. In [33], the simulators OpenGeoSys and ECLIPSE are coupled. For example, TOUGH2-FLAC3D is a reservoir simulator that also uses this methodology [173]. Iterative coupling, however, as the name suggests, uses an iterative process that is repeated until the stress and fluid flow unknowns converge. Therefore, the geomechanical problem is solved at the end of each time step of the fluid flow problem. In this case, communication takes place between the two sides and the geomechanical responses affect the fluid flow (two-way coupling). Both partial couplings are usually controversial, with some preferring the simplicity of explicit coupling with low computational cost, while others are more concerned with accuracy. In [163], comparisons between the two sub-approaches are given, noting that the explicit fails to match an analytical solution of Mandel's problem [134], while for a large number of iterations, the iterative approach matches the solution, which is also costly. It is therefore necessary to find a balance between the efficiency and accuracy of the results obtained.

There are four well-known iterative coupling procedures, referred to as the undrained split, the fixed stress split, the drained split, and the fixed strain split it-

erative methods according to [142]. Drained and undrained split concerns schemes that solve the mechanical problem first, followed by the flow. The drained split consists of solving the mechanical problem without pressure change, whereas the undrained split fixes the fluid mass during the mechanical step. Both approaches have different behaviours, the drained split has the major drawback of being only conditionally stable, whereas the undrained split leads to unconditional stability [116, 141]. These stability conditions have been determined in these articles using the Von Neumann method, which provides stability estimates for the linear poroelasticity problem. On the contrary, the fixed-stress and fixed-strain methods consist of solving the flow problem first and the mechanical problem in the second step. An obvious splitting of the coupled problem is to fix the rate of total strain during the solution of the flow problem. This split, called the fixed-strain split, is only conditionally stable and is discussed in detail in [117]. The last method, which is the most commonly used, is called the fixed stress split. It consists in imposing a constant mean total stress as in [141]. This method has a considerable advantage, which is the unconditional stability according to the stability and convergence analyses provided in [31, 117, 141]. It is assessed in [141] that the fixed-stress split seems to be the preferable option to couple flow and poromechanics because it does not introduce any new terms in the flow equations, which are often locked in an industrial reservoir simulator. Furthermore, partial coupling methods may also offer the possibility to use different meshes and time steps for the two subproblems, which can further reduce the computational cost. Especially in the case of coupling industrial reservoir simulators, which are mainly developed as black boxes, it is more convenient to use such partial methods, which are more flexible.

Fully coupling

On the other hand, full coupling involves solving the stress and flow problems simultaneously. According to [117, 201], this method requires a unified flow-mechanics simulator, complicated code management and is costly in terms of computational time due to the resolution of large monolithic systems. In [31] a fully coupled scheme gives results according to an iterative process (fixed-stress method) by validating the two computations on Mandel's problem and on homogeneous and heterogeneous test cases. In their opinion, one-way coupling with pore compressibility and without iterations can lead to significant deviations from the fully coupled solution, in particular, because transient effects are not accurately captured. In [163], a comparison between the fully coupled and an analytical solution is given as a good match of the two curves. As underlined in [182], the iteratively coupled method ensures the same result as the fully coupled method, despite a large number of iterations, which can justify the use of the fully coupled approach. Another advantage of the fully coupled method is its stability. This approach achieves unconditional stability and convergence when the coupled problem is well-posed [117].

1.2.4.2 Hydro-mechanical coupling

Numerical modelling of the coupling between hydraulic and mechanical problems allows the study of geological formation behaviour during CO_2 injection. Accord-

ing to [31], CO_2 injection can affect pressure as well as stress and deformation of the aquifer and caprock, which can compromise storage site integrity. This is an important reason to consider the coupling between hydraulics and geomechanics. A general review of geomechanical aspects in the CO_2 storage process is given in [160, 170, 172]. As explained earlier, vertical expansion can occur during the injection of a CO_2 into an aquifer where the initial brine completely saturates the area. Consequently, the pressure of the fluid will increase and changes in geomechanical aspects will be proportional to the magnitude of the pressure increase [172]. The In Salah industrial scale project in Algeria is a good example of vertical expansion due to injection, as some satellite images have highlighted a cumulative surface deformation of 20 millimetres since the start of the injection period [136]. Another numerical study by [173] showed a surface uplift of about 0.6 m just above the injection well. The general uplift can also be observed relatively far from the injection well (15 km) because the effective mean stress changes are localised far away from the injection point. In [92], a case of two-phase flow coupled with deformation processes of near-field migration during injection of supercritical CO_2 into a deep saline aquifer is investigated. The change in stress in the vicinity of the injection well is due to an instantaneous increase in pressure, which can induce mechanical damage or fractures in the surrounding well rock. In fact, the stress imposed on the reservoir during injection can be divided into vertical and horizontal stresses. According to [173], the vertical stress may be approximately constant, equal to the weight of the overburden, except very close to the borehole where it may increase. However, horizontal stress is more influenced by poroelastic stress. Other studies such as [158] are more focused on predicting failure and fault reactivation thanks to the Mohr-Coulomb criterion [146]. In [187], several hypothetical scenarios have been proposed to investigate the effects caused by fractures in the caprock by focusing on fracture location, fracture permeability, and aquifer pressure. Two approaches have been proposed to monitor and detect any faults or fractures before a leak occurs, which could potentially cause an environmental disaster. In [208], a study of the overpressure during injection is carried out with analyses of how injection can affect caprock stability according to Mohr circles. According to the conclusion presented, a peak of overpressure is obtained at the beginning of the injection, which leads to the least stable situation. This overpressure decreases continuously over time and allows the integrity of the caprock to be maintained, also by reducing the risk of creating faults. Therefore, a progressive injection would be recommended to ensure the integrity of the caprock at the beginning of the storage process. In [92], the stress changes caused by the interaction with the two-phase fluids during the injection period were explored. It was assumed that there would be no phase transition or dissolution, fracturing, or damage to the rock matrix. The results showed that the stress change in the vicinity of the CO_2 well has moved away from the initial stress state.

In general, mechanical processes are more often discretised numerically using the finite element method because the problems solve deformations of the rock matrix that is more logically defined at the nodes of a mesh [33, 135, 208]. However, a new approach has been proposed in [55, 56], where the virtual finite element method is discussed. This method allows the use of a single mesh for both mechanical and fluid flow modelling, whereas classically a finite element method for

the mechanical equilibrium equation and a finite volume method for the fluid mass conservation equation is formulated to solve the hydro-mechanical coupling. Nevertheless, other discretisation methods have been investigated, in particular, the one in [114, 155], which unifies finite volume schemes for both subproblems with multi-point flow approximation (MPFA) and multi-point stress approximation (MPSA) for poromechanics. In addition, in [202], a recent new finite volume nonlinear scheme (NLTPSA), preserving monotonicity, is developed for general poromechanics applications.

Many reservoir simulators, or couplings between two of them, have been developed to provide hydro-mechanical simulations. One can mention OpenGeoSys [92], OpenGeoSys-ECLIPSE [33], TOUGH-FLAC [172], Eclipse-Visage [158], *DuMu*^{X} [31], GEM [187], TOUGH2-Code_Aster [169], AD-GPRS [6], DARTS [2], GEOS [183], and so on. Other codes have been developed and adapted for modelling discrete fractures or flow in fractured porous media, which will not be discussed here.

1.2.4.3 Thermal-hydro-mechanical coupling

As discussed in the previous section on HM coupling Section 1.2.4.2, the temperature can play a significant role in the stress induced by injection. However, in mechanical problems, the temperature is one of the two quantities, along with pressure, that particularly affects the behaviour of the rock. When CO_2 is injected under supercritical conditions, a significant temperature difference is created between the host rock and the injected fluid. This disturbs the thermal equilibrium of the aquifer and leads to a significant increase in thermal stress. In [172], modelling studies have shown that the latter stress evolution is influenced by cooling-induced stress changes, especially close to the injection well where temperature effects are more significant. According to [163], this mechanism leads to the creation of reactivation of fractures caused by the temperature difference. Consequently, under these conditions, the stress approaches shear and tensile failure conditions [150]. In the investigation presented in [190], it is clear that the thermal-hydro-mechanical coupling has a significant effect on the caprock and perhaps less on the saline aquifer. In fact, temperature changes in the saline aquifer are not affected by the geomechanics, but the pressure is weakly changed. In the caprock, the scenario appears to be different. THM processes capture an important pressure change in the caprock that is not captured when the temperature is neglected, confirming that temperature consideration is advisable for better accuracy of storage behaviour. In addition, some sensitivity analyses have also been carried out in [190], focusing on certain parameters that affect the behaviour of the system. For example, the injected CO_2 at a temperature closer to that of the aquifer greatly reduces the potential for tensile fractures in the caprock and aquifer. As in the previous paragraph, some authors have reproduced the In Salah benchmark, this time with thermal-hydro-mechanical coupling [125]. The results obtained are consistent with satellite detection of surface uplift. The [64] and [103] studies deal with a fractured zone model with multiple aquifer layers to capture the stresses and strains involved in such a system. These numerical experiments were developed to investigate fluid leakage through geomechanical caprock fractures or activated faults. The results show that the injection

rate appears to be an important factor in fluid-driven fracturing in the caprock. A suggestion is made to reduce damage to the caprock by slowly increasing the injection rate at the beginning of CO_2 injection [103]. In a different approach to CO_2 EOR, [93] has provided numerical simulations using the coupled simulator TOUGH2MP-FLAC3D, which deals with deformations due to injection. For a recent review of TOUGH-based simulators for THM coupling, the reader is referred to [171]. In [88], a numerical framework is exposed for solving THM coupling processes dealing with two different approaches: fully implicit and sequential-implicit, where both are compared in terms of computational times. According to the results presented for elasticity and plasticity constitutive models, the fully implicit strategy performs very well but requires sophisticated development (construction of full Jacobian matrices) and advanced multi-stage linear solvers, while the sequential strategy performs well for elasticity but is degraded when the coupling strength is significant such as for nonlinear plasticity. Finally, the thermal-mechanical effects induced by coolant injection CO_2 are not yet fully understood, so further research is needed to minimise the risk of damaging the sealing capacity of the caprock and to avoid leakage, which could be catastrophic for the environment [150].

1.2.5 Thermal-Hydro-Mechanical-Chemical coupling for CO_2 storage

This last paragraph reviews studies related to thermal-hydro-mechanical-chemical coupling. Because it involves physical mechanisms that are difficult to describe in their entirety, this type of complex coupling is difficult to implement. The development of computers over the last twenty years has made it possible to deal with the expensive calculations involved in THMC processes. According to [229], it is mathematically challenging to model THMC processes because dealing with non-isothermal multiphase fluid flow, geomechanics, and geochemical reactions induce strong nonlinearities in the mass, energy, and momentum conservation equations, which are complex to solve. For this reason, there are still few numerical studies where all contributions are coupled.

In general, these problems are solved by two different approaches. The geomechanics and geochemistry can be decoupled from the flow to solve the subproblems sequentially. On the other hand, some have chosen to solve the heat flow, reactive fluid flow, and geomechanics equations simultaneously at each time step. Two studies using both strategies are proposed in [228] and [229] for sequential and fully coupled approaches, respectively. Studies of the sequential case have been carried out with a comparison of two scenarios, including one involving a fault in the caprock, which represents the behaviour of a leaky case. However, the full coupling deals with comparisons between isothermal and nonisothermal injection of CO_2 in order to realise the benefits of taking temperature effects into account. In [223], the authors have developed a fully coupled approach with a single-phase description of the flow problem. A CO_2 injection is performed with a finite element method, confronting a Galerkin method that gives oscillatory instabilities and a stabilised method called Subgrid Scale / Gradient Subgrid Scale (SGS/GSGS) that overcomes oscillations. The influence of chemistry and temperature on stress evolution is observed by concluding that thermal and chemical effects have a significant influence

on the stress and pressure change around the injection well. A similar conclusion is reached in [102]. In fact, it is argued that compared to the THM coupling results, the fluid pressure is reduced when considering the THMC coupling effects due to the increase in porosity and permeability caused by the decrease in effective mean stress and the dissolution of minerals. These influences justify the need to consider THMC coupling in reservoir analysis, as changes in pore pressure are essential in problems involving interaction between rock formations and injected fluids.

Despite the complexity of the problem, several reservoir simulators or academic simulation platforms have been developed to solve the THMC coupling. For example, the reader is referred non-exhaustively to the coupling between TOUGHREACT and FLAC3D in [102], OpenGeoSys in [120], COMSOL Multiphysics with single-phase flow in [198], GEM in [75] and so on. Other simulation codes may respond to such coupled processes and especially in fractured porous media, which are not reviewed and detailed in this work.

Consequently, this literature review presents all the couplings that may be encountered in a CO_2 storage problem in order to have an accurate description of the physics involved in the CO_2 storage scenario prior to initiating the pilot phase process.

1.3 Contribution of the thesis

In this section, the contribution of the thesis is detailed, starting with the main objectives of this work. Finally, an overall plan for the manuscript is proposed.

1.3.1 Objectives of the thesis

The main objectives of the thesis are to study the coupled processes applied to the topic of CO_2 storage in saline aquifers. Two main axes have been privileged by exploring Thermal-Hydro-Chemical and Hydro-Mechanical coupled processes. This investigation is only possible by formulating a mathematical model to obtain the numerical solution of flow models. For the THC coupling, it is possible to specify two different ways of resolution with sequential and fully coupled fully implicit approaches. Classically, the sequential approach is most commonly used on the simulation platform due to its greater simplicity and lower cost in CPU time. Indeed, solving two smaller problems may be less complex than solving a larger one. Nevertheless, it should be noted that the approach involves decoupling, which leads to splitting errors. Fully coupled, fully implicit approaches aim to avoid these inaccuracies by solving the entire system of equations simultaneously, taking into account all of the inter-dependencies between the different parts of the system. This can help to improve the accuracy of the simulation, particularly for strongly coupled systems. Therefore, one objective is to formulate sequential and fully coupled fully implicit finite volume schemes for nonisothermal multiphase flow coupled with reactive transport. The development and implementation of these schemes are achieved in the *DuMu*^{X} simulation platform. Secondly, comparisons could be made between the results of the two methods in terms of accuracy and

performance. A high-performance computing platform is therefore used to compute these comparisons.

Furthermore, the second axis deals with the hydro-mechanical coupling applied to CO_2 storage. A fully coupled fully implicit scheme is also developed and implemented for this approach. The validation of this problem type is carried out with the resolution of several benchmarks commonly treated in linear poroelasticity modelling. This part acts as a validation of the method and allowed us to proceed to the next step with CO_2 storage scenarios. Indeed, three different cases illustrate the model by focusing on the geomechanical effect applied to gas injection. The validation of the model, according to the literature is carried out with the help of comparisons with other reservoir simulators already proven in the industrial world. Consequently, this work aims to make a step towards the modelling of THMC processes.

1.3.2 Structure of the manuscript

The thesis is divided into six chapters. Chapter 1 was devoted to establish a state-of-the-art of CO_2 storage processes with a literature review. Several types of coupling have been detailed, including hydraulic, hydro-chemical, and thermal-hydro-chemical coupling processes. Furthermore, the involvement of geomechanics in the storage process was revealed by investigating all the coupling management. The hydro-mechanical and thermal-hydro-mechanical coupling models have also been reviewed. Finally, the consideration of the whole system with thermal-hydro-chemical-mechanical coupling is reviewed by presenting some contributions.

Chapter 2 describes the mathematical model developed to study Thermal-Hydro-Chemical coupling in porous media. This model is composed of mass conservation laws describing the flow in the medium, coupled with mass action laws (algebraic equations) and/or ordinary differential equations provided by the geochemical reactions, and with energy conservation to account for temperature variations due to the injection of a fluid into the domain. All these coupled partial differential equations provide a highly nonlinear system complex to solve.

Then, in Chapter 3, the methodology for numerically solving such a system is given, using two different resolution approaches that provide two different ways of solving the complex system. The fully implicit method consists of solving the system in its global under the form of a monolithic matrix, while the sequential approach consists of decoupling some equations and solving them separately and sequentially. Both approaches have been implemented in the $DuMu^X$ simulation platform. They were compared in terms of the accuracy of the results and the performance in terms of computational time resolution. High-performance computing has therefore helped us to realise the efficiency of the modules developed in this framework. Three different cases of CO_2 injection scenarios were carried out to illustrate the model with increasing complexity from one to three dimensions (1-3D).

Chapter 4 is dedicated to the description of the mathematical model for hydro-mechanical coupling. This model consists of a two-phase compositional model to solve the flow subproblem coupled with an equilibrium law to solve the mechanical subproblem. Both approaches have been coupled using a two-way coupling

method where porosity and permeability are modified. The discretisation of the fully coupled fully implicit approach is detailed.

In Chapter 5, the methodology to solve numerically hydro-mechanical processes is exposed. The validation of the hydro-mechanical coupling is performed on several benchmarks which are commonly solved in linear poroelasticity modelling. Further scenarios of CO_2 injection in layered formations are investigated to determine the geomechanical effects on the aquifer, in particular rock displacements. Comparisons with other strategies and other commercial software are addressed in order to validate results obtained using our coupling approach.

Finally, in Chapter 6 will give a summary and an outlook beyond the scope of this thesis.

Chapter 2

Thermal-Hydro-Chemical coupled model for geological CO_2 storage

Contents

2.1 Introduction 26
2.2 Fundamental terms 26
2.2.1 State variables 26
2.2.2 Fluid properties 28
2.2.3 Porous media properties 29
2.3 Geochemical model 32
2.3.1 Chemical model 33
2.3.2 Equilibrium reactions 35
2.3.3 Kinetic reactions 36
2.4 Two-phase flow model 36
2.5 Temperature processes 38
2.6 Global Thermo-Hydro-Chemical model 38
2.7 Closure relations 39
2.8 Constitutive relations 40
2.8.1 CO_2 fluid properties 40
2.8.2 Brine fluid properties 41
2.9 Conclusion 43

2.1 Introduction

In general, CO_2 storage problems are described as multiphase flow problems coupled with other processes depending on the complexity envisaged. This chapter focuses on thermal-hydro-chemical (THC) processes. This part is devoted to presenting the geochemical and mathematical models used to characterise nonisothermal two-phase multicomponent flow with reactive transport in porous media. First, in Section 2.2, the fundamental terms and variables are introduced to define the mathematical problem. Section 2.3 describes how chemical reactions are characterised mathematically and presents the different forms of reaction. These chemical reactions result in algebraic relations for equilibrium reactions or ordinary differential equations for kinetic reactions which should be coupled with the flow. Section 2.4 and Section 2.5 present the system of partial differential equations and their coupling which allow the description of nonisothermal two-phase flow. This system of PDEs is composed of constitutive laws resulting from mass and energy contributions. In order to close the latter system of coupled equations, some closure relations are given in Section 2.7. Finally, constitutive relations for gaseous CO_2 and brine properties are explained in Section 2.8 to highlight the dependence on pressure and temperature.

2.2 Fundamental terms

In order to properly define a mathematical model dealing with Thermal-Hydro-Chemical processes, it is necessary to introduce notations and variables. All these fundamental terms or quantities are related to the topic of porous media and other definitions, see for instance [152].

2.2.1 State variables

First, state variables are defined, in particular variables useful for describing the gaseous and liquid states of fluids involved in CO_2 storage problems. Then some quantities of interest are introduced to give a mathematical formulation of the problem with these unknowns.

Phases and components

In the sequel, α is defined as the phase index which stands for the well-defined region where there are no discontinuities in material properties. These phases can be found in three different states: liquid, gas, or solid phases. In the following, $\alpha = \{l, g, s\}$. In particular, the phase diagram (Figure 2.1) represents the three different states in which CO_2 can be found with respect to pressure and temperature.

A phase can contain several components, which refer to chemical substances and can be transferred between phases thanks to a possible change of state. In this work, the superscripts i and j denote components and N_c denotes the number of components.

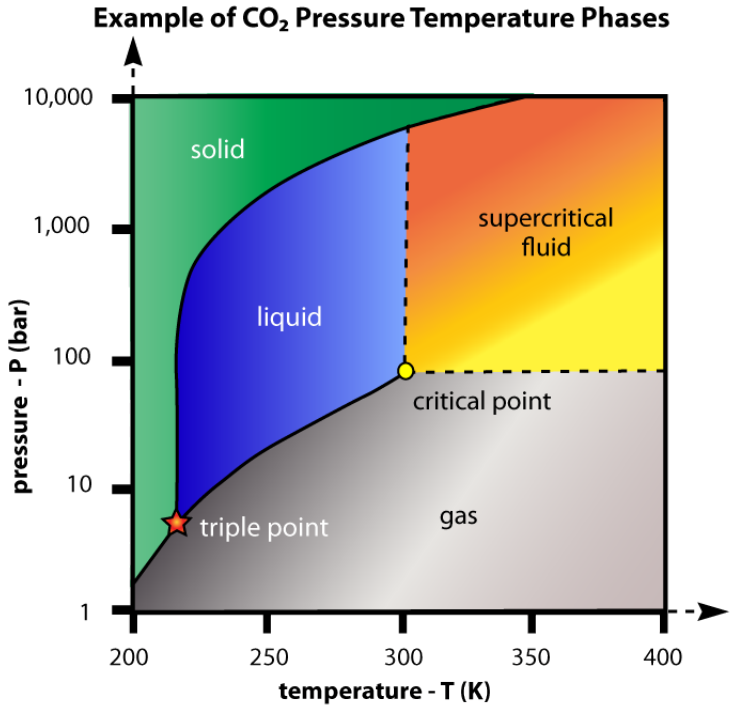

Figure 2.1: Phase diagram for CO_2 as a function of pressure and temperature. The critical point is at a pressure of 73.8 bar and a temperature of 304.25 K.

Molar fraction, concentration and molality

The molar fraction is useful to describe the composition of phases. The latter is defined as the ratio of the number of moles n_α^i of a component i to the total number of moles in the system within the phase:

$$x_\alpha^i = \frac{n_\alpha^i}{\sum_{i=1}^{N_c} n_\alpha^i}. \tag{2.2.1}$$

By analogy, the concentration of the component i is used to quantify the compositions, which are denoted as c_α^i [mol.m^{-3}]:

$$c_\alpha^i = x_\alpha^i \, \rho_\alpha, \tag{2.2.2}$$

where ρ_α [mol.m^{-3}] is the molar density and will be introduced later as a fluid property. The molality m^i [mol.kg^{-1}] is defined as the ratio between the molar fraction of the species i and the average molar mass of the phase α:

$$m^i = \frac{x_\alpha^i}{\sum_{i=1}^{N_c} x_\alpha^i M^i}, \tag{2.2.3}$$

where M^i [kg.mol^{-1}] is the molar mass of the component i.

Saturation

In the case of multiple phases flowing in a porous medium, it is necessary to have a measure of the fraction of pores filled with a fluid phase. This measure is given by the saturation S_α as follows:

$$S_\alpha = \frac{V_\alpha}{V_{\text{pores}}}, \tag{2.2.4}$$

where V_α and V_{pores} represent the volume filled by the phase α and the total pore volume considered, respectively. Consequently, S_α varies from 0 to 1 depending on the composition of the phase.

2.2.2 Fluid properties

Thermodynamic properties can have a significant effect on fluid flow, particularly on certain quantities such as density, viscosity, enthalpy, etc. It is therefore necessary to obtain an accurate description of the flow influenced by nonisothermal conditions. Most of these variables will be defined later using equations of state for CO_2 storage scenarios.

Density

Mass density is a representation of the amount of mass M [kg] (or the number of particles) of a substance, material, or object in relation to the space it occupies in the phase α (volume V_α [m^3] which depends on pressure and temperature). Thus ρ_α^{mass} [$kg.m^{-3}$] is defined as:

$$\rho_\alpha^{mass}(p_\alpha, T) = \frac{M_\alpha}{V_\alpha(p_\alpha, T)}. \tag{2.2.5}$$

This measurement is not necessarily constant, as the density depends on several factors, including temperature and pressure. It usually increases with increasing pressure and decreasing temperature [51, 152]. In the case of mixtures, the density also depends on the composition considered. For example, because brine is salt water, its density is higher than that of water ($\rho_{brine}^{mass} = 1230$ $kg.m^{-3}$ and $\rho_{H_2O}^{mass} = 1000$ $kg.m^{-3}$). Another type of density that can be used is the molar density ρ_α [$mol.m^{-3}$]. In this work, the molar density is mostly defined as:

$$\rho_\alpha(p_\alpha, T) = \frac{\rho_\alpha^{mass}(p_\alpha, T)}{\sum_{i=1}^{N_c} x_\alpha^i M^i}. \tag{2.2.6}$$

Viscosity

Viscosity μ_α [$Pa.s^{-1}$] in porous media refers to the resistance of a fluid phase α to flow through a porous material. It is a measure of how easily a fluid can flow through the spaces between particles in a porous medium. Viscosity is influenced by several factors, including the properties of the fluid (such as its density), the properties of the porous medium (such as its pore size distribution and surface roughness), and the flow rate of the fluid through the medium.

Enthalpy and internal energy

Specific enthalpy h_α [J] and specific internal energy u_α [J] are two related quantities used to describe energy changes in a nonisothermal system. In particular, the specific internal energy represents the energy stored in one kilogram of the substance under consideration. According to [51], specific enthalpy is described by:

$$h_\alpha = C_{p,\alpha}\, T, \tag{2.2.7}$$

where $C_{p,\alpha}$ is heat capacity of phase α at constant pressure. Specific enthalpy is correlated to specific internal energy by the relation:

$$h_\alpha = u_\alpha + \frac{p_\alpha}{\rho_\alpha}. \tag{2.2.8}$$

For complex systems with multiple phases and components, the enthalpy of each component must be considered. In addition, in the case of dissolution of any substance, enthalpy must also be taken into account, as dissolution can generate some heat which affects the system [210].

2.2.3 Porous media properties

Finally, to describe the system, the contribution of porous media properties must be introduced. In this part, all the quantities that play an important role in reservoir characterisation are reviewed.

Porosity

Porosity ϕ [-] is a measure of the pore volume in a porous medium. It allows us to define the voids or empty spaces in a material that are accessible to fluid:

$$\phi = \frac{V_{pores}}{V_{total}}, \tag{2.2.9}$$

where V_{pores} and V_{total} are the volume of the pores and the total volume respectively.

Permeability

Absolute permeability $\mathbb{K}$ refers to a measure of the ease with which a fluid can flow through a porous medium. It can be affected by factors such as the size, shape and distribution of the pores, as well as the properties of the fluid itself, such as its viscosity and density. It is often expressed in units of Darcy [D], milliDarcy [mD] or metres squared [m^2], which is a measure of the rate of fluid flow through a porous medium under a unit pressure gradient. Rocks with permeabilities well below 100 mD can form effective seals, particularly in the case of CO_2 storage, where a caprock is required to ensure safety.

In general, the absolute permeability is treated as a three-dimensional matrix where each diagonal term describes the permeability value in the x, y, and z directions. If all these diagonal components are equal, the porous medium is said to be isotropic.

If a contribution in one direction is different from the others, an anisotropy ratio is introduced. Consequently, the fluid will preferentially flow in the direction of higher permeability.

Capillary pressure

The interface between the two phases is characterised by an interfacial tension due to collision and adhesion effects between the two phases. This tension induces a pressure difference known as capillary pressure [152]:

$$P_c = P_g - P_l. \tag{2.2.10}$$

Some experimental models have been developed to approximate reality. In particular, the Brooks-Corey and Van-Genuchten models are used in the test cases presented later. In both of them, effective saturation S_e is defined as:

$$S_e = \Big(\frac{S_l - S_{lr}}{1 - S_{lr}}\Big), \text{ with } S_{lr} \leq S_l \leq 1, \tag{2.2.11}$$

where S_l and S_{lr} are respectively the liquid saturation and the liquid residual saturation which cannot be displaced by viscous forces. When dealing with a two-phase flow, another formulation of effective saturation is encountered in [99] as:

$$S_e = \Big(\frac{S_l - S_{lr}}{1 - S_{lr} - S_{gr}}\Big), \text{ with } S_{lr} \leq S_l \leq 1 - S_{gr}, \tag{2.2.12}$$

where S_{gr} is the gaseous residual saturation. In both cases, the capillary pressure is defined as follows:

- Brooks-Corey model [41]:

$$P_c(S_e) = P_e\, S_e^{-\frac{1}{\lambda}}, \tag{2.2.13}$$

  where P_e [Pa] is the entry pressure and λ [-] is a constant that can be interpreted as a shape parameter for the curve ($\lambda > 0$).

- Van Genuchten model [205]:

$$P_c = \frac{1}{\alpha}\Big(S_e^{-\frac{1}{m}} - 1\Big)^{\frac{1}{n}}, \tag{2.2.14}$$

  where m [-], n [-] and α [Pa^{-1}] are constant such as: $n > 1$, $m = 1 - \dfrac{1}{n}$.

Figure 2.2 depicts the evolution of capillary pressure for Brooks-Corey and Van-Genuchten models with respect to liquid saturation [51, 99]. Some regularisation on the Van-Genuchten model is performed when the liquid saturation is either 0 or 1.

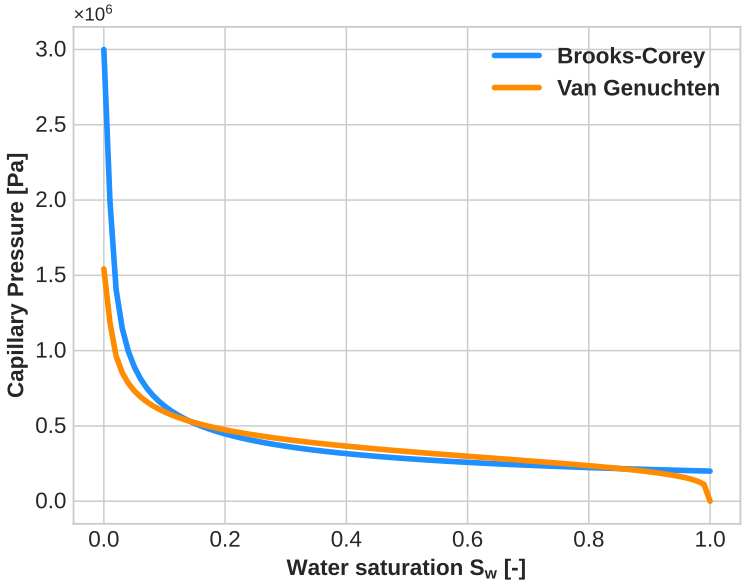

Figure 2.2: Capillary pressure evolution as a function of liquid saturation for the two empirical models of Brooks-Corey and Van-Genuchten.

Relative permeability

The relative permeability $k_{r\alpha}$ occurs when two immiscible fluids move in the porous medium. The two fluids interfere with each other by occupying the pore space and blocking the other fluid. The relative permeability is then used to give weight to the absolute permeability in Darcy's law, which characterises any flow rate. It depends on saturation and is given by empirical models or experimental measurements [152]. Again, the most commonly used laws are:

- Brooks-Corey model [41]:

$$k_{rl}(S_e) = \left(S_e\right)^{\frac{2+3\lambda}{\lambda}}, \tag{2.2.15}$$

$$k_{rg}(S_e) = \left(1-S_e\right)^2\left(1-S_e\right)^{\frac{2+\lambda}{\lambda}}, \tag{2.2.16}$$

  where λ is a constant given as a parameter.

- Van-Genuchten model [205]:

$$k_{rl}(S_e) = \sqrt{S_e}\left(1-\left(1-S_e^{\frac{1}{m}}\right)^m\right)^2, \tag{2.2.17}$$

$$k_{rg}(S_e) = \left(1-S_e\right)^{\frac{1}{3}}\left(1-S_e^{\frac{1}{m}}\right)^{2m}, \tag{2.2.18}$$

  where m, n are constants defined previously in Section 2.2.3.

Figure 2.3 shows the evolution of liquid and gas relative permeabilities for Brooks-Corey and Van-Genuchten models with respect to liquid saturation. For both capillary pressure and relative permeabilities, Table 2.1 details several parameters used to perform Figure 2.2 and Figure 2.3.

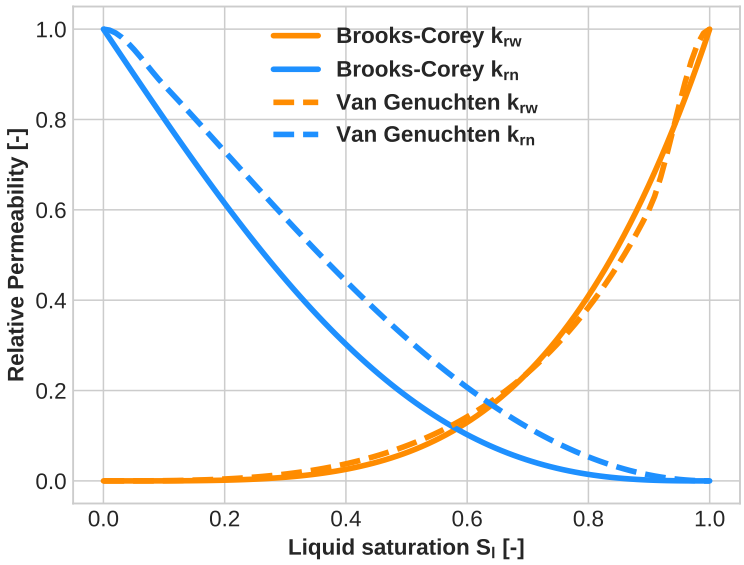

Figure 2.3: Liquid and gas relative permeability evolution as a function of liquid saturation for the two empirical models of Brooks-Corey and Van-Genuchten.

Residual liquid saturation	S_{lr}	0.0	[-]
Residual gas saturation	S_{gr}	0.0	[-]
Brooks-Corey	P_e	2×10^5	[Pa]
Brooks-Corey	λ	2	[-]
Van-Genuchten	α	3.3×10^{-6}	[Pa^{-1}]
Van-Genuchten	n	4.367	[-]

Table 2.1: Parameters for plotting capillary pressure and relative permeability.

2.3 Geochemical model

Before describing the geochemical model, it is necessary to define a framework that allows us to properly write the chemical interactions. First, I represents the set of all N_c chemical species involved in N_r chemical reactions. According to the Morel formalism [145], it is possible to divide the species into primary and secondary species. The secondary components are chosen to be formed as a set of the primary ones. Consequently, I can be divided into I_p and I_s such that $I = I_p \cup I_s$. Then, each subset I_p and I_s is divided again into two sub-subsets that describe mobile and immobile species such as inert and reactive rocks. This decomposition leads to $I_p = I_{pm} \cup I_{pi}$. For secondary species, it is also possible to add

species involved in precipitation/dissolution equilibrium I_{se} and kinetic reactions I_k such that $I_s = I_{sm} \cup I_{si} \cup I_{se} \cup I_{sk}$.

To address the sequential approach, where the two-phase flow is decoupled from the reactive transport, two further subsets are introduced, such as $I = I_{2\varphi} \cup I_{rt}$. The subset $I_{2\varphi}$ represents all species present in both the liquid and gas phases, while I_{rt} consists of the remaining species.

2.3.1 Chemical model

A chemical reaction is a process in which one or more substances, called reactants, are converted into one or more different substances, called products. The substances are either chemical elements or compounds, such as molecules or ions. The atoms in the reactants are rearranged to produce different substances as products. In mathematical terms, a chemical reaction can be written as follows

$$\sum_{j=1}^{N_c} \nu_{ij} A_j = 0, \quad i = 0, \ldots, N_r, \tag{2.3.1}$$

where ν_{ij} and A_j refer to the stoichiometric coefficient and the chemical species respectively.

Chemical reactions can be divided into two categories, homogeneous and heterogeneous reactions. Homogeneous reactions are reactions where the products and reactants involved belong to the same phase. Generally, this type of reaction corresponds to groundwater flow, where an aqueous phase reacts with resident brine or water. Conversely, heterogeneous reactions deal with species involved in two or more phases. The dissolution of minerals contained in the porous rock matrix is typically represented as a heterogeneous reaction. Another way to separate and treat different types of reactions is to describe them with a reaction speed. The latter is quantified by a reaction rate r_j. These reaction rates allow to define two types of reactions: equilibrium reactions and kinetic reactions.

- Equilibrium reactions are fast reactions (almost instantaneous for aqueous reactions). Reaction rates are significantly high and unknown.
- Kinetic reactions are relatively slow reactions and can occur over longer time scales. In these reactions, the rate is given as a function of the concentrations of the species involved.

A chemical system is generally written as a combination of reactants and products. The latter can be reformulated by substitution. According to the Morel formalism [145], it is assumed that each reaction can be written in a form that gives a single distinct product per reaction. Consequently, chemical species are divided into primary and secondary species. Each secondary species is obtained thanks to a set of primary species. This approach leads to a reduction in the size of the solved system.

To illustrate all the sets of species defined above and the division between primary and secondary species, an example of a chemical system is provided in Table 2.2.

Eight reactions are considered: two aqueous dissolution reactions, three aqueous complexation reactions under equilibrium conditions, one mineral precipitation dissolution under equilibrium conditions for calcite, and two precipitation/dissolution reactions under kinetic conditions for anorthite and kaolinite.

Reactions		
$H_2O_{(g)}$	$\rightleftharpoons$	$H_2O_{(l)}$
$CO_{2(g)}$	$\rightleftharpoons$	$CO_{2(l)}$
$OH^- + H^+$	$\rightleftharpoons$	$H_2O_{(l)}$
$CO_3^{2-} + 2\ H^+$	$\rightleftharpoons$	$H_2O_{(l)} + CO_{2(l)}$
$HCO_3^- + H^+$	$\rightleftharpoons$	$CO_{2(l)} + H_2O$
Calcite $+ 2\ H^+$	$\rightleftharpoons$	$Ca^{2+} + H_2O + CO_{2(l)}$
Anorthite $+ 8\ H^+$	$\rightleftharpoons$	$4\ H_2O_{(l)} + Ca^{2+} + 2\ Al^{3+} + 2\ SiO_2$
Kaolinite $+ 6\ H^+$	$\rightleftharpoons$	$5\ H_2O_{(l)} + 2\ Al^{3+} + 2\ SiO_2$

Table 2.2: Example of a chemical system.

For this chemical system, the different chemical species can be classified as follows:

$$
\begin{aligned}
I_{pm} &= \left\{H_2O_{(l)}, CO_{2(l)}, H^+, Ca^{2+}, Al^{3+}, SiO_2\right\},\\
I_{pi} &= \{\varnothing\},\\
I_{sm} &= \left\{H_2O_{(g)}, CO_{2(g)}, OH^-, CO_3^{2-}, HCO_3^-\right\},\\
I_{si} &= \{\varnothing\},\\
I_{se} &= \{\text{Calcite}\},\\
I_{sk} &= \{\text{Anorthite}, \text{Kaolinite}\},\\
I_{2\varphi} &= \left\{H_2O_{(l)}, H_2O_{(g)}, CO_{2(l)}, CO_{2(g)}\right\},\\
I_{rt} &= \left\{H^+, Ca^{2+}, Al^{3+}, SiO_2, OH^-, {CO_3}^{2-}, {HCO_3}^-, \text{Calcite}, \text{Anorthite}, \text{Kaolinite}\right\}.
\end{aligned}
$$

Activity model

In an aqueous solution, each chemical species, ion, or molecule will interact with its neighbours and with the solvent. The availability of the chemical species for a reaction can then be quite different from the concentration in the solution. This difference from the ideal case (i.e. the case where the species do not interact) is expressed by the term activity. It is also called the active concentration of the species and depends on the type of the latter. It is given as follows:

$$a_l^i = \gamma^i \frac{m_l^i}{m_0}, \tag{2.3.2}$$

where γ_i [-] and m_0 are the activity coefficient of aqueous species i and the reference molality [mol.kg^{-1}] (equal to 1 for water) respectively.

For ideal solutions, $\gamma_i = 1$ and the activity is equal to the molality. However, in most cases, the solution is non-ideal and there are some models that allow to characterise ionic activity coefficients. In particular, one can mention the Debye-Hückel model [35] for which the activity coefficient is:

$$log\ \gamma_i\ =\ -\ \frac{Az_i^2\sqrt{I}}{1+\mathring{a}_i B\sqrt{I}}, \tag{2.3.3}$$

where A, B are temperature dependent constants, z_i is the electric charge of the ion i and I is the ionic strength expressed as

$$I\ =\ \frac{1}{2}\sum_i m_i z_i^2. \tag{2.3.4}$$

Other extensional models have been developed such as the Davies equation, the B-dot model [35] and for higher ionic strength [22], the Pitzer activity model [161].

For gaseous species, activities are often replaced by fugacity relations [196] such as:

$$f_g^j\ =\ \varphi_g^j\ \frac{P_g^j}{P_0}, \tag{2.3.5}$$

where φ_g^j represents the fugacity coefficient of component j in the gaseous phase, P_g^j [Pa] is the partial pressure of component j and P_0 [Pa] is the atmospheric pressure.

2.3.2 Equilibrium reactions

Aqueous reactions are relatively fast and reach equilibrium instantaneously, so they can be represented by equilibrium reactions. Consequently, each aqueous reaction gives rise to a mass action law, written as an algebraic relation that links the activities of the species involved in the reaction [35]:

$$a_l^j\ =\ K_j(T)\ \prod_{i\in I_p}\left(a_l^i\right)^{\nu_{ji}},\quad j\in I_{sm}\cup I_{si}, \tag{2.3.6}$$

where a_l^j is the activity of the component j in the liquid phase and ν_{ji} is the stoichiometric coefficient of the reaction. $K_j\,(T)$ is the reaction constant of component j, which depends on the temperature T.

Equilibrium reactions can take a different form for mineral precipitation or dissolution processes. In this case, a solubility product must be verified:

$$\text{if}\ \ K_j(T)\ \prod_{i\in I_p}\left(a_l^i\right)^{\nu_{ji}}<1\ \text{then}\ c_s^j\ =\ 0,\text{else}\ K_j(T)\ \prod_{i\in I_p}\left(a_l^i\right)^{\nu_{ji}}=1\ ,\ j\in I_{se}. \tag{2.3.7}$$

Eq. (2.3.7) can be reformulated as a complementarity problem:

$$min\left(c_s^j,\ 1\ -\ K_j(T)\ \prod_{i\in I_p}\left(a_l^i\right)^{\nu_{ji}}\right)\ =\ 0\ ,\ j\in I_{se}. \tag{2.3.8}$$

2.3.3 Kinetic reactions

In contrast to equilibrium reactions, kinetic reactions are relatively slow. In this work, they are considered to occur only as mineral precipitation or dissolution. Reaction rates can be used to describe the evolution of minerals over time. Each kinetic reaction leads to an ordinary differential equation written for the mineral reaction j [123, 197]:

$$\frac{dc_s^j}{dt} = -r_j, \quad j \in I_{sk}, \tag{2.3.9}$$

where the reaction rate r_j is defined as:

$$r_j = K_j^s(T)\, A_j^s \left(1 - K_j(T) \prod_{i \in I_p} \left(a_l^i\right)^{\nu_{ji}}\right). \tag{2.3.10}$$

A_j^s is the reactive surface area $[m^2.m^{-3}]$ of component j, while K_j^s is the kinetic rate constant [mol.m^{-2}.s^{-1}], which depends on the temperature (Arrhenius law) [22, 128, 219]:

$$K_j^s(T) = K_{j,ref}\, exp\left[-\frac{E_j^a}{R}\left(\frac{1}{T} - \frac{1}{298.15}\right)\right], \tag{2.3.11}$$

where $K_{j,ref}$, E_j^a, R and T are the reaction constants at a temperature of 298.15 K, activation energy [J.mol^{-1}], gas constant [J.K^{-1}.mol^{-1}] and absolute temperature [K], respectively.

Once the geochemical model is fully introduced, the previously presented framework can be coupled to the flow to have hydraulic and chemical interactions in our model.

2.4 Two-phase flow model

This section describes the two-phase flow model in order to couple it with the geochemical part presented earlier. This coupling lies in the reaction rates on the right-hand side of the mass conservation laws written for each primary species and component. The transport of species is carried out by a transport equation characterised by a phase velocity given by Darcy's law.

Mass conservation law

The general form of the mass conservation law for the multiphase system is given for each component i in each phase α by [99] as:

$$\frac{\partial}{\partial t}\left(\phi \rho_\alpha S_\alpha x_\alpha^i\right) + \nabla \cdot \left(\rho_\alpha x_\alpha^i \overrightarrow{q_\alpha} - \phi \rho_\alpha S_\alpha D_\alpha \nabla x_\alpha^i\right) = r^i,\ i \in I \text{ and } \alpha \in \{l, g\}. \tag{2.4.1}$$

where ϕ [$-$] denotes the porosity of the porous medium, S_α [$-$] the saturation of phase α, $\vec{q}_\alpha$ is the velocity of phase α expressed in [m.s^{-1}], ρ_α is the molar density

of phase α [mol.m^{-3}], and x_α^i is the molar fraction of component i in phase α. The term r^i on the right is the reaction rate resulting from the chemical coupling. Eq. (2.4.1) is written for each component involved in the chemical system. It is possible to replace the reaction rates of primary species with a linear combination of reactions of secondary species from chemical reactions:

$$r^i = \sum_{j \in I_s} \nu_{ji} r^j \tag{2.4.2}$$

Therefore, according to [174], since the reaction rates resulting from the aqueous reaction at equilibrium are unknown, they are eliminated by substitutions and reformulations of the mass balance equations. For convenience, molar fractions are converted to concentrations thanks to Eq. (2.2.2). By neglecting the gradient of molar density $\nabla\rho_\alpha$, resulting from the diffusive flux, the approximation is done with:

$$\nabla c_\alpha^i \approx \rho_\alpha \nabla x_\alpha^i. \tag{2.4.3}$$

Therefore, it is possible to define an advection-diffusion operator in phase α such as:

$$L_\alpha(c_\alpha^i) = \nabla \cdot (c_\alpha^i \vec{q}_\alpha) - \nabla \cdot (\phi S_\alpha D_\alpha \nabla c_\alpha^i). \tag{2.4.4}$$

The dispersive-diffusive tensor D_α [m^2.s^{-1}] is defined using the Millington-Quirk formula [144] as follows:

$$\phi\, S_\alpha\, D_\alpha = \phi^{\frac{4}{3}}\, S_\alpha^{\frac{10}{3}}\, D_{m,\alpha}\mathbb{I} + d_L|\vec{q}_\alpha|\mathbb{I} + (d_L - d_T)\frac{\vec{q}_\alpha \vec{q}_\alpha{}^T}{|\vec{q}_\alpha|}, \tag{2.4.5}$$

where $D_{m\alpha}$ [m^2.s^{-1}] is the molecular diffusion in the phase α, d_L [m] and d_T [m] are the magnitudes of longitudinal and transverse dispersion, respectively. $\vec{q}_\alpha$ [m.s^{-1}] is the velocity of phase α defined by the Darcy-Muskat equation:

$$\vec{q}_\alpha = -\,\mathbb{K}\,\frac{k_{r\alpha}(S_\alpha)}{\mu_\alpha}\,(\nabla P_\alpha - \rho_\alpha^{mass}\,\vec{g}), \tag{2.4.6}$$

where $\mathbb{K}$ [m^2] is the absolute permeability tensor, $k_{r\alpha}$ [-] is the relative permeability of the fluid. μ_α [Pa.s], P_α [Pa], ρ_α^{mass} [kg.m^{-3}] are the dynamic viscosity, pressure, and mass density of the α phase respectively, while $\vec{g}$ [m.s^{-2}] is the gravitational acceleration.

Finally, the elimination of the reaction rates on the right-hand side of Eq. (2.4.1) leads to new mass conservation laws for each primary species written as:

$$\frac{\partial}{\partial t}\left(\phi S_\alpha c_\alpha^i + \sum_{j \in I_{sm}} \phi \nu_{ji} S_\alpha c_\alpha^j + \sum_{j \in I_s \setminus I_{sm}} \nu_{ji} c_s^j\right) + L_\alpha(c_\alpha^i)$$

$$+ \sum_{j \in I_{sm}} \nu_{ji} L_\alpha(c_\alpha^j) = 0, \quad i \in I_{pm}, \tag{2.4.7}$$

$$\frac{\partial}{\partial t}\left(c_s^i + \sum_{j \in I_{si}} \nu_{ji} c_s^j\right) = 0, \quad i \in I_{pi}, \tag{2.4.8}$$

2.5 Temperature processes

Thermal coupling with two-phase reactive flow is discussed in this section. It is assumed that the system under consideration is in local thermal equilibrium, i.e. all fluid phases and the porous medium have the same temperature at one point in the system. Under this assumption, it is possible to set up an energy equation for the whole system instead of considering each phase separately [99, 152]. To account for temperature effects, the conservation of energy is given:

$$\frac{dU}{dt} = \nabla \cdot F_T + q_h, \tag{2.5.1}$$

where U is the heat accumulation term consisting of rock and fluid contributions, F_T is the heat flux and q_h is the heat source/sink due to injection. This conservation of energy is a consequence of the first law of thermodynamics, which states that energy is conserved when transformed from one form to another. In order to quantify the energy of the two phases, a sum must be taken into account. The storage term U is therefore split into energy from the fluid and energy from the host rock. A heat conduction part and a convective energy transport result from the energy flux F_T. This results in the global conservation of energy:

$$\frac{\partial}{\partial t}\left(\phi \sum_\alpha \rho_\alpha^{mass} u_\alpha S_\alpha + (1-\phi)\rho_s^{mass} c_h T\right) + \nabla.\left(-\lambda_{pm}\nabla T + \sum_\alpha \rho_\alpha^{mass} h_\alpha \overrightarrow{q_\alpha}\right) = 0, \tag{2.5.2}$$

where T [K] is the temperature [K], u_α and h_α are the specific internal energy and specific enthalpy defined in Eq. (2.2.8), c_h [J.kg^{-1}.K^{-1}] denotes the heat capacity of the rock matrix and λ_{pm} [J.s^{-1}.m^{-1}.K^{-1}] is the thermal conductivity of the porous medium.

2.6 Global Thermo-Hydro-Chemical model

In order to summarize this chapter, the global model is proposed for solving non-isothermal compositional two-phase flow coupled with reactive transport. The whole system consists of:

- N_p partial differential equations modelling the mass conservation of each primary species

$$\frac{\partial}{\partial t}\left(\phi S_\alpha c_\alpha^i + \sum_{j \in I_{sm}} \phi \nu_{ji} S_\alpha c_\alpha^j + \sum_{j \in I_s \setminus I_{sm}} \nu_{ji} c_s^j\right) + L_\alpha(c_\alpha^i)$$

$$+ \sum_{j \in I_{sm}} \nu_{ji} L_\alpha(c_\alpha^j) = 0, \quad i \in I_{pm}, \tag{2.6.1}$$

$$\frac{\partial}{\partial t}\left(c_s^i + \sum_{j \in I_{si}} \nu_{ji} c_s^j\right) = 0, \quad i \in I_{pi}, \tag{2.6.2}$$

- one partial differential equation modelling the energy conservation

$$\frac{\partial}{\partial t}\left(\phi \sum_\alpha \rho_\alpha^{mass} u_\alpha S_\alpha + (1-\phi)\rho_s^{mass} c_h T\right) + \nabla.\left(-\lambda_{pm}\nabla T + \sum_\alpha \rho_\alpha^{mass} h_\alpha \overrightarrow{q_\alpha}\right) = 0\,, \tag{2.6.3}$$

- card$\{I_{sm} \cup I_{si}\}$ mass action laws modelling equilibrium reactions

$$a_l^j = K_j(T) \prod_{i \in I_p} \left(a_l^i\right)^{\nu_{ji}}, \quad j \in I_{sm} \cup I_{si}, \tag{2.6.4}$$

- card$\{I_{se}\}$ complementary problems modelling dissolution/precipitation equilibrium reactions

$$min\left(c_s^j,\, 1 - K_j(T) \prod_{i \in I_p} \left(a_\alpha^i\right)^{\nu_{ji}}\right) = 0,\, j \in I_{se}, \tag{2.6.5}$$

- card$\{I_{sk}\}$ ordinary differential equations modelling kinetic reactions

$$\frac{dc_s^j}{dt} = -K_j^s(T)\, A_j^s \left(1 - K_j(T) \prod_{i \in I_p} \left(a_\alpha^i\right)^{\nu_{ji}}\right),\, j \in I_{sk}. \tag{2.6.6}$$

2.7 Closure relations

To close the system Eq. (2.6.1) to Eq. (2.6.6), some additional relations are added to fully characterise the problem. First, total restrictions on saturations and molar fractions are added:

$$\sum_\alpha S_\alpha = 1 \quad \text{and} \quad \sum_i x_\alpha^i = 1, \quad \alpha \in \{l, g\}. \tag{2.7.1}$$

Capillary pressure characterises the pressure induced by the interfacial tensions between each phase. It is inserted into the system with:

$$P_c(S_l) = P_g - P_l. \tag{2.7.2}$$

In addition, some equations of state are required to characterise fluid properties, such as density, viscosity, or solubility laws, and depend on the problem being considered. More details about specific properties of CO_2 will be given in the following Section 2.8. Boundary conditions and initial conditions must be specified to ensure that the system is well-posed.

2.8 Constitutive relations

This section describes some fluid properties of CO_2 and brine. Two phases coexist in the CO_2 sequestration process, a liquid phase consisting of brine, water, or liquid CO_2 and a gaseous/supercritical phase composed of the injected gas. The thermodynamic properties of the fluids involved in the multiphase flow change continuously as they pass from the liquid or gaseous to the supercritical state [36]. Therefore, different functions and equations of state (EOS) are required to determine the flow properties, especially for CO_2 and resident brine.

2.8.1 CO_2 fluid properties

The quantities defined in Section 2.2.2 are generally dependent on pressure, temperature, and phase composition. In our approach, liquid and gas phase densities are defined according to Span and Wagner [192]. Figure 2.4 (a) shows the density CO_2 in the gaseous phase for various temperatures and pressures commonly encountered in geological formations. At 293.15 K the surface shows a discontinuous density change at the corresponding vapour pressure. This discontinuity is due to the CO_2 change from gas to liquid state. Up to 313.15 K, the temperature is above the supercritical value and the density increases continuously with increasing pressure, but still with a pronounced behaviour. Beyond 333.15 K, the influence of the phase change diminishes and the density, therefore, becomes more uniform.

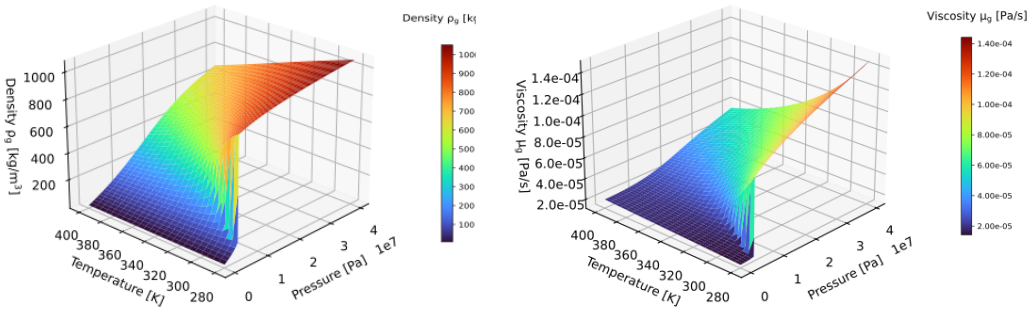

(a) Density of gaseous CO_2 $\rho_g(T, p_g)$ (b) Viscosity of gaseous CO_2 $\mu_g(T, p_g)$

Figure 2.4: Variations of CO_2 density (a) and CO_2 viscosity (b) as a function of pressure and temperature.

Based on the same principle, liquid, and gaseous viscosity are defined for fluids in Fenghour's work [80]. According to Figure 2.4 (b) the viscosities have the same behaviour as described for the density. A discontinuity is observed at $T = 293.15$ K due to the phase change at 7.38×10^6 Pa. Otherwise, the viscosity of a gas increases with increasing temperature. Taking into account the effects of temperature involves enthalpy (see Eq. (2.2.8)). It is defined as a thermodynamic potential that summarises the internal energy of the system in a single function. The approach developed in Span and Wagner [192] is used in this work to obtain this enthalpy.

Figure 2.5 (a) shows the behaviour of the CO_2 gaseous enthalpy, which also varies with pressure and temperature. The enthalpy also undergoes a discontinuity for the same reason as before. As the volume change from gaseous to liquid is large during the phase change, a jump in the specific enthalpy can be observed and quantified as the specific enthalpy of evaporation [36].

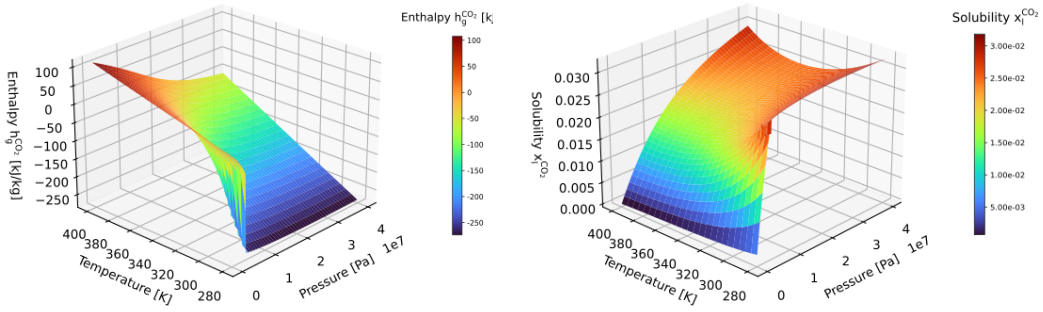

(a) Enthalpy of gaseous CO_2 $h_g(T, p_g)$ (b) Solubility $x_l^{CO_2}(T, p_g)$

Figure 2.5: Variations of CO_2 enthalpy (a) and CO_2 solubility (b) as a function of pressure and temperature.

Finally, the solubility law can be used to characterise the mixture between resident brine or water and carbon dioxide. The latter equation of state depends on pressure and temperature, but also on the salinity of the brine, which can have a significant effect on the solubility [36]. It is defined from the approach defined by Spycher and Pruess in [193] and completed by activity coefficient expression of Duan and Sun [69] and shown in Figure 2.5 (b) for a fixed zero salinity.

2.8.2 Brine fluid properties

Similar to the CO_2 properties, the brine forming the liquid phase can be characterised by several equations of state. Density, viscosity, enthalpy, and solubility for brine are shown from Figure 2.6 to Figure 2.7 for a fixed salinity of 0.1 [kg NaCl/kg solution]. The density of the liquid brine Figure 2.6 (a) depends on temperature and pressure as previously for CO_2. However, salinity and dissolved CO_2 molar fraction also appear to be significant factors in the density variation. The more salt dissolved in the brine, the higher the density. In this approach, the equations of state for brine density are based on IAPWS formulation [213] for pure water density. Then, contributions from salinity and CO_2 molar fraction complete the density calculations as:

$$\rho_{brine} = \rho_{H_2O}(T, p) + \Delta\rho(S_{sal}) + \Delta\rho(T, P, X_l^{CO_2}) \tag{2.8.1}$$

Salt contributions are defined according to Adams and Bachu [12] and Batzle and Wang [30] whereas effects of dissolved CO_2 on brine density are described thanks to Garcia [87]. The viscosity also varies with pressure and temperature, although the

effect of pressure does not appear to be significant for Figure 2.6 (b). The equation of state is also defined by Batzle and Wang [30].

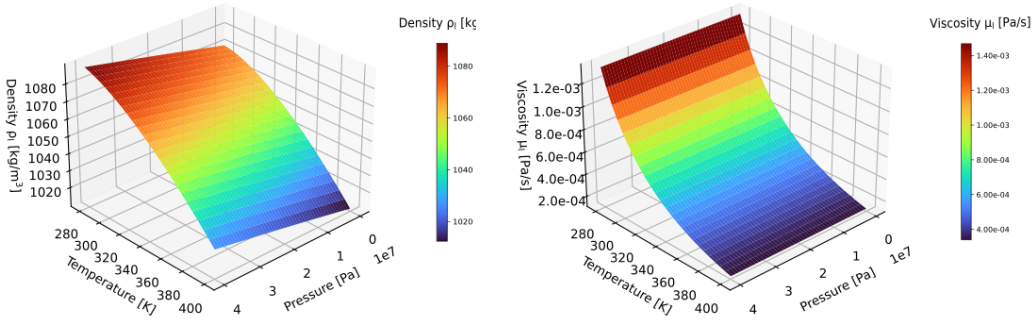

(a) Density $\rho_l(T, p_l)$ (b) Viscosity $\mu_l(T, p_l)$

Figure 2.6: Variations of brine density (a) and viscosity (b) as a function of pressure and temperature.

In Figure 2.7 (a), the enthalpy of liquid brine is represented. It is calculated from the contributions of the three components pure water, salt, and CO_2 . The pure water enthalpy is described according to IAPWS formulation [213] whereas contribution from dissolved salt are exposed from Michaelides [140] and Daubert [61]. Finally, the enthalpy contribution from the dissolved CO_2 quantity is based on Duan and Sun approach [69]. Finally, the mutual solubilities of brine and CO_2 are represented in the gas phase with Figure 2.7 (b). They are also related to Spycher and Pruess equation of state [193].

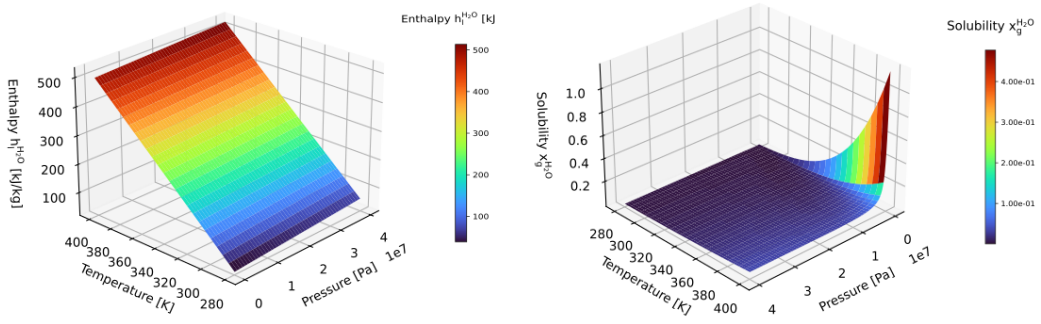

(a) Enthalpy $h_l(T, p_l)$ (b) Solubility $x_g^{H_2O}(T, p_l)$

Figure 2.7: Variations of brine enthalpy (a) and gas solubility (b) as a function of pressure and temperature.

Further information on the equations of state can be found in Table 2.3 and in [36], where they are described in detail.

Fluid property	Model Name	Literature
CO_2 density ρ_{CO_2}	Span and Wagner	[192]
CO_2 viscosity μ_{CO_2}	Fenghour	[80]
CO_2 enthalpy h_{CO_2}	Span and Wagner	[192]
Brine density ρ_{brine}	IAPWS, Adams and Bachu, Garcia	[213, 12, 30, 87]
Brine viscosity μ_{brine}	Batzle and Wang	[30]
Brine enthalpy h_{brine}	IAWPS, Michaelides, Daubert, Duan	[213, 140, 61, 69]
CO_2-Brine solubility $x_l^{CO_2}$	Spycher and Pruess, Duan and Sun	[69, 193]

Table 2.3: Summary table of the different equations of state used in our model approach, adapted from [36].

2.9 Conclusion

This chapter has been devoted to introducing the nonisothermal compositional two-phase flow model coupled with reactive transport used in this thesis. Firstly, the basic terminology has been presented to set the context of the fluid and porous medium properties. The geochemical model is then presented to introduce the equations derived from chemical reactions. Equilibrium and/or kinetic reactions form algebraic relations and/or ordinary differential equations, which are coupled to flow equations via reaction rates. The flow model is described by mass conservation laws written for each primary component in each phase. An energy conservation law is added to the framework to obtain the coupled Thermal-Hydro-Chemical model, which is given in Section 2.6 as a strongly nonlinear system of coupled PDEs. Nevertheless, several closure relations are necessary to complete the PDE system. Finally, some constitutive relations for the CO_2 and the brine are given to illustrate the equations of state used during the simulations.

Chapter 3

Numerical simulation of Thermal-Hydro-Chemical processes for CO_2 storage

Contents

3.1 Introduction 46
3.2 Resolution methods 46
3.2.1 Sequential approach 46
3.2.2 Global implicit approach 49
3.3 Numerical schemes 50
3.3.1 Time discretisation 50
3.3.2 Fully coupled fully implicit finite volume scheme 51
3.4 Implementation 53
3.4.1 $DuMu^X$ numerical simulation platform 53
3.5 Numerical simulations of CO_2 storage scenarios 54
3.5.1 Test case 1: 1D radial problem 55
3.5.2 Test case 2: 2D layered problem 61
3.5.3 Test case 3: 3D heterogeneous problem 67
3.6 Conclusion 87

3.1 Introduction

This chapter is dedicated to presenting the strategies used to solve Thermal-Hydro-Chemical processes in subsurface problems. In general, most commercial reservoir simulators or academic codes use a single-resolution approach to solve numerical problems. The choice of developers may depend on the type of application to be simulated. Some prefer the performance that comes with a sequential resolution, while others prioritise robustness and accuracy. In this thesis, both global implicit and sequential approaches are developed to compare their efficiency in terms of both accuracy and performance. Section 3.2 presents the methods used to implement such approaches. A numerical scheme must then be implemented to transfer them to a numerical simulation platform. For this, a cell-centered finite volume scheme is detailed to solve numerically the THC coupled problems. The latter is presented in Section 3.3. Both methods have been developed and implemented in the numerical simulation platform $DuMu^X$ in order to compare their capacities and performances. Section 3.4 gives all the specifications necessary to integrate new modules in $DuMu^X$. Three different test cases of increasing complexity have been investigated in Section 3.5. They illustrate the whole numerical model and framework presented in Section 2.6. It covers CO_2 storage scenarios in saline aquifers in order to realise the benefits of the technology. First, a one-dimensional (1D) problem is treated to obtain a validation of the coupled model. The second case deals with a two-dimensional (2D) stratified formation, where an extension to THC coupled processes is reformulated. Finally, the last case also deals with an extension to THC coupled processes for a three-dimensional (3D) benchmark to realise the efficiency of the numerical scheme thanks to high-performance computing.

3.2 Resolution methods

There are different ways of solving reactive multiphase flow. On the one hand, the multiphase flow and reactive transport problems can be decoupled and solved sequentially. Alternatively, the system can be solved in a fully implicit manner, where all equations are combined. This section deals with the description of both methods by giving a finite volume discretisation of the coupled schemes.

3.2.1 Sequential approach

The sequential approach, also known as the operator splitting approach, decouples the problem into two subproblems and solves them separately and sequentially. Specifically, using the sets of species defined in Chapter 2, this sequential strategy consists of first solving a nonisothermal compositional two-phase flow addressed in Eq. (2.6.1) for species $i \in I_{2\varphi}$ present in both gas and liquid phases, where the contribution of the remaining species is treated explicitly. It also includes the energy conservation law with Eq. (2.6.3). In this step, it is assumed that all exchanges between the liquid and the gas phase have been calculated. Then a reactive transport problem consisting of Eq. (2.6.1) and Eq. (2.6.2) for i $\in I_{rt}$ is solved to calculate the concentration of the remaining species using the quantities

provided by the first subproblem (velocity, saturation, molar density, temperature, etc.). Each subproblem is solved implicitly using the Direct Substitution Approach (DSA) as in [16, 17, 106]. This method consists in replacing the concentrations of the secondary species involved in the mass conversation laws (Eq. (2.6.1)-Eq. (2.6.2)) by a function depending on the concentrations of the primary species using mass action laws:

$$c_\alpha^j \overset{\text{def}}{=\!=} \mathbb{C}_\alpha^j(\mathbf{c_p}) \, , \, j \in I_{sm} \cup I_{si}. \tag{3.2.1}$$

$\mathbf{c_p}$ is defined as a vector composed of primary species concentrations: $\mathbf{c_p} = (c_\alpha^i) \, , \, i \in I_p$. The DSA has the advantage of reducing the number of unknowns thus easing the solution of the fully coupled problem.

The sequential strategy is summarised in Figure 3.1 where a schematic of the algorithm is included.

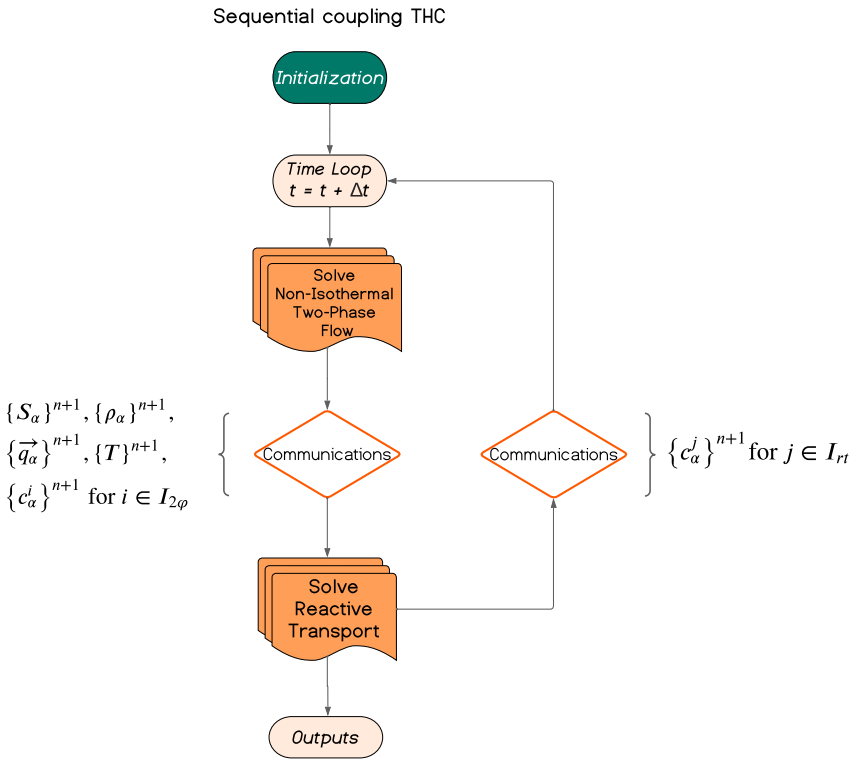

Figure 3.1: Coupling algorithm between compositional nonisothermal two-phase flow and reactive transport modules.

For further details, the reader is referred to [15] where a similar strategy has been considered for the treatment of isothermal reactive multiphase flows. Using the following notation:

$$(\square)^{n+1} = \square(x, t^{n+1}), \tag{3.2.2}$$

the semi-discretisation in time of the sequential model writes:

- Nonisothermal compositional two-phase flow:

$$\begin{aligned}
&\phi\,\frac{(S_l c_l^i)^{n+1}-(S_l c_l^i)^n}{\Delta t^n}+\phi\,\frac{(S_g \mathbb{C}_g^{\bar{i}}(\mathbf{c_p}))^{n+1}-(S_g \mathbb{C}_g^{\bar{i}}(\mathbf{c_p}))^n}{\Delta t^n}\\
&+L_l((c_l^i)^{n+1})+L_g((\mathbb{C}_g^{\bar{i}}(\mathbf{c_p}))^{n+1})\\
&=-\sum_{j\in I_{sm}\setminus I_{2\varphi}}\phi\,\nu_{ji}\,\frac{(S_\alpha \mathbb{C}_\alpha^j(\mathbf{c_p}))^n-(S_\alpha \mathbb{C}_\alpha^j(\mathbf{c_p}))^{n-1}}{\Delta t^{n-1}}\\
&-\sum_{j\in I_s\setminus I_{sm}}\phi\,\nu_{ji}\frac{(\mathbb{C}_s^j(\mathbf{c_p}))^n-(\mathbb{C}_s^j(\mathbf{c_p}))^{n-1}}{\Delta t^{n-1}}\\
&-\sum_{j\in I_{sm}\setminus I_{2\varphi}}\nu_{ji}\,L_\alpha((\mathbb{C}_\alpha^j(\mathbf{c_p}))^n),\quad i\in I_p\cap I_{2\varphi},
\end{aligned}\tag{3.2.3}$$

$$\begin{aligned}
&\phi\sum_\alpha\frac{(\rho_\alpha u_\alpha S_\alpha)^{n+1}-(\rho_\alpha u_\alpha S_\alpha)^n}{\Delta t^n}+(1-\phi)\rho_s c_h\frac{(T)^{n+1}-(T)^n}{\Delta t^n}\\
&+\nabla.\left(-\lambda_{pm}(\nabla T)^{n+1}+\sum_\alpha(\rho_\alpha h_\alpha\overrightarrow{q_\alpha})^{n+1}\right)=0.
\end{aligned}\tag{3.2.4}$$

Eq. (3.2.3) corresponds to Eq. (2.6.1) for the species present in the liquid and gas phases, where i and $\bar{i}$ represent the species in the liquid and gas phases, respectively, that are in chemical equilibrium (for instance if $i=\mathrm{CO}_{2(l)}$, $\bar{i}=\mathrm{CO}_{2(g)}$). The terms in the right-hand side of Eq. (3.2.3), corresponding to the contribution of the secondary species, are treated explicitly. Eq. (3.2.4) corresponds to the energy balance equation.

- Reactive transport problem:

$$\begin{aligned}
&\phi\,\frac{(S_\alpha c_\alpha^i)^{n+1}-(S_\alpha c_\alpha^i)^n}{\Delta t^n}+\sum_{j\in I_{sm}}\phi\,\nu_{ji}\,\frac{(S_\alpha \mathbb{C}_\alpha^j(\mathbf{c_p}))^{n+1}-(S_\alpha \mathbb{C}_\alpha^j(\mathbf{c_p}))^n}{\Delta t^n}\\
&+\sum_{j\in I_s\setminus I_{sm}}\phi\,\nu_{ji}\frac{(\mathbb{C}_s^j(\mathbf{c_p}))^{n+1}-(\mathbb{C}_s^j(\mathbf{c_p}))^n}{\Delta t^n}\\
&+L_\alpha((\mathbb{C}_\alpha^j(\mathbf{c_p}))^{n+1})+\sum_{j\in I_{sm}}\nu_{ji}L_l((\mathbb{C}_\alpha^j(\mathbf{c_p}))^{n+1})=0,\quad i\in I_{pm}\cap I_{rt},
\end{aligned}\tag{3.2.5}$$

$$\frac{(c_s^i)^{n+1}-(c_s^i)^n}{\Delta t^n}+\sum_{j\in I_{si}}\nu_{ji}\,\frac{(\mathbb{C}_s^j(\mathbf{c_p}))^{n+1}-(\mathbb{C}_s^j(\mathbf{c_p}))^n}{\Delta t^n}=0,\quad i\in I_{pi}\cap I_{rt},\tag{3.2.6}$$

$$\min\left((c_s^j)^{n+1},\,1-K_j(T^{n+1})\prod_{i\in I_p}\left((a_\alpha^i)^{\nu_{ji}}\right)\right)^{n+1}=0\,,\ j\in I_{se}\cap I_{rt}.\tag{3.2.7}$$

$$\frac{(c_s^j)^{n+1}-(c_s^j)^n}{\Delta t^n}=-K_j^s\left(T^{n+1}\right)A_j^s\left(1-K_j(T^{n+1})\prod_{i\in I_p}\left((a_\alpha^i)^{\nu_{ji}}\right)\right)^{n+1},\ j\in I_{sk}\cap I_{rt}.\tag{3.2.8}$$

Eq. (3.2.5) corresponds to the equation Eq. (2.6.1) for the primary species present in only one phase. The subsystem of Eq. (3.2.5) - Eq. (3.2.8) will explicitly provide to the subsystem Eq. (3.2.3) - Eq. (3.2.4) the contribution

of the species $j \in I_{rt}$ as well as a possible update of the porosity thanks to the calculation of the mineral concentrations.

Some boundary and initial conditions must be prescribed for each subproblem in order to close the system of PDEs.

3.2.2 Global implicit approach

On the other hand, the choice of solution method can be based on the global implicit approach, which consists of solving a global monolithic system as a large matrix at each iteration in time, leading to higher nonlinearities. However, this makes the problem more difficult for large chemical systems. This part describes the fully coupled, fully implicit solution of the system of PDEs Eq. (2.6.1)-Eq. (2.6.6). Using the same notations and a direct substitution approach as previously in Section 3.2.1, the set of equations semi-discretised in time for the fully coupled fully implicit approach can be written as follows:

- Compositional nonisothermal reactive two-phase flow:

$$\phi\frac{(S_\alpha c_\alpha^i)^{n+1} - (S_\alpha c_\alpha^i)^n}{\Delta t^n} + \sum_{j\in I_{sm}} \phi\nu_{ji}\frac{(S_\alpha \mathbb{C}_\alpha^j(\mathbf{c_p}))^{n+1} - (S_\alpha \mathbb{C}_\alpha^j(\mathbf{c_p}))^n}{\Delta t^n}$$
$$+ \sum_{j\in I_s\setminus I_{sm}} \nu_{ji}\frac{(\mathbb{C}_\alpha^j(\mathbf{c_p}))^{n+1} - (\mathbb{C}_\alpha^j(\mathbf{c_p}))^n}{\Delta t^n} + L_l((c_l^i)^{n+1}) + L_g((\mathbb{C}_g^{\bar{i}}(\mathbf{c_p}))^{n+1})$$
$$+ \sum_{j\in I_{sm}} \nu_{ji} L_\alpha((\mathbb{C}_\alpha^j(\mathbf{c_p}))^n) = 0, \quad i \in I_{pm} \tag{3.2.9}$$

$$\frac{(c_s^i)^{n+1} - (c_s^i)^n}{\Delta t^n} + \sum_{j\in I_{si}} \nu_{ji}\frac{(\mathbb{C}_s^j(\mathbf{c_p}))^{n+1} - (\mathbb{C}_s^j(\mathbf{c_p}))^n}{\Delta t^n} = 0, \quad i \in I_{pi}, \tag{3.2.10}$$

$$\phi\sum_\alpha \frac{(\rho_\alpha u_\alpha S_\alpha)^{n+1} - (\rho_\alpha u_\alpha S_\alpha)^n}{\Delta t^n} + (1-\phi)\rho_s c_h \frac{(T)^{n+1} - (T)^n}{\Delta t^n}$$
$$+ \nabla.\left(-\lambda_{pm}(\nabla T)^{n+1} + \sum_\alpha (\rho_\alpha h_\alpha \overrightarrow{q_\alpha})^{n+1}\right) = 0, \tag{3.2.11}$$

$$\min\left((c_s^j)^{n+1},\ 1 - K_j((T)^{n+1}) \prod_{i\in I_p}\left((a_\alpha^i)^{\nu_{ji}}\right)\right)^{n+1} = 0\ ,\ j \in I_{se}, \tag{3.2.12}$$

$$\frac{(c_s^j)^{n+1} - (c_s^j)^n}{\Delta t^n} = -K_j^s\left((T)^{n+1}\right) A_j^s \left(1 - K_j(T^{n+1}) \prod_{i\in I_p}\left((a_\alpha^i)^{\nu_{ji}}\right)\right)^{n+1}, j \in I_{sk}. \tag{3.2.13}$$

In both approaches, a logarithmic formulation is used in the chemical system to ensure that concentrations are positive. Boundary and initial conditions must be specified to close the latter two systems.

3.3 Numerical schemes

In order to implement a model in a numerical environment, it is necessary to provide a numerical scheme that is suitable for approximating the desired model. This section deals with the time discretisation to be applied to the numerical scheme, and the full numerical scheme is only provided here for the fully coupled fully implicit approach.

3.3.1 Time discretisation

For the implicit method, the time discretisation is achieved by an implicit Euler scheme or a second-order backward differential formula to increase the efficiency and stability of the scheme since the latter has advantages over the former in cases where the convective dissolution arises from a fingering instability at the moving CO_2 groundwater interface. In the latter case, the previous time differential term is replaced by the approximation described in [154] for variable time step strategies:

$$\frac{\partial \square}{\partial t} = \beta_1 \square^{n+1} + \beta_0 \square^{n} + \beta_{-1} \square^{n-1}, \tag{3.3.1}$$

with:

- $\Delta t^n = t^{n+1} - t^n$,
- $\beta_1 = \frac{1}{\Delta t^n}\left(1 + \frac{\Delta t^n}{\Delta t^n + \Delta t^{n-1}}\right)$,
- $\beta_{-1} = \frac{1}{\Delta t^{n-1}}\left(\frac{\Delta t^n}{\Delta t^n + \Delta t^{n-1}}\right)$,
- $\beta_0 = (\beta_1 + \beta_{-1})$.

Particularly, for the first time step, namely $n = 1$, the first-order implicit Euler scheme is employed. For a fixed time step strategy, the latter formula Eq. (3.3.1) can be simplified and written down as:

$$\frac{\partial \square}{\partial t} = \frac{3\square^{n+1} - 4\square^{n} + \square^{n-1}}{2\Delta t^n} \tag{3.3.2}$$

For the sequential approach, the first-order implicit Euler scheme is performed to compute a backward differentiation of the storage term:

$$\frac{\partial \square}{\partial t} = \frac{\square^{n+1} - \square^{n}}{\Delta t^n}. \tag{3.3.3}$$

3.3.2 Fully coupled fully implicit finite volume scheme

When considering flow problems, it is well known that finite volume (FV) schemes are efficient for discretising this type of problem because they provide mass conservative properties by construction. More specifically, a cell-centered FV scheme is implemented here, which consists of integrating the equations of the problem on a control volume and computing the fluxes at the interface of two adjacent volumes. Firstly, a notation is introduced that allows formulating the finite volume discretisation which is directly correlated from Eq. (3.2.2):

$$\{\square\}_k^{n+1} = \frac{1}{|V_k|}\int_{V_k} (\square)^{n+1}\, dV, \tag{3.3.4}$$

where V_k denotes the volume control containing the cell center k. $V(k)$ stands for the set of adjacent elements of V_k, γ_{kl} is the interface between two neighbouring volumes V_k and V_l and $\vec{n}_{kl}$ is the unit outer normal to the interface γ_{kl}. Thus, the finite volume scheme for the fully coupled fully implicit approach, defined by the set of Eq. (3.2.9) to Eq. (3.2.13), is given as:

$$\begin{aligned}
&\frac{|V_k|}{\Delta t^n}\left(\beta_1\left\{\phi S_\alpha c_\alpha^i\right\}_k^{n+1} + \beta_0\left\{\phi S_\alpha c_\alpha^i\right\}_k^{n} + \beta_{-1}\left\{\phi S_\alpha c_\alpha^i\right\}_k^{n-1}\right)\\
&+\sum_{j\in I_{sm}} \nu_{ji}\frac{|V_k|}{\Delta t^n}\left(\beta_1\left\{\phi S_\alpha \mathbb{C}_\alpha^j(\mathbf{c_p})\right\}_k^{n+1} + \beta_0\left\{\phi S_\alpha \mathbb{C}_\alpha^j(\mathbf{c_p})\right\}_k^{n} + \beta_{-1}\left\{\phi S_\alpha \mathbb{C}_\alpha^j(\mathbf{c_p})\right\}_k^{n-1}\right)\\
&+\sum_{j\in I_s\setminus I_{sm}} \nu_{ji}\frac{|V_k|}{\Delta t^n}\left(\beta_1\left\{\mathbb{C}_s^j(\mathbf{c_p})\right\}_k^{n+1} + \beta_0\left\{\mathbb{C}_s^j(\mathbf{c_p})\right\}_k^{n} + \beta_{-1}\left\{\mathbb{C}_s^j(\mathbf{c_p})\right\}_k^{n-1}\right)\\
&+\sum_{l|V_k\cap V_l\neq\emptyset} |\gamma_{kl}|\left(\left\{c_\alpha^i\right\}_{kl}^{n+1}\{\vec{q}_\alpha\}_{kl}^{n+1} - \{D_\alpha\}_{kl}^{n+1,har}\left\{\nabla c_\alpha^i\right\}_{kl}^{n+1}\right)\cdot\vec{n}_{kl}\\
&+\sum_{j\in I_{sm}}\nu_{ji}\sum_{l|V_k\cap V_l\neq\emptyset} |\gamma_{kl}|\left(\left\{\mathbb{C}_\alpha^j(\mathbf{c_p})\right\}_{kl}^{n+1}\{\vec{q}_\alpha\}_{kl}^{n+1} - \{D_\alpha\}_{kl}^{n+1,har}\left\{\nabla \mathbb{C}_\alpha^j(\mathbf{c_p})\right\}_{kl}^{n+1}\right)\cdot\vec{n}_{kl} = 0\,,\ i\in I_{pm},
\end{aligned} \tag{3.3.5}$$

$$\begin{aligned}
&\frac{|V_k|}{\Delta t^n}\left(\beta_1\left\{c_s^i\right\}_k^{n+1} + \beta_0\left\{c_s^i\right\}_k^{n} + \beta_{-1}\left\{c_s^i\right\}_k^{n-1}\right)\\
&+\sum_{j\in I_{si}} \nu_{ji}\frac{|V_k|}{\Delta t^n}\left(\beta_1\left\{\mathbb{C}_s^j(\mathbf{c_p})\right\}_k^{n+1} + \beta_0\left\{\mathbb{C}_s^j(\mathbf{c_p})\right\}_k^{n} + \beta_{-1}\left\{\mathbb{C}_s^j(\mathbf{c_p})\right\}_k^{n-1}\right) = 0\,,\ i\in I_{pi},
\end{aligned} \tag{3.3.6}$$

$$\begin{aligned}
&\frac{|V_k|}{\Delta t^n}\left(\beta_1\sum_\alpha\left\{\phi\rho_\alpha u_\alpha S_\alpha\right\}_k^{n+1} + \beta_0\sum_\alpha\left\{\phi\rho_\alpha u_\alpha S_\alpha\right\}_k^{n} + \beta_{-1}\sum_\alpha\left\{\phi\rho_\alpha u_\alpha S_\alpha\right\}_k^{n-1}\right)\\
&+\frac{|V_k|}{\Delta t^n}\left(\beta_1\left\{(1-\phi)\rho_s c_h T\right\}_k^{n+1} + \beta_0\left\{(1-\phi)\rho_s c_h T\right\}_k^{n} + \beta_{-1}\left\{(1-\phi)\rho_s c_h T\right\}_k^{n-1}\right)\\
&+\sum_{l|V_k\cap V_l\neq\emptyset}|\gamma_{kl}|\left(-\left\{\lambda_{pm}\right\}_{kl}^{n+1,har}\left\{\nabla T\right\}_{kl}^{n+1} + \sum_\alpha\left\{\rho_\alpha h_\alpha\right\}_{kl}^{n+1}\left\{\vec{q}_\alpha\right\}_{kl}^{n+1}\right)\cdot\vec{n}_{kl} = 0\,,
\end{aligned} \tag{3.3.7}$$

$$\min\left(\left\{c_s^j\right\}_k^{n+1}, 1 - K_j(T^{n+1}) \prod_{i\in I_p}\left\{\left(a_\alpha^i\right)^{\nu_{ji}}\right\}_k^{n+1}\right) = 0\,,\ j \in I_{se}, \tag{3.3.8}$$

$$\left\{c_s^j\right\}_k^{n+1} = \left\{c_s^j\right\}_k^{n} - \Delta t^n K_j^s(T^{n+1}) A_j^s\left(1 - K_j(T^{n+1}) \prod_{i\in I_p}\left\{(a_\alpha^i)^{\nu_{ji}}\right\}_k^{n+1}\right),\ j \in I_{sk}. \tag{3.3.9}$$

Finally, Darcy-Muskat's velocity is discretized:

$$\left\{\vec{q}_\alpha\right\}_{kl}^{n+1} = -\left\{\mathbb{K}\right\}_{kl}^{har}\left\{\frac{k_{r\alpha}(S_\alpha)}{\mu_\alpha}\right\}_{kl}^{n+1,up}\left(\left\{\nabla P_\alpha\right\}_{kl}^{n+1} - \left\{\rho_\alpha^{mass}\right\}_{kl}^{n+1,ari}\vec{g}\right).$$

The convective flux terms are approximated by using a fully upwinding scheme, thus unknown quantities (S_α, P_α, c_α^i, $k_{r\alpha}$ and h_α) are evaluated implicitly and upstream at the interface γ_{kl} depending on the velocity of the phase $\{\vec{q}_\alpha\}$:

$$\{\ \cdot\ \}_{kl}^{n+1,up} = \begin{cases} \{\ \cdot\ \}_k^{n+1} & \text{if} \quad \{\vec{q}_\alpha\}_{kl}^{n+1}\cdot\vec{n}_{kl} > 0, \\ \{\ \cdot\ \}_l^{n+1} & \text{else.} \end{cases}$$

The discrete gradients are computed by using either the Two-Point Flux Approximation (TPFA)[76] or Multiple Point Flux Approximation (MPFA) [8] depending on the complexity of the mesh. The TPFA has been widely used in reservoir simulators for the petroleum industry. Nonetheless, this scheme presents some limitations on the type of mesh that can be used since it requires strict K-orthogonality. Figure 3.2 presents two types of structured or unstructured meshes where TPFA is applicable. For more details on its implementation and the expression of transmissibilities, see [7].

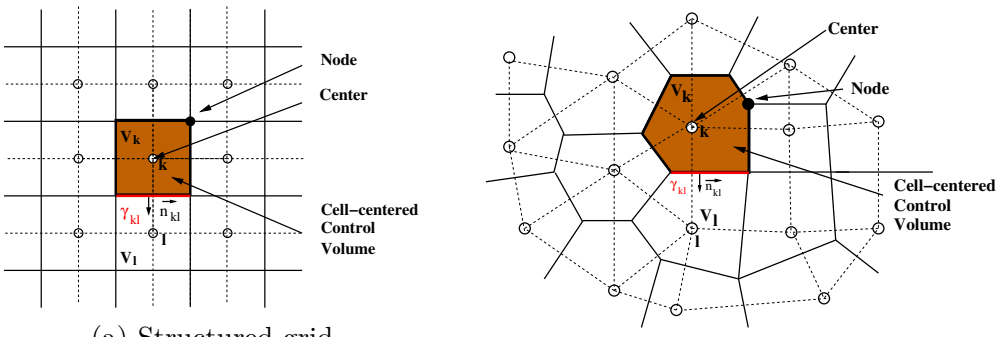

(a) Structured grid

(b) Unstructured grid

Figure 3.2: Admissible grids for using Two-Point Flux Approximation method in a cell-centered FV scheme.

For more general meshes, the Multiple-Point Flux Approximation O-method (later, simply called MPFA) [8] or the more recently developed nonlinear two-point flow approximation (NLTPFA) [179] can be used. The MPFA method increases the accuracy of the solution, particularly in the case of non-orthogonal grids or anisotropy

that require a consistent flux stencil [68, 100, 148]. Different average methods are used to calculate some quantities between two neighbouring elements, for example, a harmonic average is used for $\left\{\mathbb{K}\right\}_{kl}^{har}$, $\left\{D_\alpha\right\}_{kl}^{n+1,har}$, $\left\{\lambda_{pm}\right\}_{kl}^{har}$ and an arithmetic average is used for $\left\{\rho_\alpha^{mass}\right\}_{kl}^{n+1,ari}$.

Boundary and initial conditions complete the finite volume discretisation of the system Eq. (3.3.5) to Eq. (3.3.9). It leads to a set of strongly nonlinear equations.

The discretisation for the sequential scheme is mainly based on the same ideas as those presented for the fully implicit approach. As a consequence, this discretisation is not detailed here. The next section is dedicated to the numerical implementation of our fully implicit and sequential strategies in the simulation platform *DuMu*^{X} [119] and their validation through several CO_2 storage scenarios.

3.4 Implementation

3.4.1 *DuMu*^{X} numerical simulation platform

All the numerical developments have been implemented in *DuMu*^{X} [119], which is an open-source code developed at the University of Stuttgart, since 2007 for academic research purposes. This environment provides many numerical tools for solving PDEs, mainly related to porous media, but also allows, mesh management, discretisation, or linear and nonlinear solvers. This ability to solve PDEs is related to the fact that *DuMu*^{X} is based on the *DUNE* (Distributed and Unified Numerical Environment) library [28]. The latter is a modular toolbox for solving PDEs by finite volumes, finite elements, or finite differences methods. *DuMu*^{X} is written in *C++* to benefit from the strengths of object-oriented languages. However, the modular structure of the platform facilitates the integration of new modules, which is convenient for studying specific phenomena involved in porous media. It offers a unified environment that allows the implementation of multiple formulations while ensuring the same conditions for discretisation, physics, and linear and nonlinear solvers.

To deal with the high nonlinearities induced by the system of equations, a Newton-Raphson method is set up. For the assembly of the Jacobian matrix, a general assembler implementation is provided, in which the matrix entries are computed by numerical differentiation. The linear systems are solved thanks to an iterative linear solver, the BiConjugate Gradient STABilized (BiCGSTAB) method [26], preconditioned by an Algebraic Multigrid (AMG) solver [29]. For both nonlinear and linear solvers, a fixed tolerance must be entered by the user. An adaptive time step strategy is also supplied by the platform, which consists of evolving the value of the time step according to the number of Newton iterations of the previous time step. If the number of iterations exceeds a given threshold, the time step is decreased while it is increased if the Newton algorithm converges in fewer iterations. In addition, the simulation platform *DuMu*^{X} has been written to be highly scalable, providing high parallel efficiency and allowing simulations with several millions of degrees of freedom to be carried out, ideal for large-scale field applications. Parallel computations are possible thanks to the DUNE [28] parallel library package

based on message passing interface (MPI) communications. Consequently, *DuMu*^{X} has the ability to run on anything from single processor systems to highly parallel supercomputers with specialised hardware architectures.

Regarding the numerical strategy, two different modules have been developed to solve the CO_2 storage model with both fully coupled fully implicit and sequential approaches, described respectively by systems Eq. (3.2.9) to Eq. (3.2.13) and Eq. (3.2.3) to Eq. (3.2.8). The modularity of *DuMu*^{X} facilitated the implementation of both approaches in the same numerical environment. This allowed comparisons to be made between the two approaches to get an idea of the accuracy and performance achieved in each. Specifically, the time discretisation has been upgraded from a first-order implicit Euler scheme to a second-order method to improve the accuracy of our scheme. In particular, the second-order backward differentiation formula (BDF2) has allowed to solve convergence issues when dealing with convective dissolution tests, which are not presented here.

Initially, in [16, 17, 106], several sequential and implicit numerical strategies, were developed in previous versions of *DuMu*^{X} to deal with hydro-chemical coupling applied to CO_2 storage in saline aquifers. In this work, an extension of both sequential and implicit approaches to consider nonisothermal flow is proposed. A dependence of the temperature is taken into account in the constitutive relations (see Section 2.8) and an energy conservation law is added to the original system composed of PDEs governing the mass balance equations and differential-algebraic equations modelling the chemical reactions. In addition, the chemical system also has to be temperature dependent because reaction rates may vary as a function of temperature. Therefore, interpolation methods of chemical database values ([1]), as well as Arrhenius law (Eq. (2.3.11)) have been implemented to supply a temperature dependence in the chemical framework.

The following section presents all the numerical studies to illustrate and validate the modelling approach.

3.5 Numerical simulations of CO_2 storage scenarios

In this section, the numerical results for modelling different scenarios of THC processes for CO_2 storage in saline aquifers are presented. To validate the strategy, three test cases of increasing difficulty, involving nonisothermal two-phase flow coupled with reactive transport are presented. First, in Section 3.5.1, the approach is validated by solving a 1D radial test case. The work is then extended to 2 and 3D cases to increase the complexity and to test the competitiveness of the code on large problems with grids of millions of unknowns, where the use of high-performance computing becomes crucial. The 2D results are further developed in Section 3.5.2, where the treatment of a 2D layered formation from [179] is investigated. The extension to THC coupling is given on a non-orthogonal mesh, necessitating the use of a multi-point flux approximation. Finally, the last case focuses on a realistic 3D problem. Consequently, Section 3.5.3 presents the numerical results for the benchmark problem based on the Johansen CO_2 storage operation [54]. All test cases show that the implemented strategies are suitable to simulate coupled nonisother-

mal multiphase flow and reactive transport problems. To ensure the reproducibility of the results of the presented tests, particular care has been taken to provide all necessary data including discretisation and solvers parameters.

3.5.1 Test case 1: 1D radial problem

3.5.1.1 Problem configuration

The first test case deals with a 1D radial problem originally proposed by [229]. In this work, the authors consider a fully coupled strategy to model Thermal-Hydro-Mechanical-Chemical processes for CO_2 geological sequestration. Here, we neglect the mechanical effects and focus only on Thermal-Hydro-Chemical processes. A homogeneous aquifer with a length of 10 km and a height of 100 m is considered. A schematic of the problem is proposed in Figure 3.3. The injection is set up with a well located on the left part of the domain at a rate of 90 $kg.s^{-1}$ over 10 years. The initial aquifer temperature is set at 348.15 K, while the injection temperature is cooler at 305.15 K to inject CO_2 in its supercritical form. The low-temperature injection is expected to dissolve more supercritical CO_2 into the aqueous phase, which may enhance solubility trapping of supercritical CO_2 and prevent damage near the injection area. All the data needed to run the simulations can be found in Table 3.1.

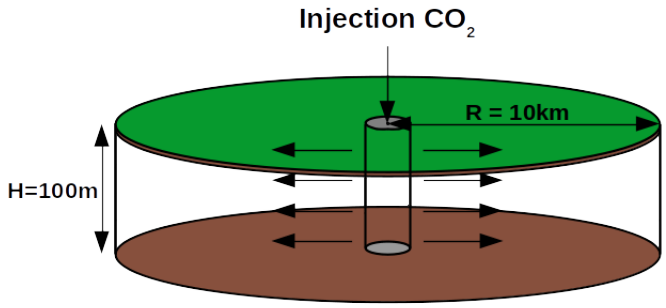

Figure 3.3: Schematic diagram of the 1D test case proposed in [229].

In [229], the authors considered three different runs of increasing complexity with different initial compositions. This case focuses on the second run, which deals with the eight chemical reactions described in Table 3.2. The first reaction expresses the dissolution of gaseous CO_2 in the liquid phase at equilibrium. Once dissolved in the liquid phase, CO_2 reacts with the resident H_2O to form bicarbonate HCO_3^- and hydrogen H^+ ions. These two ions then initiate further reactions. Thus, six aqueous complexation reactions are considered in equilibrium. The final chemical reaction describes a precipitation/dissolution reaction involving solid calcite, which is also considered at equilibrium. Calcite initially represents a volume fraction (VF) of 5 % of the rock and the remaining 95 % of the rock is inert.

Constitutive law or variable	Symbol	Parameters	Unit
Formation radius	R	10000	[m]
Formation height	H	100	[m]
Porosity	ϕ	0.3	[-]
Permeability	$\mathbb{K}$	10^{-13}	[m^2]
Initial Pressure	P_{init}	2×10^7	[Pa]
Initial Temperature	T_{init}	348.15	[K]
Injection Temperature	T_{inj}	305.15	[K]
Injection Rate	Q_{inj}	90	[$kg.s^{-1}$]
Van Genuchten parameter	α	5.1×10^{-5}	[Pa^{-1}]
Van Genuchten parameter	m	0.457	[-]
Residual liquid saturation	S_{lr}	0.3	[-]
Residual gaseous saturation	S_{gr}	0.05	[-]
Solid Density	ρ_s	2000	[$kg.m^{-3}$]
Solid Thermal Conductivity	λ_s	2.5	[$W.(m.K)^{-1}$]
Solid Heat Capacity	c_h	1000	[$J.(kg.K)^{-1}$]
Longitudinal Dispersion	d_L	0	[m]
Transverse Dispersion	d_T	0	[m]
Liquid molecular diffusion	$D_{m,l}$	0	[$m^2.s^{-1}$]
Gaseous molecular diffusion	$D_{m,g}$	0	[$m^2.s^{-1}$]

Table 3.1: Simulation data of the 1D test case proposed in [229].

Reactions		
$CO_{2(g)}$	$\rightleftharpoons$	$CO_{2(l)}$
$OH^- + H^+$	$\rightleftharpoons$	H_2O
$CO_3^{2-} + H^+$	$\rightleftharpoons$	HCO_3^-
$CO_{2(l)} + H_2O$	$\rightleftharpoons$	$H^+ + HCO_3^-$
$CaCO_{3(l)} + H^+$	$\rightleftharpoons$	$Ca^{2+} + HCO_3^-$
$CaHCO_3^+$	$\rightleftharpoons$	$Ca^{2+} + HCO_3^-$
$CaOH^+ + H^+$	$\rightleftharpoons$	$Ca^{2+} + H_2O$
$CaCO_{3(s)} + H^+$	$\rightleftharpoons$	$Ca^{2+} + HCO_3^-$

Table 3.2: Chemical reactions involved in 1D test case developed in [229].

Primary species	Initial molality [$mol.kg^{-1}$]
$CO_{2(l)}$	3.67×10^{-7}
H^+	7.51×10^{-9}
Ca^{2+}	2.38×10^{-5}

Table 3.3: Initial conditions for primary species.

Finally, thanks to the Morel formalism [145], we have chosen to divide the species into primary and secondary species, such as:

$$I_p = \left\{H_2O,\, CO_{2(l)},\, H^+,\, Ca^{2+}\right\},$$
$$I_s = \left\{CO_{2(g)}, OH^-,\, CO_3^{2-},\, HCO_3^-,\, CaCO_{3(l)},\, CaHCO_3^+,\, CaOH^+,\, CaCO_{3(s)}\right\}.$$

The initial molalities of the primary species have been recalculated at equilibrium by a flash calculation and are given in Table 3.3. This calculation uses as input geochemical data available in the thermodynamic database Chess [1]. To close the problem, a Dirichlet boundary condition is placed on the right boundary at 10 km. This condition is set to initial values for pressure and concentrations. The injection is set with a Neumann boundary condition on the left boundary, with an injection rate of 90 kg.s^{-1} in the first cell. The initial time step and the maximum time step are set to 10^{-5} s and 10^{6} s, respectively. The tolerances for the Newton-Raphson and BICGSTAB methods are 10^{-6} and 10^{-8}, respectively. In this case, the Newton-Raphson method converges rapidly in fewer than 5 iterations on average.

3.5.1.2 Numerical results

First, to validate our implementation, a numerical convergence study is performed using several structured meshes composed of 2000, 1000, 500, 250, and 125 cells, resulting in cells ranging from 5 m to 80 m. The computations for this test case were all performed using the fully coupled fully implicit approach presented in Section 3.2.2.

Mesh convergence

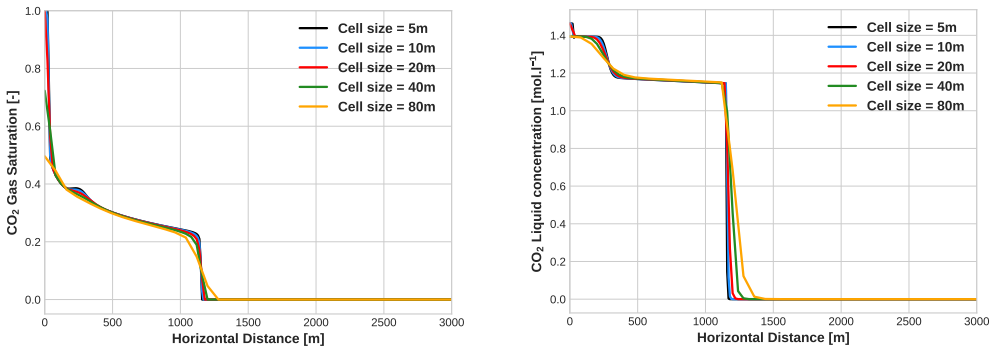

(a) Saturation of gaseous phase (b) Concentration of $CO_{2(l)}$

Figure 3.4: Mesh convergence for the saturation of the gaseous phase (a) and $CO_{2(l)}$ concentration (b) at 10 years.

The saturation profile (Figure 3.4 (a)) indicates that gaseous CO_2 completely saturates the near-well part of the domain. This phenomenon clearly depends on the mesh size since it is not observed for large cell sizes. However, the gaseous front of CO_2 can be located 1200 metres from the injection well. This gaseous CO_2 tends to dissolve into the resident brine, initially saturating the porous medium, which results in an increase in the liquid CO_2 concentration in the plume region of Figure 3.4 (b). The saturation and concentration fronts are very sharp and remarkably captured by the simulation. The injected CO_2 reacts with the brine to release H^+ ions, as observed with the decrease in pH in Figure 3.6 (a). These ions also activate the precipitation/dissolution reaction of calcite. Here, calcite is assumed to

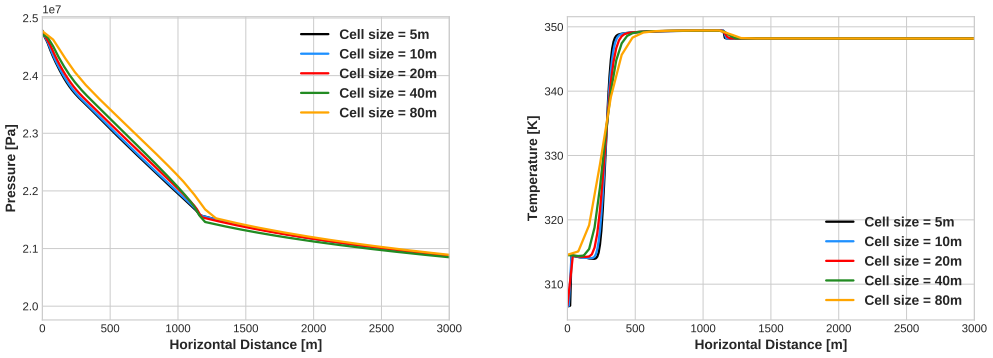

(a) Pressure of gaseous phase (b) Temperature

Figure 3.5: Mesh convergence for the pressure of the gaseous phase (a) and temperature profile (b) at 10 years.

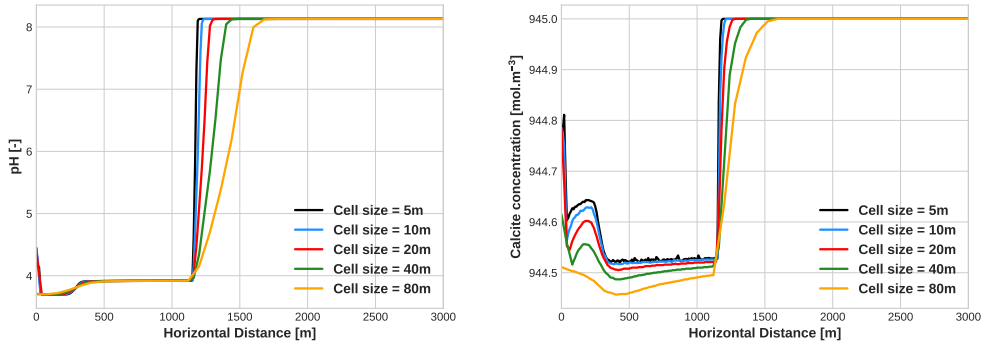

(a) pH (b) Concentration of Calcite

Figure 3.6: Mesh convergence for the pH (a) and concentration of calcite (b) profiles at 10 years.

be initially at equilibrium, and its dissolution occurs only in the CO_2 plume region (Figure 3.6 (b)). The temperature is modified only in the region close to the well. In fact, the heat transfer (Figure 3.5 (b)) appears to be driven by conduction more than convection. Consequently, only the near-well region is cooled by the low-temperature injection.

A mesh convergence analysis for several quantities is also presented in Figure 3.7. It shows the L^2-relative error between several variables and the reference solution (computed with the mesh of 2000 elements) as a function of the mesh size on the whole domain at $t = 10$ years. The discretisation schemes are essentially first-order schemes in space, which explains a convergence order close to one. The convergence of some quantities is degraded due to the complexity of the phenomena considered and their strong nonlinearity.

Isothermal and nonisothermal comparisons

To highlight the effects of temperature, comparisons have been made between

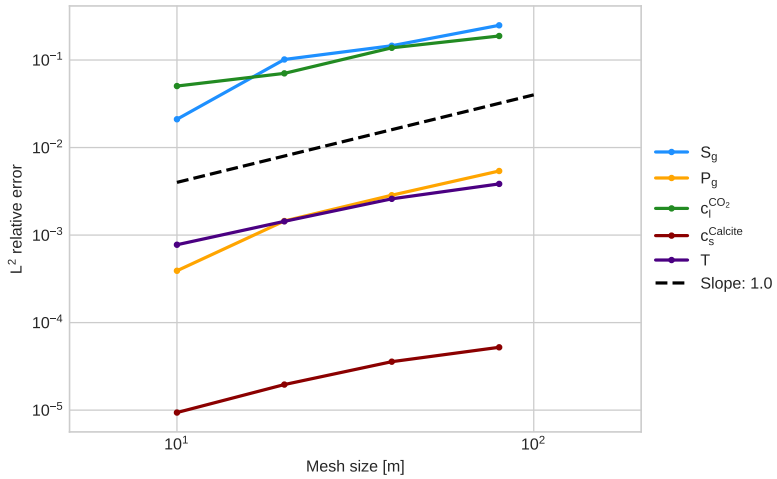

Figure 3.7: L^2-relative error for $CO_{2(l)}$ concentration, gas saturation, gas pressure, calcite, and temperature as a function of cell size.

isothermal and nonisothermal test cases. These comparisons were made on the same test case, using exactly the same data. The only difference is that the isothermal case was performed with an injection temperature equal to the aquifer temperature. Figure 3.8 to Figure 3.10 show the evolution over time of several quantities at 1, 3, 5 and 10 years for both isothermal and nonisothermal scenarios. In the figures below, solid curves represent nonisothermal runs and dashed curves represent isothermal runs.

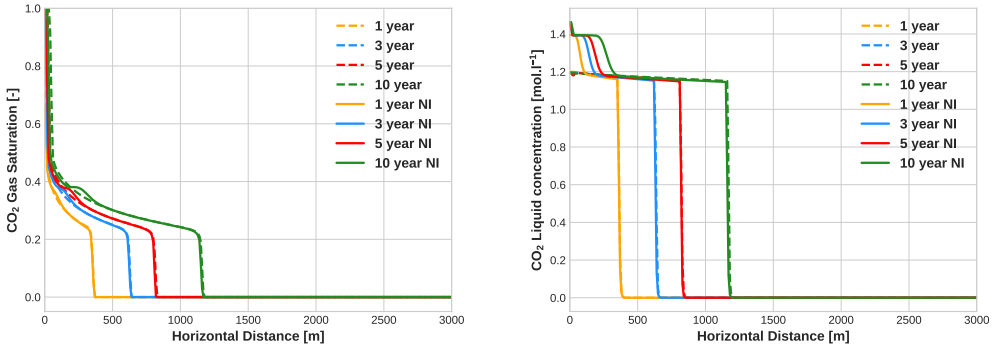

(a) Saturation of gaseous phase (b) Concentration of liquid CO_2

Figure 3.8: Evolution in time of concentration of liquid CO_2 and saturation of the gaseous phase for isothermal and nonisothermal cases.

As observed in [229], the front of the gas phase in Figure 3.8 (a) is at the same distance from the injection well even when the viscosity of the fluid is affected in the nonisothermal case. CO_2 dissolution occurs only where CO_2 and H_2O coexist. Figure 3.8 (b) shows the concentration of the liquid CO_2 and highlights a significant difference between the two cases. A 14 % increase in dissolved CO_2 is observed near the injection well in the nonisothermal configuration. Figure 3.9 (b) shows that the temperature profiles are only significantly affected near the well (up to

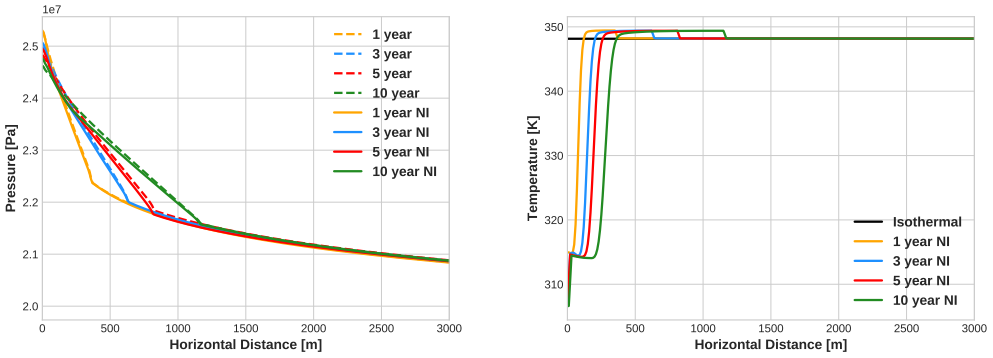

(a) Pressure of gaseous phase (b) Temperature profile

Figure 3.9: Evolution in time of gaseous phase pressure and temperature for isothermal and nonisothermal cases.

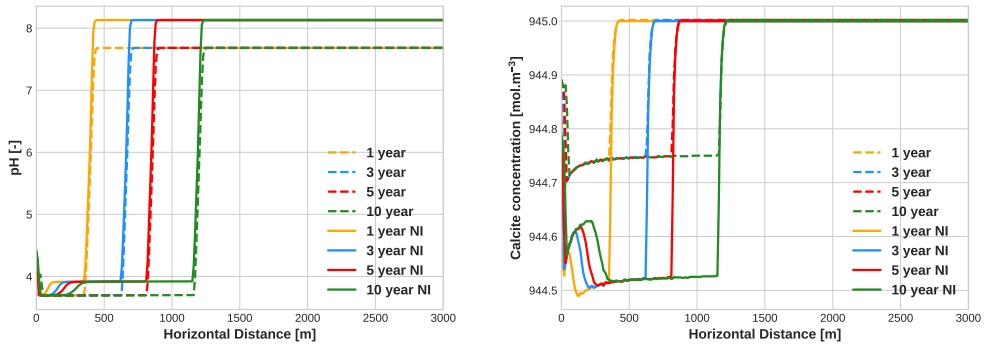

(a) pH (b) Concentration of Calcite

Figure 3.10: Evolution in time of pH and concentration of calcite for isothermal and nonisothermal cases.

250 m). A slight decrease can be observed between 0 and 250 m due to the Joule-Thompson effect. The temperature decreases due to the expansion of the gaseous CO_2 . In the same figure, it is possible to observe an increase in temperature at the front of the CO_2 plume, which expands with time. This phenomenon is caused by the dissolution of CO_2, which is an exothermic process. The pH and calcite concentration evolution are shown in Figure 3.10 (a) and (b). In both cases, the low-temperature injection significantly affects the chemical processes, particularly increasing the dissolution of calcite.

Thus, it can be concluded that the general trends of the system behaviour are in good agreement with the results obtained by [229]. More specifically, the same variations are observed between the isothermal and nonisothermal simulations as in [229]. The variations in pH and calcite concentration seem to be sensitive to temperature as well as to the concentration of liquid CO_2, which increases significantly for low-temperature injection. Therefore, the same conclusion as in [229] can be drawn about the thermal effects that have an important influence on the chemical process. As expected, low-temperature injection enhances the dissolution

of supercritical CO_2 and solubility trapping.

3.5.2 Test case 2: 2D layered problem

3.5.2.1 Problem configuration

The second case deals with a 2D problem originally proposed in [179]. Initially, this test considers only a hydraulic model for CO_2 geological sequestration. Therefore, to be consistent with the THC strategy, the thermal and chemical effects are extended. A stratified aquifer with different layers of permeability consists of a 200 m $\times$100 m area. A schematic of the problem is proposed in Figure 3.11. The domain is meshed with 11844 non-K orthogonal cells, making the use of the TPFA method inappropriate. Consequently, an MPFA method is performed to compute fluxes in the finite volume scheme.

The initial aquifer temperature is set at 283.15 K at the ground surface with a geothermal gradient of 30 °C/km. The upper surface of the domain is located at a depth of 1200 m underground. The gaseous CO_2 is injected at a cooler temperature of 293.15 K. The low-temperature injection is expected to dissolve more supercritical CO_2 into the aqueous phase, which may enhance the solubility trapping of supercritical CO_2 and avoid damage in the near-wellbore region. A hydrostatic pressure is prescribed initially with an atmospheric pressure of 1×10^5 Pa at the ground surface. Consequently, the initial liquid pressure is varying from 1.1×10^7 to 1.2×10^7 Pa from top to bottom. The injection is set up with a well located at the bottom left part of the domain at a rate of 0.003 kg.s^{-1} during 2×10^8 seconds ($\approx$ 6.3 years). This wellbore is perforated in the last 30 metres.

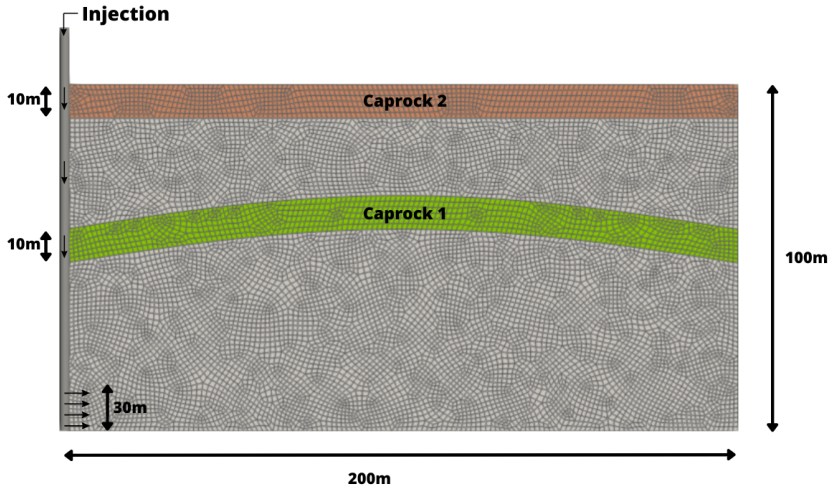

Figure 3.11: Schematic diagram of the 2D test case proposed in [179].

Two types of caprock are prescribed in the domain. The lower one describes a permeable layer that does not have a high permeability. It is defined as a 10 m thick layer located at 50 m height, and the curvature is given by the formula:

$$f(x,y) = h + t\, sin(\frac{\pi\, x}{L}),$$

where h, t and L denote respectively the height, the thickness, and the length of the domain. However, the upper one is highly impermeable and acts as a barrier preventing any leakage. Permeability and porosity layers are described in Table 3.4.

Parameter	Symbol	Aquifer	Caprock 1	Caprock 2	Unit
Porosity	ϕ	0.2	0.05	0.001	[-]
Permeability	$\mathbb{K}$	3×10^{-14}	10^{-15}	10^{-19}	[m^2]

Table 3.4: Data for the extension to THC coupled processes of the 2D test case proposed in [179].

All the data needed to run the simulations can be found in Table 3.5. For the diffusivity, the Millington-Quirk formula is used, while the thermal conductivity uses the Somerton model defined in [191].

Constitutive law or variable	Symbol	Parameters	Unit
Injection Temperature	T_{inj}	305.15	[K]
Injection Rate	Q_{inj}	0.003	[$kg.s^{-1}$]
Residual liquid saturation	S_{lr}	0.0	[-]
Residual gaseous saturation	S_{gr}	0.0	[-]
Brooks Corey parameter	P_e	1×10^4	[Pa^{-1}]
Brooks Corey parameter	λ	2.0	[-]
Solid Density	ρ_s	2500	[$kg.m^{-3}$]
Solid Thermal Conductivity	λ_s	2.5	[$W.(m.K)^{-1}$]
Solid Heat Capacity	c_h	1000	[$J.(kg.K)^{-1}$]
Longitudinal Dispersion	d_L	0	[m]
Transverse Dispersion	d_T	0	[m]
Liquid molecular diffusion	D_l	2×10^{-9}	[$m^2.s^{-1}$]
Gaseous molecular diffusion	D_g	Based on [218]	[$m^2.s^{-1}$]

Table 3.5: Simulation data of the 2D test case proposed in [179].

The chemical system considered in this test case is taken from [78]. It is composed of seven reactions, one aqueous dissolution, three aqueous complexation reactions at equilibrium, and three precipitation/dissolution reactions considered kinetic reactions. This geochemical system is highly simplified relative to real systems and does not represent the complexity of mineralization in an actual aquifer. All information on equilibrium constants, reactive constants, reactive surface area, and activation energies are given in Table 3.6 and Table 3.7.

Reactions			$\log_{10}(K_{j,ref})$
$CO_{2(g)}$	$\rightleftharpoons$	$CO_{2(l)}$	-
$OH^- + H^+$	$\rightleftharpoons$	H_2O	-13.26
$CO_3^{2-} + H^+$	$\rightleftharpoons$	HCO_3^-	-6.32
$CO_{2(l)} + H_2O$	$\rightleftharpoons$	$H^+ + HCO_3^-$	-10.23
Ano + 8 H^+	$\rightleftharpoons$	4 H_2O + Ca^{2+} + 2 Al^{3+} + 2 SiO_2	25.82
Cal + 2 H^+	$\rightleftharpoons$	$Ca^{2+} + H_2O + CO_{2(l)}$	1.6
Kao + 6 H^+	$\rightleftharpoons$	5 H_2O + 2 Al^{3+} + 2 SiO_2	6.82

Table 3.6: Chemical reactions involved in the 2D layered test case from [78].

Mineral	$\log_{10}(K^s_{j,ref})$	E^a	A_s [$m^2.m^{-3}$]	Init. conc. [$mol.m^{-3}$]
Anorthite	-12.0	67.830	88.0	87
Calcite	-8.8	41.870	88.0	238
Kaolinite	-13.0	62.760	17600	88

Table 3.7: Chemical information about mineral species involved in kinetics reactions.

Thanks to the Morel formalism [145], chemical species are divided into:

$$\begin{aligned} I_{pm} &= \left\{H_2O_{(l)}, CO_{2(l)}, H^+, Ca^{2+}, Al^{3+}, SiO_2\right\}, \\ I_{sm} &= \left\{H_2O_{(g)}, CO_{2(g)}, OH^-, CO_3^{2-}, HCO_3^-\right\}, \\ I_{sk} &= \{\text{Anorthite}, \text{Calcite}, \text{Kaolinite}\}, \end{aligned}$$

Initial mineral concentrations are given in Table 3.7, while Table 3.8 provides initial conditions for each primary species. To close the problem, impermeable Neumann boundary conditions are set at the left, lower and upper boundaries of the domain, while a Dirichlet boundary condition is prescribed at the right boundary equal to the initial values for pressure and concentrations.

Primary species	Initial molality [$mol.kg^{-1}$]
$CO_{2(l)}$	$3.55\times\ 10^{-3}$
H^+	$5.71\times\ 10^{-7}$
Ca^{2+}	$2.52\times\ 10^{-2}$
Al^{3+}	$3.13\times\ 10^{-12}$
SiO_2	$4.73\times\ 10^{-4}$

Table 3.8: Initial conditions for primary species.

The simulation is conducted over 2×10^8 s, the period during which CO_2 is injected into the formation. The initial time step is set to 10^{-2} s and the maximum time step is set to 10^6 s. The tolerances for the Newton-Raphson and BICGSTAB methods are 10^{-6} and 10^{-10} respectively.

3.5.2.2 Numerical results

This section presents the numerical results obtained for the extension of the case to the THC approach. The calculations have been performed exclusively with the fully coupled, fully implicit scheme using the DSA method explained previously. Figure 3.12 to Figure 3.14 show the evolution of results for different quantities of interest at one, two, and four years of injection.

The gas saturation presented in Figure 3.12 (a) shows that the CO_2 injected at the lower left boundary moves upwards due to buoyancy until the plume reaches the first caprock. This buoyancy phenomenon is due to the density difference between the gaseous CO_2 and the resident brine, which completely saturates the domain at the beginning. As shown at 2 years, the lower caprock tends to block the upward movement, but due to a permeability close to that of the aquifer, a small amount of CO_2 gas passes through this layer. Nevertheless, the major quantity of gaseous CO_2 moves laterally being trapped by the lower caprock. Finally, at 4 years, another accumulation zone appears at the top of the domain. The higher caprock acts as a real barrier, preventing the gas from moving higher in the domain. However, the velocity of the higher plume is lower than that of the other plume because it consists of only a small amount of CO_2 penetrating the first caprock. Figure 3.12 (b) represents the amount of CO_2 dissolved in the liquid phase. The same behaviour as for gas saturation is observed, but a single plume of dissolved CO_2 is captured. Figure 3.13 (a) and (b) show the overpressure due to injection and the temperature evolution, respectively. The main overpressure in the area is near the injection well. After 4 years, the pressure evolution shows that the greatest change is in the upper caprock. This justifies the need to monitor the integrity of the caprock as it appears to be the region that overcomes large pressure changes. As highlighted in the 1D case, temperature changes are also located in the vicinity of the injection well. Cooler injection temperature leads to a cooling region close to the wellbore. However, a warmer region, coinciding with the CO_2 plume appears, demonstrating the exothermic process of CO_2 dissolution.

For the chemical quantities of interest, the pH overcomes a decrease at the beginning of the simulation due to injection. In fact, the dissolution of gas causes an acidification of the medium which is observed in the region where the CO_2 liquid molar fraction is concentrated, ensuring a strong correlation between these two quantities Figure 3.14 (a). This activates mineral reactions in the region affected by the CO_2 plume. The calcite is dissolved in the domain as displayed in Figure 3.14 (b). The other two minerals are slightly affected in a short time due to kinetic chemical reactions. The anorthite also dissolves whereas the kaolinite precipitates in the CO_2 plume region. Finally, these various behaviours are confirmed in Figure 3.16, which shows the mineral evolution as a function of time over the whole domain. At the beginning of the simulation, when the minerals are not necessarily in equilibrium with the aqueous solution, an increase in the quantity of calcite is captured before the dissolution process occurs in the plume region. This dissolution appears to be much faster than other mineral changes where anorthite and kaolinite seem to have very slow changes.

This test demonstrates the ability of the THC module to operate with an MPFA

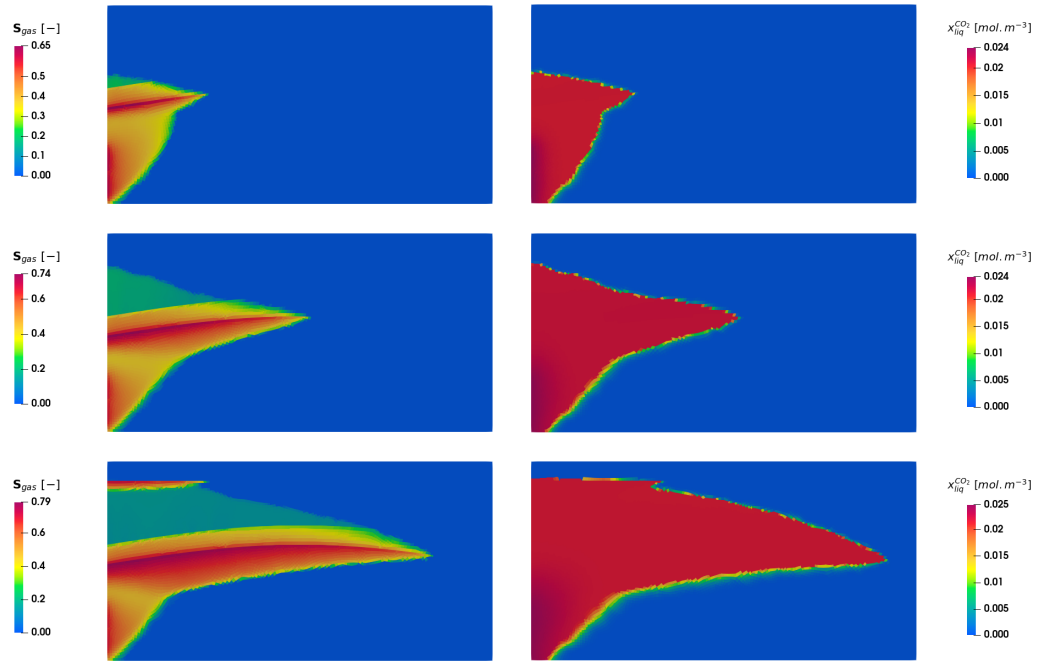

(a) (b)

Figure 3.12: Evolution of gaseous saturation and CO_2 liquid molar fraction at 1, 2 and 4 years from top to bottom.

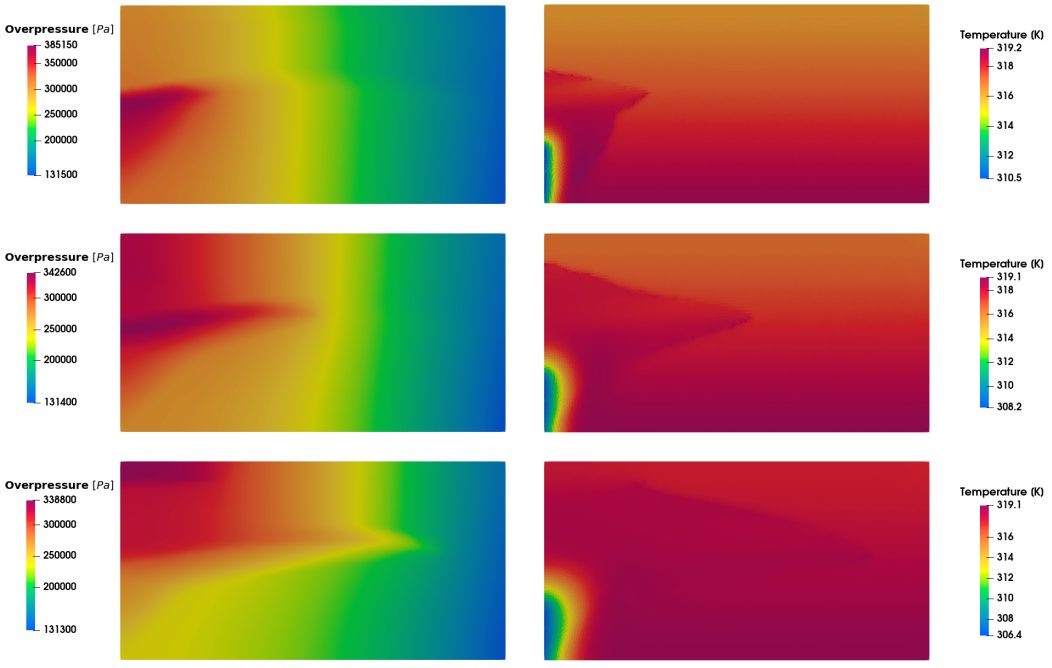

(a) (b)

Figure 3.13: Evolution of liquid overpressure and temperature at 1, 2, and 4 years from top to bottom.

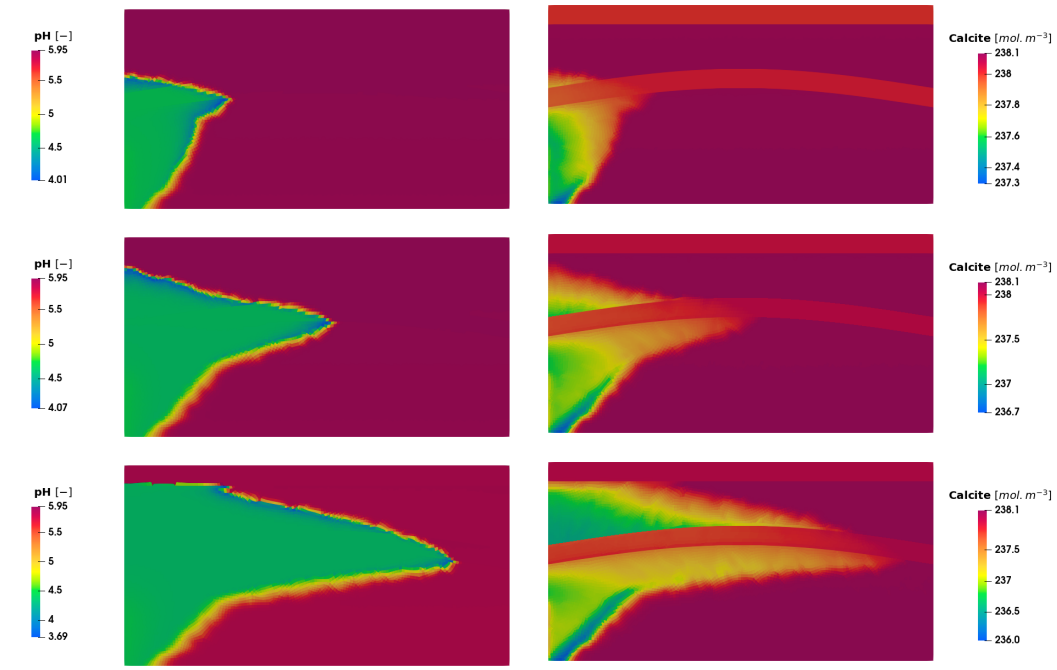

(a) (b)

Figure 3.14: Evolution of pH and calcite at 1, 2, and 4 years from top to bottom.

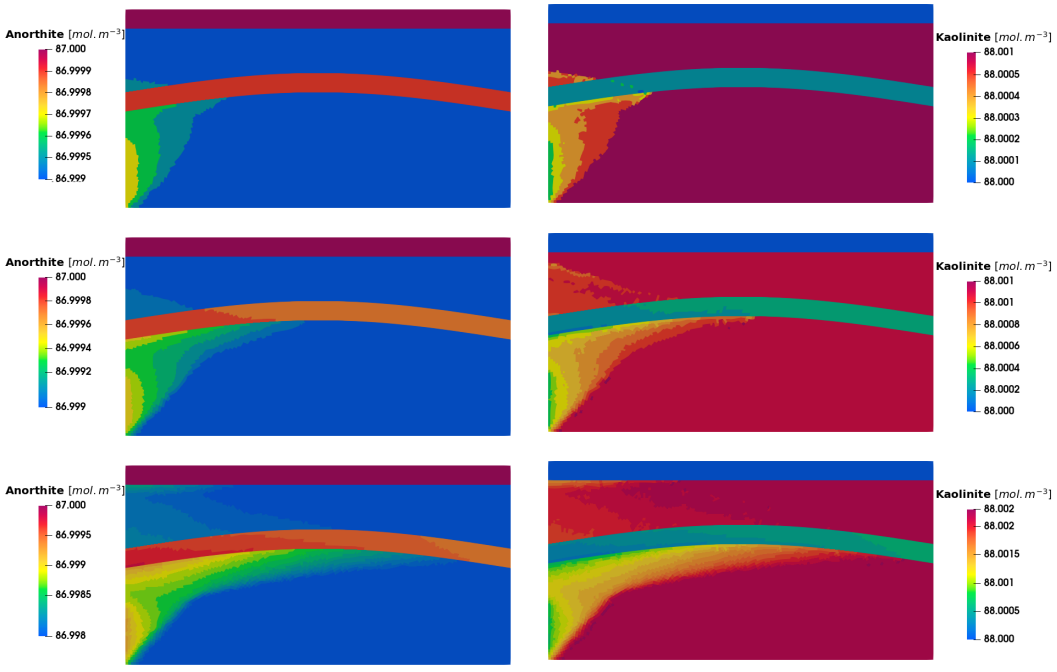

(a) (b)

Figure 3.15: Evolution of anorthite and kaolinite at 1, 2, and 4 years from top to bottom.

method. It improves the accuracy with such a mesh configuration, although the computation time is affected due to a greater sparsity pattern in the matrices of

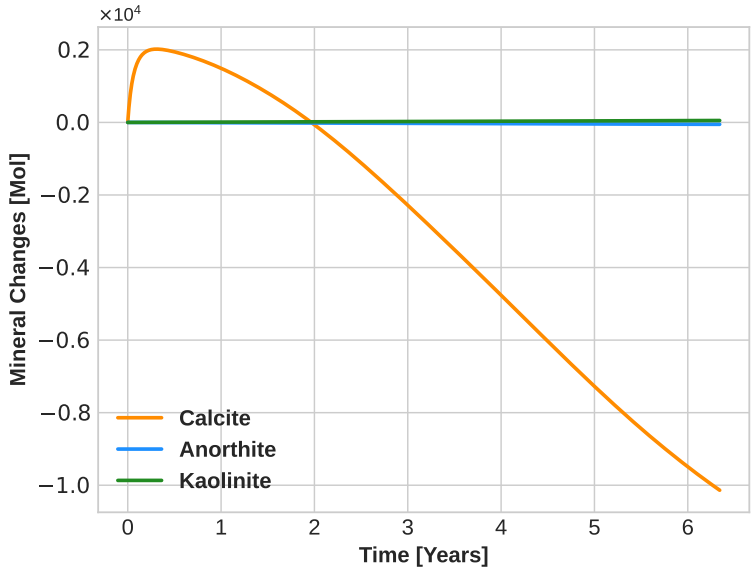

Figure 3.16: Evolution of mineral quantities as a function of time.

the system.

3.5.3 Test case 3: 3D heterogeneous problem

The third test case consists of a benchmark [54] involving a 3D heterogeneous domain with complex geometry. It is worth noting that most of the participants in the benchmark provided isothermal results on several industrial reservoir simulators or academic simulation platforms. As part of this work, an attempt will be made to replicate the benchmark with a THC coupling. A comparison between isothermal and nonisothermal will be made to characterise the benefits of including thermal effects. Performance comparisons will also be made between the global implicit and sequential approaches. Finally, some high-performance computations are discussed to highlight the capabilities of *DuMu*^{X} .

3.5.3.1 Problem configuration

The Lower Jurassic Johansen Formation is a sandstone geological formation in the northern North Sea. It has been studied by Norwegian authorities as an aquifer candidate for CO_2 storage in the project *Northern Lights* which finally focused on another storage site. The mesh considered in this benchmark is a simplified structured geometry composed of the same material properties as the real Johansen model [186]. Figure 3.17 depicts the 3D geometry as well as the heterogeneous properties of the domain. Porosity, permeability, and other grid information are given within the mesh format, which is constructed as a corner-point grid. To read such a grid, the opm-grid module from the Open Porous Media (OPM) [5] initiative is used, which supports the standard corner-point grid format. The dimensions of the domain are approximately 9600 m × 8900 m, and the latter is composed of

9 layers of grid blocks in the vertical direction. The injection well is located at $x = 5440$ m and $y = 3300$ m. The pressure of the liquid phase is set to be hydrostatic and gravity-dependent. Initially, a pressure of 2.53×10^7 Pa is set at a depth of 2500 m.

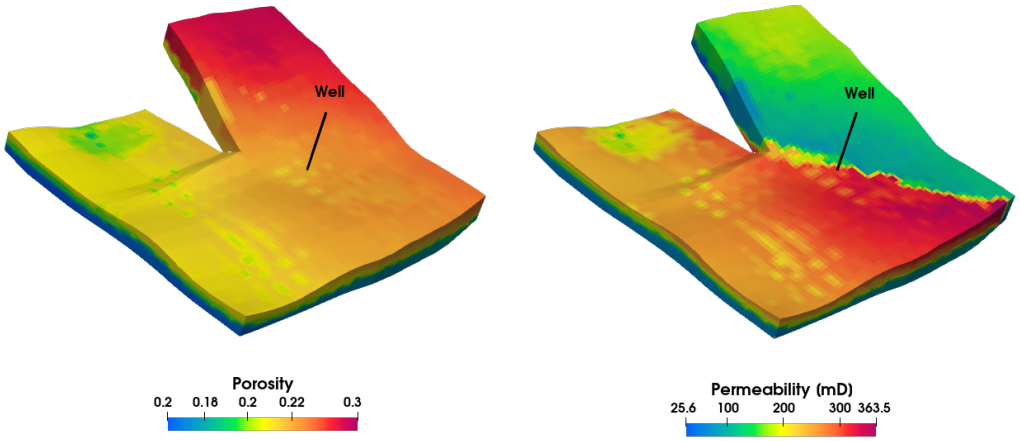

(a) Porosity (b) Permeability

Figure 3.17: Geophysical configuration of the aquifer for the 3D Benchmark [54].

The simulation is conducted over a 25-year period of CO_2 injection at 15 kg.s^{-1} into the formation, followed by a 25-year postinjection period during which the well is shut in. The simulation data are listed in Table 3.9. The initial time step is set to 10^{-2} s and the maximum time step is set to 10^7 s. The tolerances for the Newton-Raphson and BICGSTAB methods are 5 $\times 10^{-6}$ and 10^{-8}, respectively.

Constitutive law or variable	Symbol	Parameters	Unit
Initial Temperature	T_{init}	373.15	[K]
Injection Temperature	T_{inj}	323.15	[K]
Injection Rate	Q_{inj}	15	[kg.s^{-1}]
Residual liquid saturation	S_{lr}	0.2	[-]
Residual gaseous saturation	S_{gr}	0.05	[-]
Brooks Corey parameter	P_e	1×10^4	[Pa^{-1}]
Brooks Corey parameter	λ	2.0	[-]
Solid Density	ρ_s	2500	[kg.m^{-3}]
Solid Thermal Conductivity	λ_s	2.5	[W.(m.K)$^{-1}$]
Solid Heat Capacity	c_h	1000	[J.(kg.K)$^{-1}$]
Longitudinal Dispersion	d_L	0	[m]
Transverse Dispersion	d_T	0	[m]
Liquid molecular diffusion	D_l	2×10^{-9}	[m^2.s^{-1}]
Gaseous molecular diffusion	D_g	Based on [218]	[m^2.s^{-1}]

Table 3.9: Simulation data for the 3D heterogeneous test case from [54].

The chemical system considered in this test case is taken from [78]. It is composed

of seven reactions: one aqueous dissolution, three aqueous complexation reactions at equilibrium, and three precipitation/dissolution reactions solved as kinetic reactions. All information on equilibrium constants, reactive constants, reactive surfaces, and activation energies are given in Table 3.10 and Table 3.11. For the diffusivity, the Millington-Quirk formula is used, while the thermal conductivity uses the Somerton model defined in [191].

Reactions			$\log_{10}(K_{j,ref})$
$CO_{2(g)}$	$\rightleftharpoons$	$CO_{2(l)}$	-
$OH^- + H^+$	$\rightleftharpoons$	H_2O	-13.26
$CO_3^{2-} + H^+$	$\rightleftharpoons$	HCO_3^-	-6.32
$CO_{2(l)} + H_2O$	$\rightleftharpoons$	$H^+ + HCO_3^-$	-10.23
Ano + 8 H^+	$\rightleftharpoons$	4 H_2O + Ca^{2+} + 2 Al^{3+} + 2 SiO_2	25.82
Cal + 2 H^+	$\rightleftharpoons$	$Ca^{2+} + H_2O + CO_{2(l)}$	1.6
Kao + 6 H^+	$\rightleftharpoons$	5 H_2O + 2 Al^{3+} + 2 SiO_2	6.82

Table 3.10: Chemical reactions involved in the 3D heterogeneous test case from [78].

Mineral	$\log_{10}(K_{j,ref})$	E^a	A_s [$m^2.m^{-3}$]	Init. conc. [$mol.m^{-3}$]
Anorthite	-12.0	67.830	88.0	87
Calcite	-8.8	41.870	88.0	238
Kaolinite	-13.0	62.760	17600	88

Table 3.11: Chemical information about mineral species involved in kinetics reactions.

Thanks to the Morel formalism [145], chemical species are divided into:

- for fully implicit approach:

$$\begin{aligned} I_{pm} &= \left\{H_2O_{(l)}, CO_{2(l)}, H^+, Ca^{2+}, Al^{3+}, SiO_2\right\}, \\ I_{sm} &= \left\{H_2O_{(g)}, CO_{2(g)}, OH^-, CO_3^{2-}, HCO_3^-\right\}, \\ I_{sk} &= \{\text{Anorthite}, \text{Calcite}, \text{Kaolinite}\}, \end{aligned}$$

- for sequential approach:

$$\begin{aligned} I_{2\varphi} &= \{H_2O_{(l)}, H_2O_{(g)}, CO_{2(l)}, CO_{2(g)}\}, \\ I_{rt} &= \left\{H^+, Ca^{2+}, Al^{3+}, SiO_2, OH^-, {CO_3}^{2-}, {HCO_3}^-, \text{Calcite}, \text{Anorthite}, \text{Kaolinite}\right\}. \end{aligned}$$

The initial mineral concentrations are given in Table 3.11, while Table 3.12 provides initial conditions for each primary species. To close the problem, an impermeable Neumann boundary condition is set at the upper and lower boundaries of the domain, while Dirichlet boundary conditions are set to initial values at the lateral boundaries for pressure and concentrations.

Primary species	Initial molality [mol.kg^{-1}]
$CO_{2(l)}$	3.55×10^{-3}
H^+	5.71×10^{-1}
Ca^{2+}	2.52×10^{-2}
Al^{3+}	3.13×10^{-12}
SiO_2	4.73×10^{-4}

Table 3.12: Initial conditions for primary species.

3.5.3.2 Numerical results

This section presents numerical results obtained from simulations based on the [54] benchmark, including a THC coupling extension. The results are in good agreement with those obtained by many participants. First, general results of the benchmark are developed by emphasizing the mass conservation curves, which show the evolution of CO_2 in all its forms. For the hydraulic case, results from another reservoir simulator are presented as well as comparisons with other benchmark participants.

Benchmark results

The results of some quantities of interest are shown here as a function of time. The solution images are shown at 25 years, which is the end of the injection period, and at the final time, 50 years.

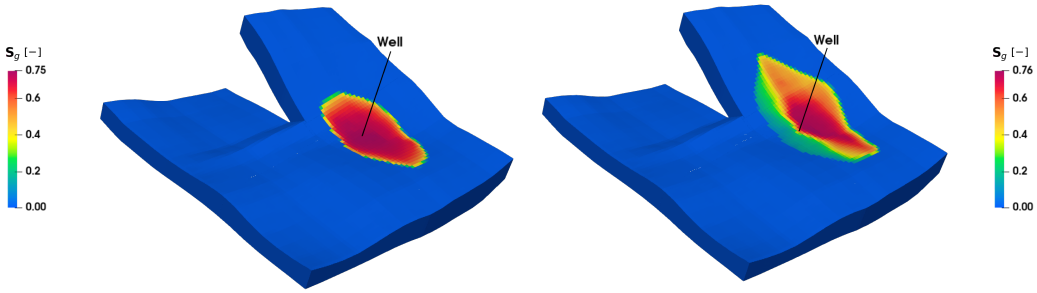

(a) 25 years (b) 50 years

Figure 3.18: Evolution of gaseous saturation over time.

Computations were first performed with the fully coupled fully implicit scheme using the DSA method. Figure 3.18 to Figure 3.23 show results for different quantities of interest. As CO_2 is injected from the bottom of the saline aquifer, it tends to move upwards due to buoyancy and spreads laterally once the plume reaches the top of the aquifer. This phenomenon is due to the density difference between the gaseous CO_2 and the resident brine that fully saturates the domain at the beginning. The gaseous saturation represented in Figure 3.18, shows that the CO_2 injected at the boundary between two levels of heterogeneity tends to move preferentially in the lower permeability zone, but also in the shallower part of the aquifer. This implies CO_2 advection is dominated by gravity more than permeability, at least in that test

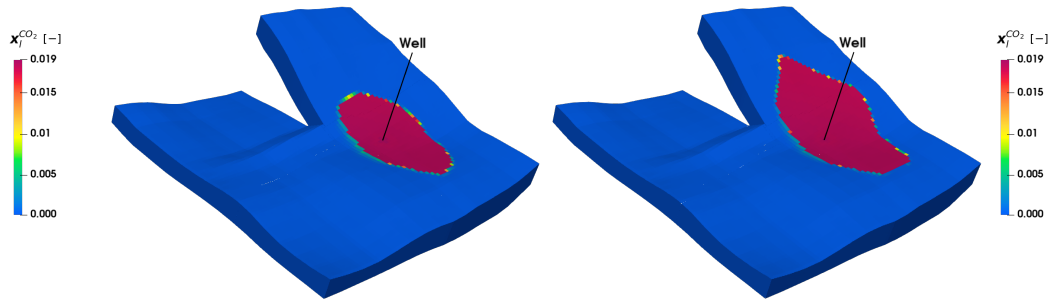

(a) 25 years (b) 50 years

Figure 3.19: Evolution of CO_2 liquid molar fraction over time.

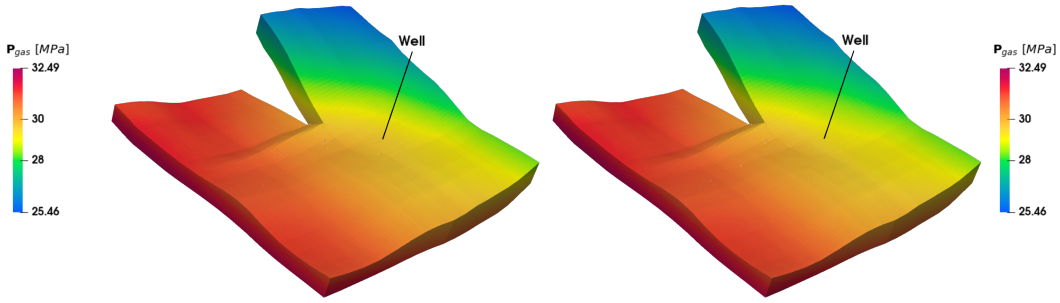

(a) 25 years (b) 50 years

Figure 3.20: Evolution of gaseous pressure over time.

case. The temperature effects are visible in Figure 3.21 due to an injection at 50 K lower than the initial temperature of the aquifer. The temperature changes are localised to about three to four grid cells around the injection well which is consistent with what has been observed in the 1D radial test case presented previously. The minimum temperature of 340 K is reached at the end of the injection scenario at 25 years, and then the heat conduction of the host rock tends to warm the cooled region step by step. In addition, the pH is modified in the CO_2 plume region (see Figure 3.22), as is calcite. When CO_2 is converted from the gaseous to liquid form due to aquifer conditions, it reacts with the resident brine, releasing hydrogen and bicarbonate ions. A pH decrease means that more hydrogen ions H^+ are released than hydroxide ions OH^-. This tends to activate mineral reactions of precipitation or dissolution over large time scales. In this case, the dissolution of calcite can be observed in the same zone (see Figure 3.23). The concentration of calcite has decreased by approximately 0.5 mol.m^{-3} in the region where CO_2 is localised.

It is worth noting that for this 3D mesh, a convergence analysis for the TPFA scheme has not been carried out. In fact, despite a not particularly demanding mesh, the K-orthogonality property is not perfectly guaranteed, although in [179], the results obtained by TPFA and NLTPFA differ only slightly.

Mass conservation

The mass conservation is a quantity of interest emphasised in the benchmark. It

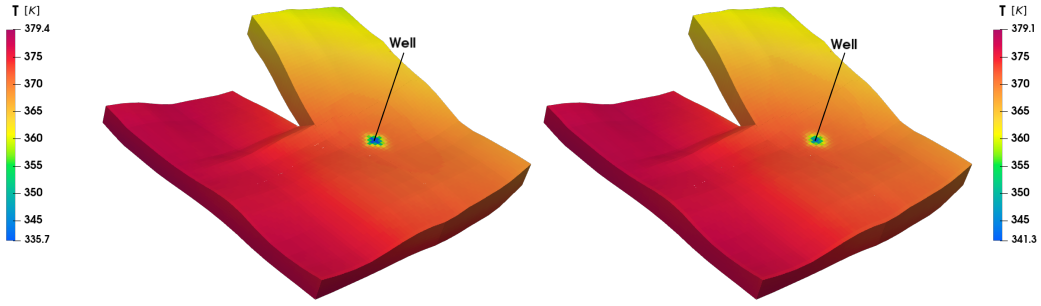

(a) 25 years (b) 50 years

Figure 3.21: Evolution of temperature over time.

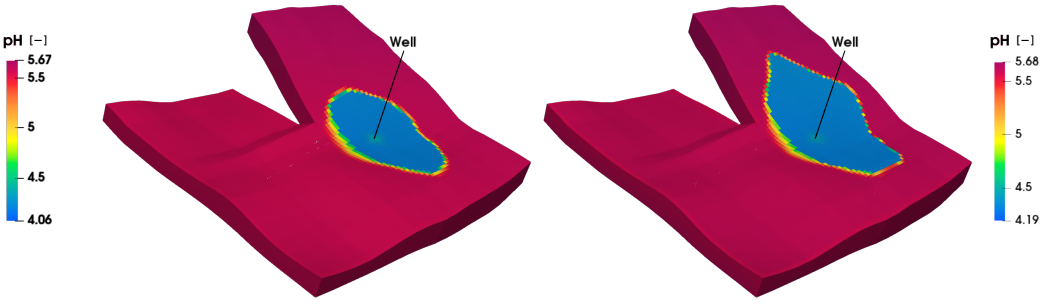

(a) 25 years (b) 50 years

Figure 3.22: Evolution of pH over time.

allows us to visualize the behavior of CO_2 quantities injected into the aquifer, as well as the evolution of CO_2 in different states.

Figure 3.24 represents the amount of CO_2 in the gas phase, dissolved in brine and converted to calcite within the model domain, over the simulation time, for the implicit and the sequential methods. The distribution of CO_2 in the liquid and gas phase is very close to results obtained with industrial simulators such as GEOS and Eclipse also shown in the figure, but also with other benchmark participants [54]. During the injection step, the gaseous saturation roughly increases before decreasing slightly in the post-injection phase due to the dissolution of CO_2 in the liquid phase. Solubility trapping is indeed a process that has a significant impact on storage efficiency. However, mineral trapping is not very efficient on short time scales, and therefore the CO_2 turned into calcite increases very slowly until 50 years. Nevertheless, mineral trapping is known to be efficient from 100 years [139].

In general, the results obtained by our approach are in line with those presented in the benchmark for several quantities of interest, in particular from simulations that have been carried out with the GEOS software [183] provided in Figure 3.25 and CO_2 evolution curves extracted from several industrial or academic software Figure 3.24. GEOS is an open-source multiphysics simulator developed in collaboration with Lawrence Livermore National Laboratory, Stanford University, TotalEnergies, and Chevron. It provides a framework for handling coupled complex fluid flow, thermal, and geomechanical effects as a highly scalable high-performance computing platform.

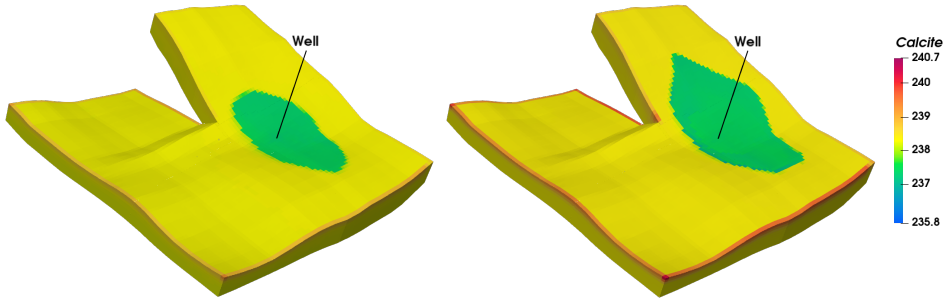

(a) 25 years (b) 50 years

Figure 3.23: Evolution of calcite concentration over time.

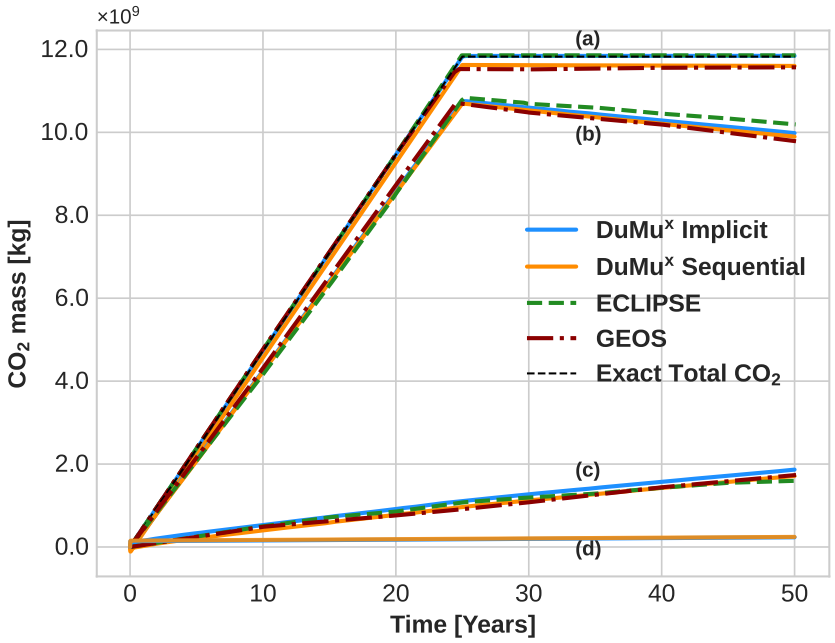

Figure 3.24: Evolution of CO_2 quantities as a function of time. (a) total injected mass of CO_2, (b) mass of CO_2 in gas phase, (c) mass of CO_2 dissolved in liquid phase, (d) mass of CO_2 in mineral phase.

3.5.3.3 Sequential and implicit comparisons

As exposed in Section 3.3, the resolution of the problem can be tackled by two different approaches. Generally in reservoir simulation software or academic platforms, only one resolution method is privileged. In this work, both of them have been implemented in order to be able to compare them quantitatively and qualitatively. Figure 3.26 to Figure 3.29 shows a comparison of several quantities between the fully implicit and the sequential methods at $t = 50$ years. A small difference is noticeable in the shape of the CO_2 plume. The sequential scheme is not fully conservative by construction. The splitting errors are mainly due to the explicit treatment of the data between the two subproblems. The fully implicit scheme is

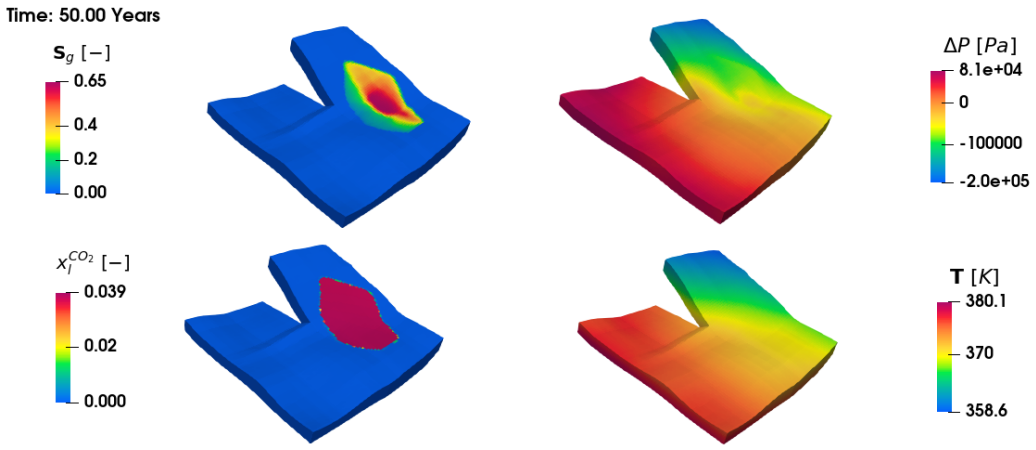

Figure 3.25: Simulation results obtained by GEOS at $t = 50$ years.

more accurate but more complicated to solve numerically. Table 3.13 represents the relative difference in the L^2-norm on the whole domain between the sequential and fully implicit solutions at $t = 50$ years. The difference decreases when the maximum time step is reduced.

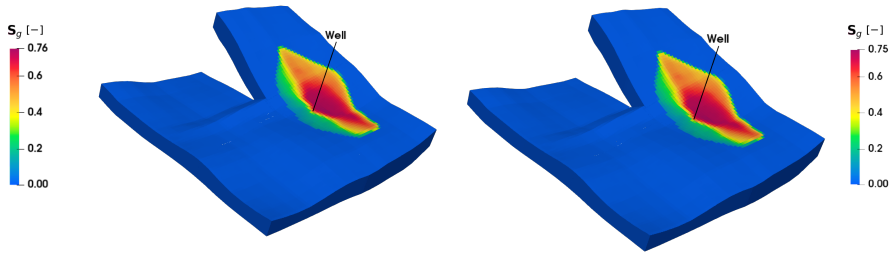

(a) Implicit 50 years (b) Sequential 50 years

Figure 3.26: Comparison of gaseous saturation profile for the sequential and implicit approaches at 50 years.

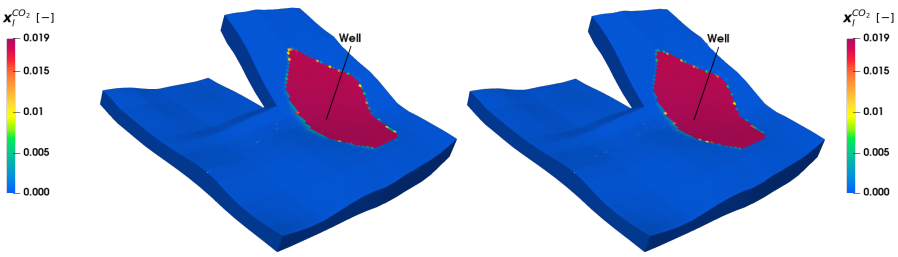

(a) Implicit 50 years (b) Sequential 50 years

Figure 3.27: Comparison of liquid CO_2 molar fraction profile for the sequential and implicit approaches at 50 years.

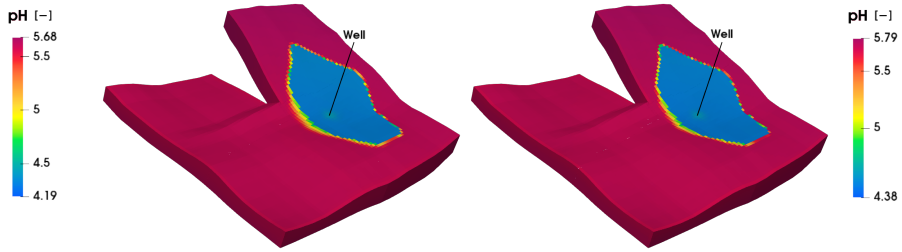

(a) Implicit 50 years (b) Sequential 50 years

Figure 3.28: Comparison of pH profile for the sequential and implicit approaches at 50 years.

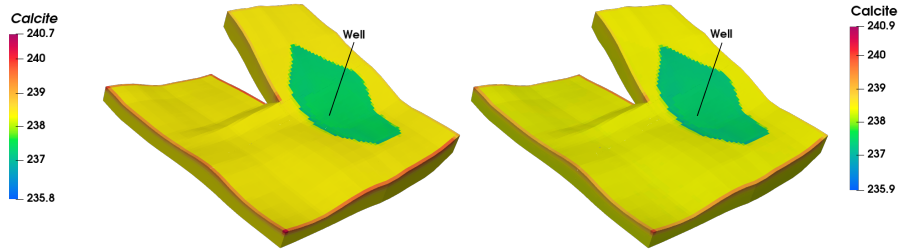

(a) Implicit 50 years (b) Sequential 50 years

Figure 3.29: Comparison of calcite dissolution profile for the sequential and implicit approaches at 50 years.

dt_{max}	S_g	P_g	$x_l^{CO_2}$	Calcite	pH
5×10^6	1.52×10^{-2}	7.41×10^{-5}	3.29×10^{-2}	1.0×10^{-4}	1.90×10^{-2}
2×10^6	9.13×10^{-3}	4.00×10^{-6}	2.10×10^{-2}	9.78×10^{-5}	2.01×10^{-2}
1×10^6	7.27×10^{-3}	2.26×10^{-6}	1.97×10^{-2}	9.84×10^{-5}	2.21×10^{-2}

Table 3.13: Relative difference in L^2-norm between several quantities computed by the fully implicit and sequential approaches on 54756 cells at 50 years.

Mass conservation

Figure 3.30 depicts the distribution of CO_2 into its different forms for both implicit and sequential strategies and highlights differences between them. On the one hand, the quantity is not conserved in the sequential one because a difference of 2.73% is measurable between the total quantity of CO_2 and the theoretical value injected. On the other hand, the total mass of CO_2 computed by the fully implicit approaches perfectly matches exactly the injected value, demonstrating a better conservation property.

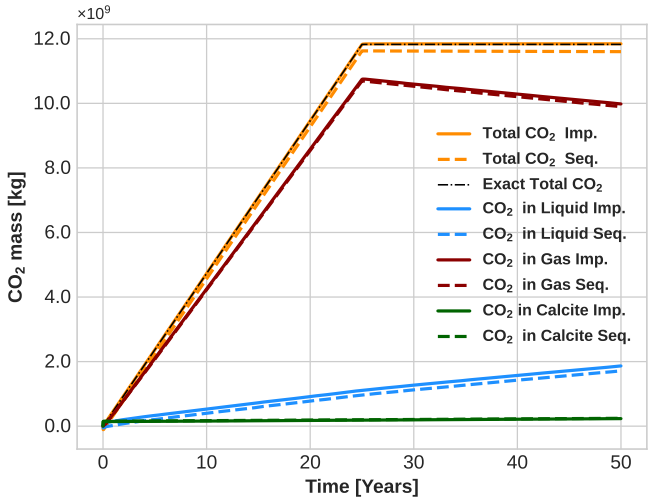

Figure 3.30: Comparison of the evolution of CO_2 quantities as a function of time between fully implicit and sequential approaches.

Performance comparison

In *DuMu*^{X}, runtimes are reported separately for three stages of time integration: linearisation and assembly of the linear system (Jacobian matrix and residual vector), solving the linear system, and updating the variables. The individual runtimes are accumulated over all Newton-Raphson iterations needed until convergence. Figure 3.31 (a) shows the evolution of these three computational times throughout the simulation. The main difference between the sequential and fully implicit approaches is due to the solving step. Indeed, as shown in the inset in Figure 3.31 (a) for the implicit scheme, the computational time for the solve step is thirteen times higher than that of the sequential scheme (approximately 13000 s versus 1000 s) while the other times are comparable or negligible. Figure 3.31 (b) shows that the two approaches use very similar time step sizes. Figure 3.31 (c) displays the number of Newton iterations per time step for each approach. For the sequential case, this number corresponds to the sum of the number of Newton iterations for each subproblem: two-phase nonisothermal flow and reactive transport. This cumulative number of iterations is higher for the sequential approach than for the implicit approach. Finally, the longer time for the solving step can be explained by Figure 3.31 (d). It is clear that the total number of linear iterations per time step is greater for the implicit approach. The computation for the inversion of the system

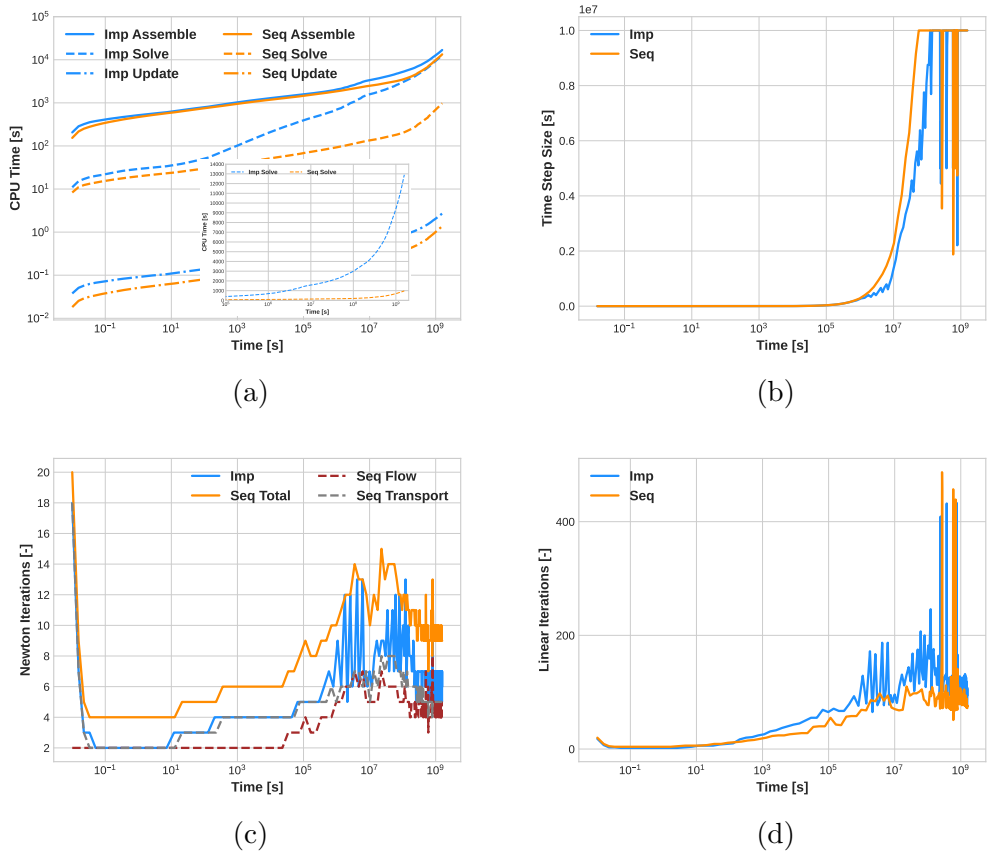

Figure 3.31: Comparison between the implicit and sequential approaches: (a) CPU time evolution as a function of time for the different stages of the computation, (b) time step, (c) number of Newton iterations per time step, (d) total number of linear iterations per time step.

in the fully implicit approach is much more expensive in terms of CPU time. There are two main reasons for this. First, for each Newton iteration, two linear systems have to be solved in the sequential approach as opposed to one in the implicit approach. However, the size of the linear systems for the sequential approach is smaller than the size of the linear system involved in the implicit approach. Secondly, the nonlinearities are stronger for the implicit approach, particularly those due to saturation and temperature, since all the equilibrium and kinetic chemical constants are temperature dependent. For the sequential strategy, the nonlinearities of saturation and temperature are concentrated in the first linear system dedicated to the nonisothermal two-phase flow, while the second linear system dedicated to the reactive transport is solved at the imposed saturation and temperature. Heat transfer takes place slowly by conduction. Therefore, at the beginning of the simulation, thermal effects do not play a major role in the nonlinearities of the linear systems and the CPU time devoted to the solution step is comparable for the sequential and implicit approaches. Both approaches use the same solver and preconditioner. The use of a different preconditioner would certainly be more advantageous for the implicit approach than for the sequential one. To conclude this comparison, despite a significant difference between sequential and implicit CPU times for the full

simulation, the splitting error in the sequential scheme may also remain important. This error is very sensitive to the maximum time step size of the problem and can therefore be minimised.

Maximum time step size effect

To quantify the effect of the maximum time step on the mass conservation, we define the following quantity:

$$\varepsilon_{\mathrm{CO_2}} = \frac{|Tot_{inj}^{End} - Tot_{\mathrm{CO_2}}^{End} - Tot_{\Gamma_{Dir}}^{End}|}{Tot_{inj}^{End}}, \tag{3.5.1}$$

where Tot_{inj}^{End} represents the quantity of CO_2 injected at the final time, $Tot_{\mathrm{CO_2}}^{End}$ represents the total quantity of CO_2 present in the liquid, gas and mineral phases at the final time and $Tot_{\Gamma_{Dir}}^{End}$ is the cumulative flux of CO_2 across boundary faces where Dirichlet boundary conditions are imposed. Several simulations were carried out with different maximum time step sizes to investigate its effect on mass conservation using the original mesh. Table 3.14 represents the total computation time for several maximum time steps as well as the quantity $\varepsilon_{\mathrm{CO_2}}$, the total number of time steps, the average number of nonlinear iterations per time step and the average number of linear iterations per Newton iteration. As expected, the implicit scheme is perfectly mass conservative since the error $\varepsilon_{\mathrm{CO_2}}$ is close to the numerical precision. For the sequential approach, the error $\varepsilon_{\mathrm{CO_2}}$ is due to splitting errors and decreases with the time step. The implicit approach remains more accurate even if we take a smaller maximum time step size. For a given maximum time step, the number of time steps is comparable for the two approaches. As seen in Fig. 3.31, the number of Newton iterations for the sequential approach is larger than for the implicit approach, but the average number of linear iterations per Newton iteration is smaller for the sequential approach. Moreover, the size of the two linear systems to be solved for each subproblem of the sequential approach is smaller than the size of the linear system involved in the implicit approach. This may explain why the implicit approach takes longer than the sequential approach. Nonetheless, it is clearly visible that to reduce the splitting error of the sequential scheme and reach the same level as the implicit scheme, it is necessary to use smaller time steps. This obviously lengthens the computational time of the sequential approach and the implicit approach can be faster in some cases if a certain precision is expected. Thus, the desired computational time and accuracy of the calculation can be an argument for the choice to use a sequential or implicit method.

Isothermal and nonisothermal comparisons

Differences between the two configurations occur mainly near the injection well when CO_2 is injected colder than the aquifer temperature. As shown in the left part of Figure 3.32, the isothermal simulation does not take the injection temperature into account. Nevertheless, the initial temperature gradient is set to correctly characterise the fluid properties. For the nonisothermal case, the cold injection temperature reduces the latter in the wellbore region until it reaches 335 K at 25

Table 3.14: Numerical performances. CPU: elapsed time, TS: number of time steps, NI: average number of nonlinear iterations per time step, LI / NI: average number of linear iterations per Newton iteration

Method	dt_{max} [s]	CPU	TS	NI	LI/NI	ε_{CO_2}
Implicit	1×10^7	9h20min	236	6.37	15.89	1.02×10^{-14}
Implicit	5×10^6	12h03min	376	5.25	15.55	2.99×10^{-14}
Implicit	1×10^6	35h42min	1626	3.64	15.61	1.40×10^{-13}
Sequential	1×10^7	5h50min	222	8.63	9.41	2.73×10^{-2}
Sequential	5×10^6	7h19min	373	8.34	8.41	1.89×10^{-2}
Sequential	1×10^6	24h27min	1620	6.18	8.26	1.39×10^{-2}

years. Then the rock conduction process takes over and the temperature returns to a steady state.

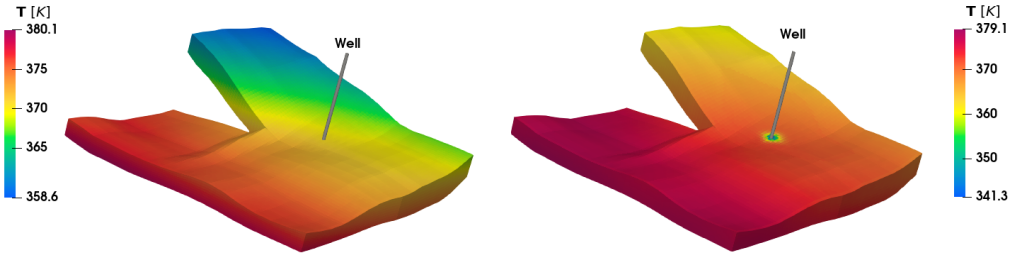

Figure 3.32: Temperature profiles for both isothermal (left) and nonisothermal (right) problems.

The difference between the last two profiles is calculated in Figure 3.33 to clearly show the temperature variations due to cold injection. Indeed, the temperature decreases by about 30 K in the well region. However, there is also a warming effect in the CO_2 plume region, which is highlighted by the white contour lines. The exothermic dissolution process of CO_2 increases the temperature at which chemical reactions occur by about 1.6 K.

Studies have also been carried out on different injection temperatures. According to Figure 3.34, the amount of dissolved CO_2 does not vary significantly with different injection temperatures as well as for the isothermal case. However, it should be noted that the isothermal case differs slightly from the non-isothermal case. The liquid solubility of the isothermal case is just below the nonisothermal curves.

3.5.3.4 High Performance Computing

Complex calculations or large-scale simulations can be very time-consuming. High-performance computing helps to reduce the computational cost of a numerical simulation. The grid is partitioned using a domain decomposition method and all processors perform their own calculations simultaneously. The processors communicate by calling MPI (Message Passing Interface) routines. This section specifically compares the performance of the sequential and fully implicit approaches, and some specific terms need to be defined.

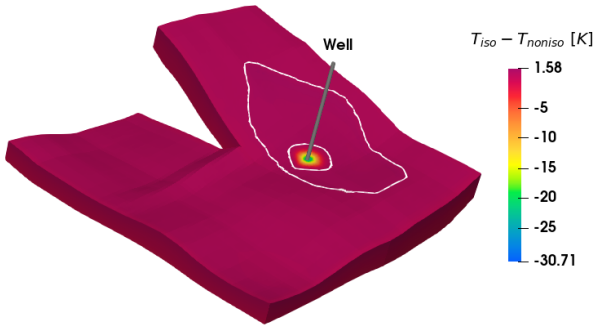

Figure 3.33: Temperature difference between isothermal and nonisothermal profiles at 50 years.

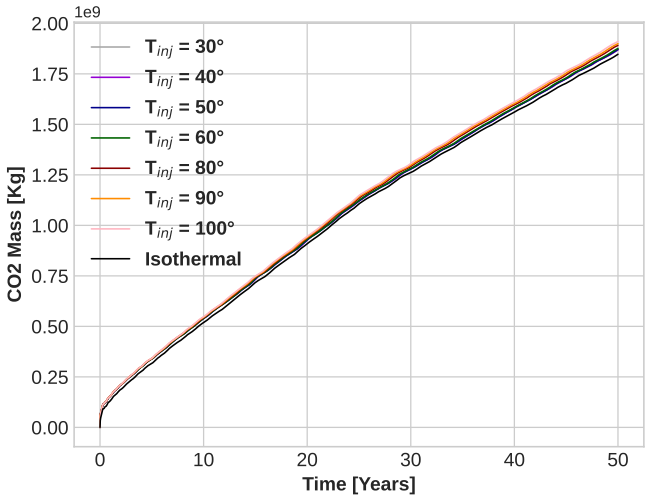

Figure 3.34: Evolution of CO_2 dissolved in the liquid phase for the isothermal and nonisothermal case with several temperature injections.

Firstly, we define the speedup S_p and the ideal speedup S_p^{ideal} as:

$$S_p = \frac{T_{base} p_{base}}{T_p} \quad \text{and} \quad S_p^{ideal} = \frac{p}{p_{base}}, \tag{3.5.2}$$

where p_{base} and T_{base} are the reference number of processors and CPU time, respectively. p and T_p are the variable number of processors and the associated CPU time, respectively. These quantities allow us to define the behaviour of the CPU time for different configurations.

It is also possible to define the strong scaling efficiency as:

$$E_s(p) = \frac{S_p}{S_p^{ideal}}. \tag{3.5.3}$$

E_s is useful to define how the simulation time varies with the number of processors for a fixed-size problem. The strong scaling efficiency reflects the ideal behaviour

of the algorithm's parallelism. An ideal efficiency (close to one) indicates that inter-processor communications and synchronisations using the MPI protocol are negligible and that for a number of processors p the CPU time would be almost divided by p.

We also define weak efficiency:

$$E_w(n,p) = \frac{T_{n_{base},p_{base}}}{T_{n,p}}, \tag{3.5.4}$$

where E_w is the ratio between the execution time of the base configuration ($T_{n_{base},p_{base}}$) and an alternative configuration. It defines how the computational time varies with the number of processors for the same load on the processors. A weak efficiency close to one indicates an optimal behaviour for the algorithm and the computer architecture. In this case, the CPU time remains constant, equal to the reference time, while the total size of the problem increases with the number of processors. A constant factor α allows to scale any configuration, such as $n = \alpha n_{base}$ and $p = \alpha p_{base}$.

Simulation performance is also related to domain decomposition parallelization. In particular, the load of each processor must be fairly distributed in order to benefit from the best production. The load imbalance due to uneven domain decomposition measures the deviations in the distribution:

$$\text{Load Imbalance} = \frac{\text{dof}_{max} - \text{dof}_{min}}{\text{dof}_{min}}, \tag{3.5.5}$$

where dof_{max} and dof_{min} define the maximum and minimum degrees of freedom respectively. For uniform distribution, the load imbalance approaches zero.

Parallel performances

All the high-performance computations were performed on a supercomputer called CURTA, the latest machine from the Mesocentre de Calcul Intensif Aquitain (MCIA *https://redmine.mcia.fr*). The computing nodes of this machine are composed of 2 hexadecacore processors (32 cores per node) Intel ®Xeon ®Gold SKL-6130 at a frequency of 2.1 GHz.

The initial mesh of 54756 cells was refined to obtain two meshes of 876096 and 3504384 cells, which were used to run parallel simulations on up to 256 processors. All computations were performed for the first year of the simulation in order to capture the phenomenon at later stages than the initialisation. This period includes part of the simulation where the linear solver for the implicit method starts to deteriorate. Figure 3.35 (a) and (b) show the CPU times evolution with respect to the number of processors for the two size problems. For the sequential approach, times are decomposed into nonisothermal multiphase flow and reactive transport problems which allows us to realise that the reactive transport problem is slightly more expensive to solve than the flow one. From these two histograms, it is visible that there is a significant difference between the simulation times of the problem

solved in sequential and implicit forms whatever the configuration considered. Nevertheless, a clear tendency of decreasing CPU time is observed when the number of processors is increased.

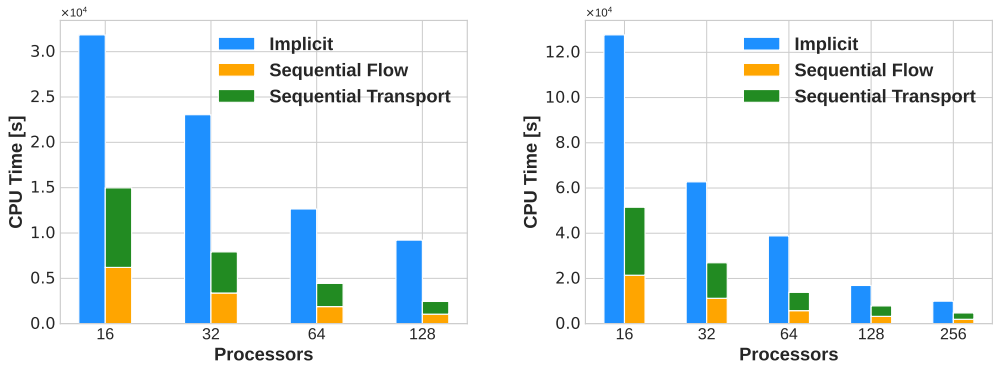

(a) 876096 elements (b) 3504384 elements

Figure 3.35: CPU time evolution for the two different mesh sizes

From another point of view, Figure 3.36 (a) and (b) show the speedup and strong scaling efficiency as the number of processors increases. Both curves are correlated but scaled differently. The speedup represents the deviation from the ideal behaviour, shown by the dashed line. The two configurations do not seem to have the same behaviour. In fact, for the 876096 cells, the implicit case has a speedup that tends to drift away from the ideal speedup, while for the 3504384 cells configuration, the opposite behaviour is observed. Figure 3.36 (b) represents the strong scaling efficiency. For the smaller mesh, the communication overload is mainly due to the workload per processor becoming too low, leading to a rapid decrease in efficiency, especially for the implicit scheme. For the larger mesh, the workload seems sufficient and a good efficiency is observed for both sequential and implicit schemes. The comparison of the efficiency of two different numerical methods is difficult. Indeed the size of the linear problems to be solved and their complexity are different for the sequential and the implicit schemes, leading to different communications for each scheme. Figure 3.36 (c) represents the CPU time evolution with respect to the number of processors for the two problem sizes. The fully implicit and sequential CPU times are significantly different, as the fully implicit approach is twice as long as the sequential approach, regardless of the configuration. The more we increase the number of processors, the more the CPU time deviates from the ideal behaviour. In Figure 3.36 (d), the CPU time per iteration is plotted. There is a monotonic trend where the CPU time per iteration drops sharply for small numbers of processors and then tends to stabilise slightly. Figure 3.36 (e) and (f) give a more detailed representation of the three main steps of the computation for the two different meshes. As seen earlier in Figure 3.31 (a), the main difference between the CPU times for the sequential and implicit approaches concerns the solving step, as there is an order of magnitude difference between the time taken by the two approaches for this step.

The weak scalability and efficiency shown in Figure 3.37 (a) and (b) have been investigated for fully implicit and sequential approaches. Four different meshes (from

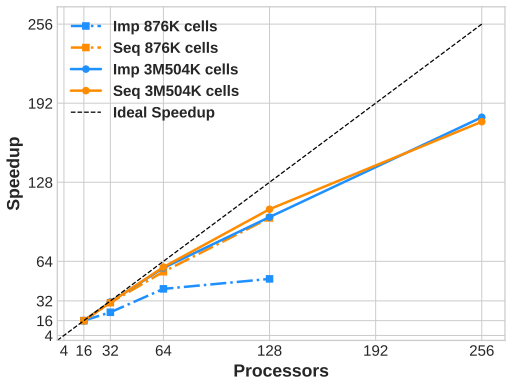

(a) Speedup

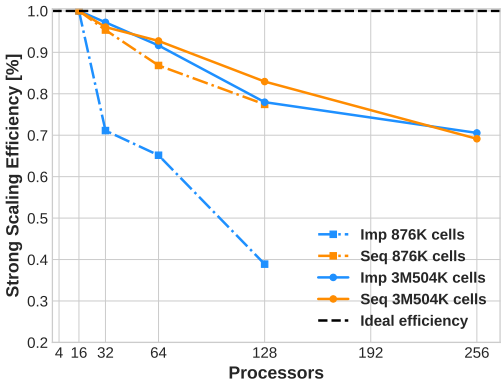

(b) Strong scaling efficiency

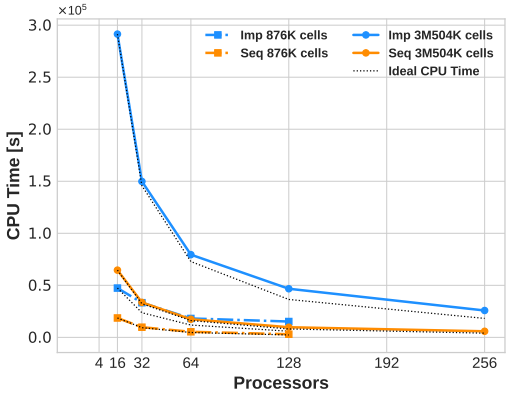

(c) CPU Time

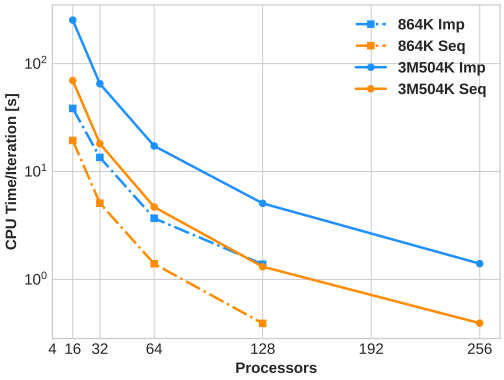

(d) CPU Time per iteration

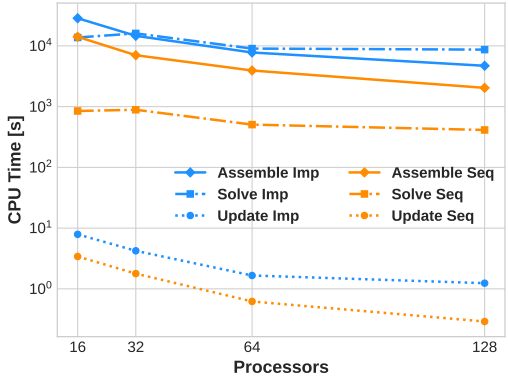

(e) Detailed CPU time for the mesh composed of 876096 elements

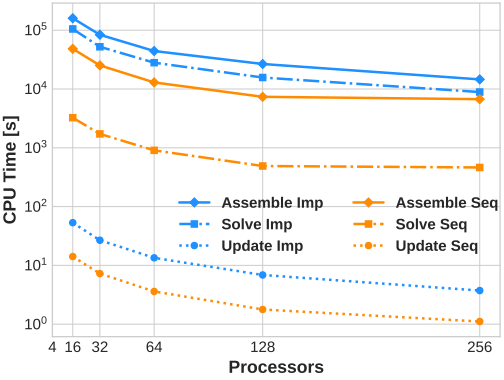

(f) Detailed CPU time for the mesh composed of 3504384 elements

Figure 3.36: Evolution of quantities with respect to the number of processors: (a) Speedup, (b) strong scaling efficiency, (c) global CPU time, (d) average CPU Time per iteration, (e) detailed CPU time for the mesh composed of 876096 elements, (f) detailed CPU time for the mesh composed of 3504384 elements.

54756 to 3504384 elements) are considered, keeping the same load of 13689 cells on each processor by increasing the number of processors from 4 to 256. Simulations are also run for 1 year of injection. Sequential results show that for the same load on the processors for different problem sizes, the CPU time tends to remain almost constant and a curve with a plateau can be observed. However, the implicit seems to have a peak on CPU time formed with 64 processors on the mesh of 876096 elements. The low efficiency indicates a fairly good scaling for these problem configurations, staying above 0.6% in contrast to the implicit, which drops to 0.5%.

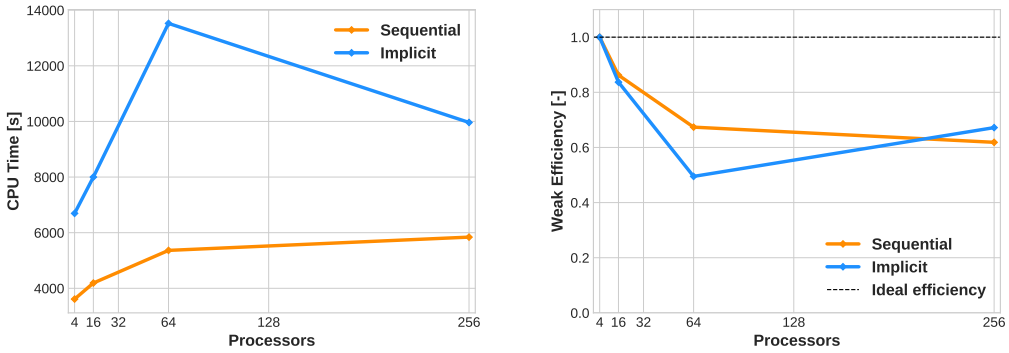

(a) Weak scalability (b) Weak efficiency

Figure 3.37: Weak scalability (a) and weak efficiency (b) for fully implicit and sequential approaches.

The load imbalance has been measured for three meshes composed of 219024, 876096, and 3504384 elements with various numbers of processors. It is shown in Figure 3.38 (a). The load imbalance quickly becomes high, indicating that the partitioning is not optimal. In fact, this phenomenon can also be observed on Figure 3.38 (b), where some partitions created by the Zoltan library [39] are not well distributed. The area marked with a star appears to be smaller than the area marked with a rectangle. Consequently, each processor does not take responsibility for exactly the same number of cells of the mesh. In particular, for the mesh of 219024 elements, on 128 processors, an imbalance of about 8 is observed, which allows us to realise that one processor has a load 8 times higher than another. Therefore, this part of partitioning could be improved by testing other types of partitioners.

3.5.3.5 Long-term evolution of CO_2

As detailed in Figure 1.3, mineralisation is known to be a long-term process, affecting the aquifer for at least centuries [139]. It is clear that dissolution and precipitation have not yet begun to be significant according to the results presented above. For this reason, longer simulation times are considered to capture the mineralisation phenomena. However, the initial benchmark was not configured for long-term simulation. In fact, the CO_2 plume will tend to disappear as it approaches the edge due to the fixed pressure boundaries on the lateral surfaces. Therefore, if a longer time horizon is studied, the boundary conditions must be modified in order

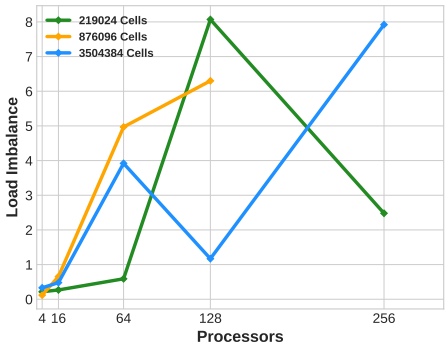

(a) Load imbalance

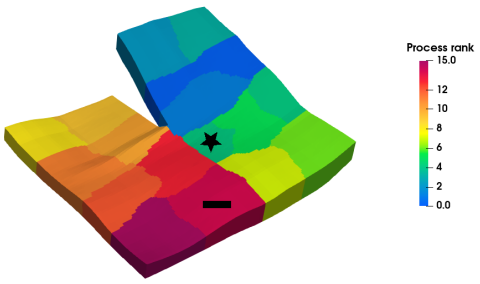

(b) Mesh partitioning

Figure 3.38: Load imbalance (a) for different meshes and mesh partitioning (b) for 16 processors with 219024 elements.

to contain the CO_2 plume within the domain without any leakage.

As a result, homogeneous Neumann boundary conditions are imposed, except for a single face on the front side, as shown in Figure 3.39 and defined by:

$$\Gamma_D = \left\{ K_i \begin{pmatrix} x_i \\ y_i \\ z_i \end{pmatrix} \in \Gamma \mid K_i \cdot \vec{n}_x \begin{pmatrix} 1 \\ 0 \\ 0 \end{pmatrix} \leq -0.5 \right\}$$

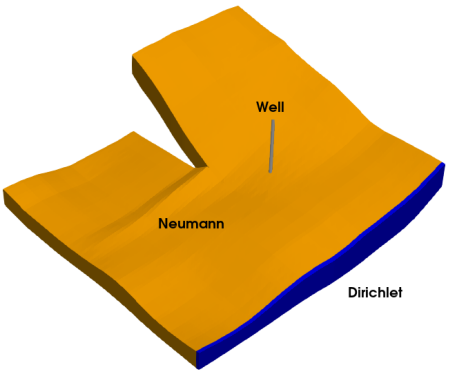

Figure 3.39: Modifications of configuration for long-term CO_2 storage benchmark.

Specifically, the simulation time is extended to 300 years to capture stronger mineralisation effects. The simulation is run using the implicit approach to take advantage of the accuracy provided by this method. Mineral dissolution/precipitation can affect the porosity of the rock matrix. More specifically, the porosity ϕ depends on the concentrations of the minerals according to the relationship:

$$\phi = \phi_0 - \sum_{j=1}^{N_m} \nu^j \, (c_s^j - c_{s,0}^j), \tag{3.5.6}$$

where ϕ_0 is the initial porosity, N_m is the number of reactive minerals, ν^j is the molar volume [$m^3.mol^{-1}$] for mineral j. Finally, c_s^j and $c_{s,0}^j$ are the current and initial molar concentrations of mineral j [$mol.m^{-3}$] in the solid phase, respectively. The Kozeny-Carman relationship is used to address the porosity dependence of permeability:

$$\mathbb{K} = \mathbb{K}_0 \left(\frac{1-\phi_0}{1-\phi} \right)^2 \left(\frac{\phi}{\phi_0} \right)^3, \tag{3.5.7}$$

where $\mathbb{K}_0$ is the initial permeability. The maximum time step size is fixed to $dt_{max} = 5 \times 10^6 s$.

As shown in Figure 3.40 (a), the gaseous CO_2 plume moves toward the upper part of the domain due to buoyancy. The Neumann boundary condition acts as a barrier, preventing any leakage and inducing an accumulation zone of gaseous CO_2. Variations in overpressure (c) and temperature (d) due to the injection period dissipate over time, returning the aquifer to its original state. However, the long-term movement of the plume increases the contact surface between CO_2 dissolved in the liquid phase and the host rock, as seen in Figure 3.40 (b). This enhances the dissolution/precipitation process and it can be observed in Figure 3.40 (e, f, g, h) that the shapes of the relative variation of porosity and permeability (i, j) are strongly correlated with the shape of the dissolved CO_2 . This implies greater importance of the mineralisation process. Indeed, the amount of dissolved calcite and anorthite and precipitated kaolinite increased significantly with time. The evolution of CO_2 quantity in Figure 3.41 confirms what is claimed and allows to demonstrate time scales of solubility and mineral trapping from Section 1.1.4. The blue curve representing the CO_2 in its liquid form increases drastically from 0 to 200 years and gradually stabilises towards an upper limit. Therefore, solubility trapping seems to be effective in the short time after injection. In contrast, mineral trapping starts later and could not be captured in the initial configuration due to the short exposure times. In fact, mineralisation has the tendency to immobilize the CO_2 thanks to precipitation or dissolution of chemically reactive rocks. As depicted by the green line, the amount of CO_2 transformed into calcite gradually increases and becomes more and more important over time. After 300 years the amount of mineralised CO_2 represents around 10%, demonstrating the efficiency of this long-term process in ensuring safe storage.

Consequently, this study allows us to highlight and confirm the long-term benefits of CO_2 storage in order to maximise the amount of gas trapped with optimal safety.

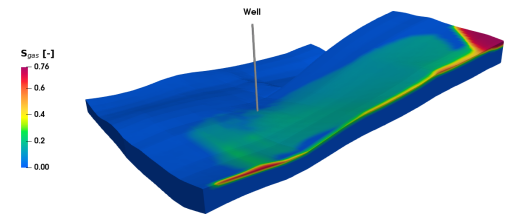

(a) Gaseous saturation

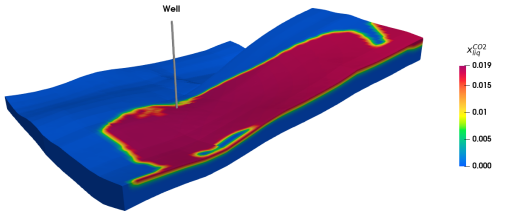

(b) Molar fraction of dissolved CO_2 in liquid phase

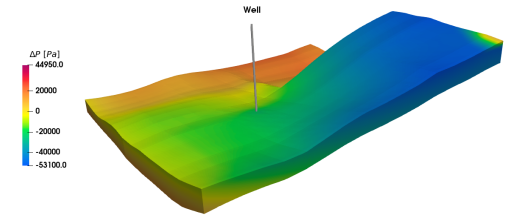

(c) Liquid pressure difference from initial state

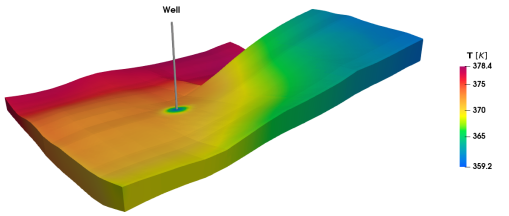

(d) Temperature

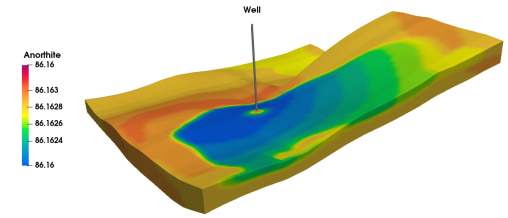

(e) Concentration of anorthite

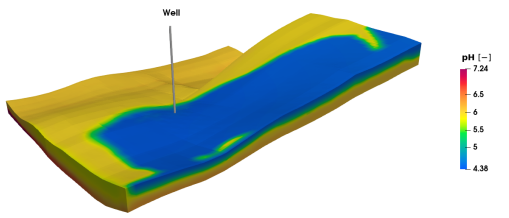

(f) pH

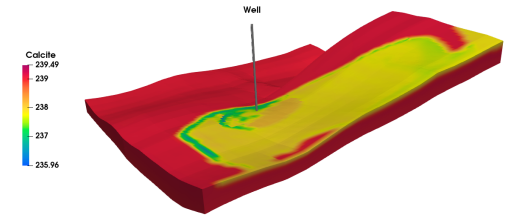

(g) Concentration of calcite

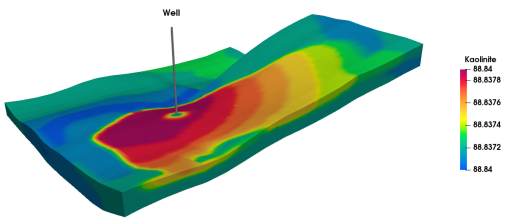

(h) Concentration of kaolinite

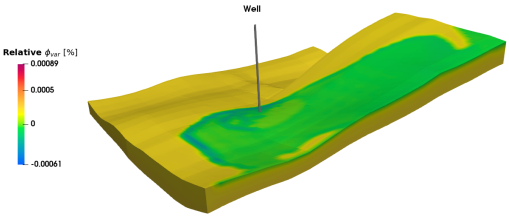

(i) Relative difference Porosity

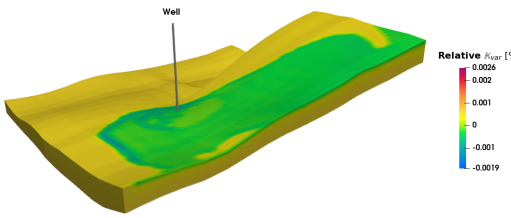

(j) Relative difference Permeability

Figure 3.40: Evolution of several quantities of interest at 300 years.

3.6 Conclusion

In this chapter, an extension of sequential and fully coupled fully implicit strategies to THC processes is proposed. For this purpose, the mathematical formula-

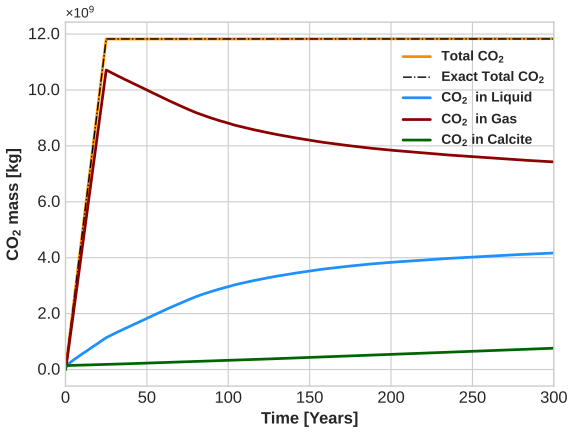

Figure 3.41: Long-term evolution of CO_2 quantities in the aquifer.

tion for nonisothermal multiphase multicomponent flow with reactive transport has been exposed and discretised with a finite volume scheme. The implementation of both strategies was performed on the same simulation platform $DuMu^X$, which has allowed us to validate our model on several numerical test cases involving CO_2 sequestration scenarios. Accounting for temperature effects results in increased dissolution of CO_2 and calcite, in the near-well and CO_2 plume regions, respectively. This can enhance both well injectivity and dissolution trapping. Comparisons have also been made between the sequential and fully implicit approaches, highlighting the fact that the fully implicit approach is mass conservative. The sequential approach introduces a splitting error which degrades the accuracy of the scheme despite a gain in computational time. The long-term behaviour of the mineralisation has also been investigated and the results are consistent with the CO_2 sequestration literature. Furthermore, validations must be continued by considering other studies and benchmarks. Geomechanics is not taken into consideration in this study, but it should be considered for the assessment of the safety and durability of geological storage. Due to the localised temperature changes in the near-well regions, the latter should impact the mechanical effects more significantly. Finally, efforts have been made to provide a maximum of data and to ensure the reproducibility of the tests carried out in this study.

Chapter 4

Hydro-Mechanical processes coupled model for CO_2 storage

Contents

4.1 Introduction 90
4.2 Fundamental terms in geomechanics 90
4.3 Mathematical model for Hydro-Mechanical coupling . . 93
4.3.1 Momentum balance equation 93
4.3.2 Constitutive relations and constraints 94
4.3.3 Mass balance equation 95
4.3.4 Closure relations 96
4.4 Numerical scheme for Hydro-Mechanical coupling . . . 97
4.5 Conclusion 101

4.1 Introduction

In general, CO_2 storage problems are described as multiphase flow problems coupled with other processes depending on the desired complexity. In this thesis, the interest is mainly focused on hydro-mechanical (HM) processes based on the coupling of linear poroelastic and two-phase flow describing the evolution of CO_2. The field of geomechanics makes it possible to characterise the behavior of the host rock, its integrity, and the stresses to which it is subjected during the injection. This chapter presents the mathematical models used to define isothermal two-phase flow in porous media coupled with geomechanics. First, the fundamental terms needed to correctly define the mathematical problem are introduced in Section 4.2. Then the isothermal model describing a two-phase flow coupled with mechanical deformations is detailed in Section 4.3. In this model, the governing equations are mainly given by the coupling of a mechanical equilibrium equation and a mass conservation law describing the flow, under the assumptions of quasi-static strains and slightly compressible flow. Finally, the numerical scheme including the discretisation of the latter model is presented in Section 4.4.

4.2 Fundamental terms in geomechanics

In the field of geomechanics, and more specifically in the field of poroelasticity, there are three fundamental terms that allow us to describe the behavior of the rock matrix. These terms are strongly correlated thanks to the relationships that define them. When a fluid is injected into a geological formation, it causes an increase in pressure in the surrounding area, which then spreads throughout the formation. The increase in pressure also leads to the deformation of the rock matrix under the stress created by the injection.

Stress

In continuum mechanics, the Cauchy stress tensor σ (also called the stress tensor) is the force exerted on a unit volume of material [152]. It describes the magnitude of the forces that cause deformation and quantifies the perturbation of lithostatic conditions [72]. It is measured in Pascal as units of pressure. There are three different types of stress, such as normal or compressive stress, tensile stress, and shear or tangential stress. Compression stress involves forces pushing against each other in the direction of the porous rock. Tensile stress involves forces pulling in opposite directions, while shear stress involves transverse forces. Ultimately, the total stress in a material is defined by the sum of the different types of stress acting on it.

Strain

The strain or deformation tensor denoted ε, represents the deviation in length of a porous medium from an initial state [152]. The different types of stress applied to a rock result in different types of deformation. For example, compressive force causes compaction of the medium and is manifested as folding and thickening of

the rock. The tensile force causes strain, which stretches and thins the rock, and the tangential force causes movement between two opposing blocks or regions of the material moving in different directions [72].

In the case of linear elasticity, a stress-strain relationship can be formulated using a fourth-order tensor $\mathbb{C}$ composed of 81 entries, which relates each stress component linearly to each strain component. It is called the stiffness matrix and the stress-strain relation is written as:

$$\sigma = \mathbb{C} : \varepsilon. \tag{4.2.1}$$

Displacement

The displacement vector $\vec{u}$ in a porous medium describes the motion of the rock, in particular the simultaneous translation and rotation influenced by the mechanical conditions applied to the medium. This characterisation of displacement does not include changes in the shape or size of the rock. In general, the displacement vector $\vec{u} = \{u_x, u_y, u_z\}$ is considered the primary variable in solving geomechanical problems.

Poisson's ratio and Young modulus

In linear elasticity, in the case of an isotropic material where all axes are materially identical, the description of the mechanical response of the rock is expressed in terms of two elastic constants:

- Young's modulus E [Pa] is the constant ratio of stress and strain during elastic deformation.
- Poisson's ratio ν [-] is the dimensionless ratio of transverse compressive strain to longitudinal extensional strain in the direction of the stretching force. This parameter is less than 0.5, at which point the solid becomes incompressible.

Because of symmetry and energy considerations, but also because of the assumption of isotropy, the stiffness matrix can be reduced to two independent entries E and ν. Therefore the stress-strain relation Eq. (4.2.1) can be expressed as:

$$\begin{pmatrix} \sigma_{xx} \\ \sigma_{yy} \\ \sigma_{zz} \\ \sigma_{xy} \\ \sigma_{yz} \\ \sigma_{xz} \end{pmatrix} = \frac{E}{(1+\nu)(1-2\nu)} \begin{pmatrix} 1-\nu & \nu & \nu & & & \\ \nu & 1-\nu & \nu & & & \\ \nu & \nu & 1-\nu & & & \\ & & & 1-2\nu & & \\ & & & & 1-2\nu & \\ & & & & & 1-2\nu \end{pmatrix} \begin{pmatrix} \varepsilon_{xx} \\ \varepsilon_{yy} \\ \varepsilon_{zz} \\ \varepsilon_{xy} \\ \varepsilon_{yz} \\ \varepsilon_{xz} \end{pmatrix} \tag{4.2.2}$$

Lamé parameters

In the isotropic case, it is possible to reformulate Eq. (4.2.2) with the help of two other constants λ and μ $[Pa]$ called Lamé parameters:

$$\lambda = \frac{E\,\nu}{(1+\nu)(1-2\nu)}, \qquad \mu = \frac{E}{2(1+\nu)}. \tag{4.2.3}$$

The latter provides a simplified formulation of the stress-strain relationship as Hooke's law [109]:

$$\sigma = 2\,\mu\varepsilon + \lambda\varepsilon_{\mathbf{v}}\mathbf{I_d}, \tag{4.2.4}$$

where $\varepsilon_{\mathbf{v}} = tr(\varepsilon) = \nabla \cdot \vec{u}$ is the volumetric strain.

Sign convention for mechanics

Sign conventions are a standardised set of widely accepted rules that provide a consistent method of setting up, solving, and describing solutions in the field of mechanics. There are two different ways of expressing such a law. On the one hand, continuum mechanics are accustomed to stating that normal stress is positive for components denoting tension, while negative normal components denote compression. For shear stress, it is assumed that rotation of the material in a counterclockwise direction indicates a positive shear stress [216]. On the other hand, the sign convention in rock mechanics is that positive normal stress indicates compression and negative normal stress indicates tension.

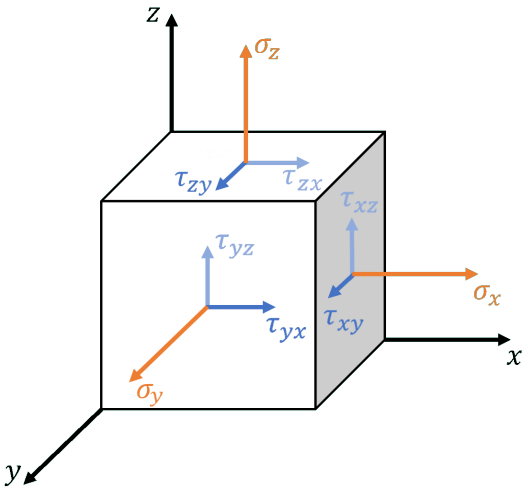

Figure 4.1: Continuum mechanics sign convention for stress

In our modelling approach, the sign convention of continuum mechanics is adopted according to Figure 4.1.

4.3 Mathematical model for Hydro-Mechanical coupling

The governing equations for the coupled flow and geomechanics are derived from the conservation of mass and the balance of linear momentum. Some assumptions are formulated by assuming small deformations, the geomaterial is isotropic and isothermal conditions are imposed. For further references on geomechanical models, the reader is referred to [57, 66, 152, 207].

4.3.1 Momentum balance equation

The deformation of the solid matrix is described by a quasi-stationary momentum balance equation, which leads to an overall equilibrium of the solid-fluid mixture given by [57]:

$$\nabla \cdot \sigma + \rho_b \overrightarrow{g} + \overrightarrow{f} = \rho_b \frac{\partial^2 \overrightarrow{u}}{\partial t^2}, \tag{4.3.1}$$

where σ_{eff} is the effective stress, $\overrightarrow{g}$ is the gravitational acceleration constant, $\overrightarrow{f}$ [N.m^{-1}] is the external force acting on the body per unit volume. ρ_b [kg.m^{-3}] is the effective density defined as:

- $\rho_b = \phi\rho_l + (1-\phi)\,\rho_s$ for single-phase flow, (4.3.2)
- $\rho_b = \phi\sum_{\alpha} S_\alpha\rho_\alpha + (1-\phi)\,\rho_s$ for multiphase flow. (4.3.3)

The assumption of quasi-stationary momentum balance leads to neglecting the acceleration term $\rho_b \frac{\partial^2 \overrightarrow{u}}{\partial t^2} \approx 0$. In addition, $\overrightarrow{f} = \overrightarrow{0}$ is also assumed.

As defined in Terzaghi's theory [199], it is possible to decompose the effective stress as the difference between the total stress σ driven by mechanical deformations and the pore pressure fluid imposed:

$$\sigma = \sigma_{\text{eff}} + P_{\text{eff}}\,\mathbf{I_d}, \tag{4.3.4}$$

where $\mathbf{I}_d$ is the second-order identity tensor of dimension d. This formulation assumes the sign convention of soil mechanics (i.e. compressive stresses are negative).

In the case of single-phase flow, the effective pressure P_{eff} is only characterised by the single-phase pressure. However, in the case of multiphase flow, the effective pore pressure is more likely to be defined as:

$$P_{\text{eff}} = \sum_{\alpha} S_\alpha P_\alpha. \tag{4.3.5}$$

According to Biot's theory of poroelasticity [38], the effective pressure is taken into account by describing the stress of the solid phase with the effective stress tensor:

$$\sigma = \sigma_{\text{eff}} + \alpha_B P_{\text{eff}} \mathbf{I}, \tag{4.3.6}$$

where α_B represents the Biot-Willis coefficient. The latter coefficient can be seen as a quantifier of the change in stress with increasing fluid pressure at constant pore volume or, symmetrically, as a quantifier of the change in pore volume with increasing pressure at constant stress. It is defined as:

$$\alpha_B = 1 - \frac{K_{dr}}{K_s}, \tag{4.3.7}$$

with K_{dr} and K_s designating respectively the drained bulk modulus and the bulk modulus of the solid. For $K_s \to \infty$, Biot's formulation coincides with Terzaghi's definition of the effective stress.

4.3.2 Constitutive relations and constraints

In this work, linear poroelasticity is assumed. Therefore, a constitutive relation is added to the system that allows defining the effective stress as a function of the strain thanks to Hooke's law [109]:

$$\sigma_{\text{eff}} = 2\,\mu\varepsilon + \lambda \nabla \cdot \vec{u}\,\mathbf{I_d}. \tag{4.3.8}$$

By applying the small strain theory, which considers the regime of small deformations, it is possible to linearise the strain tensor thanks to the solid skeleton displacement vector $\vec{u}$, such as:

$$\varepsilon = \frac{1}{2}\left(\nabla\vec{u} + \nabla^T\vec{u}\right) \tag{4.3.9}$$

Porosity variations

There are several descriptions to characterise porosity variations due to pressure and displacement changes. One of the most commonly used is the one defined for example in [141, 142]:

$$\phi_{\text{eff}} = \frac{1}{M} P_{\text{eff}} + \alpha_B \nabla \cdot \vec{u}, \tag{4.3.10}$$

where M [Pa] is the Biot modulus. The Biot porosity model is also used, in particular in GEOSX [183], where the porosity depends on the initial porosity ϕ_0, the volumetric strain ε_v and the effective pressure P_{eff}:

$$\phi_{\text{eff}} = \phi_0 + \alpha_B \nabla \cdot (\vec{u} - \vec{u}_0) + \frac{P_{\text{eff}} - P_0}{N}, \tag{4.3.11}$$

with $N = \dfrac{K_s}{\alpha_B - \phi_0}$.

Another model, developed in [53] and used in [32, 43], makes use of volumetric strain such as:

$$\phi_{\text{eff}} = 1-(1-\phi_0)\,e^{-\nabla\,\cdot\,\vec{u}}. \tag{4.3.12}$$

However, like in [103, 173], where a residual porosity ϕ_r, a constant a, and the effective mean stress σ'_m are introduced, it is possible to find a porosity law with:

$$\phi_{\text{eff}} = (\phi_0-\phi_r)\;e^{a\,\sigma'_m} + \phi_r. \tag{4.3.13}$$

Finally, we can mention the model used in [97] and particularly in *DuMu*^{X} [31], which is defined with the continuum mechanics sign convention as:

$$\phi_{\text{eff}} = \frac{\phi_0 + \nabla\cdot\vec{u}}{1+\nabla\cdot\vec{u}}. \tag{4.3.14}$$

Permeability variations

Similarly, several permeability variation laws are formulated in the literature. In particular, a permeability correlated to the porosity variation is proposed in [103, 173]:

$$\mathbb{K}_{\text{eff}} = \mathbb{K}_0\,\exp\left(c\,\frac{\phi_{\text{eff}}}{\phi_0-1}\right), \tag{4.3.15}$$

where $\mathbb{K}_0$ is the initial permeability and c is an empiric parameter obtained by correlation with laboratory measurements. A power law related to Eq. (4.3.12) has also been developed in [53], which allows us to determine how strong changes in porosity affect permeability with respect to the exponent n, ranging from 3 to 25:

$$\mathbb{K}_{\text{eff}} = \mathbb{K}_0\left(\frac{\phi_{\text{eff}}}{\phi_0}\right)^n. \tag{4.3.16}$$

In the *DuMu*^{X} simulation platform, the Kozeny-Carman [49] relation was chosen to account for variations in permeability:

$$\mathbb{K}_{\text{eff}} = \mathbb{K}_0\left(\frac{1-\phi_0}{1-\phi_{\text{eff}}}\right)^2\left(\frac{\phi_{\text{eff}}}{\phi_0}\right)^3. \tag{4.3.17}$$

The various relationships presented above to characterise porosity and permeability variations are a non-exhaustive list of what is found in the literature to take into account the geomechanical response to flow.

4.3.3 Mass balance equation

As presented previously in Section 2.4, the mass conservation of a component i in a liquid or gaseous fluid phase α is given as:

$$\frac{\partial\,\phi S_\alpha\rho_\alpha x^i_\alpha}{\partial t} + \nabla\cdot\left(\rho_\alpha x^i_\alpha\overrightarrow{q_\alpha} - \phi\rho_\alpha S_\alpha D_\alpha\nabla x^i_\alpha\right) = 0,\; i\in\{CO_2,H_2O\}\;\text{and}\;\alpha\in\{l,g\}. \tag{4.3.18}$$

Due to geomechanics, the solid part of the porous medium in which the fluid or gas flows must be taken into account. For this reason, it is necessary to couple effective variables that depend on the displacement of the solid skeleton using in particular, the effective porosity ϕ_{eff} and the permeability $\mathbb{K}_{\text{eff}}$. These considerations are then incorporated into a modified Darcy-Muskat equation that characterises the velocity of each phase:

$$\vec{q_\alpha} = -\mathbb{K}_{\text{eff}} \frac{k_{r\alpha}(S_\alpha)}{\mu_\alpha} (\nabla P_\alpha - \rho_\alpha^{mass} \vec{g}). \tag{4.3.19}$$

By inserting Eq. (4.3.19) into Eq. (4.3.18), and modifying the porosity by effective law Eq. (4.3.14) involving the displacement $\vec{u}$, this leads to the following mass conservation law:

$$\frac{\partial \phi_{\text{eff}} S_\alpha \rho_\alpha x_\alpha^i}{\partial t} + \nabla \cdot \left(\rho_\alpha x_\alpha^i \overrightarrow{q_\alpha} - \phi_{\text{eff}} \rho_\alpha S_\alpha D_\alpha \nabla x_\alpha^i \right) = 0, i \in \{CO_2, H_2O\} \text{ and } \alpha \in \{l, g\}. \tag{4.3.20}$$

4.3.4 Closure relations

The flow part of the system needs to consider closure relations to fully characterise the primary variables depending on the number of unknowns. For this purpose, total constraints on saturations and molar fractions are provided:

$$\sum_\alpha S_\alpha = 1 \quad \text{and} \quad \sum_i x_\alpha^i = 1, \alpha \in \{l, g\}, \tag{4.3.21}$$

but also the capillary pressure already defined as:

$$P_c(S_l) = P_g - P_l. \tag{4.3.22}$$

As in the Thermal-Hydro-Chemical coupling model Section 2.8, some equations of state are added to characterise the fluid properties as a function of pressure, temperature, and salinity.

Boundary conditions

Finally, the primary variables of the model are the wetting phase pressure p_l, the non-wetting phase saturation S_g, the molar fractions x_i^α and the solid displacement vector $\vec{u}$ (changes in solid displacement with respect to initial conditions).

The previous set of partial differential equations are valid over a domain Ω, but they must be supplemented with appropriate boundary conditions over the boundary $\Gamma = \partial\Omega$ in order to close the system.

For the flow problem, depending on the model, the classical Neumann or Dirichlet boundary conditions can be enforced for the liquid pressure P_l, the gas saturation S_g, and the molar fractions x_i^α.

For the geomechanical problem, two different types of boundary conditions can be imposed:

- Dirichlet boundary conditions which prescribe known displacement values u_D^m on the boundary domain such as $\overrightarrow{u} \cdot \overrightarrow{n} = u_D^m$ on Γ_D^m,
- Neumann boundary conditions which prescribe forces on the boundary domain such as $\sigma \cdot \overrightarrow{n} = \overrightarrow{0}$ for free-movement boundaries and $\sigma \cdot \overrightarrow{n} = \overrightarrow{f_N^m}$ for an oriented force acting on the surface Γ_N^m.

Finally, the full linear poroelasticity model coupled with a multiphase flow is defined by:

- partial differential equations modelling the mass conservation laws with a compositional two-phase flow:

$$\frac{\partial}{\partial t}\left(\phi_{\text{eff}} S_\alpha \rho_\alpha x_\alpha^i\right) + \nabla \cdot \left(\rho_\alpha x_\alpha^i \overrightarrow{q_\alpha} - \phi_{\text{eff}} \rho_\alpha S_\alpha D_\alpha \nabla x_\alpha^i\right) = 0, \tag{4.3.23}$$

- one partial differential equation modelling the momentum balance equation:

$$\nabla \cdot \sigma + \rho_b \overrightarrow{g} = \overrightarrow{0}, \tag{4.3.24}$$

- constitutive relation of linear poroelasticity with Biot's definition of the effective stress:

$$\sigma = \sigma_{\text{eff}} + \alpha_B P_{\text{eff}} \mathbf{I_d}, \tag{4.3.25}$$

- constitutive relation of the total stress with Hooke's law:

$$\sigma_{\text{eff}} = 2\mu\varepsilon + \lambda\varepsilon_{\mathbf{v}}\mathbf{I_d}. \tag{4.3.26}$$

4.4 Numerical scheme for Hydro-Mechanical coupling

Once the model used for Hydro-Mechanical coupling has been properly exposed, it is necessary to provide a numerical scheme suitable for approximating the desired model in order to implement it in a numerical environment. This section details the numerical scheme used to solve the Hydro-Mechanical coupled processes. In particular, some details of the discretisation are exposed before giving the fully discretised model.

Due to the time independence of the poromechanical balance equation, the time discretisation concerns only the flow subproblem. In this part, a fully implicit Euler scheme is used to replace the time differential with a backward difference approximation.

As presented in Section 1.2.4.2, several discretisation methods can be set up to discretise an HM coupling. Most studies deal with either full finite element methods for both subproblems or finite volume and finite element methods for flow and poromechanics respectively. Here the cell-centered finite volume method presented in Section 3.3.2 for THC model is considered for the discretisation of Eq. (4.3.23) governing the compositional two-phase flow while a Control Volume Finite Element Method (CVFEM) is used for the discretisation of Eq. (4.3.24), Eq. (4.3.25)

and Eq. (4.3.26) modeling the poroelasticity equations. As a consequence, primary variables are computed for each subproblem on different degrees of freedom. More precisely, the $N_{elements}$ global degrees of freedom for the flow primary variables $(S_\alpha, P_\alpha, x^i_\alpha)$ are evaluated at the centers of elements composing the mesh and the N_{nodes} global degrees of freedom for the poromechanical primary variables (u_x, u_y, u_z) are evaluated at the nodes of the mesh.

The CVFEM was studied in [25, 51, 58, 95] and gives good results with efficient numerical stability. In the context of flow in porous media, this method has been shown to be effective in solving multiphase flow approaches in heterogeneous domain [50, 70, 71, 84, 85, 89, 105, 147, 175, 176]. Nevertheless, this approach also presents numerical drawbacks in particular because of large sparsity patterns in the matrix that affect significantly the computational time [180]. More precisely, we consider here a Box method, which has been used to solve complex flow processes in porous media, see for example [83, 91, 99, 104]. *DuMu*^{X} natively supports this type of approach, which discretises the poromechanical part of the coupling. The box method is a widely used discretisation approach in several numerical environments because it inherits features from both finite volume and finite element methods. It therefore satisfies conservative principles [99]. The box method is a mixture of a vertex-centered finite volume method and a continuous Galerkin finite element method [81]. In fact, the main idea of this method is to construct a dual mesh of new control volumes surrounding each node of the primary mesh.

Before giving the discretisation details for each subproblem, some notations need to be defined. The notation B_i is introduced for the box surrounding the node i at coordinate $\mathbf{x}_i$ (see Figure 4.2 (a)). Then each box is divided into subcontrol volumes, introduced as SB_i. Figure 4.2 (b) shows that these subcontrol volumes are constructed using the node i, the barycenter of the elements of the primary mesh to which the node i belongs, and the midpoint of the faces of the elements. Furthermore, $\vec{n}_{ij}$ is the unit outer normal to the interface ξ_{ij} between the subcontrol volume SB_i and B_j, which is a neighboring box of B_i.

The main idea of the box method consists in calculating the fluxes at each interface ξ_{ij} of the box B_i. The box scheme uses piecewise (per primary mesh element) linear basis functions φ_i as first-order Lagrangian polynomials such that:

$$\varphi_i(\mathbf{x}_j) \;=\; \delta_{ij}, \tag{4.4.1}$$

in order to approximate variables within the primary mesh elements. δ_{ij} denotes the Kronecker symbol. For instance, any scalar function $\tilde{v}$ can be decomposed using Lagrangian interpolation as:

$$\tilde{v}(\mathbf{x}) \;=\; \sum_{i=1}^{N_{nodes}} \tilde{v}(\mathbf{x}_i)\, \varphi_i(\mathbf{x}). \tag{4.4.2}$$

To deal with the elasticity problem, which is vector-based, vectorial functions $\vec{\tilde{v}}$ are decomposed as:

$$\vec{\tilde{v}} = \left(\tilde{v}_x,\, \tilde{v}_y,\, \tilde{v}_z\right)^T,$$

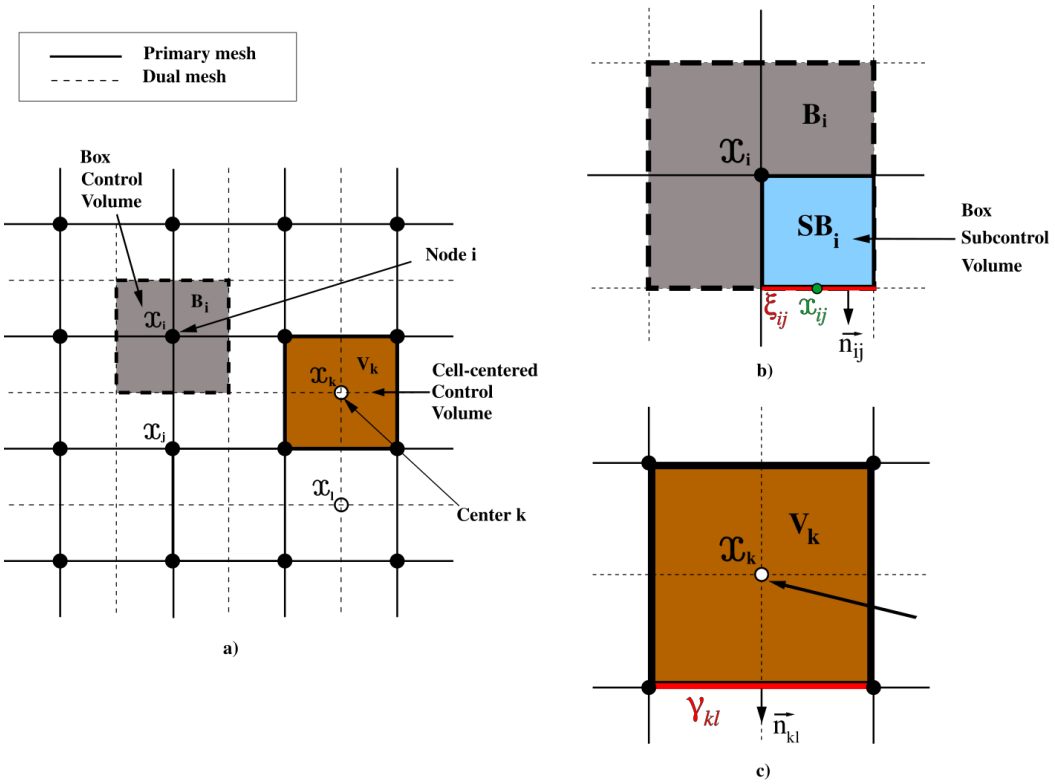

Figure 4.2: Schematic of the discretisation of a control volume with the Box method.

$$= \Big(\sum_{i=1}^{N_{nodes}} \tilde{v}_x(\mathbf{x}_i)\varphi_i(\mathbf{x}), \sum_{i=1}^{N_{nodes}} \tilde{v}_y(\mathbf{x}_i)\varphi_i(\mathbf{x}), \sum_{i=1}^{N_{nodes}} \tilde{v}_z(\mathbf{x}_i)\varphi_i(\mathbf{x}) \Big)^T. \tag{4.4.3}$$

Finally, to provide a discretisation of the coupled problem, the integration for the cell-centered finite volume method is realised on each control volume V_k of the mesh for Eq. (4.3.23). In the box scheme, on the other hand, the integration is performed on each box control volume B_i for Eq. (4.3.24). By using the formalism established in Section 3.3.2 and Section 4.4, the fully coupled fully implicit discretisation scheme is given by:

- Cell-centered finite volume discretisation for the compositional two-phase flow subproblem:

$$\frac{|V_k|}{\Delta t^n}\Big(\{\phi_{\text{eff}}\}_k^{n+1}\{S_\alpha\rho_\alpha x_\alpha^i\}_k^{n+1} - \{\phi_{\text{eff}}\}_k^{n}\{S_\alpha\rho_\alpha x_\alpha^i\}_k^{n}\Big) + \sum_{l|V_k\cap V_l\neq\emptyset} |\gamma_{kl}|\Big(\{\rho_\alpha x_\alpha^i\}_{kl}^{n+1}\{\vec{q}_\alpha\}_{kl}^{n+1} - \{D_\alpha\}_{kl}^{n+1,har}\{\rho_\alpha\nabla x_\alpha^i\}_{kl}^{n1}\Big)\cdot\vec{n}_{kl} = 0, \tag{4.4.4}$$

$$\{\vec{q}_\alpha\}_{kl}^{n+1} = -\{\mathbb{K}_{\text{eff}}\}_{kl}^{har}\Big\{\frac{k_{r\alpha}(S_\alpha)}{\mu_\alpha}\Big\}_{kl}^{n+1,up}\Big(\{\nabla P_\alpha\}_{kl}^{n+1} - \{\rho_\alpha^{mass}\}_{kl}^{n+1,ari}\vec{g}\Big), \tag{4.4.5}$$

As previously for the discretisation of the THC processes, terms in convective fluxes are approximated by using a fully upwinding scheme, thus unknown

quantities (S_α, P_α, x^i_α, $k_{r\alpha}$) are evaluated implicitly and upstream at the interface γ_{kl} depending on the velocity of the phase $\{\vec{q}_\alpha\}$:

$$\{\ \cdot\ \}^{n+1,up}_{kl} = \begin{cases} \{\ \cdot\ \}^{n+1}_{k} & \text{if} \quad \{\vec{q}_\alpha\}^{n+1}_{kl} \cdot \vec{n}_{kl} > 0, \\ \{\ \cdot\ \}^{n+1}_{l} & \text{else.} \end{cases}$$

Discrete gradients are computed by using either Two-Point Flux Approximation (TPFA) or Multiple Point Flux Approximation (MPFA) depending on the nature of the mesh. Different average methods are used to calculate some quantities between two neighboring elements, for example, a harmonic average is used for $\left\{\mathbb{K}_{\text{eff}}\right\}^{har}_{kl}$ and $\left\{D_\alpha\right\}^{n+1,har}_{kl}$ while an arithmetic average is used for $\left\{\rho^{mass}_\alpha\right\}^{n+1,ari}_{kl}$.

Moreover, the approximation of the term $\left\{\phi_{\text{eff}}\right\}^{n+1}_{k}$, which depends on $\nabla \cdot \vec{u}$, needs to approximate the quantity $\nabla \cdot \vec{u}$ at the point $\mathbf{x}_k$, the barycenter of V_k. Consequently, using the approximation for vectorial functions defined in Eq. (4.4.3), $\nabla \cdot \vec{u}$ is approximated by:

$$\left(\nabla \cdot \tilde{\vec{u}}\right)(\mathbf{x}_k) = \Big(\sum_{i=1}^{N_{nodes}} \tilde{u}_x(\mathbf{x}_i) \frac{\partial \varphi_i}{\partial x}(\mathbf{x}_k) + \sum_{i=1}^{N_{nodes}} \tilde{u}_y(\mathbf{x}_i) \frac{\partial \varphi_i}{\partial y}(\mathbf{x}_k) + \sum_{i=1}^{N_{nodes}} \tilde{u}_z(\mathbf{x}_i) \frac{\partial \varphi_i}{\partial z}(\mathbf{x}_k) \Big) \tag{4.4.6}$$

- Box finite volume discretisation for the linear poroelastic subproblem: integrating the Eq. (4.3.24) over B_i and applying the Green formula leads to:

$$\int_{\partial B_i} (\sigma_{\text{eff}} + \alpha_B\, P_{\text{eff}}\, \mathbf{I_d}) \cdot \vec{n}_{\Xi}\, dV + \int_{B_i} \rho_b \vec{g}\, dV = 0, \tag{4.4.7}$$

where $\vec{n}_{\Xi}$ stands for the outer normal of the box B_i. Then, the integrals over the boundary ∂B_i and B_i are decomposed as:

$$\begin{aligned} &\sum_{SB_i} \sum_{j | SB_i \cap B_j \neq \emptyset} |\xi_{ij}| \left(\left\{\sigma_{\text{eff}}\right\}^{n+1}_{ij} + \alpha_B \left\{ P_{\text{eff}} \right\}^{n+1}_{ij} \mathbf{I_d} \right) \cdot \vec{n}_{ij} \\ &+ \sum_{SB_i} \left(\int_{SB_i} \rho_b\, dV \right) \vec{g} = 0, \end{aligned} \tag{4.4.8}$$

with:

$$\left\{\sigma_{\text{eff}}\right\}^{n+1}_{ij} = \mu \left(\left\{\nabla \vec{u}\right\}^{n+1}_{ij} + \left\{\nabla^T \vec{u}\right\}^{n+1}_{ij} \right) + \lambda \left\{\nabla \cdot \vec{u}\right\}^{n+1}_{ij} \mathbf{I_d}. \tag{4.4.9}$$

More specifically, the details of the terms that require special treatment are set out below.

– The term $\{P_{\text{eff}}\}_{ij}^{n+1}$ necessitates to approximate on the interface ξ_{ij} (see Figure 4.2 (b)) the effective pressure computed by the compositional two-phase flow subproblem. It is evaluated at the point $\mathbf{x}_{ij}$ using the value of the effective pressure of the cell-centered control volume $V_{\bar{k}}$ to which belongs the subcontrol volume SB_i as:

$$\left\{P_{\text{eff}}\right\}_{ij}^{n+1} = \sum_{\alpha} \left\{S_\alpha\right\}_{\bar{k}}^{n+1} \left\{P_\alpha\right\}_{\bar{k}}^{n+1} \text{ such as } SB_i \cap V_{\bar{k}} \neq \emptyset. \tag{4.4.10}$$

– The integral $\int_{SB_i} \rho_b \, dV$ is approximated as:

$$\int_{SB_i} \rho_b \, dV = |SB_i| \, \{\rho_b\}_{\bar{k}}^{n+1} \text{ such as } SB_i \cap V_{\bar{k}} \neq \emptyset.$$

ρ_b is assumed to be constant on the subcontrol volume SB_i and is approximated by the value of the effective density computed by the compositional two-phase flow subproblem on the cell-centered control volume $V_{\bar{k}}$ to which belongs the subcontrol volume SB_i.

– As a consequence of Eq. (4.4.3), the gradient of the displacement $\nabla \overrightarrow{u}$ is approximated by:

$$\nabla \widetilde{\overrightarrow{u}} = \begin{pmatrix} \sum_{i=1}^{N_{nodes}} \tilde{u}_x(\mathbf{x}_i) \dfrac{\partial \varphi_i}{\partial x}(\mathbf{x}) & \sum_{i=1}^{N_{nodes}} \tilde{u}_y(\mathbf{x}_i) \dfrac{\partial \varphi_i}{\partial x}(\mathbf{x}) & \sum_{i=1}^{N_{nodes}} \tilde{u}_z(\mathbf{x}_i) \dfrac{\partial \varphi_i}{\partial x}(\mathbf{x}) \\ \sum_{i=1}^{N_{nodes}} \tilde{u}_x(\mathbf{x}_i) \dfrac{\partial \varphi_i}{\partial y}(\mathbf{x}) & \sum_{i=1}^{N_{nodes}} \tilde{u}_y(\mathbf{x}_i) \dfrac{\partial \varphi_i}{\partial y}(\mathbf{x}) & \sum_{i=1}^{N_{nodes}} \tilde{u}_z(\mathbf{x}_i) \dfrac{\partial \varphi_i}{\partial y}(\mathbf{x}) \\ \sum_{i=1}^{N_{nodes}} \tilde{u}_x(\mathbf{x}_i) \dfrac{\partial \varphi_i}{\partial z}(\mathbf{x}) & \sum_{i=1}^{N_{nodes}} \tilde{u}_y(\mathbf{x}_i) \dfrac{\partial \varphi_i}{\partial z}(\mathbf{x}) & \sum_{i=1}^{N_{nodes}} \tilde{u}_z(\mathbf{x}_i) \dfrac{\partial \varphi_i}{\partial z}(\mathbf{x}) \end{pmatrix}. \tag{4.4.11}$$

Then, in the approximation defined in the discretised constitutive relation of σ (Eq. (4.4.9)), the quantity $\left\{\nabla \vec{u}\right\}_{ij}^{n+1}$ is computed on the interface ξ_{ij} using the approximation defined in Eq. (4.4.11) and evaluated at the point $\mathbf{x}_{ij}$. The transposed gradient and divergence terms in Eq. (4.4.9) follow the same rules and are approximated in the same way at the point $\mathbf{x}_{ij}$.

Finally, the boundary and the initial conditions for both subproblems complete the finite volume discretisation which are not detailed here.

4.5 Conclusion

This chapter has been devoted to introducing the isothermal compositional two-phase flow model coupled with linear poroelasticity in this thesis. Firstly, the basic geomechanical terminology has been presented to set the context of the variables and constitutive relations used in porous media. The geomechanical model is then presented to introduce the equations derived from the momentum balance equation. Some constitutive laws are introduced to characterise the effective and total stresses using linear poroelasticity. The flow model is described by the mass conservation law written as an isothermal compositional two-phase flow. Therefore,

the coupling between these two subproblems is done by means of effective variables. Consequently, a strongly nonlinear system of coupled PDEs is formulated in Hydro-Mechanical coupled processes. In addition, the discretisation of the coupled model is given in detail. A cell-centered finite volume scheme is formulated for the discretisation of the compositional two-phase flow, while a box scheme is performed for the poroelasticity discretisation.

Chapter 5

Numerical simulation of Hydro-Mechanical processes

Contents

5.1 Introduction 104
5.2 Resolution strategies 104
5.2.1 Fully coupled approach 104
5.2.2 Sequential methods 105
5.2.3 Two-step procedure for solution strategy 106
5.2.4 Implementation 106
5.3 Numerical simulations 106
5.3.1 Consolidation problems 107
5.3.2 Hydro-Mechanical simulations for CO_2 storage 115
5.4 Conclusion 135

5.1 Introduction

Numerical codes integrating a Hydro-Mechanical coupling have become common, particularly for commercial software such as GEM [3], ABAQUS [189], etc... Nevertheless, it is also possible to encounter open-source codes, which provide either an all-in-one approach or coupled software that can work together thanks to an interface. One can mention for example Code_Aster [63], TOUGH-FLAC3D [166], OpenGeoSys [120], GEOSX [183], DARTS [2], etc ... *DuMu*^{X} , in its latest versions [119], falls into the latter category by integrating a coupling management interfacing both hydraulic and mechanical processes.

This chapter outlines the methodology used to tackle the problems associated with typical CO_2 storage problems. First, resolution strategies are discussed in order to understand how the coupled problem is handled. In addition, the establishment of a resolution procedure necessary to perform computations in the *DuMu*^{X} simulation platform is detailed later in this section. Finally, several test cases involving consolidation theory are discussed to validate the coupling, but also CO_2 injection scenarios. Further comparisons with other software are undertaken to provide a kind of benchmarking comparison on CO_2 injection problems, but also to ensure accurate results from the coupling approach on *DuMu*^{X} .

5.2 Resolution strategies

The Hydro-Mechanical coupling literature provides various resolution methods, in particular fully coupled and sequential approaches. Both give accurate results in terms of accuracy and computational time. However, most industrial reservoir software tends to consider sequential coupling for performance reasons. In addition, a degree of coupling can also be considered for geomechanical feedback with one or two-way coupling methods.

5.2.1 Fully coupled approach

The fully coupled strategy consists of solving the flow and geomechanics subproblems simultaneously by considering a single system. In fact, the unknowns p_g, S_l (eventually x_α^i for compositional flows), and $\vec{u}$ are solved simultaneously for each time step. Therefore, the flow equations are coupled to the momentum balance equation due to the dependence of the porosity/permeability on the displacement $\vec{u}$ (Eq. (4.3.14) and Eq. (4.3.17)). Conversely, the poromechanical equations are related to the flow equations by effective variables depending on fluid pressures and saturations (Eq. (4.3.5) and Eq. (4.3.2) or Eq. (4.3.3)). Figure 5.1 (a) shows the algorithm to solve such a fully coupled strategy.

Numerically, a Jacobian matrix must be computed, consisting of pure flow and poromechanics on its diagonal blocks and extra-diagonal block terms representing coupling contributions. This strategy leads to systems that are more complex to solve numerically but guarantee better accuracy.

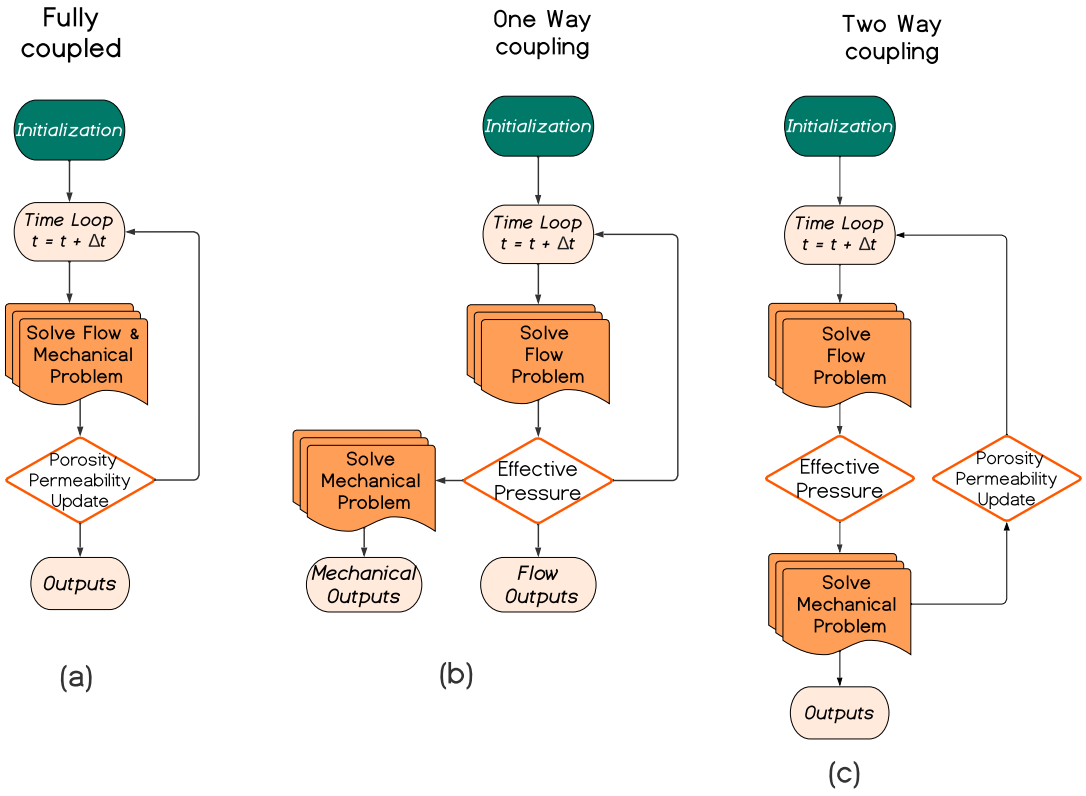

Figure 5.1: Algorithms of fully coupled, one-way, and two-way coupling approaches to solve Hydro-Mechanical problems.

5.2.2 Sequential methods

One and two-way coupling

In fact, there are two different approaches to quantifying the degree of coupling. On the one hand, one-way coupling is the simplest way to run a coupled model with a low degree of coupling. It consists of solving the flow and geomechanical subproblems separately, as shown in Figure 5.1 (b). Only the effective pressure acting on the porous medium is transferred to the geomechanical subproblem. There is no feedback from the geomechanical calculations to the flow subproblem. In general, this approach is used to get a general idea of the displacements. On the other hand, the two-way coupling method is more difficult to set up because it involves a porosity and permeability update that affects the flow at the next iteration Figure 5.1 (c). In turn, effective variables such as body forces and fluid pressures are communicated to the poromechanical solver to calculate a new stress state. However, the bidirectional coupling approach is often preferred because variations in porosity and permeability allow the geomechanical feedback to be reflected in the coupling.

In this work, we consider the fully coupled method to deal with the HM coupling.

5.2.3 Two-step procedure for solution strategy

In *DuMu*^{X}, the solution strategy is determined by solving a two-step procedure. In fact, it is necessary for the solver that the global problem is well defined in order to achieve convergence. The strategy for achieving that is splitting the solution into two steps. First, in order to solve the mechanical problem, the area under consideration must undergo an initial stress state that is well-posed with respect to the geological conditions [20]. In fact, lithostatic stress must be calculated during the initialisation period in order to correctly set up the poromechanical problem. Lithostatic stress is the vertical stress resulting from the weight of the overlying rock and sediment layers in the Earth's crust. This stress is an important parameter in geomechanical analysis, as is the horizontal stress, which is often defined as a ratio of the vertical stress. A fixed initial time step is used to calculate these conditions, which are necessary for the simulation to start with a convergence of the nonlinear solver. In order not to impact the problem, this initial time step is considered very small, in the order of 10^{-9} s. In addition, a delay in the start of the injection is taken into account so that no stress associated with the injection is introduced initially.

Once the different stress values have been correctly initialised, the second step of the procedure can be started where the injection can begin. The global simulation has normally overcome convergence problems due to initialisation with a small time step. The latter can be slightly increased thanks to the variable strategy already revealed in Section 3.4.1.

In conclusion, the framework presented above has allowed the implementation, simulation, and testing of this type of Hydro-Mechanical coupling model in *DuMu*^{X}.

5.2.4 Implementation

All the implementation of the models has been performed on the *DuMu*^{X} simulation platform as detailed in Section 3.4.1. The latest *DuMu*^{X} release features a framework for multi-domain simulations, where each subdomain is represented by an individual model. The coupling between flow and poroelastic is handled by the multi-domain assembly called "*el2p*" which stands for *elastic* and *two-phase flow*.

For the assembly of the Jacobian matrix, it provides a general multi-domain assembler implementation, in which the matrix entries are computed by means of numeric differentiation. The direct solver UMFPack [62] is used to solve the linear systems of equations related to the linearisation of the Newton-Raphson process. It provides good computational capabilities for solving linear systems due to the large matrix construction involved in the coupling.

5.3 Numerical simulations

According to the previously presented framework for modelling the Hydro-Mechanical coupling, we have been able to perform numerical simulations to validate the model. In fact, these validations have been carried out on known consolidation

processes. This type of coupling has then been tentatively applied to CO_2 storage problems to investigate the mechanical effects of gas injection in suitable geological formations.

5.3.1 Consolidation problems

In general, when soils are subjected to vertical loading, porosity decreases, resulting in less space available for pore water, which is forced to move to where pore space is available. This process is known as consolidation. In the literature there are generally three famous problems: Terzaghi's problem, Mandel's problem, and Cryer's problem. These three tests are designed to gradually increase dimensional complexity and cover the typical range of consolidation problems. They also offer the advantage of the existence of analytical solutions, which are useful to produce accurate verification and thus validate the model coupling. For further studies and applications of consolidation theories, some references are given in [40, 94, 110, 182, 207, 226].

5.3.1.1 One-dimensional consolidation

The first problem that we consider is the well-known Terzaghi consolidation formulated in [199]. Generally, the purpose of this problem is to test the accuracy of the numerical code for fluid-to-solid coupling [110]. It consists of a 1D vertical column of height H, considered a fully saturated porous medium. At the start of the experiment, a constant downward force is applied to the upper boundary. This loading force will result in a drained response of the fluid due to an open-top surface. Therefore, the boundary conditions for the flow problem consist of impermeable boundaries at the bottom and side surfaces, resulting in a homogeneous Neumann condition. The top is open to drainage, so a homogeneous Dirichlet condition is imposed on the pressure. The boundary conditions of the poromechanical problem are considered roller conditions, which means that the normal displacement is set to zero. To express the loading force, a constant stress is applied to the top with a Neumann boundary condition. Also, the effects of gravity are not considered in this problem. A 2D schematic overview of the problem configuration is given in Figure 5.2, as well as the data used to reproduce the case.

Initially, the domain is considered to be fully saturated with water. Consequently, a single-phase flow model is considered to solve this problem. The simulation time was set to 200 s with a constant time step $\Delta t = 1$ s. Figure 5.3 represents the pressure evolution at several times.

After the initial time, the column compacts and the pore pressure rises to its undrained value due to the sudden application of load, also known as the Skempton effect [110, 188]. The load then tends to reduce the liquid pressure over time, as shown by Figure 5.3. In fact, the fluid is allowed to drain through the upper surface due to the boundary condition imposed. The reduction in fluid pressure increases the compressive stress in the beam and produces a consolidation effect. This phenomenon has a name: the drained response. When the fluid pressure reaches zero everywhere, the consolidation process stops and the sample is in a steady state.

Constitutive law or variable	Symbol	Parameters	Unit
Height	H	10	[m]
Length	L	1	[m]
Cell size	ΔH	0.01	[m]
Cell size	ΔL	0.1	[m]
Porosity	ϕ	0.3	[-]
Permeability	$\mathbb{K}$	10^{-4}	[m^2]
Initial Pressure	p_0	1	[Pa]
Loading force	F	1	[Pa]
Poisson ratio	ν	0.2	[-]
Young modulus	E	10^4	[Pa]
Biot constant	α_B	1	[-]
Solid Density	ρ_s	2700	[kg.m^{-3}]
Liquid Density	ρ_l	1	[kg.m^{-3}]
Liquid Viscosity	μ_l	1	[Pa.s^{-1}]

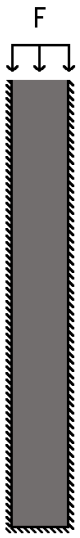

Figure 5.2: Table data and schematic configuration for the 1D consolidation problem.

The analytical solutions to the 1D consolidation have been proposed in [199] by using the Laplace transformation. The liquid pressure distribution is characterized by the formula:

$$p_l(y,t) = \frac{4}{\pi} p_0 \sum_{j=1}^{\infty} \frac{(-1)^{j-1}}{2j-1} \cos\left((2j-1)\frac{\pi}{2}\frac{y}{H}\right) \exp\left(-(2j-1)^2 \frac{\pi^2}{4}\frac{c_c t}{H^2}\right), \quad (5.3.1)$$

where $p_0 = p_l(y,0) = \dfrac{\alpha m_v}{1/M + \alpha^2 m_v} F$ [Pa], c_c [-] is the coefficient of consolidation and m_v [Pa^{-1}] is the confined compressibility of the porous medium.

The mechanical effects can be studied by introducing the degree of consolidation, a dimensionless measure of the state of consolidation, i.e. 0 for unconsolidated and 1 for fully consolidated. The degree of consolidation is defined analytically as:

$$U(t) = \frac{u_y - u_{y,0}}{u_{y,\infty} - u_{y,0}} = 1 - \frac{8}{\pi^2} \sum_{k=1}^{\infty} \frac{1}{(2k-1)^2} \exp\left(-(2k-1)^2 \frac{\pi^2}{4}\frac{c_c t}{H^2}\right), \quad (5.3.2)$$

where $u_{y,\infty} = \dfrac{HF}{2\mu + \lambda}$ is the final vertical displacement and $u_{y,0} = 0$ is the initial vertical displacement.

A comparison between analytical and numerical solutions of the pressure obtained with *DuMu*^{X} is proposed in Figure 5.4. The pressure drop over time closely follows the trend of the analytical values. These curves clearly show the drainage phenomenon through the top of the beam. The numerical solutions obtained are in agreement with the analytical solutions resulting from the coupling effect.

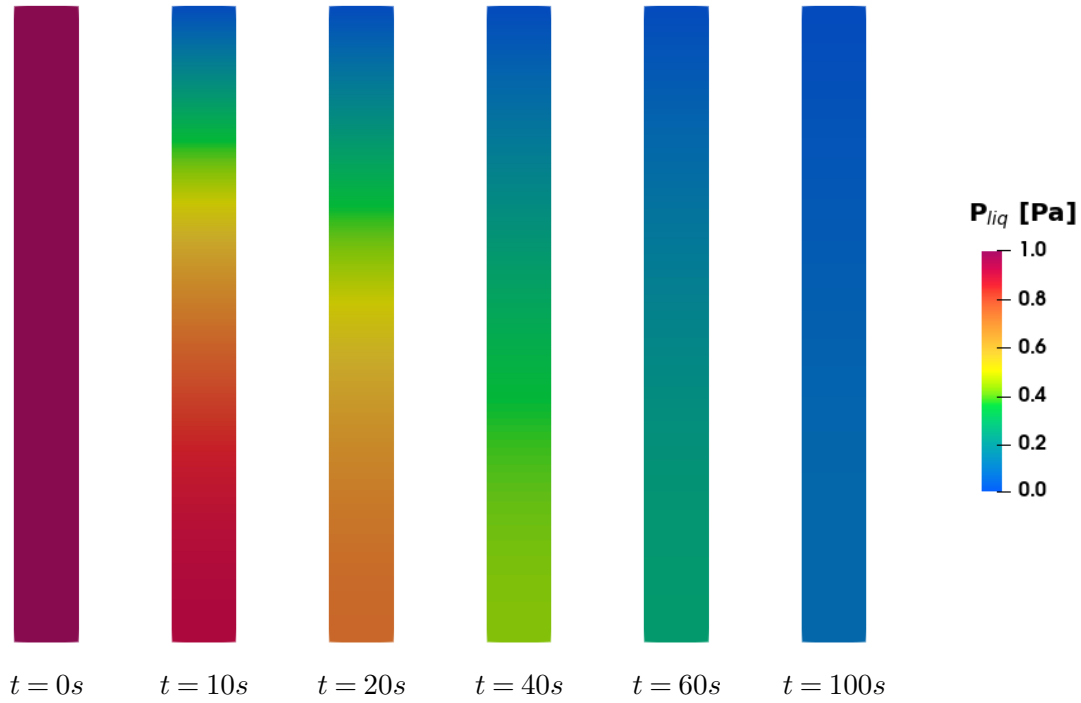

Figure 5.3: Representation of the pressure evolution at several times for Terzaghi's consolidation problem.

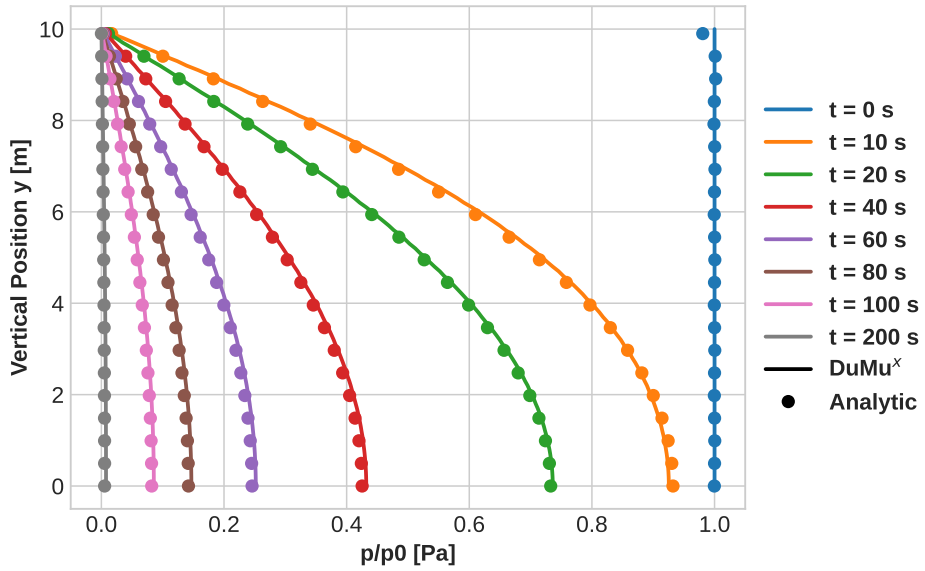

(a)

Figure 5.4: Evolution of the pressure as a function of the vertical position in the beam for several times.

5.3.1.2 Two-dimensional consolidation

The second problem described here is the well-known Mandel's problem. It was developed as a benchmark to test the validity of numerical codes for poroelasticity

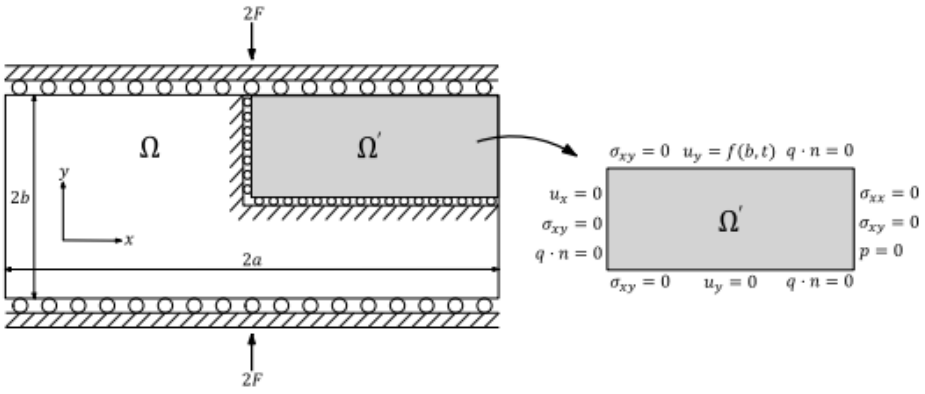

Figure 5.5: Configuration of the 2D consolidation problem (taken from [113]).

[10, 134]. This problem defines a 2D rectangular sample of saturated poroelastic material of width $2a$ and height $2b$ loaded by a constant compressive force of intensity $2F$ applied on rigid impervious plates at $y = \pm b$. The load is applied immediately after the initial time, as before. The sample is free to drain laterally at $x = \pm a$ and the lateral edges are stress-free. Due to the bi-axial symmetry of the problem, the computational domain is restricted to the quarter of the original physical domain, as shown in the schematic of the configuration in Figure 5.5. This figure also shows the boundary conditions necessary to describe the problem correctly. In fact, for the flow subproblem, no flow conditions are set on the left, top, and bottom boundaries with a homogeneous Neumann condition. The drainage phenomenon on the right side of the example is modelled by a zero-pressure Dirichlet boundary condition. The mechanical subproblem is described with zero normal displacements on the left and bottom boundaries, a freely moving boundary on the right with a Neumann condition on the stress, and a vertical displacement at the top set by using the analytical displacement value $u_y(b,t)$, expressed in Eq. (5.3.6). As in Terzaghi's problem, the domain is initially considered to be fully saturated with water, so a single-phase flow model is used to describe it. Table 5.1 gives all the data used to reproduce the simulation.

The initial pressure is given by:

$$p_l(x,0) \;=\; \frac{2FB(1+\nu_u)}{3a}. \tag{5.3.3}$$

The simulation time parameters are set to a step size of $\Delta t \;=\; 10s$ and a final time of $10000s$. The results are shown above in Figure 5.6 for different times.

The analytical solutions were originally given in [134] for pore pressure. Then [10] extended the analytical solutions to all fields, and in particular to horizontal and vertical displacements, given by:

$$p_l(x,t) \;=\; p_l(x,0)\sum_{n=1}^{\infty}\frac{\sin\alpha_n}{\alpha_n-\sin\alpha_n\cos\alpha_n}\left(\cos\frac{\alpha_n x}{a}-\cos\alpha_n\right)\exp\left(\frac{-\alpha_n^2 c_c t}{a^2}\right), \tag{5.3.4}$$

Constitutive law or variable	Symbol	Parameters	Unit
Length	a	100	[m]
Height	b	10	[m]
Cell size	Δx	1	[m]
Cell size	Δy	1	[m]
Porosity	ϕ	0.2	[-]
Permeability	$\mathbb{K}$	10^{-12}	[m^2]
Loading force	F	5×10^8	[$N.m^{-1}$]
Poisson ratio	ν	0.2	[-]
Undrained Poisson ratio	ν_u	0.44	[-]
Young modulus	E	5.94×10^9	[Pa]
Biot modulus	M	1.65×10^{10}	[Pa]
Biot constant	α_B	1	[-]
Skempton coefficient	B	0.833	[-]
Solid Density	ρ_s	2650	[$kg.m^{-3}$]
Liquid Density	ρ_l	998	[$kg.m^{-3}$]
Liquid Viscosity	μ_l	8.9×10^{-4}	[$Pa.s^{-1}$]

Table 5.1: Data for the 2D consolidation problem.

$$u_x(x,t) = \left[\frac{F\nu}{2Ga} - \frac{F\nu_u}{Ga}\sum_{n=1}^{\infty}\frac{\sin\alpha_n\cos\alpha_n}{\alpha_n - \sin\alpha_n\cos\alpha_n}\exp\left(\frac{-\alpha_n^2 c_c t}{a^2}\right)\right]x + \frac{F}{G}\sum_{n=1}^{\infty}\frac{\cos\alpha_n}{\alpha_n - \sin\alpha_n\cos\alpha_n}\sin\frac{\alpha_n x}{a}\exp\left(\frac{-\alpha_n^2 c_c t}{a^2}\right), \tag{5.3.5}$$

$$u_y(y,t) = \left[\frac{-F(1-\nu)}{2Ga} + \frac{F(1-\nu_u)}{Ga}\sum_{n=1}^{\infty}\frac{\sin\alpha_n\cos\alpha_n}{\alpha_n - \sin\alpha_n\cos\alpha_n}\exp\left(\frac{-\alpha_n^2 c_c t}{a^2}\right)\right]y. \tag{5.3.6}$$

G stands for the shear modulus also designated by the second Lamé parameters μ. c_c is the consolidation coefficient defined by:

$$c_c = \frac{2\,\kappa\,G\,(1-\nu)(\nu_u-\nu)}{(1-\nu_u)(1-2\nu)^2}, \tag{5.3.7}$$

where κ is the ratio of permeability to viscosity. Furthermore, α_n represents the positive roots of the nonlinear equation to be solved numerically:

$$tan\,\alpha_n = \frac{1-\nu}{\nu_u-\nu}\alpha_n. \tag{5.3.8}$$

For comparison with the analytical values, the liquid pressure values have been extracted from a line crossing the domain in the x direction. Figure 5.7 and Figure 5.8 compare the analytical and numerical results for several times.

Figure 5.7 clearly shows two different trends in the results. The first trend is represented by a pressure increase for short times and a maximum 10 % rise is

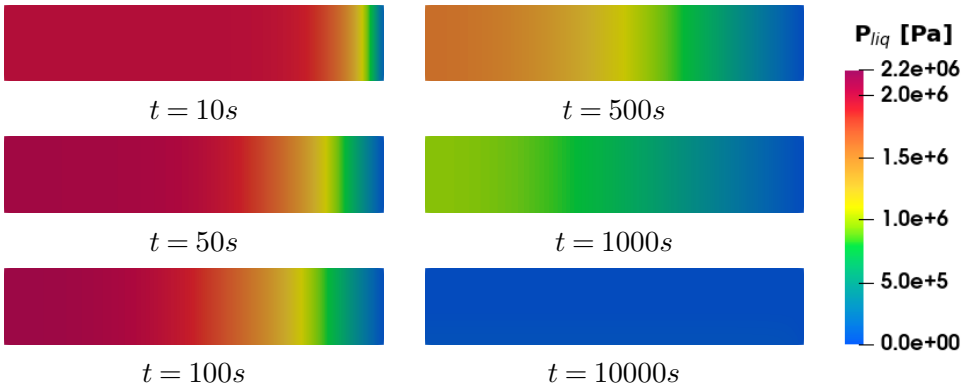

Figure 5.6: Representation of the pressure evolution at several times for Mandel's consolidation problem.

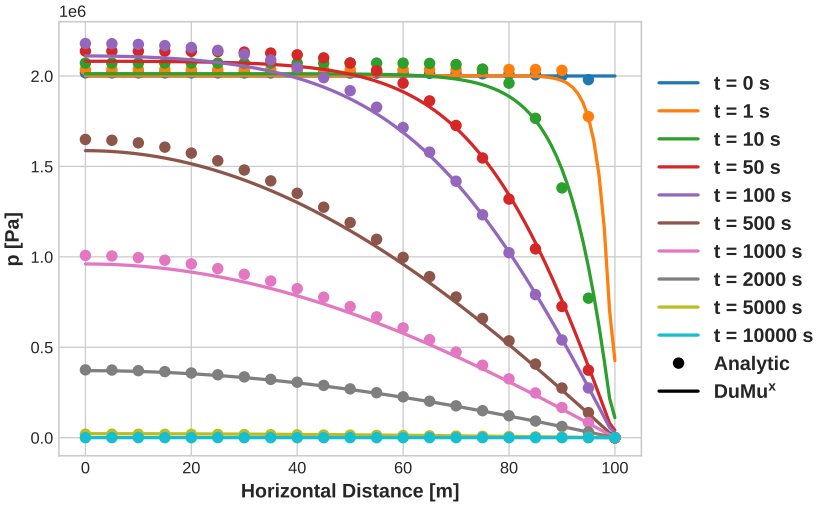

Figure 5.7: Evolution of the liquid pressure for the 2D consolidation as a function of time.

reached at about 100 s. This increase is mainly due to undrained conditions and is identified as the Mandel-Cryer effect [134]. This phenomenon demonstrates a nonmonotonic pressure response under constant boundary conditions and highlights the coupling effects between fluid flow and geomechanics that cannot be captured by uncoupled models. Finally, after some time, the second trend appears as a gradual decrease in pressure until consolidation is achieved. The material is then completely drained by the boundary condition. The results presented here are in agreement with the analytical values, therefore the consolidation phenomena are well captured in our simulation platform.

5.3.1.3 Three-dimensional consolidation

The third consolidation problem that allows the verification of coupling effects is Cryer's problem [59]. It consists of a poroelastic, spherical, porous medium fully saturated by a fluid. Hence a single-phase flow is considered as in the last two

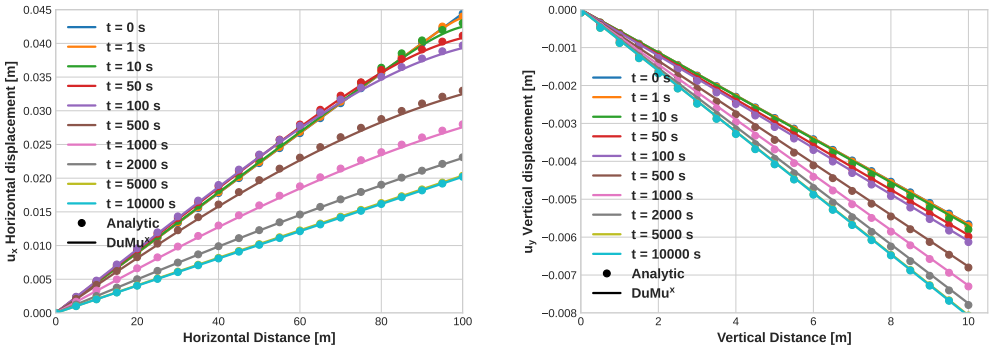

Figure 5.8: Evolution of horizontal and vertical displacements as a function of time.

consolidation problems. Figure 5.9 gives a schematic of the case configuration. The tri-axial symmetry allows the domain study to be limited to one octant of a sphere. The curved surface is instantaneously loaded by a constant force and also defines a drained region through which the fluid can flow. However, the plane surfaces are fixed to prevent normal displacements.

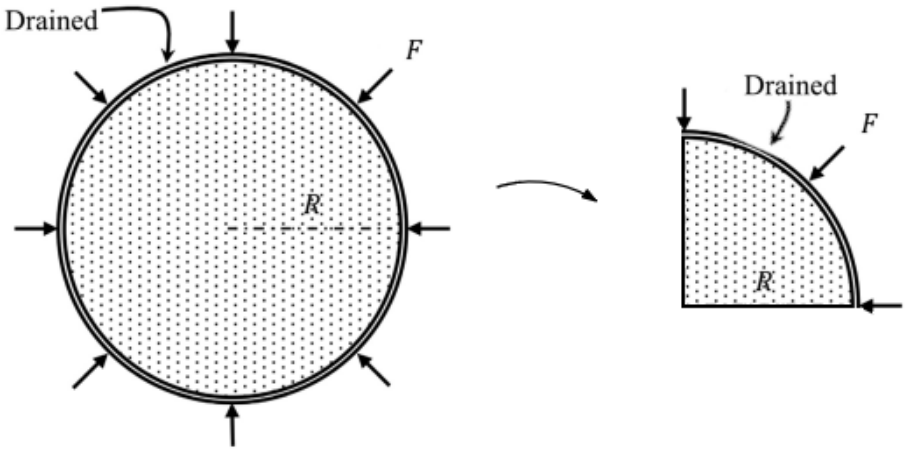

Figure 5.9: Configuration of Cryer's consolidation problem [94].

Initially, zero pressure is considered throughout the domain as well as zero displacements. A constant compressive force F is applied at the initial time, generating a pressure increase due to mechanical coupling. The flow boundary conditions are described by:

$$\frac{\partial p_l}{\partial n} = 0 \text{ on } \Gamma_{\text{plane}}\,, \tag{5.3.9}$$

$$p_l \cdot \vec{n} = 0 \text{ on } \Gamma_{\text{curve}}\,, \tag{5.3.10}$$

the latter reflecting a drained condition where the fluid can flow through the spherical boundary. In addition, poromechanical boundary conditions for planar and curved surfaces are set as:

$$\vec{u} \cdot \vec{n} = 0 \text{ on } \Gamma_{\text{plane}} , \tag{5.3.11}$$

$$\sigma \cdot \vec{n} = F \text{ on } \Gamma_{\text{curve}} , \tag{5.3.12}$$

where F is the constant load applied to the curved surface. The data used to reproduce the case are given in Table 5.2. Several values have been considered for the Poisson ratio.

Constitutive law or variable	Symbol	Parameters	Unit
Sphere radius	R	1	[m]
Porosity	ϕ	0.2	[-]
Permeability	$\mathbb{K}$	10^{-12}	[m^2]
Loading force	F	1000	[Pa]
Initial pressure	p_0	0	[Pa]
Poisson ratio	ν	$\{0.1, \ldots, 0.4\}$	[-]
Young modulus	E	10^7	[Pa]
Biot constant	α_B	1	[-]
Solid Density	ρ_s	2500	[kg.m^{-3}]
Liquid Density	ρ_l	1000	[kg.m^{-3}]
Liquid Viscosity	μ_l	1×10^{-3}	[Pa.s^{-1}]
Fluid compressibility	c_f	0.0	[Pa^{-1}]

Table 5.2: Data for Cryer's problem.

At $t = 0.01$ s, a sudden rise in pressure is captured due to the application of compressive force to the outer surface, as can be seen in Figure 5.10. It can be seen that the increase corresponds exactly to the load value. At later stages, the Mandel-Cryer effect can also be seen. Indeed, the pressure rises above the value imposed by the compressive load in the central region of the sphere, where the maximum is reached at about 4 s. This non-monotonic increase in pressure is mainly due to a transfer of the load towards the center of the sphere, which becomes effectively stiffer as a result of the consolidation process. Then, under the effect of the drainage boundary condition, the pressure gradually dissipates. Finally, the spherical domain returns to its initial pressure state when consolidation is complete.

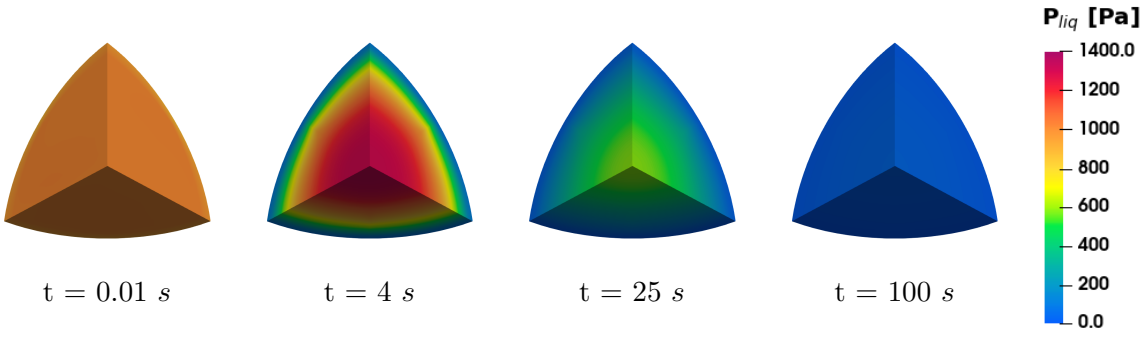

Figure 5.10: Evolution of the liquid pressure in the domain as a function of time.

As in the previous consolidation problems, analytical solutions have been derived using Laplace transforms in [207]. The analytical pressure at the center of the sphere is given by the following formula:

$$p_l(r=0,t) \;=\; \eta\, p_0 \sum_{n=1}^{\infty} \frac{\sin\alpha_n - \alpha_n}{\eta\alpha_n\, \cos\alpha_n/2 \,+(\eta-1)\sin\alpha_n} \exp\left(\frac{-\alpha_n^2 c_c t}{R^2}\right), \qquad (5.3.13)$$

where η, p_0 and c_c are defined respectively by:

$$\eta \;=\; \frac{\lambda+2G}{2G}, \qquad p_0 \;=\; \frac{\alpha\, F}{\alpha^2+K\, S_e}, \qquad c_c \;=\; \frac{\mathbb{K}}{\mu_l}\,\frac{K_v}{K_v\, S_e+\alpha^2},$$

where S_e is the specific storage, K and K_v are the bulk and uni-axial bulk moduli, defined as:

$$S_e \;=\; \frac{(\alpha-\phi)(1-\phi)}{K}+\phi\, c_f, \qquad K \;=\; \frac{E}{3(1-2\,\nu)}, \qquad K_v \;=\; \frac{E\,(1-\nu)}{(1+\nu)(1-2\nu)}.$$

α_n represent the n positive roots of the equation that needs to be solved numerically:

$$\left(1-\eta\frac{\alpha_n^2}{2}\right)\tan\alpha_n \;=\; \alpha_n, \qquad (5.3.14)$$

Figure 5.11 shows the time evolution of the pressure at the center of the sphere for four values of the Poisson coefficient. The results are in good agreement with the analytical solutions shown by the dashed lines, but also with the literature, in particular in [24]. It is noticeable that the non-monotonic pressure rise, known as the Mandel-Cryer phenomenon, is affected by the value of Poisson's coefficient. For small values of ν, the pressure rise appears to be more pronounced and to occur later than for large values of ν.

Conclusion of consolidation processes

Consequently, the proposed mathematical model and numerical framework have been verified for their ability to capture the coupling effect induced by fluid flow and geomechanical interactions, using the well-known consolidation examples of a fluid-saturated poroelastic medium. This coupling effect is mainly related to the Mandel-Cryer phenomenon, which reflects a significant nonmonotonic pressure increase that needs to be considered for flow problems in geological formations.

5.3.2 Hydro-Mechanical simulations for CO_2 storage

In general, geomechanical field studies help to explain phenomena such as reservoir compaction, subsidence, rock failure, pore collapse, or wellbore stability [201]. Numerical simulations are therefore an excellent tool to provide a priori investigations that approximate the phenomena that occur in real processes. When this field is specifically applied to the modelling of CO_2 sequestration, it generally gives an

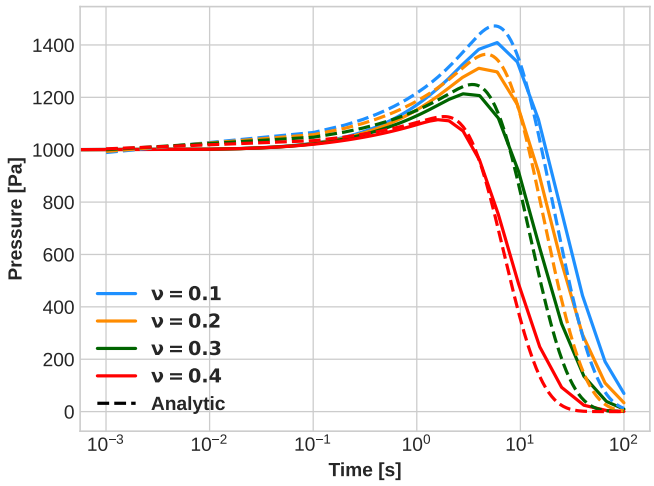

Figure 5.11: Comparison of the evolution of the pressure for different values of the Poisson coefficient as a function of time.

idea of the vertical displacement captured by injection. In fact, the behaviour of the host rock is mainly influenced by injection because it significantly increases the pore pressure. This increase leads to rock displacements that can affect the stability of the overburden or induce fractures that create preferential pathways for leakage. This section considers three CO_2 injection scenarios based on layered heterogeneous formations.

5.3.2.1 Test 1: 2D domain involving a heterogeneous band

The first test case concerning the hydro-mechanical coupling to be investigated is based on the work of [31]. The development of the case was carried out with an old version of $DuMu^X$, where simulations were computed with a different solver approach. In fact, the fluid flow subproblem was computed using a box finite volume scheme, while the geomechanical subproblem was solved using a finite element approach based on a DUNE library (Dune-PDELAB). From version 3 onwards, a complete revision of the simulation platform was carried out, resulting in a different way of formulating the problems [119]. The main aim of this work was to ensure that the results obtained by the above approach were consistent with those originally produced in [31].

Configuration of the problem

The problem defined in [31] investigates a CO_2 injection scenario in a layered formation. This formulation is quite consistent with real-world scenarios, as the injected CO_2 is structurally trapped due to a high degree of heterogeneity in permeability and/or porosity. However, the problem specifies two different subcases of varying complexity. The first consists of a single aquifer surrounded by two caprocks, while the second involves a "fracture" considered as a small heterogeneous band passing through the aquifer at 500 m of injection at an angle of 80 °C.

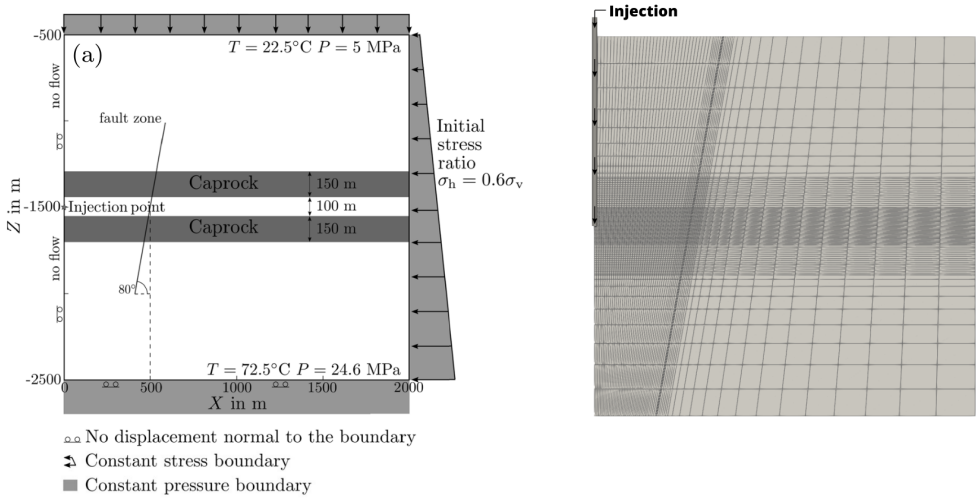

Figure 5.12: Configuration for the "fracture" test case (a) and the mesh used (b) (taken from [31]).

Figure 5.12 depicts the configuration of the problem with the "fracture" as well as the mesh used to perform simulations. The mesh used for the calculation is not perfectly K-orthogonal and is slightly distorted due to the fault consideration. As a result, an MPFA scheme is performed for the finite volume discretisation of the flow problem. In both cases, the area is considered to be a square with sides of 2 km, where the top layer is at 500 m deep. A 100 m aquifer is located in the middle of the domain surrounded by two caprocks of 150 m height. An injection well is drilled on the left part of the domain and perforated in two cells in the middle of the aquifer. A hydrostatic pressure gradient is imposed varying from 5 MPa at the top to 24.6 MPa at the bottom. In the same way, a temperature gradient is fixed from 295.65 to 345.65 K. Temperature effects are not considered in this work, but the temperature is necessary to characterise fluid properties. Boundary conditions are also depicted in Figure 5.12. For the flow problem, a Dirichlet boundary condition to initial values is set on top, bottom, and right boundaries. A null-flux is imposed to the left boundary in order to maintain the CO_2 plume within the domain due to injection in the left part. Concerning geomechanical boundary conditions, no normal displacements are set to the left and bottom boundaries in horizontal and vertical directions respectively. The top and right boundaries are free to move with the help of a Neumann condition also used to fix vertical and horizontal stresses by imposing forces. The formula to impose such stress is given by the lithostatic state:

$$\sigma_v = \rho_l \, \phi \, g \, (d - z) + (1 - \phi) \, \rho_s \, g \, (d - z), \tag{5.3.15}$$

where d and z are the depth and the vertical position respectively. In this case, the depth is fixed at 1500 m. A ratio of $\sigma_h = 0.6 \, \sigma_v$ is applied to initialize the horizontal stress. Several parameters are introduced in Table 5.3 for the mechanical constitutive law, which depend on the layer depth and are prescribed for the small heterogeneous band acting as a "fracture". However fluid properties are exposed in Table 5.4. The simulation is run over 1800 days with a CO_2 continuous injection.

In order to avoid numerical divergence of solvers, the two-step procedure is used with an initial time step $\Delta t = 1 \times 10^{-9}$ s. Then, the time step is increased with the variable time step strategy already exposed. The tolerance for the Newton-Raphson methods is fixed to 10^{-6}.

Mechanical constitutive law	Symbol	Aquifer	Caprock	Fault	Unit
Porosity	ϕ	0.1	0.01	0.1	[-]
Permeability	$\mathbb{K}$	10^{-13}	10^{-19}	10^{-15}	[m^2]
Poisson ratio	ν	0.25	0.25	0.25	[-]
Young modulus	E	10^{10}	10^{10}	5×10^9	[Pa]
Biot constant	α	1	1	1	[-]
Solid Density	ρ_s	2260	2260	2260	[kg.m^{-3}]

Table 5.3: Mechanical data for case modelling from [31].

Fluid constitutive law	Symbol	Parameters	Unit
Injection Rate	Q_{inj}	0.02	[kg.s^{-1}]
Liquid Density	ρ_l	1000	[kg.m^{-3}]
Liquid Viscosity	μ_l	1×10^{-3}	[Pa.s^{-1}]
Residual saturation	S_{rl}	0.2	[-]
Residual saturation	S_{rg}	0.05	[-]
Van Genuchten	α	5.025×10^{-5}	[-]
Van Genuchten	n	1.8462	[-]
Brine salinity	s_{sal}	0.1	[kg/kg]

Table 5.4: Fluid data for case modelling from [31].

Numerical results

Figure 5.13 (a) and Figure 5.14 (a) give the numerical results for the flow at 5 years, obtained taking into account the Hydro-Mechanical coupling. The results are quite similar to those obtained in [31] (b). Indeed, in both cases, the injected gaseous CO_2 quickly rises to the top layer due to buoyancy caused by the difference in density between the gaseous and liquid phases. The top caprock structurally traps the CO_2 plume and prevents any upward movement. Advection then causes the plume to move laterally within the domain. A slight difference in gaseous saturation appears at the front of the CO_2 plume between (a) and (b), which does not reach the right boundary in the saturation profiles. This can be explained by the different numerical schemes: in [31] a CVFE (box scheme) is applied for the flow discretisation, while in our approach an MPFA is used. In addition, an immiscible two-phase flow is taken into account for the description of the fluid flow, which results in a different contribution of the CO_2 dissolution. The overpressure is computed by differentiation with the initial state of the liquid pressure. Due to injection, the aquifer is subjected to a greater pressure increase, which can lead to a failure of the caprock integrity if the rise reaches a significant level. Concerning the geomechanical results, Figure 5.15 (a) and Figure 5.16 (a) highlight horizontal and vertical displacements undergone by the host rock. The vertical uplift captured is

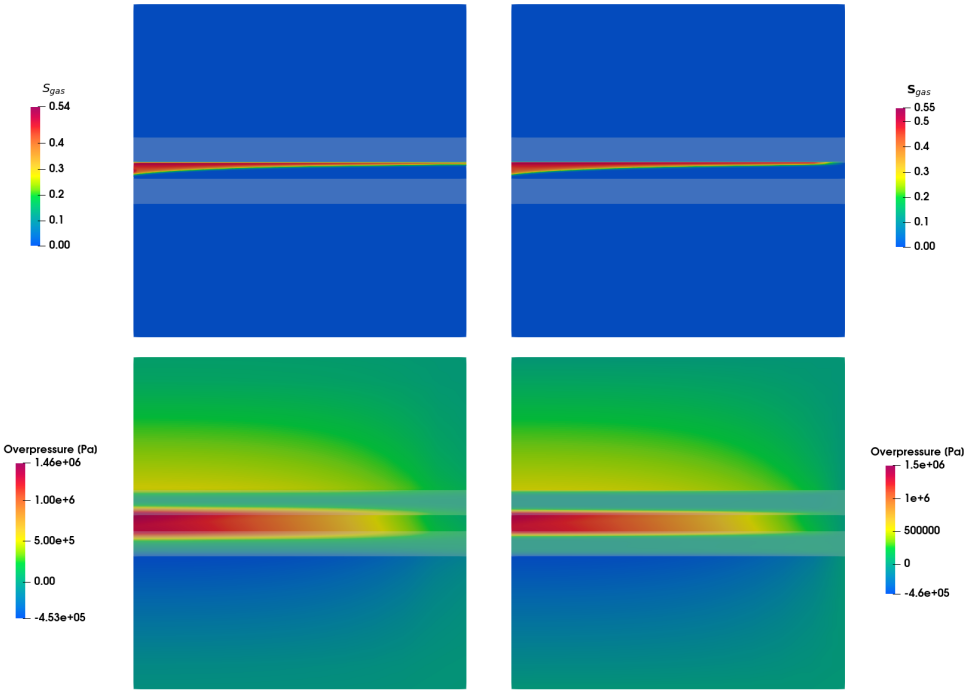

(a) (b)

Figure 5.13: Gaseous saturation and overpressure profiles obtained with *DuMu*^{X} (a) and from [31] (b) for the case without "fracture" at the final time.

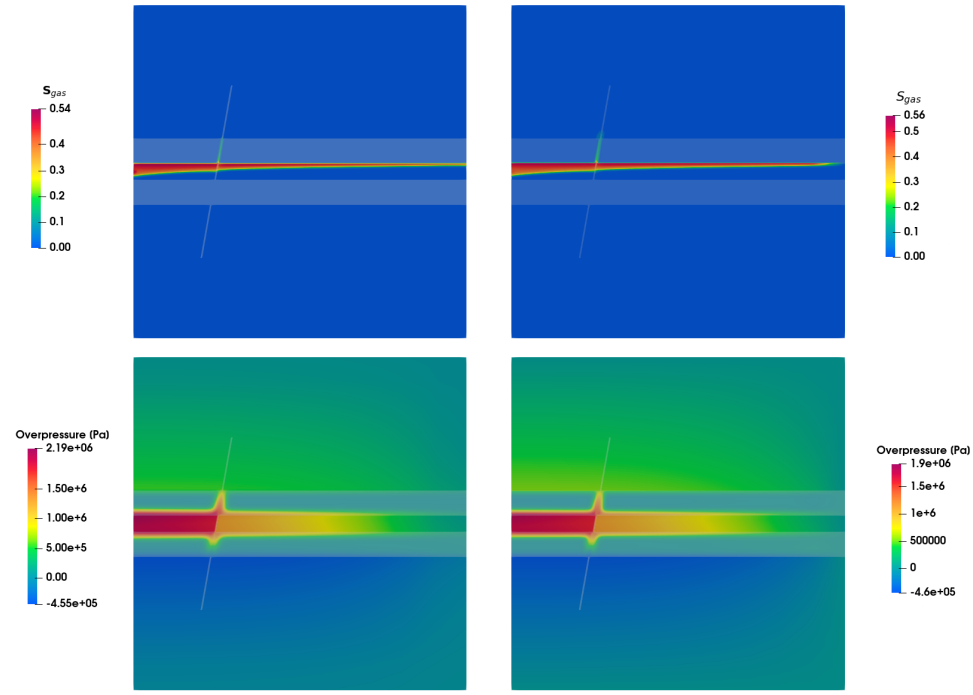

(a) (b)

Figure 5.14: Gaseous saturation and overpressure profiles obtained with *DuMu*^{X} (a) and from [31] (b) for the case with a "fracture" at the final time.

mainly located from the ground surface to the top caprock. The values of horizontal displacements are quite similar to those obtained in [31], however, the values of vertical displacements seem to be more affected by the differences in formulation and schemes. Indeed, in [31], an incremental formulation describes the geomechanical problem which is different from the total formulation implemented in the current *DuMu*^{X} version. Furthermore, a finite element method was used to discretise the geomechanical problem, as opposed to a CVFE in our approach.

Comparison between the presence and absence of a fracture

The two configurations can be compared to understand the effects of the presence or absence of "fracture" on flow and geomechanical behaviour. In fact, in Figure 5.14 (a), once the plume reaches the "fracture", a small amount of gaseous CO_2 leaks through and overflows into the upper aquifer. Although the leak represents a small amount of CO_2 due to the short time simulation, the plume continues to expand laterally until it reaches the right boundary. In terms of pressure profiles, an overpressure of 30 % is recorded in the presence of a "fracture", which appears to maintain this increase in the area between the injection well and the "fracture". With regard to the geomechanical results, the vertical displacements are even more pronounced due to the higher overpressure in the case of "fracture" and can reach values twice as high. Horizontal displacements are not much affected and are almost similar in both cases. On the effective stress profiles, the injection tends to induce a swelling of the rock described as tensile stress. The same effect as the pressure is observed where the "fracture" maintains the stress increase in the area between the borehole and the "fracture".

A comparison is made between the variations in pressure and porosity between [31] and the approach developed here. In fact, a vertical plot is performed on the left side of the domain. Values are extracted from bottom to top and plotted varying from left to right. According to Figure 5.17 (a), the main pressure variations are captured within the aquifer layer between the two caprocks shown in grey. The presence of a small heterogeneous band seems to increase the pressure even more, up to 0.15%. Porosity variations occur mainly at the boundary of two different regions as shown in Figure 5.17 (b). Major movements are at the boundary between caprock and aquifer where a porosity decrease of 1.5% is recorded.

Finally, the framework set up to simulate CO_2 injection problems in the HM coupling seems to give results that are consistent with previous studies. Although the results are quite close to those obtained in [31], it is clear that the same global behaviour is well captured. The differences may be potentially explained by the fact:

- *DuMu*^{X} used an incremental formulation for the poromechanical problem at the time. Indeed, it divides the analysis into a series of incremental steps, each increment representing a small change or perturbation in the system. The analysis proceeds incrementally by solving the governing equations for each step. This formulation also makes use of a linearisation of the equations governing material behaviour by assuming small changes relative to the current state. However, in the *DuMu*^{X} version used in this work, a total

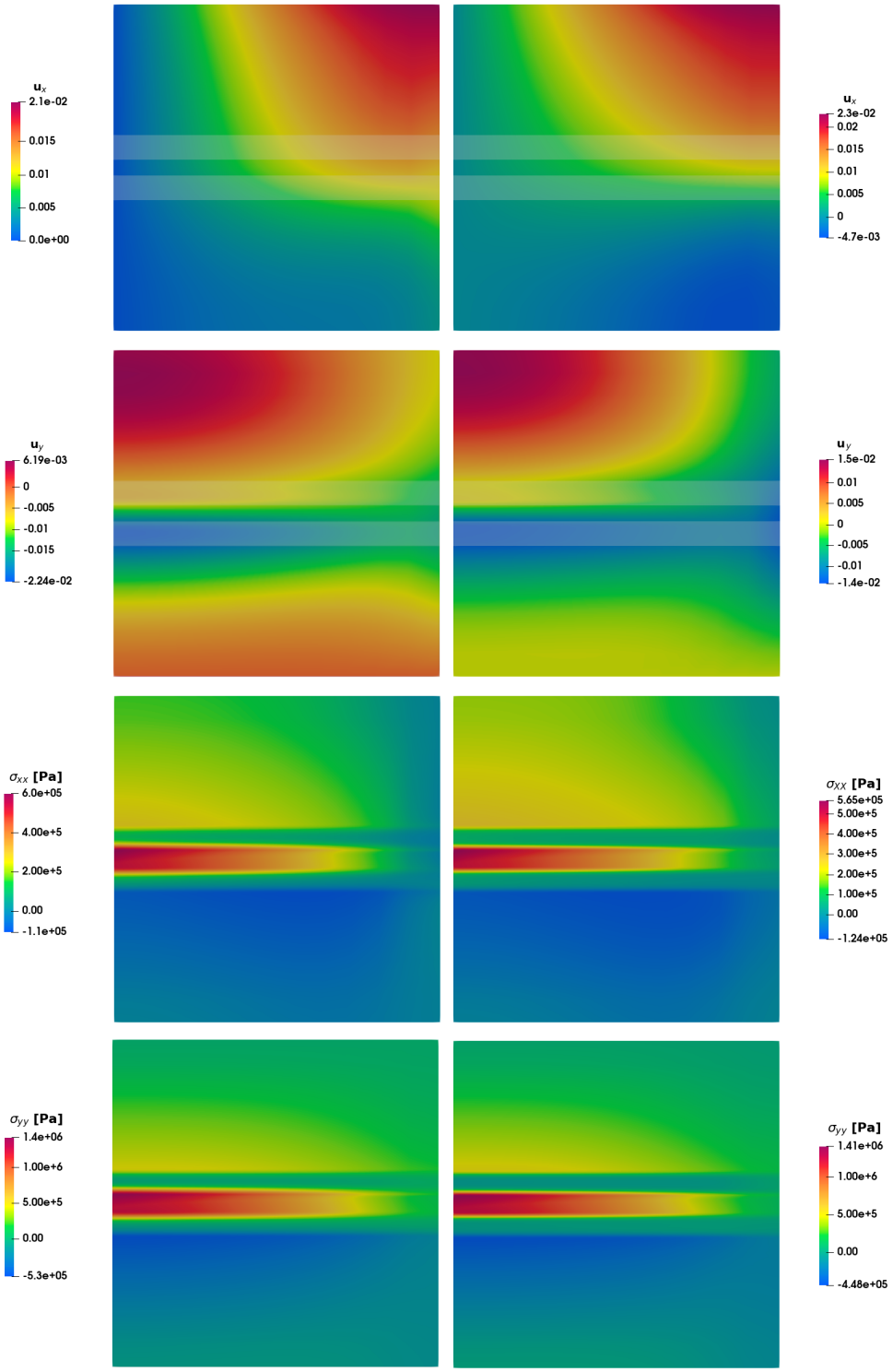

(a) (b)

Figure 5.15: Horizontal and vertical, displacements and stresses results obtained with *DuMu*^{X} (a) and from [31] (b) for the case without "fracture" at the final time.

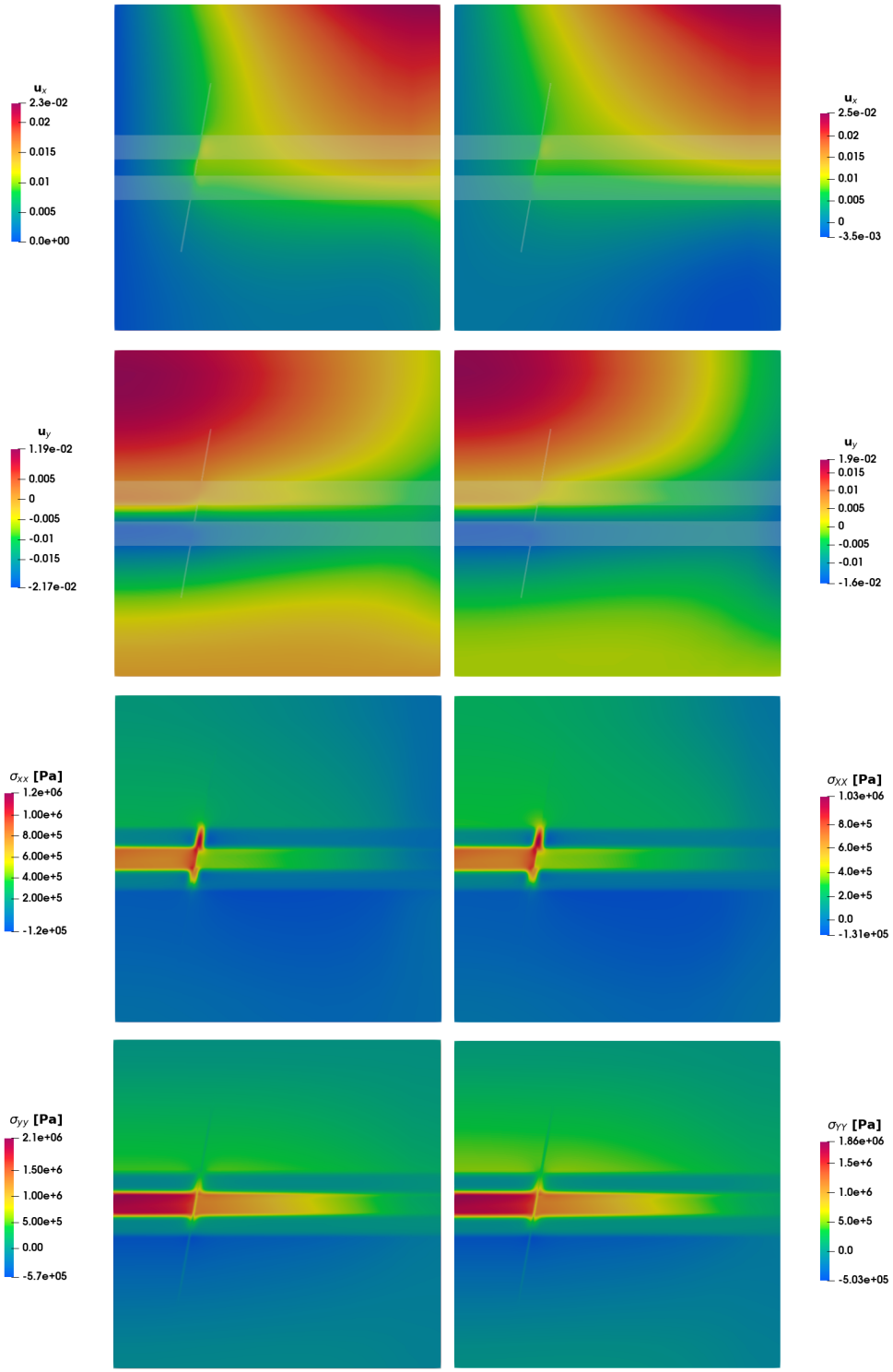

(a) (b)

Figure 5.16: Horizontal and vertical, displacements and stresses results obtained with *DuMu*^{X} (a) and from [31] (b) for the case with a "fracture" at the final time.

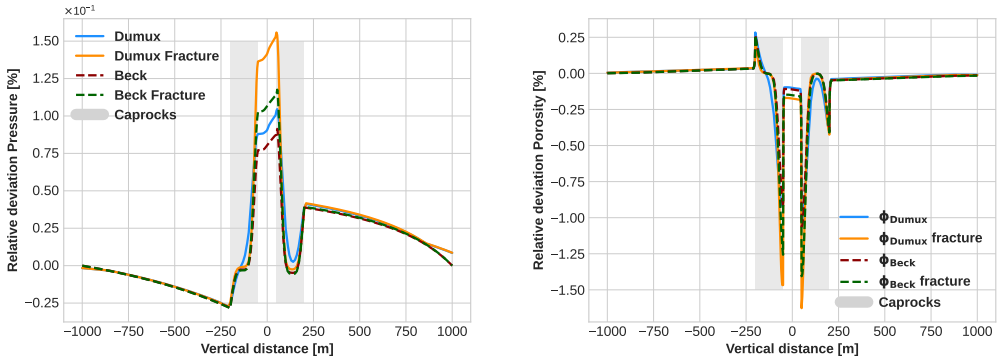

(a) (b)

Figure 5.17: Relative deviation in percentage of the pressure (a) and porosity (b) with respect to initial values.

formulation is used. In the latter, the complete set of equations, such as equilibrium equations and constitutive relations, is solved simultaneously for the entire system. This means that the entire loading history or boundary condition is taken into account from the beginning, without dividing it into incremental steps.

- a modified porosity variation is applied in [31]. Indeed, since the term $\nabla \cdot \vec{u}$ is very small, the relation $\phi_{\text{eff}} = \phi_0 + \nabla \cdot \vec{u}$ is assumed to be a good approximation.

5.3.2.2 Test 2: 2D layered problem

The second case to be investigated concerns a layered formation with a non-K orthogonal mesh, for which the consistency of the TPFA method is no longer valid. A different discretisation strategy must be applied. For this reason, the MPFA replaces the latter method for the finite volume discretisation of the flow problem, since it allows dealing with a non-orthogonal grid.

Configuration

Initially, this problem has been developed in [179]. The mesh is modified and adapted by adding an upper part to avoid major changes in the porosity and permeability of the caprock layers. In order to capture the movement of the CO_2 plume, a refinement is made in the lower region where the CO_2 is injected. It is therefore made up of 25403 quadrangles. Figure 5.18 shows the configuration of the domain considered. The injection area has a height of 30 m and is located at the bottom left. As in the case of Section 3.5.2, an initial hydrostatic pressure of 1×10^5 Pa is assumed at the soil surface. The top surface of the domain is at a depth of 1200 m. The initial temperature is set at 283.15 K at the ground surface, accounting for a geothermal gradient of 30 °C/km.

The first caprock is a 10 m thick curved layer at a height of 50 m and is given by the formula:

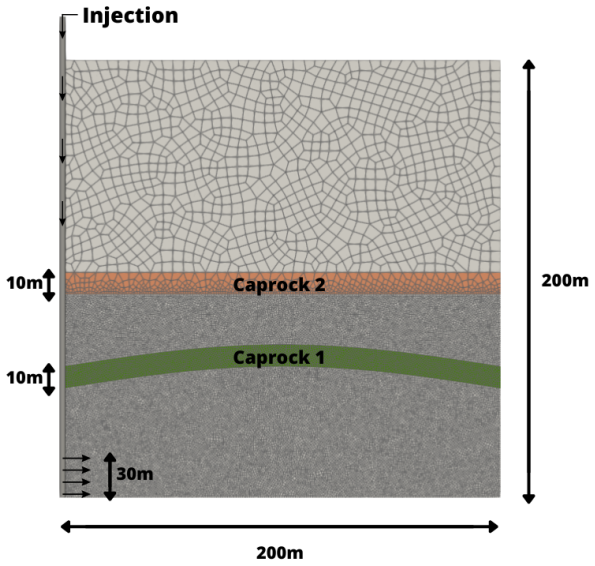

Figure 5.18: Configuration and mesh used to simulate the test case from [179].

$$f(x,y) = h + t\, sin(\frac{\pi\, x}{L}),$$

where h, t, and L denote the height, thickness, and length of the domain respectively. The second is a straight layer of similar thickness located at a height of 90 m. To close the problem, the boundary conditions for the flow subproblem are specified by no-flow conditions everywhere except on the right part of the domain where a Dirichlet boundary condition is set to initial values. However, no normal displacements are fixed on the bottom and left boundaries thanks to the Dirichlet condition for the geomechanical problem. The other two boundaries are free to move. A force is applied at the top of the domain to fix initial horizontal and vertical stresses given by the formula Eq. (5.3.15). The same horizontal-to-vertical ratio of 0.6 is enforced. Table 5.5 and Table 5.6 give some data extracted from [179] to reproduce the case. The simulation time is 2×10^8 s and initialised with an initial time step of $\Delta t_{init} = 1 \times 10^{-9}$ s. The latter is increased during the simulation thanks to a variable strategy and limited to a maximum value of $\Delta t_{max} = 2 \times 10^6$ s.

Fluid constitutive law	Symbol	Parameters	Unit
Injection Rate	Q_{inj}	0.003	[kg.s^{-1}]
Liquid Density	ρ_l	1000	[kg.m^{-3}]
Liquid Viscosity	μ_l	1×10^{-3}	[Pa.s^{-1}]
Residual saturation	S_{rl}	0.0	[-]
Residual saturation	S_{rg}	0.0	[-]
Brooks Corey	P_e	10^4	[Pa]
Brooks Corey	λ	2.0	[-]
Brine salinity	s_{sal}	0.1	[kg NaCl/kg H_2O]

Table 5.5: Fluid constitutive laws for the flow part of problem [179].

Mechanical constitutive law	Symbol	Aquifer	Caprock 1	Caprock 2	Unit
Porosity	ϕ	0.2	0.05	0.001	[-]
Permeability	$\mathbb{K}$	3×10^{-14}	10^{-15}	10^{-19}	[m^2]
Poisson ratio	ν	0.25	0.25	0.25	[-]
Young modulus	E	10^9	10^9	10^9	[Pa]
Biot constant	α	1	1	1	[-]
Solid Density	ρ_s	2700	2700	2700	[$kg.m^{-3}$]

Table 5.6: Mechanical properties for the different layers from [179].

Numerical results

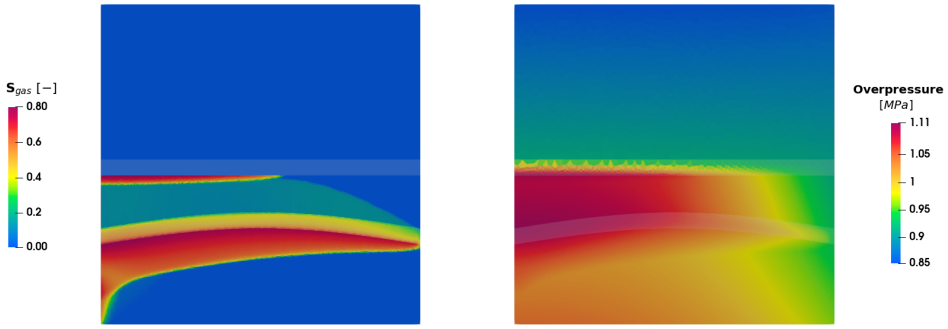

(a) Saturation of gaseous phase (b) Overpressure

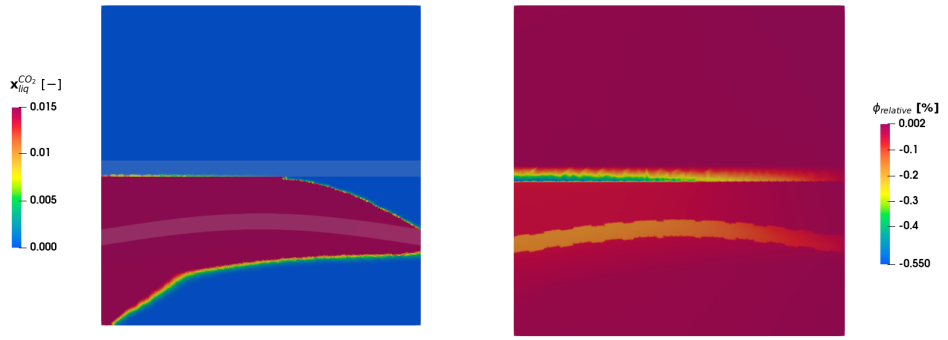

(c) Liquid CO_2 concentration (d) Relative variations of porosity

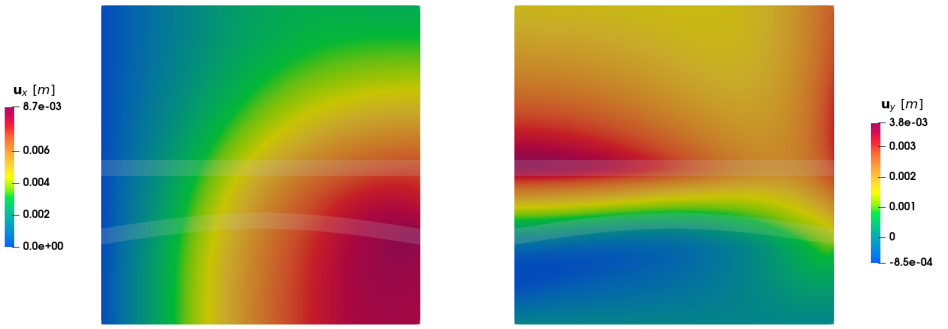

(e) Horizontal displacements (f) Vertical displacements

Figure 5.19: Results for several quantities at 2315 days of injection.

Figure 5.19 gives results for several quantities of interest. The injected CO_2 rises to the first layer due to buoyancy caused by the high-density difference. Due to a slightly lower permeability, the first layer is penetrated by a small amount of CO_2 plume until it reaches the second layer (a). An accumulation of gaseous CO_2 occurs at the second impermeable layer. Due to its much lower permeability, this layer acts as a barrier preventing any leakage. The overpressure profile (b) shows that the pressure increases where the CO_2 plume is located, particularly near the second caprock layer. This results in a vertical uplift that is significant at the same location as the pressure increase (f). The main displacements in the horizontal direction are located in the right part of the domain due to the movement caused by injection in the left part. The porosity seems to decrease in the upper part of the caprock (d), where the CO_2 accumulates in the zone of large variations in pressure and displacements.

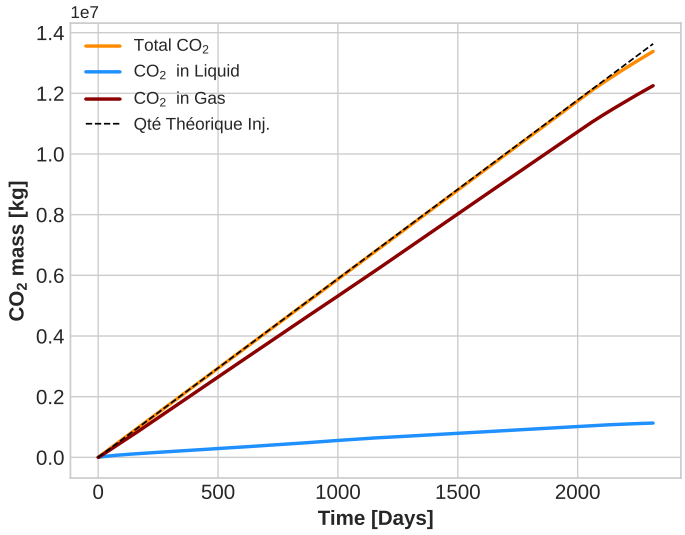

Figure 5.20: Evolution of CO_2 quantities in different phases

The distribution of the CO_2 in different forms is shown in Figure 5.20. As in most of the cases presented previously, the CO_2 is injected under its gaseous/supercritical state, leading to a large increase in the red curve. The blue curve shows the dissolution of CO_2 in the water phase, which highlights the solubility trapping. After more than 2000 days, this process is small compared to the amount still in the gas phase. However, there is a loss of mass on the yellow curve at the top right, because the CO_2 plume arrives close to the right boundary, which is fixed as a Dirichlet condition. Consequently, a small amount of CO_2 disappears due to this condition. The salinity of the domain seems to have an important effect on CO_2 dissolution [111]. The more sodium chloride in the water, the less CO_2 dissolves in the brine. This phenomenon is well illustrated in Figure 5.21 (a), where a maximum factor of 3 appears between the maximum and minimum salinity values. So salinity can be a lever to maximise CO_2 dissolution. However, it has no effect on the gaseous state where no variations are captured in Figure 5.21 (b).

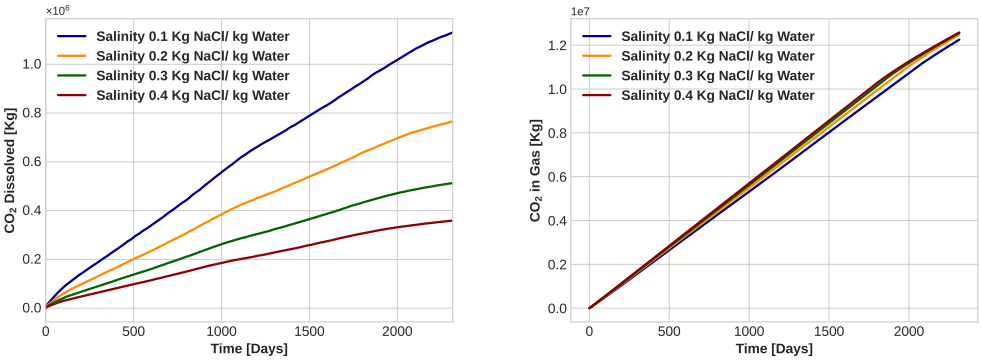

(a) Liquid solubility (b) Gaseous solubility

Figure 5.21: Differences for CO_2 liquid and gas quantities for several salinity values.

Comparison between MPFA and TPFA schemes for flow

Even though the TPFA scheme is not suitable for simulating non-K orthogonal meshes, a study has been conducted to analyze the outcomes obtained by using this method.

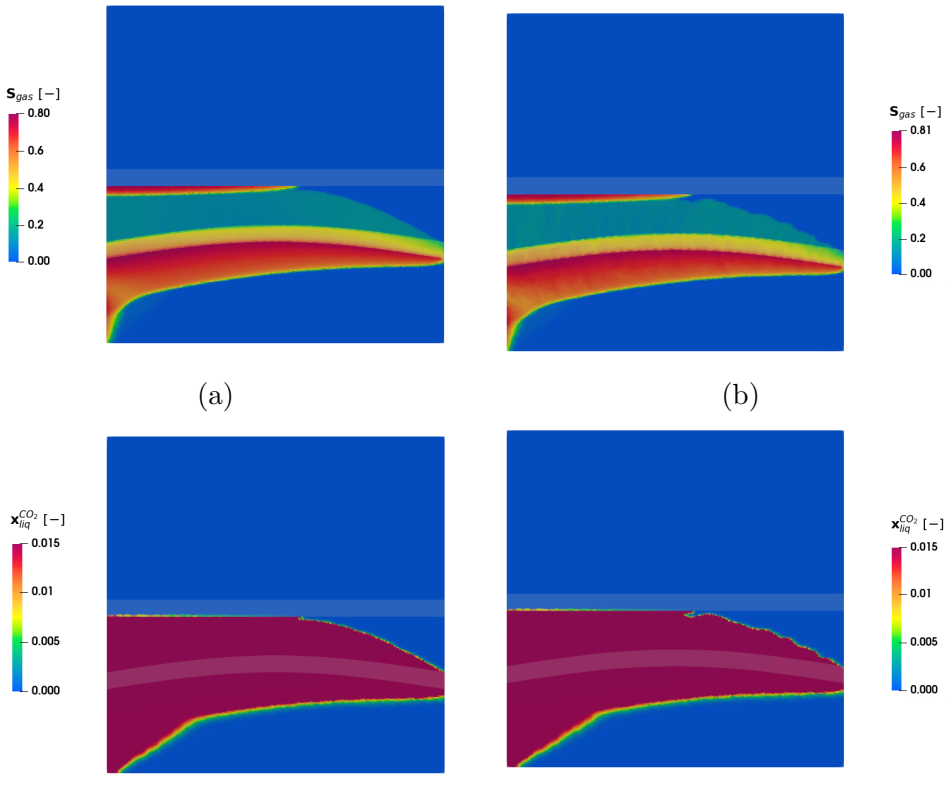

Figure 5.22: Results for the MPFA (a-c) and TPFA (b-d) approaches for gas saturation (left) and CO_2 liquid molar fraction (right) at the final time.

Figure 5.22 shows the results for the two approaches for gaseous saturation and

liquid pressure. It is clear that there is a notable contrast in the amount of CO_2 present at the forefront of the plume, particularly within the region situated between the two caprock layers. An absolute difference between the two saturation profiles in Figure 5.23 (a) confirms that the contrast lies at the interface between the gaseous CO_2 plume and the residual brine. Moreover, in Figure 5.23 (b), the difference between the two liquid pressure profiles indicates that the TPFA scheme underestimates the pressure increase.

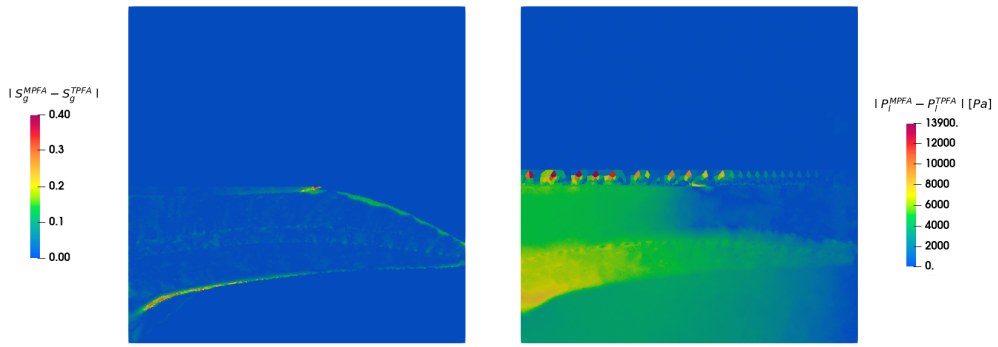

(a) (b)

Figure 5.23: Difference between MPFA and TPFA schemes for gas saturation and liquid pressure at the final time.

The Table 5.7 highlights the computational time for the two approaches. A huge difference is notable which can be explained by the fact that the MPFA is computationally very expensive. Based on the configuration in question, TPFA yields results that are not entirely accurate, but it does so in 7.4 less time than MPFA.

Method	CPU Time [s]
MPFA - CVFE	71h 46min
TPFA - CVFE	9h 38min

Table 5.7: Computational time for the two different approaches for flow description.

Consequently, this study demonstrates, on the one hand, the capabilities of the *DuMu*^{X} simulation platform to provide accurate hydro-mechanical coupling simulations using an MPFA scheme for the discretisation of the flow coupled to a box scheme to solve the poromechanics model. On the other hand, the very high computational cost of the MPFA method may be a limiting factor for meshes with more elements.

5.3.2.3 Test 3: Comparison with reservoir simulator

Configuration

The last case to be studied was first developed in [201]. It also consists of a layered formation with caprock and overburden layers with different geomechanical properties. The vertical uplift of the caprock is attempted to be captured by several software packages in order to compare the results given by the different ap-

proaches. Two test cases with different injection rates were distinguished. The aim was to demonstrate the influence of geomechanics on the stability of the impermeable caprock, in particular when the minimum effective stress exceeds a threshold that induces fracturing. However, in this work, only the first low injection rate case is considered, as the second is more difficult to implement.

The domain considered is an aquifer of 12100 m $\times$100 m $\times$321 m discretised by $101 \times 1 \times 33$ cell blocks. Two caprocks and two overburden layers are added to see the structural trapping effects as well as the vertical uplift on the upward layers. Figure 5.24 shows the domain configuration, while cell size and layer height information is given in Table 5.8.

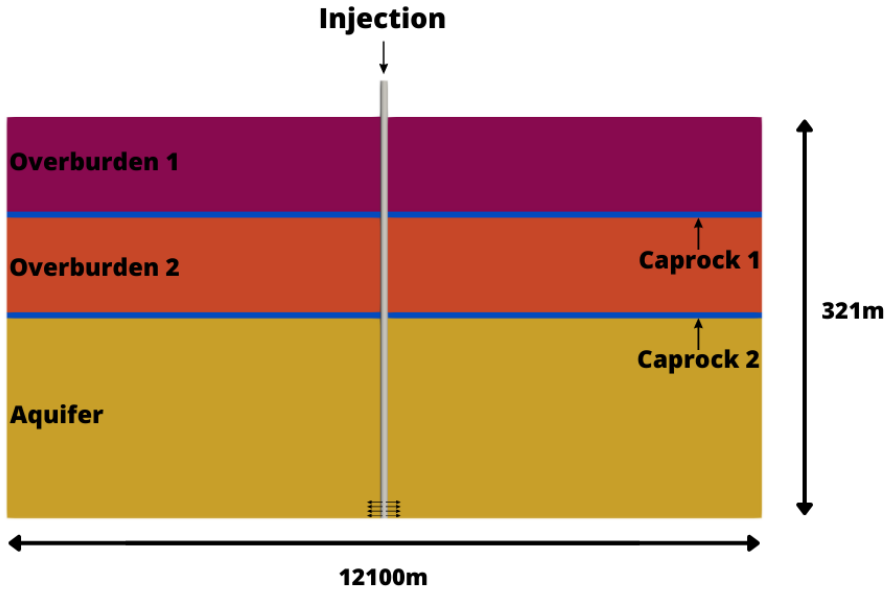

Figure 5.24: Configuration for the test cases developed in [201].

Zone	Thickness [m]	Cells [-]
Overburden 1 (OB 1)	76.2	5
Caprock 1	4.572	1
Overburden 2 (OB 2)	76.2	5
Caprock 2	4.572	1
Aquifer	160.02	21

Table 5.8: Thickness and number of cells that constitute each layer of the domain.

The information about the different layers is given in Table 5.9. A uniform porosity is applied throughout the domain, while a slight anisotropy is imposed on the different layers, favouring flow in the horizontal direction. For this reason, the TPFA scheme is not appropriate [68, 100]. Consequently, spatial discretisation is performed by using the MPFA scheme. Table 5.10 gives some fluid parameters to generate the simulation. The entry pressure P_e is set to 0 in order to neglect the capillary pressure p_c.

Boundary conditions are required to define the behaviour around the domain. For the flow problem, no-flux is set on entire boundaries using a homogeneous Neumann condition. This configuration is possible here because the injection as well as the CO_2 plume will only be inside the domain and far away from the boundaries. For the geomechanical boundary condition, the aquifer is constrained at the bottom and sides, allowing the top to move freely. A horizontal stress of 3.447×10^6 Pa is prescribed at the top, while a value of 6.894×10^6 Pa is set for the initial vertical stress. The vertical and horizontal effective stress gradients are set to 20938 and 10469 Pa.m^{-1} respectively.

Initially, the domain is considered to be fully saturated with resident brine, which accounts for a small amount of salinity (see Table 5.10). Consequently, there is no CO_2 at initial conditions. An injection well is drilled in the center of the field and perforated in the lower 4 cells of the field. Gaseous CO_2 is injected at a rate of 0.9188 kg.s^{-1} for 5 years, and the evolution of the plume is then studied for a further 3 years. An initial time step of $\Delta t_{init} = 1 \times 10^{-9}$ s is prescribed and increased thanks to the variable strategy. However, the latter is limited to a maximum value of $\Delta t_{max} = 2 \times 10^6$ s.

Const. law	Symbol	Aquifer	Caprock 2	OB 2	Caprock 1	OB 1	Unit
Porosity	ϕ	0.13	0.13	0.13	0.13	0.13	[-]
Permeability	$\mathbb{K}_x$	15	10^{-7}	20	10^{-7}	25	[mD]
Permeability	$\mathbb{K}_z$	3.75	$2.5e^{-8}$	5	$2.5e^{-8}$	6.25	[mD]
Poisson ratio	ν	0.25	0.25	0.3	0.25	0.25	[-]
Young modulus	E	$5e^9$	$5e^9$	$8.62e^8$	$5e^9$	$5e^9$	[Pa]
Biot constant	α	1	1	1	1	1	[-]
Solid Density	ρ_s	2600	2600	2600	2600	2600	[kg.m^{-3}]

Table 5.9: Constitutive laws for the different layers for the problem extracted from [201].

Fluid constitutive law	Symbol	Parameters	Unit
Injection Rate	Q_{inj}	0.9188	[kg.s^{-1}]
Residual saturation	S_{rl}	0.2	[-]
Residual saturation	S_{rg}	0.05	[-]
Brooks Corey	P_e	0.0	[Pa]
Brooks Corey	λ	2.0	[-]
Brine salinity	s_{sal}	0.1	[kg NaCl/kg H_2O]

Table 5.10: Data for the fluid part of the problem from [201].

Numerical results

Figure 5.25 to Figure 5.27 (a) give results obtained with the approach implemented in *DuMu*^{X}. They are displayed at three different times so that the trend can be seen over a period of up to eight years. In this case, five years of injection at a low rate is not enough time to see the evolution of a plume reaching the caprock, represented by the grey lines in the left figures. Nevertheless, the aim of this study was to

capture the geomechanical displacement experienced by the caprock layers. In fact, calculations were also carried out by our own means on the GEM composition simulator in order to compare the results between the two platforms. GEM is an unconventional reservoir and compositional simulator developed by the Computer Modelling Group (CMG). It provides an adaptive implicit formulation to solve flow problems with the possibility of coupling geochemical modules. The calculation of geomechanical effects is based on a finite element module coupled iteratively to a fluid flow solver with a two-way coupling described in Section 5.2.2. Results for GEM are depicted in Figure 5.25 to Figure 5.27 (b).

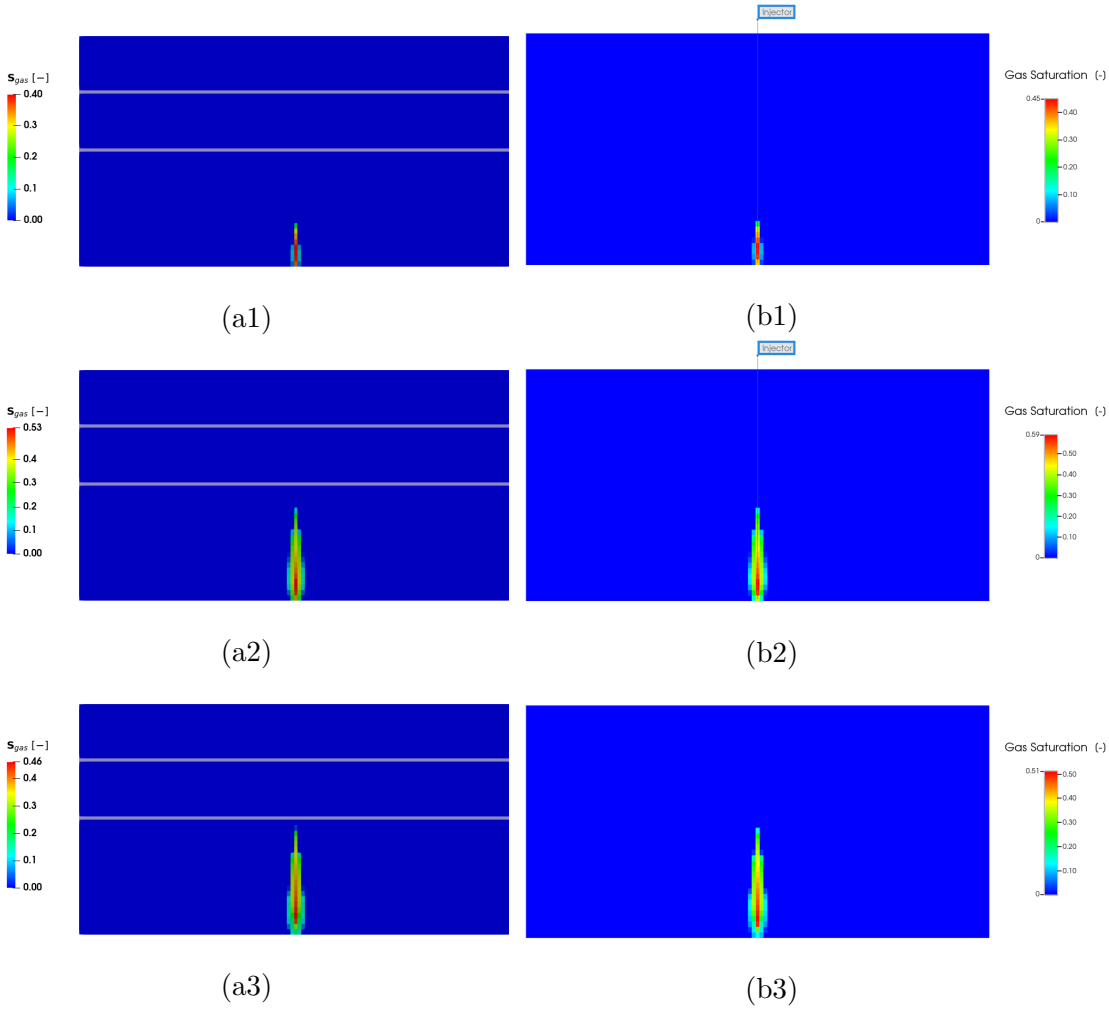

Figure 5.25: Saturation results on the left from *DuMu*^{X} (a) and GEM on the right (b). Results are shown for three different times, 397 days (a1-b1), 5 years (a2-b2), and 8 years (a3-b3).

The pressure profiles (see Figure 5.26) show that the increase is clearly localised in the wellbore region and extends laterally at the bottom of the domain to the lateral boundaries. After stopping the injection, the pressure increase is confined to the aquifer region and gradually dissipates to return to the initial state after longer times. The vertical displacement profiles (see Figure 5.27) show significant uplift of the domain above the injection zone, from the caprock to the top of the

domain. In GEM, the mechanical sign convention is not applied in the same way as in *DuMu*^{X}. This is why vertical displacements are represented here by negative values, even though they represent vertical uplift of the ground towards the surface. This phenomenon is a consequence of the injection, which increases the pressure in this area of the domain and creates an uplift. In addition, the vertical displacement profiles appear to be more extensive at the lateral edges in the *DuMu*^{X} results for 397 days and 5 years than in GEM.

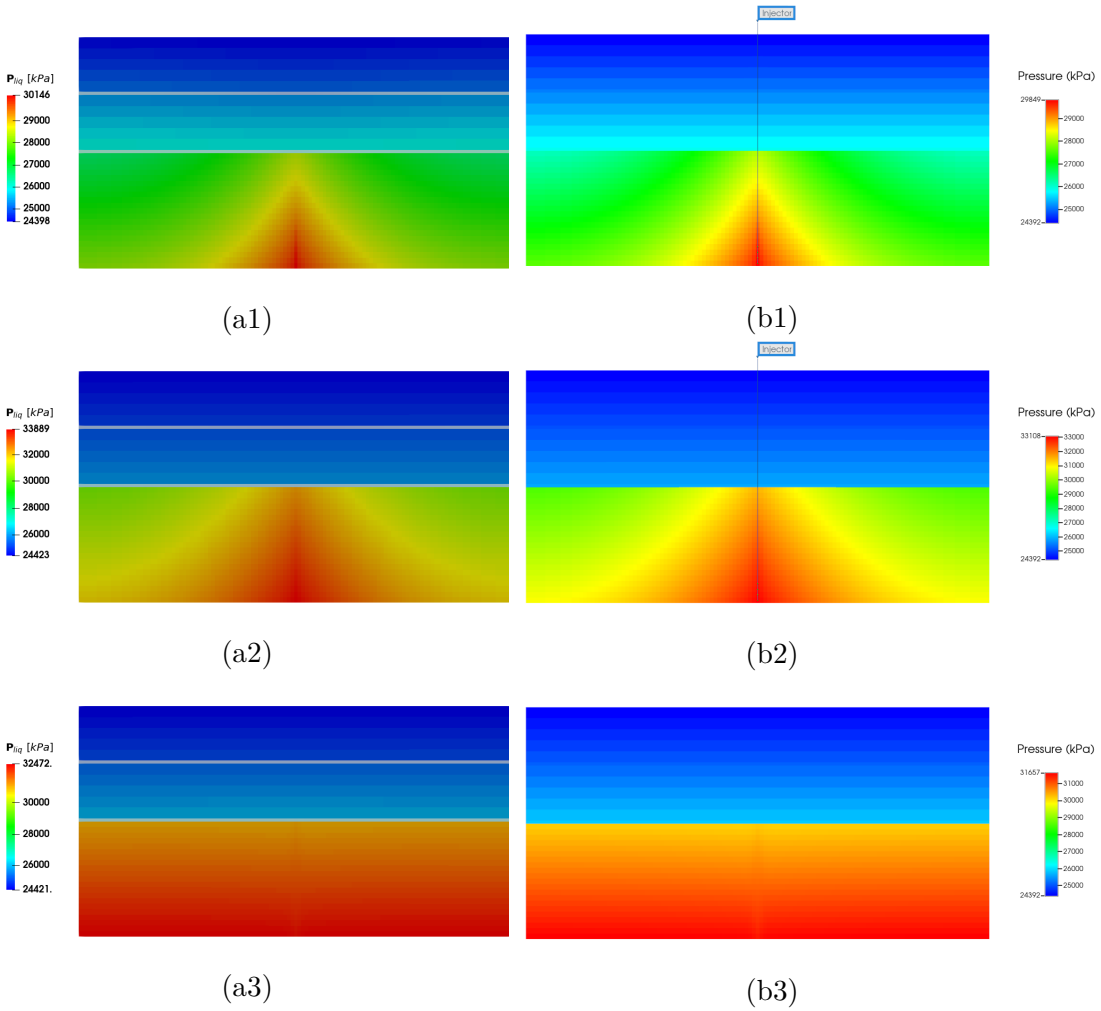

Figure 5.26: Pressure results on the left from *DuMu*^{X} (a) and GEM on the right (b). Results are shown for three different times, 397 days (a1-b1), 5 years (a2-b2), and 8 years (a3-b3).

In general terms, a good agreement between the two platforms is clearly visible in the left and right figures. The behaviour is clearly the same and the vertical uplift is well captured. A slight difference lies in the values of pressures and saturations at different times. These differences may be due to the difference in the strategies of resolution implemented in the two platforms. Indeed, GEM uses a sequential approach while in *DuMu*^{X}, a fully implicit approach is considered. The evolution over time of the distribution of CO_2 in its different forms is shown in Figure 5.28 for the two codes. Although the two total amounts of CO_2 injected are in perfect

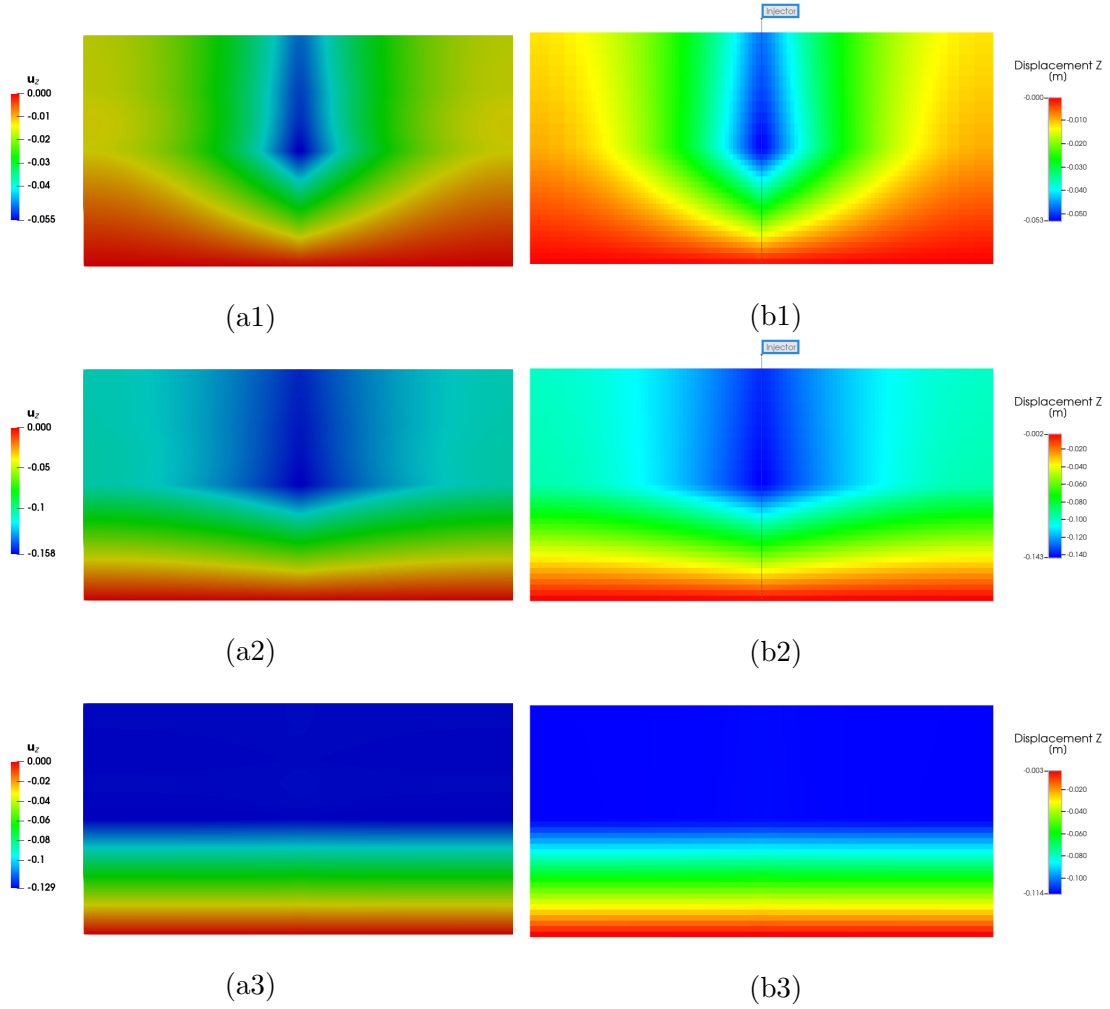

Figure 5.27: Vertical displacement results on the left from *DuMu*^{X} (a) and GEM on the right (b). Results are shown for three different times, 397 days (a1-b1), 5 years (a2-b2), and 8 years (a3-b3).

agreement with the theoretical value, CO_2 in the gas phase and CO_2 dissolved in the liquid phase are slightly different in the two codes. These differences may be explained by the different equations of state used in the two platforms.

For a deeper analysis, a profile of vertical displacements of the lower caprock (caprock 2) at different times is provided in Figure 5.29. The values of vertical displacements appear to be similar at 1 year and then tend to deviate slightly up to 5 years. These deviations may be due to the slight difference in pressure profile values which has an impact on the vertical displacements due to the coupling. Also, the resolution strategies are different: fully implicit and sequential were used in the two platforms respectively.

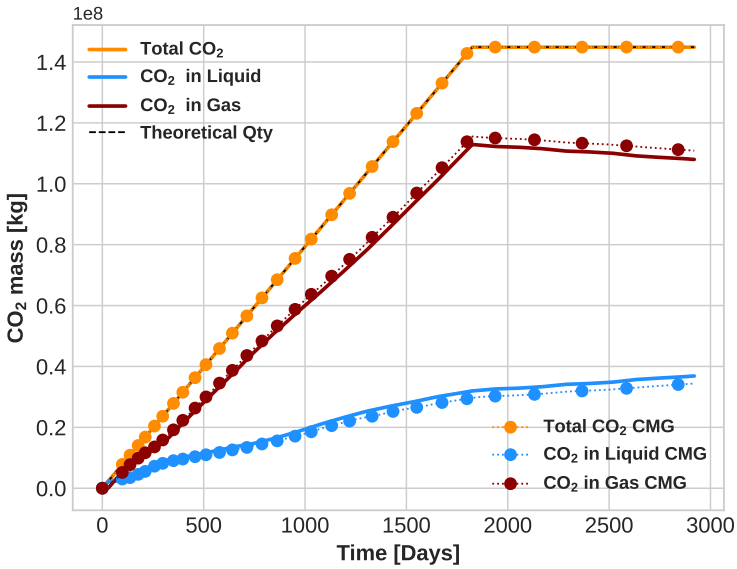

Figure 5.28: Comparison of the CO_2 quantities evolution for both simulators *DuMu*^{X} and GEM, with respect to the simulation time.

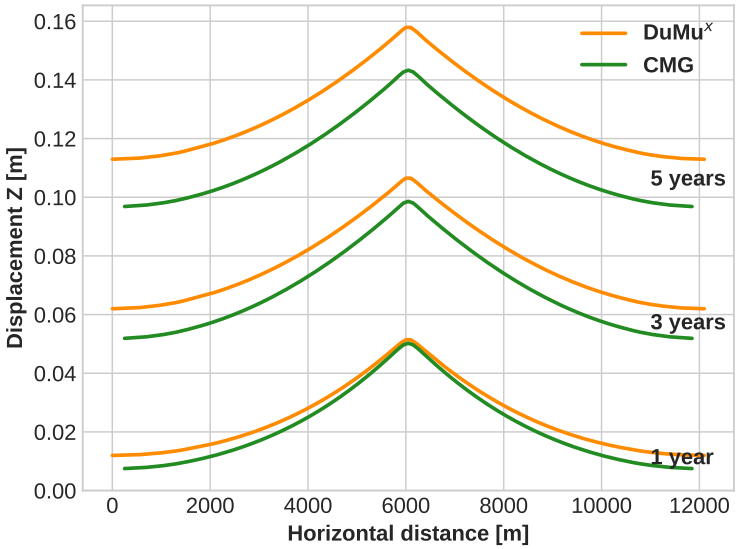

Figure 5.29: Comparison of the vertical displacement between *DuMu*^{X} and GEM at several times.

Consequently, the comparison between the two simulation platforms validates the approach developed here. It highlights the potential to capture vertical uplift correlated with CO_2 injection that may cause damage or induce fracture in critical zones for storage. Due to a regular mesh and a rather small anisotropy ratio of 4, the TPFA delivers satisfactory results. However, for a general case, the MPFA is more convenient and provides more robustness. To get a comparative idea, calculations

have been performed with both schemes, but also using GEM. Table 5.11 shows the CPU times for simulations with a grid of 3333 cell blocks. The simulations were run on a single processor of a computer equipped with an Intel ®Core ™i7-10700 CPU at a frequency of 2.90 GHz.

Simulator	Method	CPU time
DuMu^X	MPFA - CVFE	5 h 02 min
DuMu^X	TPFA - CVFE	15 min
GEM	FV - FEM	13 min

Table 5.11: Computational time comparison between GEM and *DuMu*^{X}.

This table clearly shows that the combined MPFA-CVFE schemes must be used to obtain consistent results. However, the computational time is really affected, mainly due to the stencil of matrices constructed by the latter methods. As a result, it has not yet been possible to produce a 3D simulation using such a framework.

5.4 Conclusion

In this chapter, a numerical framework is proposed to perform CO_2 storage simulations taking into account the Hydro-Mechanical coupling. Some solution strategies for the numerical approach are discussed, where the flow and poromechanical problems are solved together. For this purpose, a cell-centered finite volume scheme is formulated for the flow part combined with a control volume finite element method (CVFEM) for the poromechanical part, in particular the vertex-centered box scheme. In this work, the fully coupled approach is used, which means that both subproblems are solved as a monolithic system. The coupling is performed through the effective pressure and the effective density, which influence the stress calculations. However, porosity and permeability variations as a function of mechanical displacements contribute to flow modifications. The implementation of the model presented in Chapter 4 is carried out in the *DuMu*^{X} simulation platform. Validations of the numerical scheme are first carried out thanks to consolidation phenomena. In particular, three test cases allowed us to compare the results of the developed approach with analytical values. The Terzaghi, Mandel, and Cryer consolidation problems provide good agreement with analytical values, which deal with the multi-dimensional formulation of the HM coupling. CO_2 storage scenarios are then investigated dealing with a compositional two-phase flow coupled with poromechanical effects. Three test cases are discussed to illustrate the effects of gas injection in layered heterogeneous formations. In addition, the results obtained from the developed approach are compared with another reservoir simulator capable of reproducing the case. This validates both the model and the numerical scheme used to perform CO_2 storage simulation with hydro-mechanical coupling, where the results are consistent with the CO_2 sequestration literature. Consequently, all the studies presented here highlight the importance of considering geomechanical effects in CO_2 sequestration simulations. Further validation needs to be continued by considering other studies and benchmarks. Temperature is not considered in

this study but should be considered when assessing the safety and durability of geological storage. Due to local temperature changes in the vicinity of the injection well, the latter is likely to have a more significant impact on mechanical effects. Finally, an effort has been made to provide as much data as possible and to ensure the reproducibility of the tests carried out in this contribution.

Chapter 6

Conclusion and perspectives

6.1 Conclusion

The work presented in this thesis deals with several numerical approaches to model multiphase flow coupled with other physical processes commonly encountered in CO_2 storage scenarios. This process appears to be an efficient way to mitigate atmospheric CO_2 emissions, which are mainly responsible for global warming. Consequently, this method of mitigating gaseous emissions is consistent with an environmental objective. The general context of carbon sequestration is given in Chapter 1, with an overview of all the physical phenomena involved in the sequestration process. Indeed, CO_2 injection induces coupled Thermo-Hydro-Mechanical-Chemical (THMC) processes that may compromise the safety and durability of the storage. Furthermore, the different types of numerical methods used to deal with such couplings are reviewed from the literature. This topic has been widely investigated with many contributions to different coupling approaches. This work mainly focuses on two different axes which are the Thermal-Hydro-Chemical and Hydro-Mechanical coupling methods.

In Chapter 2, the mathematical model for Thermal-Hydro-Chemical coupling is exposed. For this purpose, a geochemical model is introduced with the equations derived from the two types of chemical reactions. Indeed, equilibrium reactions provide algebraic relations while kinetic reactions result in ordinary differential equations which are coupled to the flow equations via reaction rates. Nevertheless, a contribution of the temperature on reactive constants is provided by means of relations and database values that are interpolated. All this framework is coupled to a nonisothermal multiphase flow model. The latter is described by mass conservation laws formulated for each primary component of the chemical system, and in each phase. In addition, an energy conservation law is added to take into account temperature variation in the coupled model, which forms a strongly nonlinear system of coupled PDEs.

The Chapter 3 is dedicated to presenting the numerical framework established in order to perform THC numerical simulations of CO_2 storage scenarios. Two resolution strategies are considered, namely fully coupled fully implicit, and sequential approaches. On the one hand, the fully coupled fully implicit approach solves the

system as a single global monolithic system at each iteration in time, leading to higher nonlinearities. Conversely, the sequential approach splits the system into two subproblems: a nonisothermal compositional two-phase flow and a reactive transport problem. Both strategies have been implemented in the *DuMu*^{X} simulation platform. For this purpose, the fully coupled fully implicit, and sequential approaches have been discretised by a cell-centred finite volume scheme using a two-point flux approximation (TPFA) or a multi-point flux approximation (MPFA) depending on the complexity of the mesh. The time discretisation is carried out with an implicit Euler scheme or a second-order Backward Differentiation Formula (BDF2). A Newton-Raphson method is used to tackle the nonlinear system combined with a BiConjugate Gradient Stabilized linear solver preconditioned by Algebraic Multigrid (AMG) preconditioner. An adaptive time-stepping method based on the number of iterations required by the Newton-Raphson method to reach convergence is employed. Multi-dimensional simulations were performed to illustrate the capacity of the model. The 1D case acts as a validation. Accounting for temperature effects results in increased dissolution of CO_2 and calcite, respectively, in the near-well and CO_2 plume regions, which can improve both well injectivity and dissolution trapping. The 2 and 3D cases are extended to THC processes and the results obtained are in agreement with the literature. For the 3D configuration, comparisons between the two resolution strategies have been performed, highlighting the fact that the fully implicit approach is mass conservative. The sequential approach introduces a splitting error which degrades the accuracy of the scheme despite a gain in computational time. The ability of both methods to simulate scenarios with several million degrees of freedom is tested thanks to High-Performance Computing involving several hundred processors. Furthermore, the latter case has been modified to examine the long-term behaviour of the mineralisation, which was not expected with the original formulation of the problem. The results obtained with precipitation and dissolution involving mineral species are consistent with the literature on CO_2 sequestration, showing increasing efficiency over long time scales (up to 100 to 1000 years). A part of this chapter has given rise to an article under revision for publication in the journal Mathematical Geosciences.

In Chapter 4, the mathematical model for Hydro-Mechanical coupling is introduced. The basic geomechanical terminology has been presented to set the context of the variables and constitutive relations used in porous media. Further, the geomechanical model is exposed by introducing the equations derived from the momentum balance equation. Some constitutive laws are introduced to characterise the effective and total stresses by using linear poroelasticity relations from the literature. The isothermal compositional two-phase flow is described by mass conservation laws. Several closure relations are also required to correctly define the problem. The coupling between these two subproblems is done by means of effective variables. In one way, the stress relations require the use of effective pressure and density, which come directly from the flow part. On the other hand, the effective porosity and permeability are modified due to geomechanical displacements acting at the same time and affecting the flow. Consequently, a strongly nonlinear system of coupled PDEs is formulated for Hydro-Mechanical coupled processes. The discretisation of the coupled model is also given in detail. A cell-centered finite volume scheme is formulated for the discretisation of the compositional two-phase flow using TPFA

or MPFA schemes. The poroelasticity discretisation uses a vertex-centred Control Volume Finite Element method, specifically the box scheme, resulting in piecewise linear basis functions to approximate variables and gradients within the mesh.

Finally, the Chapter 5 deals with the resolution strategy, the implementation, and the illustration of the model with some test cases. Indeed, a fully coupled approach is used, meaning that both subproblems are solved simultaneously as a single system. The implementation of the model has been performed in $DuMu^X$. Well-known multi-dimensional consolidation problems have been used to validate the numerical scheme by confronting the results with analytical formulas from the literature. Subsequently, three different 2D test cases have been treated to investigate and validate the behaviour of the model dealing with CO_2 sequestration. More precisely, the first case focused on the validation of the model thanks to a comparison with a previous version of $DuMu^X$ that used a different mechanical formulation. An extension to Hydro-Mechanical coupling was carried out in the second case where the mesh of the domain consists of non K-orthogonal cells which necessitates the use of the MPFA. In the third case, the calculations were also carried out with the industrial simulator GEM in order to compare precisely the two different platforms. Small deviations were obtained resulting from different resolution strategies involved in each simulation framework. Consequently, all the studies presented highlight the importance of considering geomechanical effects in CO_2 sequestration simulations.

6.2 Perspectives

Although the results of both types of coupling are encouraging, some perspectives can be formulated to improve both accuracy and performance. In fact, for the Thermal-Hydro-Chemical coupling, the current numerical implementation could be improved on several points:

- Reducing the overall computational cost is a crucial issue when dealing with nonisothermal multiphase flow coupled with a large chemical system. For that, several factors can be adjusted to reduce this time. Non-exhaustively, we can mention:
  - the time step strategy employed. Theoretically, a fully implicit method has no stability limit on the timestep size. In practice, standard Newton's method often fails to converge for large timestep sizes and must therefore cut the timestep multiple times to achieve convergence, resulting in a large number of unnecessary iterations. Future research could explore adaptive time step techniques that dynamically adjust the time step size according to maximum variable change in [11], or according to the initial residual of Newton iterations [127]. In [224], different time-stepping techniques are used to study the effect of temporal truncation errors for density-dependent flow problems. The first approach is similar to the one used in our work, but with smoother coefficients to deal with sharp fronts. In the second scheme, the time step is automatically varied according to the local time truncation error, by using an

adaptive predictor-corrector one-step Newton scheme. More recently, another technique has been used in [225], namely the method of lines (MOL). This method consists of discretising the variables and their spatial derivatives, resulting in a large system of ordinary differential and algebraic equations. A high-order adaptive time integration technique (DASPK [206]) is applied to tackle the integration of ODE and DAE systems. The latter integration technique provides an automatic adaptation of both the integration order and the time step length to minimise the computational effort while keeping the time truncation error small. Local time-stepping techniques represent also an efficient improvement that could be carried out. These methods deal with time steps that are asynchronously updated in adjacent cells or regions depending on the dynamics of transient processes [126].

- a posteriori error estimators associated with solvers. The error measured by the dual norm of the residual can be decomposed into different components, including the spatial discretization error, the temporal discretization error, the linearisation error, the iterative coupling error, and the algebraic solver error. Therefore, stopping criteria are constructed for linear and nonlinear solvers, based on these components. In [211], the authors developed a posteriori estimators for immiscible incompressible two-phase flow in porous media, while in [90], an extension to compositional multiphase flow with phase change is proposed. In [14], both the timestep adaptive strategy and the error estimators are related, ensuring balanced temporal and spatial errors while maintaining sufficiently small nonlinear errors. Consequently, implementing these stopping criteria would reduce the number of iterations for both linear and nonlinear solvers and increase the tolerance to error when conditions are met, resulting in CPU time savings.

These adaptive approaches could potentially improve the accuracy and stability of the simulations while reducing the overall computational cost.

- In this study, the effectiveness of cell-centered approaches was examined. It was found that the TPFA scheme, which is widely used in many simulators, lacks consistency when implemented on grids that are not perfectly K-orthogonal. On the other hand, the MPFA scheme, which was also considered, is computationally expensive when applied to unstructured discretisations, especially on tetrahedral grids. To overcome these limitations, future research could explore the utilization of more recently developed nonlinear finite volume schemes (NLTPFA) [179]. These schemes have been shown to be both consistent and computationally efficient, as they typically maintain smaller stencil sizes.

For the Hydro-Mechanical coupling, some improvements could be formulated:

- In this work, only 2D problems are considered for the Hydro-Mechanical coupling. As the multi-domain assembler is not yet parallelised, the computational time really depends on the discretisation scheme used. A first step of

improvement would be the parallelisation of this assembler in order to solve fully implicit strategies for larger meshes. This could also result in an extension to 3D problems, which would be a challenging step as such simulations are computationally expensive due to the strong coupling between the different physical processes.

- The implementation of a sequential coupling between the flow and the geomechanics could also reduce the computational time for the 3D problems, although this approach has its advantages and disadvantages, as seen previously. A fixed-stress algorithm could be employed which has been widely studied in the literature and remains unconditionally stable [115, 117]. In order to perform a sequential coupling, two different axes of implementation can be considered:

  – the use of *DuMu*^{X} only, as conducted for the THC coupling, where two different modules communicated in the same simulation platform.

  – the use of an external simulator could be envisaged to compute the geomechanical problem (for example Code_Aster ([63]) coupled with the *DuMu*^{X} simulation platform to deal with the flow part of the problem.

  Further comparisons between fully implicit and sequential approaches, such as those presented in this work for the THC coupling, could be carried out to highlight the accuracy and performance of these methods in a high-performance computing framework.

  In addition, a direct linear solver (see Section 5.2.4) is used to simulate the HM coupling. Direct solvers are generally robust and can guarantee an exact solution, but their computational complexity is typically higher than that of iterative solvers, especially for large-scale systems. The use of an iterative solver could improve the performance of the solver and therefore reduce the computational time.

- The integration of temperature effects in the latter Hydro-Mechanical coupling framework would be a challenging approach. Indeed, Thermal-Hydro-Mechanical coupling processes lie in the consideration of nonisothermal multiphase flow, combined with equations of state depending on temperature variations. The temperature variations affect the stress computations by modifying their constitutive relation. The implementation of a THM module could be carried out in *DuMu*^{X} using a fully implicit [103] or a sequential method [125, 173, 201].

Finally, the culmination of this project would lie in the consideration of the whole THMC processes where temperature variations, multiphase flow, geomechanics, and chemical interactions are coupled [75, 120, 228, 229]. This contribution is a continuation of the research work carried out at LMAP in collaboration with LFCR, aimed at developing a new generation framework and simulator, suitable for massively parallel processors, for large-scale reservoir simulation of coupled THMC modelling.

Bibliography

[1] Chess database. *https://thermoddem.brgm.fr/databases/chess*.

[2] Delft Advanced Research Terra Simulator - DARTS. *https://darts.citg.tudelft.nl/*.

[3] GEM compositional & unconventional simulator. *https://www.cmgl.ca/gem*.

[4] Global status report 2021 policy fact sheet. *https://www.globalccsinstitute.com/*.

[5] Open Porous Media initiative. *http://opm-project.org/*.

[6] Automatic Differentiation General Purpose Research Simulator - AD-GPRS. *https://supri-b.stanford.edu/research-areas/ad-gprs*, 2017.

[7] *DuMu^X* Handbook. *https://dumux.org/docs/handbook/releases/3.7/dumux-handbook.pdf*, 2023.

[8] I. Aavatsmark, G. Eigestad, R. Klausen, M. Wheeler, and I. Yotov. Convergence of a symmetric MPFA method on quadrilateral grids. *Computational Geosciences*, 11:333–345, 2007.

[9] A.S. Abd and A.S. Abushaikha. Reactive transport in porous media: a review of recent mathematical efforts in modeling geochemical reactions in petroleum subsurface reservoirs. *SN Applied Sciences*, 3:401, 2021.

[10] Y. Abousleiman, A.H.-D. Cheng, L. Cui, E. Detournay, and J.-C. Roegiers. Mandel's problem revisited. *Géotechnique*, 46:187–195, 1996.

[11] A. Abushaikha, D. Voskov, and H. Tchelepi. Fully implicit mixed-hybrid finite-element discretization for general purpose subsurface reservoir simulation. *Journal of Computational Physics*, 346:514–538, 2017.

[12] J. Adams and S. Bachu. Equations of state for basin geofluids: Algorithm review and intercomparison for brines. *Geofluids*, 2:257–271, 2002.

[13] N. Ahmad, X. Sanchez-Vila, J. Jarsjö, A. Bottacin-Busolin, and H. Hellevang. Injection of CO_2-saturated brine in geological reservoir: A way to enhanced storage safety. *International Journal of Greenhouse Gas Control*, 54:129–144, 2016.

[14] E. Ahmed, Ø. Klemetsdal, X. Raynaud, O. Møyner, and H.M. Nilsen. Adaptive timestepping, linearization, and a posteriori error control for multiphase flow of immiscible fluids in porous media with wells. *SPE Journal*, 28:554–574, 2023.

[15] E. Ahusborde, B. Amaziane, and M. El Ossmani. Improvement of numerical approximation of coupled multiphase multicomponent flow with reactive geochemical transport in porous media. *Oil & Gas Science and Technology – Revue d'IFP Energies nouvelles*, 73:73, 2018.

[16] E. Ahusborde, B. Amaziane, and M. Id Moulay. High performance computing of 3D reactive multiphase flow in porous media: application to geological storage of CO_2. *Computational Geosciences*, 25:2131–2147, 2021.

[17] E. Ahusborde, M. El Ossmani, and M. Id Moulay. A fully implicit finite volume scheme for single phase flow with reactive transport in porous media. *Mathematics and Computers in Simulation*, 164:3–23, 2019.

[18] R. Al-Khoury and J. Bundschuh. *Computational models for CO_2 geosequestration and compressed air energy storage*. CRC Press, 2014.

[19] S. Al Nazer, M. Jazar, and C. Rosier. Convergence acceleration of iterative sequences for equilibrium chemistry computations. *Computational Geosciences*, 25(5):1509–1538, 2021.

[20] I. Aliguer, C. Rafels, I. Carol, P. Prat, M R Lakshmikantha, and J.M. Segura. Numerical stress initialization in geomechanics via the FEM and a two step procedure. COMPLAS XIII: proceedings of the XIII International Conference on Computational Plasticity: fundamentals and applications, pages 676–677, 2015.

[21] L. Amir and M. Kern. A global method for coupling transport with chemistry in heterogeneous porous media. *Computational Geosciences*, 14:465, 2010.

[22] L. André, M. Azaroual, and A. Menjoz. Numerical simulations of the thermal impact of supercritical CO_2 injection on chemical reactivity in a carbonate saline reservoir. *Transport in Porous Media*, 82:247–274, 2010.

[23] S. Bachu, W.D. Gunter, and E.H. Perkins. Aquifer disposal of CO_2 : Hydrodynamic and mineral trapping. *Energy Conversion and Management*, 35:269–279, 1994.

[24] S. Bandara and K. Soga. Coupling of soil deformation and pore fluid flow using material point method. *Computers and Geotechnics*, 63:194–214, 2015.

[25] R.E. Bank and D.J. Rose. Some errors estimates for the box method. *SIAM Journal on Numerical Analysis*, 24:777–787, 1987.

[26] R.M. Barrett, M. Berry, T. Chan, J.W. Demmel, J.M. Donato, J. Dongarra, V. Eijkhout, R. Pozo, C. Romine, and H. Van der Vorst. *Templates for the Solution of Linear Systems: Building Blocks for Iterative Methods*. Society for Industrial and Applied Mathematics, 1994.

[27] P. Bastian. *Numerical Computation of Multiphase Flows in Porous Media*. Habilitation thesis, Universität Kiel-Technische Fakultät der Christian–Albrechts, 1999.

[28] P. Bastian, M. Blatt, A. Dedner, N.A. Dreier, C. Engwer, R. Fritze, C. Gräser, D. Kempf, R. Klöfkorn, M. Ohlberger, and O. Sander. The DUNE framework: Basic concepts and recent developments. *Computers & Mathematics with Applications*, 81:72–112, 2020.

[29] P. Bastian, M. Blatt, and R. Scheichl. Algebraic multigrid for discontinuous Galerkin discretizations of heterogeneous elliptic problems. *Numerical Linear Algebra with Applications*, 19:367–388, 2012.

[30] M.L. Batzle and Z. Wang. Seismic properties of pore fluids. *Geophysics*, 57:1396–1408, 1992.

[31] M. Beck, A.P. Rinaldi, B. Flemisch, and H. Class. Accuracy of fully coupled and sequential approaches for modeling hydro and geomechanical processes. *Computational Geosciences*, 24:1707–1723, 2020.

[32] M. Beck, G. Seitz, and H. Class. Volume-based modelling of fault reactivation in porous media using a visco-elastic proxy model. *Transport in Porous Media*, 114:505–524, 2016.

[33] K. Benisch, B. Graupner, and S. Bauer. The Coupled OpenGeoSys-ECLIPSE simulator for simulation of CO_2 storage – code comparison for fluid flow and geomechanical processes. *Energy Procedia*, 37:3663–3671, 2013.

[34] M. Bentham and G. Kirby. CO_2 storage in saline aquifers. *Oil & Gas Science and Technology - Revue d'IFP Energies nouvelles*, 60:559–567, 2005.

[35] C.M. Bethke. *Geochemical and Biogeochemical Reaction Modeling: Second Edition*. Cambridge University Press, 2007.

[36] A. Bielinski. *Numerical Simulation of CO_2 Sequestration in Geological Formations*. PhD thesis, University of Stuttgart, 2007.

[37] A. Bielinski, A. Kopp, H. Schütt, and H. Class. Monitoring of CO_2 plumes during storage in geological formations using temperature signals: Numerical investigation. *International Journal of Greenhouse Gas Control*, 2:319–328, 2008.

[38] M. A. Biot. General theory of three-dimensional consolidation. *Journal of Applied Physics*, 12(2):155–164, 1941.

[39] E. Boman, K. Devine, L.A. Fisk, R. Heaphy, B. Hendrickson, V. Leung, C. Vaughan., U. Catalyurek, D. Bozdag, and W. Mitchell. Zoltan home page. *http://cs.sandia.gov/Zoltan*.

[40] M. Borregales Reverón, K. Kumar, F. Radu, C. Rodrigo, and F. Gaspar. A parallel-in-time fixed-stress splitting method for Biot's consolidation model. *Computers & Mathematics with Applications*, 77:1466–1478, 2018.

[41] A.N. Brooks and A.T. Corey. Hydraulic properties of porous media. *Hydrology Papers*, 1964.

[42] F. Brunner and P. Knabner. A global implicit solver for miscible reactive multiphase multicomponent flow in porous media. *Computational Geosciences*, 23:127–148, 2019.

[43] F. Cappa and J. Rutqvist. Modeling of coupled deformation and permeability evolution during fault reactivation induced by deep underground injection of CO_2. *International Journal of Greenhouse Gas Control*, 5:336–346, 2011.

[44] J. Carrayrou. Looking for some reference solutions for the reactive transport benchmark of MoMaS with SPECY. *Computational Geosciences*, 14:393–403, 2010.

[45] J. Carrayrou, C. Bertagnolli, and M. Fahs. Algorithms for activity correction models for geochemical speciation and reactive transport modeling. *American Institute of Chemical Engineers Journal*, 68(1):e17391, 2022.

[46] J. Carrayrou, J. Hoffmann, P. Knabner, S. Kräutle, C. Dieuleveult, J. Erhel, J. Lee, V. Lagneau, K. Mayer, and K. Macquarrie. Comparison of numerical methods for simulating strongly nonlinear and heterogeneous reactive transport problems—the MoMaS benchmark case. *Computational Geosciences*, 14:486–502, 2010.

[47] J. Carrayrou, M. Kern, and P. Knabner. Reactive transport benchmark of MoMaS. *Computational Geosciences*, 14:385–392, 2010.

[48] J. Carrera, M.W. Saaltink, J. Soler-Sagarra, J. Wang, and C. Valhondo. Reactive transport: A review of basic concepts with emphasis on biochemical processes. *Energies*, 15(3):925, 2022.

[49] W.D. Carrier. Goodbye, Hazen; Hello, Kozeny-Carman. *Journal of Geotechnical and Geoenvironmental Engineering*, 129:1054–1056, 2003.

[50] Z. Chen. On the control volume finite element methods and their applications to multiphase flow. *Networks and Heterogeneous Media*, 1(4):689–706, 2006.

[51] Z. Chen, G. Huan, and Y. Ma. *Computational Methods for Multiphase Flows in Porous Media*. Society for Industrial and Applied Mathematics, 2006.

[52] I. Cherezov. *Modelling Convective Dissolution and Reaction of Carbon Dioxide in Saline Aquifers*. PhD thesis, University of Cambridge, 2017.

[53] L.Y. Chin, R. Raghavan, and L. K. Thomas. Fully coupled geomechanics and fluid-flow analysis of wells with stress-dependent permeability. *SPE Journal*, 5:32–45, 2000.

[54] H. Class, A. Ebigbo, R. Helmig, H.K. Dahle, J.M. Nordbotten, M.A. Celia, P. Audigane, M. Darcis, J. Ennis-King, Y. Fan, and B. et al. Flemisch. A benchmark study on problems related to CO_2 storage in geologic formations. *Computational Geosciences*, 13:409–434, 2009.

[55] J. Coulet. *Méthode des Éléments Virtuels pour le Calcul de la Déformation Mécanique Couplée aux Écoulements en Milieux Poreux*. PhD thesis, Sorbonne Université, 2019.

[56] J. Coulet, I. Faille, V. Girault, N. Guy, and F. Nataf. A fully coupled scheme using virtual element method and finite volume for poroelasticity. *Computational Geosciences*, 24(2):381–403, 2020.

[57] O. Coussy. *Mechanics of Porous Continua*. Wiley, 1995.

[58] J.P. Croisille. Finite volume box schemes and mixed methods. *ESAIM: Mathematical Modelling and Numerical Analysis*, 34:1087–1106, 2000.

[59] C.W. Cryer. A comparison of the three-dimensional consolidation theories of Biot and Terzaghi. *The Quarterly Journal of Mechanics and Applied Mathematics*, 16(4):401–412, 1963.

[60] G. Cui, Z. Hu, F. Ning, S. Jiang, and R. Wang. A review of salt precipitation during CO_2 injection into saline aquifers and its potential impact on carbon sequestration projects in china. *Fuel*, 334:126615, 2023.

[61] T.E. Daubert and R.P. Danner. *Physical and thermodynamic properties of pure chemicals: Data compilation*. Taylor & Francis, Washington, DC, 1989.

[62] T. Davis. Algorithm 832: UMFPACK V4.3 - an unsymmetric-pattern multifrontal method. *ACM Transactions on Mathematical Software*, 30:196–199, 2004.

[63] Electricité de France. Finite element *Code_Aster*, analysis of structures and thermomechanics for studies and research. *www.code-aster.org*, 1989-2023.

[64] S. De Simone, V. Vilarrasa, J. Ramírez, A. Alcolea, and P. Meier. Thermal coupling may control mechanical stability of geothermal reservoirs during cold water injection. *Physics and Chemistry of the Earth Parts A/B/C*, 64:117–126, 2013.

[65] D. Denney. Lacq Carbon-Capture and -Sequestration Pilot. *Journal of Petroleum Technology*, 65:128–130, 2013.

[66] E. Detournay and A.H.-D. Cheng. Fundamentals of Poroelasticity. In C. Fairhurst, editor, *Analysis and Design Methods*, pages 113–171. Pergamon, Oxford, 1993.

[67] C. Dieuleveult and J. Erhel. A global approach to reactive transport: application to the MoMas benchmark. *Computational Geosciences*, 14:451–464, 2010.

[68] J. Droniou. Finite volume schemes for diffusion equations: Introduction to and review of modern methods. *Mathematical Models and Methods in Applied Sciences*, 24:1575–1619, 2014.

[69] Z. Duan, N. Møller, and J.H. Weare. An equation of state for the CH_4-CO_2 -H_2O system: Pure systems from 0 to 1000°C and 0 to 8000 bar. *Geochimica et Cosmochimica Acta*, 56(7):2605–2617, 1992.

[70] L.J. Durlofsky. A triangle based mixed finite element—finite volume technique for modeling two phase flow through porous media. *Journal of Computational Physics*, 105(2):252–266, 1993.

[71] L.J. Durlofsky. Accuracy of mixed and control volume finite element approximations to darcy velocity and related quantities. *Water Resources Research*, 30(4):965–973, 1994.

[72] S. Earle. *Physical Geology – 2nd Edition*. Victoria, B.C.: BCcampus, 2019.

[73] M.T. Elenius, D.V. Voskov, and H. Tchelepi. Interactions between gravity currents and convective dissolution. *Advances in Water Resources*, 83:77–88, 2015.

[74] H. Emami-Meybodi, H. Hassanzadeh, C.P. Green, and J. Ennis-King. Convective dissolution of CO_2 in saline aquifers: Progress in modeling and experiments. *International Journal of Greenhouse Gas Control*, 40:238–266, 2015.

[75] R. Ershadnia, C. Wallace, S. Hajirezaie, S. Hosseini, T. Nguyen, D. Sturmer, Z. Dai, and R. Soltanian. Hydro-thermo-chemo-mechanical modeling of carbon dioxide injection in fluvial heterogeneous aquifers. *Chemical Engineering Journal*, 431:133451, 2021.

[76] R. Eymard, T. Gallouët, C. Guichard, R. Herbin, and R. Masson. Tp or not tp, that is the question. *Computational Geosciences*, 18:285–296, 2014.

[77] M. Fahs, J. Carrayrou, A. Younes, and P. Ackerer. On the efficiency of the direct substitution approach for reactive transport problems in porous media. *Water Air and Soil Pollution*, 193:299–308, 2008.

[78] Y. Fan, L.J. Durlofsky, and H.A. Tchelepi. A fully-coupled flow-reactive-transport formulation based on element conservation, with application to CO_2 storage simulations. *Advances in Water Resources*, 42:47–61, 2012.

[79] S.F. Farshidi, Y. Fan, L.J. Durlofsky, and H.A. Tchelepi. Chemical reaction modeling in a compositional reservoir simulation framework. SPE Reservoir Simulation Conference, 2013.

[80] A. Fenghour, W. Wakeham, and V. Vesovic. The viscosity of carbon dioxide. *Journal of Physical and Chemical Reference Data*, 27:31–44, 1998.

[81] B. Flemisch. *Tackling Coupled Problems in Porous Media: Development of Numerical Models and an Open Source Simulator*. Habilitation thesis, Universität Stuttgart, Institut für Wasser- und Umweltsystemmodellierung, 2013.

[82] B. Flemisch, I. Berre, W. Boon, A. Fumagalli, N. Schwenck, A. Scotti, I. Stefansson, and A. Tatomir. Benchmarks for single-phase flow in fractured porous media. *Advances in Water Resources*, 111:239–258, 2018.

[83] B. Flemisch, M. Darcis, K. Erbertseder, B. Faigle, A. Lauser, K. Mosthaf, S. Müthing, P. Nuske, A. Tatomir, M. Wolff, and R. Helmig. DuMux: DUNE for multi-{phase,component,scale,physics,...} flow and transport in porous media. *Advances in Water Resources*, 34:1102–1112, 2011.

[84] P.A. Forsyth. A control volume finite element approach to napl groundwater contamination. *SIAM Journal on Scientific and Statistical Computing*, 12(5):1029–1057, 1991.

[85] L.K. Fung, A.D. Hiebert, and L.X. Nghiem. Reservoir simulation with a control-volume finite-element method. *SPE Reservoir Engineering*, 7(03):349–357, 1992.

[86] P. Gamazo, L.J. Slooten, J. Carrera, M.W. Saaltink, S. Bea, and J. Soler. PROOST: object-oriented approach to multiphase reactive transport modeling in porous media. *Journal of Hydroinformatics*, 18:310–328, 2015.

[87] J. Garcia. Density of aqueous solutions of CO_2 . *Density of Aqueous Solutions of CO_2* , 2001.

[88] T.T. Garipov, P. Tomin, R. Rin, D.V. Voskov, and H.A. Tchelepi. Unified thermo-compositional-mechanical framework for reservoir simulation. *Computational Geosciences*, 22(4):1039–1057, 2018.

[89] S. Geiger, S. Roberts, S.K. Matthäi, C. Zoppou, and A. Burri. Combining finite element and finite volume methods for efficient multiphase flow simulations in highly heterogeneous and structurally complex geologic media. *Geofluids*, 4(4):284–299, 2004.

[90] I.B. Gharbia, J. Dabaghi, V. Martin, and M. Vohralík. A posteriori error estimates for a compositional two-phase flow with nonlinear complementarity constraints. *Computational Geosciences*, 24:1031–1055, 2020.

[91] D. Gläser. *Discrete fracture modeling of multi-phase flow and deformation in fractured poroelastic media.* PhD thesis, Universität Stuttgart, 2020.

[92] U.J. Goerke, C.H. Park, W. Wang, A. Singh, and O. Kolditz. Numerical simulation of multiphase hydromechanical processes induced by CO_2 injection into deep saline aquifers. *Oil & Gas Science and Technology – Rev. IFP Energies nouvelles*, 66:105–118, 2011.

[93] Y. Gou, Z. Hou, M. Li, W. Feng, and H. Liu. Coupled thermo–hydro–mechanical simulation of CO_2 enhanced gas recovery with an extended equation of state module for TOUGH2MP-FLAC3D. *Journal of Rock Mechanics and Geotechnical Engineering*, 8:904–920, 2016.

[94] R. Haagenson, H. Rajaram, and J. Allen. A generalized poroelastic model using FEniCS with insights into the Noordbergum effect. *Computers & Geosciences*, 135:104399, 2019.

[95] W. Hackbusch. On first and second order box schemes. *Computing*, 41:277–296, 1989.

[96] G.E. Hammond, P.C. Lichtner, C. Lu, and R.T. Mills. PFLOTRAN: Reactive flow & transport code for use on laptops to leadership-class supercomputers. In Zhang et al. [227], pages 141–159.

[97] G. Han and M.B. Dusseault. Description of fluid flow around a wellbore with stress-dependent porosity and permeability. *Journal of Petroleum Science and Engineering*, 40(1):1–16, 2003.

[98] Y. Hao, Y. Sun, and J. Nitao. Overview of NUFT: A versatile numerical model for simulating flow and reactive transport in porous media. In Zhang et al. [227], pages 213–240.

[99] R. Helmig. *Multiphase Flow and Transport Processes in the Subsurface: a Contribution to the Modeling of Hydrosystems*. Springer Berlin, 1997.

[100] R. Herbin and F. Hubert. Benchmark on discretization schemes for anisotropic diffusion problems on general grids. In *Finite volumes for complex applications V*, pages 659–692. ISTE, London, 2008.

[101] J. Hoffmann, S. Kräutle, and P. Knabner. A parallel global-implicit 2D solver for reactive transport problems in porous media based on a reduction scheme and its application to the MoMaS benchmark problem. *Computational Geosciences*, 14:421–433, 2010.

[102] Z. Hou, Y. Gou, and J. Rutqvist. Integration of the codes FLAC3D and TOUGHREACT for THMC coupled geo–process in reservoirs. SPE EUROPEC 2010. European Association of Geoscientists & Engineers, 2010.

[103] Z.Q. Huang, P.H. Winterfeld, Y. Xiong, Wu Y.S., and J. Yao. Parallel simulation of fully-coupled thermal-hydro-mechanical processes in CO_2 leakage through fluid-driven fracture zones. *International Journal of Greenhouse Gas Control*, 34:39–51, 2015.

[104] R. Huber and R. Helmig. Node-centered finite volume discretizations for the numerical simulation of multiphase flow in heterogeneous porous media. *Computational Geosciences*, 4:141–164, 2000.

[105] P.S. Huyakorn and G.F. Pinder. A new finite element technique for the solution of two-phase flow through porous media. *Advances in Water Resources*, 1(5):285–298, 1978.

[106] M. Id Moulay. *Simulation Numérique 3D d'Écoulement Multiphysiques Réactifs en Milieux Poreux*. PhD thesis, Université de Pau et des Pays de l'Adour, 2019.

[107] IEA. Energy Technology Perspectives 2012 – Analysis, 2012.

[108] IEA. Net zero by 2050. *https://www.iea.org/reports/net-zero-by-2050/*, 2021.

[109] J.C. Jaeger, N.G.W. Cook, and R.W. Zimmerman. *Fundamentals of rock mechanics (4th ed.)*. Blackwell Pub., 2007.

[110] B. Jha and R. Juanes. Coupled multiphase flow and poromechanics: A computational model of pore pressure effects on fault slip and earthquake triggering. *Water Resources Research*, 50:3776–3808, 2014.

[111] L. Jiang, S. Wang, D. Liu, W. Zhang, G. Lu, Y. Liu, and J. Zhao. Change in convection mixing properties with salinity and temperature: CO_2 storage application. *Polymers*, 12(9):2084, 2020.

[112] T.B. Johansson, A. Patwardhan, N. Nakićenović, and L. Gomez-Echeverri, editors. *Global Energy Assessment (GEA)*. Cambridge University Press ; International Institute for Applied Systems Analysis, Cambridge: Laxenburg, Austria, 2012.

[113] E. Keilegavlen, R. Berge, A. Fumagalli, M. Starnoni, I. Stefansson, J. Varela, and I. Berre. Porepy: an open-source software for simulation of multiphysics processes in fractured porous media. *Computational Geosciences*, 25:243–265, 2021.

[114] E. Keilegavlen and J.M. Nordbotten. Finite volume methods for elasticity with weak symmetry. *International Journal for Numerical Methods in Engineering*, 112:939–962, 2015.

[115] J. Kim. *Sequential Methods for Coupled Geomechanics and Multiphase Flow*. PhD thesis, Stanford University, 2010.

[116] J. Kim, H.A. Tchelepi, and R. Juanes. Stability and convergence of sequential methods for coupled flow and geomechanics: Drained and undrained splits. *Computer Methods in Applied Mechanics and Engineering*, 200:2094–2116, 2011.

[117] J. Kim, H.A. Tchelepi, and R. Juanes. Stability and convergence of sequential methods for coupled flow and geomechanics: Fixed-stress and fixed-strain splits. *Computer Methods in Applied Mechanics and Engineering*, 200(13):1591–1606, 2011.

[118] M.M. Knodel, S. Kräutle, and P. Knabner. Global implicit solver for multiphase multicomponent flow in porous media with multiple gas components and general reactions. *Computational Geosciences*, 26:697–724, 2022.

[119] T. Koch, D. Gläser, K. Weishaupt, S. Ackermann, M. Beck, B. Becker, S. Burbulla, H. Class, E. Coltman, S. Emmert, T. Fetzer, C. Grüninger, K. Heck, J. Hommel, T. Kurz, M. Lipp, F. Mohammadi, S. Scherrer, M. Schneider, G. Seitz, L. Stadler, M. Utz, F. Weinhardt, and B. Flemisch. *DuMu*^{X} 3 – an open-source simulator for solving flow and transport problems in porous media with a focus on model coupling. *Computers & Mathematics with Applications*, 81:423–443, 2021.

[120] O. Kolditz, S. Bauer, et al. OpenGeoSys: an open-source initiative for numerical simulation of thermo-hydro-mechanical/chemical (THM/C) processes in porous media. *Environmental Earth Sciences*, 67:589–599, 2012.

[121] S. Krevor, M.J. Blunt, S.M. Benson, C.H. Pentland, C. Reynolds, A. Al-Menhali, and B. Niu. Capillary trapping for geologic carbon dioxide storage – From pore scale physics to field scale implications. *International Journal of Greenhouse Gas Control*, 40:221–237, 2015.

[122] V. Lagneau and J. Van Der Lee. HYTEC results of the MoMaS reactive transport benchmark. *Computational Geosciences*, 14:435–449, 2010.

[123] A.C. Lasaga. Chemical kinetics of water-rock interactions. *Journal of Geophysical Research: Solid Earth*, 89:4009–4025, 1984.

[124] Y. Le Gallo, L. Trenty, and A. Michel. Thermo-hydro-chemical performance assessment of CO_2 storage in saline aquifer. Eurotherm 2007: reactive heat transfer in porous media, 2007.

[125] C. Li and L. Laloui. Coupled multiphase thermo-hydro-mechanical analysis of supercritical CO_2 injection: Benchmark for the In Salah surface uplift problem. *International Journal of Greenhouse Gas Control*, 51:394–408, 2016.

[126] G. Linga, O. Møyner, H.M. Nilsen, A. Moncorgé, and K.A. Lie. An implicit local time-stepping method based on cell reordering for multiphase flow in porous media. *Journal of Computational Physics*, 6:100051, 2020.

[127] Y. Liu, H. Yang, C. Jiang, and C. Yang. A scalable fully implicit method with adaptive time stepping for unsteady compressible inviscid flows. *Computers & Structures*, 176:1–12, 2016.

[128] S.R. Logan. The origin and status of the Arrhenius Equation. *Journal of Chemical Education*, 59:279, 1982.

[129] P. Longuemare, M. Mainguy, P. Lemonnier, A. Onaisi, C. Gérard, and N. Koutsabeloulis. Geomechanics in reservoir simulation: Overview of coupling methods and field case study. *Oil & Gas Science and Technology - Revue d'IFP Energies nouvelles, Institut Français du Pétrole (IFP)*, 57:471–483, 2002.

[130] P. Loria and M.B.H. Bright. Lessons captured from 50 years of CCS projects. *The Electricity Journal*, 34:106998, 2021.

[131] X. Lyu and D. Voskov. Advanced modeling of enhanced CO_2 dissolution trapping in saline aquifers. *International Journal of Greenhouse Gas Control*, 127:103907, 2023.

[132] X. Lyu, D. Voskov, and W.R. Rossen. Numerical investigations of foam-assisted CO_2 storage in saline aquifers. *International Journal of Greenhouse Gas Control*, 108, 2021.

[133] H. Machat and J. Carrayrou. Comparison of linear solvers for equilibrium geochemistry computations. *Computational Geosciences*, 21(1):131–150, 2017.

[134] J. Mandel. Consolidation des sols (étude mathématique). *Geotechnique*, 3:287–299, 1953.

[135] M.J. Martinez, P. Newell, J.E. Bishop, and D. Turner. Coupled multiphase flow and geomechanics model for analysis of joint reactivation during CO_2 sequestration operations. *International Journal of Greenhouse Gas Control*, 17:148–160, 2013.

[136] A. Mathieson, J. Midgely, I.W. Wright, N. Saoula, and P.S. Ringrose. In Salah CO_2 storage JIP: CO_2 sequestration monitoring and verification technologies applied at Krechba, Algeria. *Energy Procedia*, 4:3596–3603, 2011.

[137] K. Mayer, E. Frind, and D. Blowes. Multicomponent reactive transport modeling in variably saturated porous media using a generalized formulation for kinetically controlled reactions. *Water Resources Research*, 38:1–21, 2002.

[138] K. Mayer and K. Macquarrie. Solution of the MoMaS reactive transport benchmark with MIN3P—model formulation and simulation results. *Computational Geosciences*, 14:405–419, 2010.

[139] B. Metz, O. Davidson, H. de Coninck, M. Loos, and L. Meyer. IPCC special report on carbon dioxide capture and storage. *Policy Stud.*, 2005.

[140] E.E. Michaelides. Thermodynamic properties of geothermal fluids. *Transactions - Geothermal Resources Council (United States)*, 5, 1981.

[141] A. Mikelić, B. Wang, and M.F. Wheeler. Numerical convergence study of iterative coupling for coupled flow and geomechanics. *Computational Geosciences*, 18:325–341, 2014.

[142] A. Mikelić and M.F. Wheeler. Convergence of iterative coupling for coupled flow and geomechanics. *Computational Geosciences*, 17:455–461, 2013.

[143] G. Miller and S. Spoolman. *Environmental Science: Problems, Connections and Solutions*. Cengage Learning, 2007.

[144] R.J. Millington and J.P. Quirk. Permeability of porous solids. *Transactions of the Faraday Society*, 57:1200–1207, 1961.

[145] F.M.M. Morel and J.G. Hering. *Principles and Applications of Aquatic Chemistry*. John Wiley & Sons, 1993.

[146] A.P. Morris, D.A. Ferrill, and D.B. Henderson. Slip-tendency analysis and fault reactivation. *Geology*, 24:275–278, 1996.

[147] P. Mostaghimi, J.R. Percival, D. Pavlidis, R.J. Ferrier, G.J. Gomes, Jefferson L.M.A.and Gorman, M.D. Jackson, S.J. Neethling, and C.C. Pain. Anisotropic mesh adaptivity and control volume finite element methods for numerical simulation of multiphase flow in porous media. *Mathematical Geosciences*, 47(4):417–440, 2015.

[148] A. Negara, A. Salama, and S. Sun. Multiphase flow simulation with gravity effect in anisotropic porous media using multipoint flux approximation. *Computers & Fluids*, 114:66–74, 2015.

[149] R. Neumann, P. Bastian, and O. Ippisch. Modeling and simulation of two-phase two-component flow with disappearing nonwetting phase. *Computational Geosciences*, 17:139–149, 2012.

[150] P. Newell, A. Ilgen, V. Vilarrasa, K. Bandilla, B. Mcpherson, J. Rutqvist, R. Pawar, L. Lake, N. Espinoza, J. Ajo-Franklin, S. Hovorka, M. Hu, S. Bryant, M. Celia, M. Cha, Z. Dai, A. Freedman, G. Guthrie, A. Hakala, and R. Zhang. *Science of Carbon Storage in Deep Saline Formations: Process Coupling across Time and Spatial Scales*. Elsevier, 2019.

[151] J.P. Nicot, S.A. Hosseini, and S.V. Solano. Are single-phase flow numerical models sufficient to estimate pressure distribution in CO_2 sequestration projects? *Energy Procedia*, 4:3919–3926, 2011.

[152] A. Niemi, J. Bear, and J. Bensabat. *Geological Storage of CO_2 in Deep Saline Formations*. Springer, 2017.

[153] J. Niessner and R. Helmig. Multi-scale modelling of two-phase–two-component processes in heterogeneous porous media. *Numerical Linear Algebra with Applications*, 13:699–715, 2006.

[154] H. Nishikawa. On large start-up error of BDF2. *Journal of Computational Physics*, 392:456–461, 2019.

[155] J.M. Nordbotten. Stable cell-centered finite volume discretization for Biot equations. *SIAM Journal on Numerical Analysis*, 54:942–968, 2016.

[156] J.M. Nordbotten and M.A. Celia. *Geological Storage of CO_2: Modeling Approaches for Large-Scale Simulation*. John Wiley & Sons, 2011.

[157] J.M. Nordbotten, M.A. Celia, and S. Bachu. Injection and storage of CO_2 in deep saline aquifers: Analytical solution for CO_2 plume evolution during injection. *Transport in Porous Media*, 58:339–360, 2005.

[158] P.H. Olden, G. Pickup, M. Jin, E.J. Mackay, S.A. Hamilton, J.M. Somerville, and A.C. Todd. Use of rock mechanics laboratory data in geomechanical modelling to increase confidence in CO_2 geological storage. *International Journal of Greenhouse Gas Control*, 11:304–315, 2012.

[159] F.M. Orr Jr. CO_2 capture and storage: are we ready? *Energy & Environmental Science*, 2:449–458, 2009.

[160] P. Pan, Z. Wu, X. Feng, and F. Yan. Geomechanical modeling of CO_2 geological storage: A review. *Journal of Rock Mechanics and Geotechnical Engineering*, 8:936–947, 2016.

[161] K.S. Pitzer. Thermodynamics of electrolytes. I. Theoretical basis and general equations. *The Journal of Physical Chemistry*, 77:268–277, 1973.

[162] S. Prasun, S. Kim, and S.A. Hosseini. Geologic carbon storage: Implications of two-phase flow on injection-induced stress on faults. COMSOL Conference, Boston, 2018.

[163] M. Preisig and J. Prevost. Coupled multi-phase thermo-poromechanical effects. Case study: CO_2 injection at In Salah, Algeria. *International Journal of Greenhouse Gas Control*, 5:1055–1064, 2011.

[164] Global Carbon Project. Supplemental data of Global Carbon Budget 2019 [Data set], 2019.

[165] A. Raza, R. Gholami, R. Rezaee, C. Bing, R. Nagarajan, and M. Ali. CO_2 storage in heterogeneous aquifer: A study on the effect of temperature and mineral precipitation. *IOP Conference Series: Materials Science and Engineering*, 206:012002, 06 2017.

[166] A.P. Rinaldi, J. Rutqvist, K. Luu, L. Blanco-Martín, M. Hu, M.L. Sentís, L. Eberle, and P. Kaestli. TOUGH3-FLAC3D: a modeling approach for parallel computing of fluid flow and geomechanics. *Computational Geosciences*, 26:1563–1580, 2022.

[167] P.S. Ringrose and A.S. Mathieson et al. The In Salah CO_2 storage project: Lessons learned and knowledge transfer. *Energy Procedia*, 37:6226–6236, 2013.

[168] B. Riviere and X. Yang. A DG method for the simulation of CO_2 storage in saline aquifer. In A. Deines, D. Ferrero, E. Graham, M.S. Im, C. Manore, and C. Price, editors, *Advances in the Mathematical Sciences*, pages 205–232. Springer International Publishing, 2018.

[169] J. Rohmer and D. Seyedi. Coupled large scale hydromechanical modelling for caprock failure risk assessment of CO_2 storage in deep saline aquifers. *Oil & Gas Science and Technology - Revue de l'IFP Energies Nouvelles*, 65(3):503–517, 2010.

[170] J. Rutqvist. The geomechanics of CO_2 storage in deep sedimentary formations. *Geotechnical and Geological Engineering*, 30:525–551, 2012.

[171] J. Rutqvist. An overview of TOUGH-based geomechanics models. *Computers & Geosciences*, 108:56–63, 2017.

[172] J. Rutqvist, A. Pio Rinaldi, V. Vilarrasa, and F. Cappa. Chapter 10 - Numerical geomechanics studies of geological carbon storage (GCS). In P. Newell and A.G. Ilgen, editors, *Science of Carbon Storage in Deep Saline Formations*, pages 237–252. Elsevier, 2019.

[173] J. Rutqvist and C.F. Tsang. A study of caprock hydromechanical changes associated with CO_2 injection into a brine aquifer. *Environmental Geology*, 42:296–305, 2002.

[174] M.W. Saaltink, C. Ayora, and J. Carrera. A mathematical formulation for reactive transport that eliminates mineral concentrations. *Water Resources Research*, 34:1649–1656, 1998.

[175] P. Salinas, D. Pavlidis, Z. Xie, C. Jacquemyn, Y. Melnikova, M.D. Jackson, and C.C. Pain. Improving the robustness of the control volume finite element method with application to multiphase porous media flow. *International Journal for Numerical Methods in Fluids*, 85(4):235–246, 2017.

[176] P. Salinas, D. Pavlidis, Z. Xie, H. Osman, C.C. Pain, and M.D. Jackson. A discontinuous control volume finite element method for multi-phase flow in heterogeneous porous media. *Journal of Computational Physics*, 352:602–614, 2018.

[177] J. Samper, C. Yang, L. Zheng, L. Montenegro, Y. Xu, Z. Dai, G. Zhang, C. Lu, and S. Moreira. CORE^{2D} V4: A code for water flow, heat and solute transport, geochemical reactions, and microbial processes. In Zhang et al. [227], pages 160–185.

[178] D. Scheer, H. Class, and B. Flemisch. *Subsurface Environmental Modelling Between Science and Policy*. Springer, 2021.

[179] M. Schneider, B. Flemisch, and R. Helmig. Monotone nonlinear finite-volume method for nonisothermal two-phase two-component flow in porous media. *International Journal for Numerical Methods in Fluids*, 84:352–381, 2016.

[180] M. Schneider, D. Gläser, B. Flemisch, and R. Helmig. Comparison of finite-volume schemes for diffusion problems. *Oil & Gas Science and Technology*, 73:82, 2018.

[181] N. Seigneur, A. Socié, and K.U. Mayer. A compositional global implicit approach for modeling coupled multicomponent reactive transport. *Water Resources Research*, 59:e2021WR031774, 2023.

[182] A. Settari and D. Walters. Advances in coupled geomechanical and reservoir modeling with applications to reservoir compaction. *SPE Journal*, 6:334–342, 2001.

[183] R.R. Settgast, B.C. Corbett, S. Klevtsov, F. Hamon, C. Sherman, M. Cusini, T. Gazzola, W. Tobin, J. White, N. Castelletto, A. Borio, A. Franceschini, J. Huang, B. Han, H. Gross, J. Franc, A. Mazuyer, J. Besset, A. Citrain, A. Vargas, M. Cremon, Y. Hao, M. Khait, X. Lacoste, S. Semnani, S. Frambati, M. N'diaye, S. Nguyen, and H.M. Morgan. GEOS next-gen simulation for geologic carbon storage. *https://www.geosx.org/*, 2022.

[184] I. Sin and J. Corvisier. Multiphase multicomponent reactive transport and flow modeling. *Reviews in Mineralogy and Geochemistry*, 85:143–195, 2019.

[185] I. Sin, V. Lagneau, L. De Windt, and J. Corvisier. 2D simulation of natural gas reservoir by two-phase multicomponent reactive flow and transport—description of a benchmarking exercise. *Mathematics and Computers in Simulation*, 137:431–447, 2017.

[186] SINTEF. Johansen data set. *https://www.sintef.no/projectweb/matmora/downloads/johansen/*,.

[187] H. Siriwardane, R. Gondle, and G. Bromhal. Coupled flow and deformation modeling of carbon dioxide migration in the presence of a caprock fracture during injection. *Energy & Fuels*, 27:4232–4243, 2013.

[188] A.W. Skempton. The pore-pressure coefficients a and b. *Géotechnique*, 4:143–147, 1954.

[189] M. Smith. *ABAQUS/Standard User's Manual, Version 6.9*. Dassault Systèmes Simulia Corp, United States, 2009.

[190] H. Soltanzadeh and A. Jafari. Thermo-poro-mechanical analysis of the effects of low-temperature CO_2 injection on caprock integrity. SPE Canada Unconventional Resources Conference, 2013.

[191] W.H. Somerton, A.H. El-Shaarani, and S.M. Mobarak. High temperature behavior of rocks associated with geothermal type reservoirs. *SPE Western Regional Meeting, Proceedings*, 1974.

[192] R. Span and W. Wagner. A new equation of state for carbon dioxide covering the fluid region from the triple-point temperature to 1100 K at pressures up to 800 MPa. *Journal of Physical and Chemical Reference Data*, 25(6):1509–1596, 1996.

[193] N. Spycher and K. Pruess. CO_2-H_2O mixtures in the geological sequestration of CO_2. II. Partitioning in chloride brines at 12-100 °C and up to 600 bar. *Geochimica et Cosmochimica Acta*, 69:3309–3320, 2005.

[194] IEA Statistics. CO_2 emissions from fuel combustion 2019 - Highlights. page 165, 2019.

[195] C.I. Steefel. Reactive transport at the crossroads. *Reviews in Mineralogy and Geochemistry*, 85(1):1–26, 2019.

[196] C.I. Steefel, C.A.J. Appelo, B. Arora, D. Jacques, T. Kalbacher, O. Kolditz, V. Lagneau, P.C. Lichtner, K.U. Mayer, J.C.L. Meeussen, S. Molins, D. Moulton, H. Shao, J. Šimůnek, N. Spycher, S.B. Yabusaki, and G.T. Yeh. Reactive transport codes for subsurface environmental simulation. *Computational Geosciences*, 19:445–478, 2015.

[197] C.I. Steefel and A. Lasaga. A coupled model for transport of multiple chemical-species and kinetic precipitation dissolution reactions with application to reactive flow in single-phase hydrothermal systems. *Americal Journal of Science*, 294:529–592, 1994.

[198] J. Tao, Y. Wu, D. Elsworth, P. Li, and Y. Hao. Coupled thermo-hydro-mechanical-chemical modeling of permeability evolution in a CO_2-circulated geothermal reservoir. *Geofluids*, 2019:5210730, 2019.

[199] K. Terzaghi. *Theoretical Soil Mechanics*. John Wiley & Sons, 1943.

[200] S. Thibeau, P. Chiquet, C. Prinet, and M. Lescanne. Lacq-Rousse CO_2 capture and storage demonstration pilot: Lessons learnt from reservoir modelling studies. *Energy Procedia*, 37:6306–6316, 2013.

[201] D. Tran, L. Nghiem, and L. Buchanan. Improved iterative coupling of geomechanics with reservoir simulation. *SPE Reservoir Simulation Symposium, Proceedings*, 2005.

[202] S.R.T. Tripuraneni, A. Novikov, and D. Voskov. Nonlinear finite volume discretization of geomechanical problem. *International Journal for Numerical and Analytical Methods in Geomechanics*.

[203] B.M. Tutolo, X.-Z. Kong, W.E. Seyfried, and M.O. Saar. High performance reactive transport simulations examining the effects of thermal, hydraulic, and chemical (THC) gradients on fluid injectivity at carbonate CCUS reservoir scales. *International Journal of Greenhouse Gas Control*, 39:285–301, 2015.

[204] J. Van Der Lee, L. De Windt, V. Lagneau, and P. Goblet. Module-oriented modeling of reactive transport with HYTEC. *Computers & Geosciences*, 29:265–275, 2003.

[205] M. Van Genuchten. A closed-form equation for predicting the hydraulic conductivity of unsaturated soils. *Soil Science Society of America Journal*, 44:892–898, 1980.

[206] P.E. Van Keken, D.A. Yuen, and L.R. Petzold. DASPK: A new high order and adaptive time-integration technique with applications to mantle convection with strongly temperature-and pressure-dependent rheology. *Geophysical & Astrophysical Fluid Dynamics*, 80(1):57–74, 1995.

[207] A. Verruijt. *Theory and Problems of Poroelasticity*. 2013.

[208] V. Vilarrasa, J. Carrera, and S. Olivella. Two-phase flow effects on the CO_2 injection pressure evolution and implications for the caprock geomechanical stability. *E3S Web of Conferences*, 9:04007, 2016.

[209] V. Vilarrasa, J. Ramírez, D. Bolster, and M. Dentz. Semi-analytical solution for CO_2 plume shape and pressure evolution during CO_2 injection in deep saline formations. *Transport in Porous Media*, 97:43–65, 2013.

[210] V. Vilarrasa and J. Rutqvist. Thermal effects on geologic carbon storage. *Earth-Science Reviews*, 165:245–256, 2017.

[211] M. Vohralík and M.F. Wheeler. A posteriori error estimates, stopping criteria, and adaptivity for two-phase flows. *Computational Geosciences*, 17:789–812, 2013.

[212] D.V. Voskov, H. Henley, and A. Lucia. Fully compositional multi-scale reservoir simulation of various CO_2 sequestration mechanisms. *Computers & Chemical Engineering*, 96:183–195, 2017.

[213] W. Wagner, J. R. Cooper, A. Dittmann, J. Kijima, H.-J. Kretzschmar, A. Kruse, R. Mares˘, K. Oguchi, H. Sato, I. Sto¨cker, O. S˘ifner, Y. Takaishi, I. Tanishita, J. Tru¨benbach, and Th. Willkommen. The IAPWS industrial formulation 1997 for the thermodynamic properties of water and steam. *Journal of Engineering for Gas Turbines and Power*, 122(1):150–184, 2000.

[214] M.F. Wheeler, S. Sun, and S.G. Thomas. Modeling of flow and reactive transport in IPARS. In Zhang et al. [227], pages 42–73.

[215] S.P. White. Multiphase nonisothermal transport of systems of reacting chemicals. *Water Resources Research*, 31:1761–1772, 1995.

[216] H. Wu, V. Vilarrasa, S. De Simone, M. Saaltink, and F. Parisio. Analytical solution to assess the induced seismicity potential of faults in pressurized and depleted reservoirs. *Journal of Geophysical Research: Solid Earth*, 126(1), 2021.

[217] M. Xie, O. Kolditz, and H. Moog. A geochemical transport model for thermo-hydro-chemical (THC) coupled processes with saline water. *Water Resources Research*, 47:W02545, 2011.

[218] B. Xu, K. Nagashima, J.M. DeSimone, and C.S. Johnson. Diffusion of water in liquid and supercritical carbon dioxide: An NMR study. *Journal of Physical Chemistry A*, 107:1–3, 2003.

[219] T. Xu, J. Apps, and K. Pruess. Numerical simulation to study mineral trapping for CO_2 disposal in deep aquifers. *Applied Geochemistry*, 19:917–936, 2004.

[220] T. Xu, E. Sonnenthal, N. Spycher, G. Zhang, L. Zheng, and K. Pruess. TOUGHREACT: A simulation program for subsurface reactive chemical transport under non-isothermal multiphase flow conditions. In Zhang et al. [227], pages 74–95.

[221] G.T. Yeh and V.S. Tripathi. A critical evaluation of recent developments in hydrogeochemical transport models of reactive multichemical components. *Water Resources Research*, 25:93–108, 1989.

[222] G.T. Yeh, V.S. Tripathi, J.P. Gwo, H.P. Cheng, R.J. Cheng, K.M. Salvage, M.H. Li, Y.L. Fang, Y. Li, J.T. Sun, F. Zhang, and M.D. Siegel. HYDROGEOCHEM: A coupled model of variably saturated flow, thermal transport, and reactive biogeochemical transport. Groundwater reactive transport models. In Zhang et al. [227], pages 3–41.

[223] S. Yin, M.B. Dusseault, and L. Rothenburg. Coupled THMC modeling of CO_2 injection by finite element methods. *Journal of Petroleum Science and Engineering*, 80:53–60, 2011.

[224] A. Younes and P. Ackerer. Empirical versus time stepping with embedded error control for density-driven flow in porous media. *Water Resources Research*, 46(8), 2010.

[225] A. Younes, B. Koohbor, M. Fahs, and H. Hoteit. An efficient discontinuous Galerkin - mixed finite element model for variable density flow in fractured porous media. *Journal of Computational Physics*, 477:111937, 2023.

[226] C. Zhang, S. Zarrouk, and R. Archer. Development of a fully coupled flow-geomechanics simulator for flow in saturated porous media. *Proceedings of ICCM15*, 2015.

[227] F. Zhang, G.T. Yeh, and J.C. Parker, editors. *Groundwater Reactive Transport Models*. Bentham Publishers, United Arab Emirates, 2012.

[228] R. Zhang, P.H. Winterfeld, X. Yin, Y. Xiong, and Y.S. Wu. Sequentially coupled THMC model for CO_2 geological sequestration into a 2D heterogeneous saline aquifer. *Journal of Natural Gas Science and Engineering*, 27:579–615, 2015.

[229] R. Zhang, X. Yin, P.H. Winterfeld, and Y.S Wu. A fully coupled thermal-hydrological-mechanical-chemical model for CO_2 geological sequestration. *Journal of Natural Gas Science and Engineering*, 28:280–304, 2016.

[230] R. Zhao and J. Cheng. Non-isothermal modeling of CO_2 injection into saline aquifers at a low temperature. *Environmental Earth Sciences*, 73:5307–5316, 2015.

[231] R. Zhao and J. Cheng. Effects of temperature on salt precipitation due to formation dry-out during CO_2 injection. *Greenhouse Gases: Science and Technology*, 7:624–637, 2017.